Nanoscale Liquid Dynamics in Membrane Matrices: Insights into Confinement, Molecular Interactions, and Hydration

Rui Zhang

Dissertation submitted to the faculty of the Virginia Polytechnic Institute and State University in partial fulfillment of the requirements for the degree of

Doctor of Philosophy
In
Chemistry

Louis A. Madsen, Chair
Diego Troya, Co-Chair
James M. Tanko
Guoliang Liu

April 21, 2021
Blacksburg, Virginia

Keywords: ionomer membrane, confined liquid, NMR diffusometry, MD simulations, self-diffusion, activation energy, residence time

Nanoscale Liquid Dynamics in Membrane Matrices: Insights into Confinement, Molecular Interactions, and Hydration

Rui Zhang

Abstract

This dissertation focuses on the fundamental understanding of liquid dynamics confined in polymer membranes. Such knowledge guides the development of better polymer membranes for practical applications and contributes to the general understanding of confined liquid dynamics in various nanoporous materials. First, we investigate the membrane transport by experimental measurements on a PFSA membrane and computer modeling of the confined liquid molecules. We probe the nano-scale environment in the ionomer membrane by determining the activation energy of diffusion. We notice two structural features of the PFSA membrane that dominate membrane transport. At relatively high hydrations, the nano-scale phase-separation creates bulk-like water in the ionomer membrane and prompts fast transport of mobile species. At relatively low hydrations, the nanoconfinement of the polymer matrix leads to the ordering of confined water and prompts a high energy barrier for transport. We then delve deeper into the confinement effect by molecular modeling of various nanoconfining geometries, including carbon nanotubes, parallel graphene sheets, and parallel rigid rods. We notice retarded water dynamics under hydrophobic confinement regardless of the geometry. We further investigate the confined water by determining the residence time of water around water, which evaluates the timescale of associations between water molecules. We learn that a decreasing confinement size prompts longer associations among water molecules. Further, we propose that the prolonged associations are responsible for the retarded water dynamics under hydrophobic confinement. Next, we turn our attention to the effect of interactions between mobile species (mostly water molecules) and a confining surface. In ionomer membranes, interactions between mobile species and the ionic groups dominate the water-

surface interactions. We start by looking at water-ion interactions in bulk solutions. Using solutions at varying concentrations, we notice a temperature-concentration superposition behavior from diffusion coefficients of water molecules and ions in the solutions in both experimental and computational results. Observation of this superposition behavior in bulk solutions is unprecedented. The temperature-concentration superposition parallels the well-known time-temperature superposition. We are able to extract the offset of reciprocal temperature, which fits well to a Williams-Landel-Ferry type equation. The temperature-concentration superposition points to the new perspective that the effect of ions on water dynamics can be similar to the effect of lowering temperature. We further investigate the effect of ions by modeling ions/charges onto confining geometries. Remarkably, we reveal that the presence of ions can break the ordered water structure induced by confinement. The hydrophobic confinement prompts the ordering of water molecules, which leads to slower diffusion and higher activation energy. The presence of ions/charges on the confining surface has multiple effects on the dynamics of confined water. First, the ions associate strongly with neighboring water molecules while breaking the hydrogen-bonding network between water molecules. Second, the disruption of the hydrogen-bonding network leads to decreased activation energy of diffusion and enhanced water mobility. At relatively high ion density, the water-ion interactions overcome the structure-breaking effect and lead to retarded water diffusion. Overall, the studies presented in this dissertation augment our understanding of water transport in nanostructures by revealing the rich behavior of liquid-water dynamics under both hydrophobic and ionic confinement.

Nanoscale Liquid Dynamics in Membrane Matrices: Insights into Confinement, Molecular Interactions, and Hydration

Rui Zhang

General Audience Abstract

Polymer membranes, which are thin films of synthetic polymers such as plastics and rubbers, find applications in a variety of important fields. For example, the hydrogen fuel cell, which converts hydrogen fuel into electricity and is a promising candidate for electric vehicles, relies on a polymer membrane to transport hydrogen fuel. Polymer membranes are also the state-of-art solution to water desalination, which converts sea water into fresh drinking water. Thus, the broad applications of polymer membranes are of great environmental and social merit. It is widely accepted that the performance of a polymer membrane depends on its microscopic structure. This dissertation aims to reveal the microscopic structure-performance relations in polymer membranes. We utilize both experimental and computational methods to probe the transport performance of target molecules in polymer membranes and then relate the performance with the membrane structures. Such knowledge guides the development of high-performance polymer membranes and will contribute to the broader applications of polymer membranes in human society.

Acknowledgments

I would like to thank my advisor Dr. Louis A. Madsen and my co-advisor Dr. Diego Troya for their guidance and advice. Dr. Madsen is enthusiastic and has always encouraged me to be open and bold in research and life. Dr. Troya has always been insightful through our discussions of research. Through my Ph.D. career, I have learned numerous useful skills, including but not limited to presentation skills, writing skills, communication skills, technical skills, and hiking skills. I would also like to thank my committee Dr. Jim Tanko and Dr. Guoliang Liu for their comments/suggestions in my committee meetings and their time reading my dissertation.

I am grateful to the Madsen group members. Dr. Ying Chen started the MD simulation project. Dr. Bryce Kidd helped me to fit in when I first joined the group. Andrew Korovich instructed me on operating the NMR spectrometer. Dr. Xiuli Li first introduced me to the research in the Madsen group. Curt Zanelotti was my roommate during our campus visits and had always been cheering up other people in the group and me. Deyang Yu is always a close friend of mine.

Last, I would like to show my gratitude to my parents, Zhongxiang Zhang and Xiaoying Nan, without whom I will not be the person I am today.

Attribution

A brief description of peers who have contributed to the work in this dissertation is included below.

Chapter 3

Dr. Ying Chen is a former member of the Madsen group who started the simulation of carbon nanotubes and wrote several programs to generate the starting configuration file and to analyze output files.

Prof. Diego Troya is my Ph.D. co-advisor and helped me transfer the computational knowledge and understand the procedures in running simulations.

Prof. Louis Madsen is my Ph.D. advisor and guided me with knowledge both in NMR techniques and soft materials.

Chapter 7

Section 7.1: James Mitchell and Prof. Veronica Augustyn from North Carolina State University provided us with the tungsten oxide materials and are the main contributors to the publication.

Section 7.2: William Harrison from NanoSonic Inc. provided us with the polysulfone membranes. Melissa Novy and Prof. Robert Moore from Virginia Tech collaborated with us on this project.

Section 7.3: Megan Matta and Prof. Michael Hickner from Penn State University provided us with the polyolefin-based membranes and held discussions with us on the understandings of the membranes.

Section 7.4: Niloofar Shivyari and Prof. Charles Frazier from Virginia Tech provided us with the sample adduct and the ^{13}C labeled standard.

Table of Contents

List of Figures

List of Tables

Chapter 1 Transport in Membranes with Nanoconfining Structures

1.1 Motivations and Objectives

Ionic polymer membranes, also known as ionomer membranes, which are membranes made of polymers containing ionic groups, can selectively transport ions or small molecules, and thus these membranes find application in important fields such as hydrogen fuel cells and water desalination.[1-2] While ionomer membranes emerged more than half a century ago, a thorough fundamental understanding of how transport in these membranes relates to their structure is still lacking. The major challenge in our understanding relates to the incomplete picture of the ionomer membrane nanostructure.[2-3] Researchers have produced numerous models to describe the nanostructure of typical ionomer membranes such as perfluorosulfonic acid (PFSA) membranes. While debates persist, there is substantial consensus on the critical structural features of ionomer membranes. Ionomer membranes usually consist of hydrophobic polymer backbones and ionic sidechains, which phase separate on the nanometer scale into hydrophobic and hydrophilic (ionic) domains.[4-12] The ionic domains form nanometer-sized interconnected hydrophilic channels that conduct small mobile species (water molecules and counterions in most scenarios). Thus, understanding the transport of mobile species through the hydrophilic channels is crucial for understanding macroscopic membrane transport and guiding the development of high-performance ionomer membranes.

Nuclear magnetic resonance (NMR) provides a powerful and non-destructive toolset for analyzing the transport properties of soft materials. Our group is dedicated to studying the structure and transport properties of various soft materials such as cation exchange membranes (CEMs), anion exchange membranes (AEMs), other polymer-based electrolytes, and micelles.[13-17] More specifically, we heavily focus on *NMR diffusometry*, a class of techniques which can quantify the

diffusion coefficients of different mobile species. With the additional ability to probe varying timescales, NMR diffusometry reveals valuable information about the multi-scale (hundreds of nanometers to tens of microns) transport properties of polymer membranes. NMR diffusometry is also able to trace the dynamics of mobile species in different directions and at different temperatures, revealing rich information about the structural heterogeneity and the energy landscape for transport in various materials. Another inherent advantage of NMR diffusometry roots in the principle of NMR. Different types of nuclei resonate at vastly different frequencies, and the chemical shift further separates the same nuclei that exist in chemically distinct environments. Consequently, NMR diffusometry can separately measure the dynamics of multiple mobile species in the same sample, for example, ions and neutral species in the same ionomer membrane.

To add to the power of NMR studies, we utilize molecular dynamics (MD) simulations to provide insights into structure-transport relations on the nanometer lengthscale, which can be difficult to measure experimentally. With modern computational resources, MD simulations can easily model nanoscale molecular motions within a matter of hours, making it a suitable tool to study liquid dynamics under the nanoscale environment.

In this dissertation, I strive to better understand how *nanoconfinement* – the presence of rigid structures on the 1 nm scale that interact strongly with liquids – influences the dynamics and transport of the small mobile species in the liquid. Such understanding not only serves to inform the design of ion-exchange polymer membranes but can also inform the broad field of confined liquid dynamics. Liquids experience confined motion in many living tissues and organs, in natural minerals, and in myriad synthetic materials that possess nanoscale cavities. This dissertation contains studies of the nanoscale dynamics and energetics of confined liquids, investigated with

NMR diffusometry and MD simulations. This chapter introduces background information in the field of ionomer membranes and confined liquid dynamics. Chapter 2 covers the principles and concepts involved in diffusion, NMR spectroscopy and diffusometry, and MD simulations. In Chapter 3, we report the effect of confinement size and phase-separation in polymer membranes on water dynamics via the combination of NMR diffusometry experiments and MD simulations of confined water in carbon nanotubes (CNTs). In Chapter 4, we connect retarded water dynamics with the residence time of water in various hydrophobic confinement environments with different geometries. In Chapter 5, we investigate the dynamics of bulk solutions in the presence of ions and describe an observation and concept of concentration-temperature superposition. In Chapter 6, we simulate water dynamics under confining structures that contain surface charges to further approach the realistic environment in ionomer membranes. In Chapter 7, we summarize additional brief NMR studies on various materials, including polymer composites and tungsten oxide hydrate.

1.2 Structure-Transport Relations in Ionomer Membranes

1.2.1 Multi-scale Structures of Ionomer Membranes

In an ionomer membrane, the hydrophobic backbone forms the polymer matrix that provides chemical and mechanical stability, while the hydrophilic ionic groups form the ionic domains. Based on small-angle X-ray scattering (SAXS) studies, the size of the ionic domains is about a few nanometers.[5-6, 18] It is now widely accepted that the ionic domains are interconnected and form the hydrophilic channel network in benchmark ionomer membranes such as perfluorosulfonic acid ionomers (PFSAs). These hydrophilic channels conduct water molecules and ions, highlighting the importance of the ionic domain on molecular transport. Understanding the structure-transport interplay in these nanosized ionic domains is crucial for optimizing the

performance of ionomer membranes. The ionic domains possess different structural features on different lengthscales.[19]

On the larger lengthscale of 1 to 5 nm, the individual hydrophilic channels dominate mobile species transport. On this lengthscale, nanoscale phase separation leads to segregation of the polymer hydrophobic matrix and the hydrophilic channels. The degree of phase separation also depends on the chemical nature of the membrane.[20-21] Also, on the 1 nm lengthscale, both the confinement geometry and the intermolecular interactions between water and the confining surface dominate the dynamics of mobile species.[22-25] On the lengthscale of 10-100 nm, the major structural feature is the interconnectivity of the hydrophilic channels.[15-16] The connectivity of these hydrophilic channels, which would impact membrane transport performance, depends on the chemical nature and the processing of the membrane.[26] The hydrophilic channels form locally ordered collections of channels (or grains) with lengthscale typically up to the hundreds of nanometers or a few microns. The boundaries that exist between adjacent grains would further restrict the transport of mobile species.[15] Finally, on the lengthscale of 1 μm, the alignment of the hydrophilic channel grains can also impact the anisotropy of membrane transport.[27] **Figure 1.1** summarizes this structure-transport interplay in an ionomer membrane.

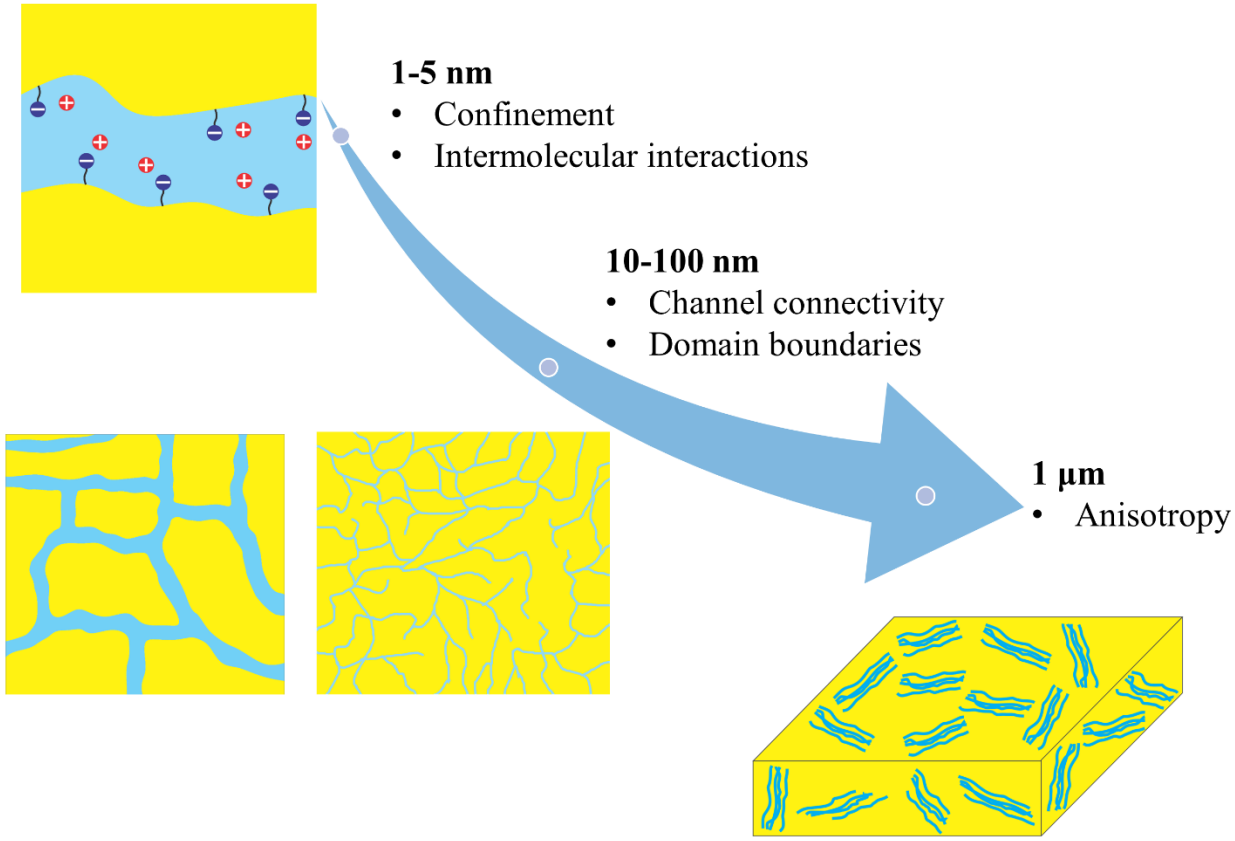

Figure 1.1 Structure-transport relations in ionomer membranes on different lengthscales. On the lengthscale of 1-5 nm, the confinement of the hydrophilic channels and the interactions between mobile spices and the fixed ionic groups affect the local transport of mobile species. On the lengthscale of 10 nm to 1 µm, the connectivity of the hydrophilic channels and the grain boundaries between the locally ordered hydrophilic channel grains are the most important factors governing transport performance. On the lengthscale of 1 µm, the alignment of the hydrophilic grains can also govern the anisotropy of membrane transport.

Perfluorosulfonic acid (PFSA) polymers represent the state-of-the-art membranes in proton exchange membrane fuel cell (PEMFC) applications. Researchers have intensively studied PFSA membranes to understand the various aspects and scales of membrane structure. Revealing the detailed nanostructure of the ionic domains in PFSA membranes remains a particular challenge

and has attracted intense attention and generated numerous debates over the past few decades. Gierke[5] and co-workers first originated the famous spherical cluster model. In this model, water molecules form larger size clusters (~4 nm) in the ionic domains, and the clusters are interconnected by smaller channels (~1 nm). Gebel et al.[7-8] proposed the bundle model where hydrophobic polymer chains aggregate to form rod-like bundles, which are surrounded by ionic groups. Schmidt et al.[28] proposed a parallel cylindrical model where ionic domains form parallel cylindrical pores based on theoretical calculations. Contrary to the parallel cylindrical model, Kreuer et al.[12] proposed a ribbon-like structure in which water domains are locally elongated and yet flattened. Based on Dissipative Particle Dynamics simulations, Elliott et al.[11] claimed a bicontinuous network would fit this ionic domain structure. These studies indicate that a comprehensive picture of the nanostructure of ionomer membranes is still lacking, and indeed, membranes made in different ways show quite different nanoscale morphologies.[2-3] The goal here, however, is not to address the exact structure of any particular ionomer membrane. Instead, we aim to shed light on how the transport properties of ionomer membranes are affected by the typical structural features of these materials. Such understanding broadly impacts the fields of polymer separations membranes, as well as other hard and soft materials with nm-sized transport networks.

The sidechains of an ionomer contain ionic head groups and counterions that balance the charges of the head groups. Based on the identity of the counterion (either cation or anion), ionomer membranes are categorized into cation-exchange membranes (CEMs) and anion-exchange membranes (AEMs). **Figure 1.2** depicts the chemical structure of several common ionomer membranes. The PFSA membranes belong to CEMs. Compared to CEMs, AEMs possess several advantages in fuel-cell applications. The operation of a PEMFC usually requires a platinum catalyst, which is expensive and suffers from catalysis poisoning at the typical operation

temperature of PEMFC (~70 °C).[29] Constructing fuel cells with AEMs enables cheaper catalysts that suffer less from catalyst poisoning (e.g., Fe or Ni) as well as faster catalytic kinetics.[30-31] The major drawbacks of AEMs are the relatively low chemical stability and low ionic conductivity.[21, 32-33] In anion-exchange membrane fuel cells (AEMFCs), the counterion in the AEMs is typically the hydroxide ion, as opposed to the mobile proton in PEMFC. The typical cationic head group in AEMs is quaternary ammonium (example in **Figure 1.2**). The stability of AEMs under basic conditions tends to be much weaker than the stability of CEMs under acidic conditions. The stability issue of AEMs is attributed to the lack of charge delocalization in the cationic head group, making the sidechains vulnerable to nucleophilic substitution reactions.[34] Nevertheless, the potential reduction of electrode catalyst cost still drives the recent expansion of research into AEMs.[16, 20-21, 30-31, 33-34]

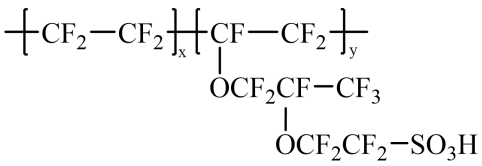

Acid-form Nafion

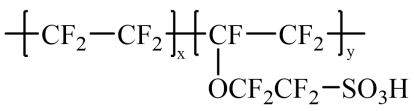

Acid-form Aquivion

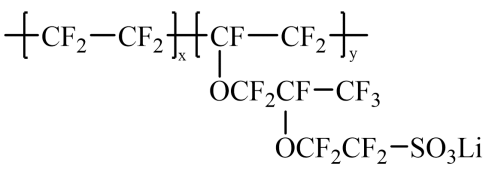

Lithium-form Nafion

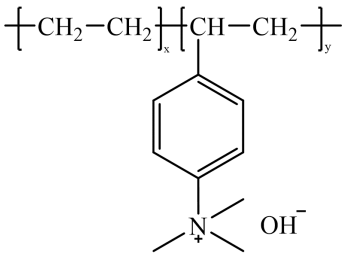

Quaternary ammonium based AEM

Figure 1.2 Chemical structure of selected ionomers that constitute PFSA polymers and an AEM polymer. PFSA membranes consist of polytetrafluoroethylene-based backbones and sulfonated sidechains. Acid-form PFSA membranes contain and conduct protons and are popular in the application of PEMFCs. Ion exchange generates different forms of PFSA membranes, such as

lithium-form and sodium-form. In AEMs, the ionic head group in the sidechain is typically quaternary ammonium or an imidazolium group. The sample AEM in the figure above contains hydroxide as the counterion.[22] Various forms (e.g., chloride-form, bromide-form) of AEMs also exist through ion exchange.

1.2.2 Structure-Transport Interplay Above the Lengthscale of 10 Nanometers

Optimizing the morphology of ionomer membranes and understanding morphology-transport relationships have attracted intensive studies in recent years.[16, 19, 27, 35-43] On lengthscale above 10 nm, the most important membrane structure includes the connectivity of the hydrophilic channels, the grain boundaries between the hydrophilic channel grains, the alignment of the grains.[16] Lyonnard et al.[26] suggest that a shorter sidechain in PFSA membranes leads to better connectivity of hydrophilic channels. Thieu et al.[16] observed that the hydrophilic channels are generally better connected in CEMs than in AEMs. The tortuosity of an ionomer membrane quantifies the connectivity of the hydrophilic channels. Experimentally, NMR diffusometry (see more details in **Chapter 2**) is able to measure the tortuosity. Within the context of NMR diffusion experiments, the tortuosity of a material is defined as

$$\alpha = \frac{D_0}{D_\infty} \tag{1.1}$$

where α is the tortuosity, D_0 is the local diffusion coefficient on the molecular level, D_∞ is the diffusion coefficient on the macroscopic level.[15-16, 44-45] For a bulk free liquid, the local diffusion coefficient is the same as the macroscopic diffusion coefficient. Thus, the tortuosity of a bulk liquid is unity. Inside an ionomer membrane, mobile species frequently hit restrictions inside the membrane matrix, causing the macroscopic diffusion to be slower than the local diffusion value. Thus, the tortuosity of an ionomer membrane is larger than unity. In general, the tortuosity of an

ionomer membrane would affect membrane transport from tens of nanometers to micrometers.[15] Figure **1.3** illustrates the relationship between membrane structure and diffusion rate at multiple lengthscales. When the diffusion time is short enough (e.g., sub nanosecond), the molecules in the hydrophilic channels have not extensively interacted with the channel walls and would travel at a rate similar to that in the bulk liquid. As the average diffusion length grows to several nanometers, most of the molecules will slow down due to restrictions or repulsions from the channel wall. As the diffusion length grows to tens of nanometers, the molecules see multiple hydrophilic channels. The channel connectivity determines the number of possible pathways for the diffusing molecules and impacts diffusion rate.[15] On the ~100 nm lengthscale, collections of hydrophilic channels form hydrophilic channel grains, with grain boundaries between them.[27] When the diffusing molecules meet grain boundaries, their average diffusion rate further slows down.

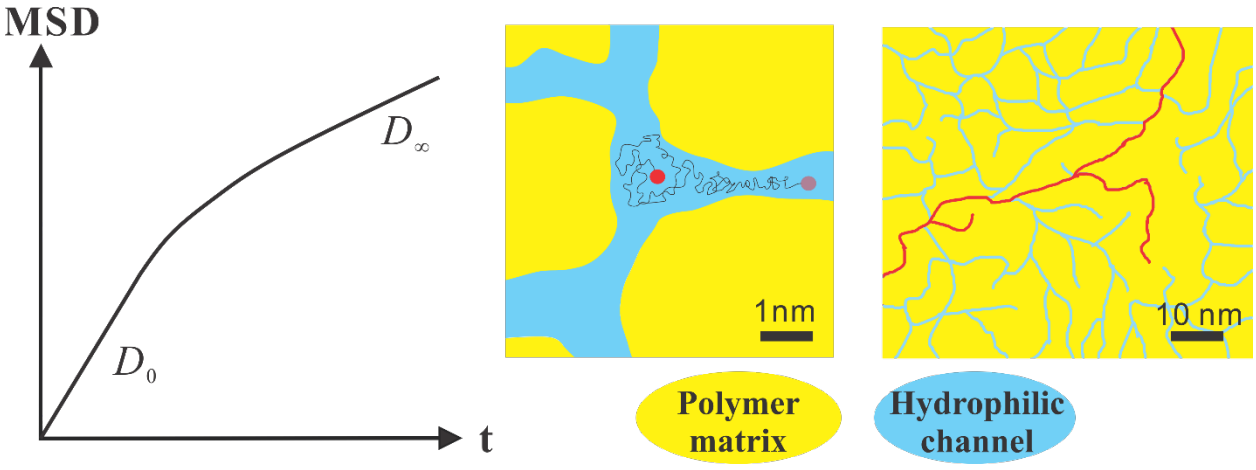

Figure 1.3 Multi-scale restricted diffusion in ionomer membranes and its relationship with the tortuosity and grain boundaries. The direct impact of restricted diffusion is reduced diffusion coefficient as a function of diffusion time. In other words, the reduced slope on the mean squared displacement (MSD) vs. time plot (see more details in chapter 2). On different lengthscales, the membrane structures that restrict the diffusion of mobile species are different. From a few

nanometers to tens of nanometers, mobile species see multiple interconnected hydrophilic channels, and the size and connectivity of the hydrophilic channels both restrict the diffusion. From tens of nanometers to hundreds of nanometers, the collection of hydrophilic channels forms hydrophilic channel grains. The grain boundaries, which separate individual grains, further restrict the diffusion of mobile species.

On the lengthscale of ~1 μm, the alignment of the hydrophilic channel grains can influence the anisotropy of membrane transport. Researchers recognized that the hydrophilic channel grains in PFSAs and in block-copolymer systems are locally aligned (meaning the hydrophilic channels in the same grain are partially aligned) but globally disordered without further processing.[36-37, 46] Through mechanical stretching or magnetic field alignment, an ionomer membrane can become globally anisotropic.[27, 46-47] The stretching makes the grains more aligned to the stretching axis, increasing the diffusion rate along the stretching direction and decreasing the diffusion rate perpendicular to the stretching directions. It is also important to notice that, in such a membrane system, macroscopic stretching does not disturb the internal structure of the hydrophilic channel grains (**Figure 1.4**).

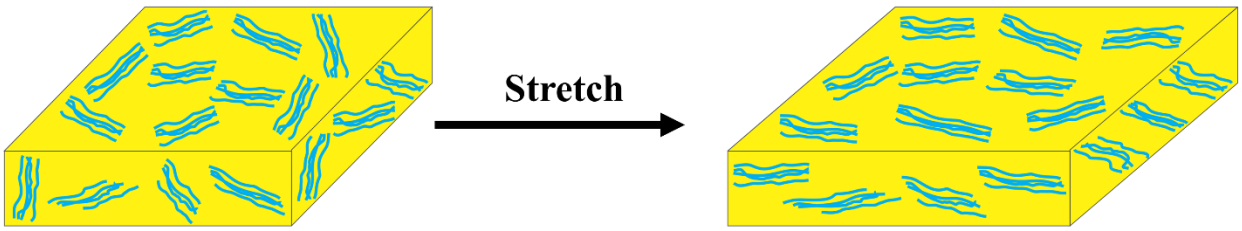

Figure 1.4 In some ionomer membranes, locally aligned hydrophilic channel grains are globally disordered. Most ionomer membranes exhibit isotropic diffusion behavior. Through mechanical elongation (deformation) in one direction or magnetic field alignment (both above the glass transition temperature), it is possible to make the hydrophilic grains align globally. Through

experimental observations,[27, 47] the diffusion coefficient along the alignment axis increases while the diffusion coefficients along other directions decrease.

1.2.3 Structure-Transport Interplay on the Lengthscale of Several Nanometers

The major structural features of ionomer membranes on the nanometer lengthscale separate into three categories: the nanometer-scale confinement, the degree of phase separation, and the chemical structure of the sidechains.

Nanoconfinement leads to unique behaviors of confined water that are different from the bulk.[23] Researchers observe that water molecules become ice-like under hydrophobic confinement[23, 48] and glass-like under hydrophilic confinement.[48-49] In ionomer membranes, where the diameter of the hydrophilic channels is of order one nanometer, the nanoconfinement effect can be strong. We observe a sharp increase of activation energy of diffusion in ionomer membranes when the hydration is low.[23] As the hydration of an ionomer membrane becomes higher, other structure feature becomes dominant. The phase separation in ionomer membranes creates locally bulk-like water. The population of the bulk-like water becomes dominant at relatively high hydration, which gives rise to the bulk-like transport behavior of water molecules as well as counterions.[12] The degree of phase separation depends on the chemical structure of the ionomer membrane. To efficiently increase the extent of phase separation, researchers have also tried to create ionomer membranes based on block copolymers.[50-51]

The quickest way to modify the sidechain of an ionomer membrane would be to change the counterions. Through ion exchange, different forms of ionomer membranes can be achieved. Lithium-form, sodium-form, and even divalent counterions have all been studied throughout the literature. Researchers generally found that the diffusion of both water and counterions is faster in

the presence of a counterion with a smaller radius. Monovalent counterions also tend to give faster dynamics than divalent ones.[43, 52-54] The chemical structure of the sidechain could impact both the confinement size and the phase-separation in an ionomer membrane. Aquivion, one of the PFSA membranes, possesses the same backbone as Nafion but it differs in the sidechain (**Figure 1.4**). With shorter sidechains, researchers have observed the confinement effect to be more significant in Aquivion,[26] hinting that smaller ionic domains and narrower hydrophilic channels exist in Aquivion. AEMs, in general, possess a less well-defined phase-separated morphology compared to CEMs. By creating a triple-cationic sidechain,[21] researchers managed to increase the degree of phase separation in an AEM.

Experimentally, the only way to directly measure the diffusion coefficient averaged at the nanoscale is Quasielastic Neutron Scattering (QENS).[26, 55] Considering the relative difficulty in accessing a neutron source, our group has been pursuing an alternate way to probe nanoscale dynamics. Our group has observed that the activation energy of diffusion arises from intermolecular interactions on the nanometer length scale.[23-25] The activation energy of diffusion can thus serve as a probe for studying molecular transport on the nanometer lengthscale. To help understand dynamical behavior, there have been many efforts to reveal nanostructure in PFSAs using SAXS,[5] small-angle neutral scattering (SANS),[7] and cryo-TEM.[9] However, direct visualization of the ionic domains in PFSAs remains challenging.

Due to difficulties in experiments, computer simulations have played an essential role in understanding nanoconfined transport. With current computational power, simulations of macroscale systems are still too time-consuming to conduct using a detailed atomistic description. However, simulations of nanoscale structures and dynamics are feasible and have received growing attention in recent years. Habenicht et al.,[56-57] Clark et al.,[58-59] and Zelovich et al.[60] studied

the transport of proton and small molecules under nanoscale confinement with ab-initio molecular dynamics simulations.

In this dissertation, we combine various NMR experiments and MD simulations with a focus on developing fundamental understandings of nanoscale structure-transport relations.

1.3 Dynamics and Structure of Nanoconfined Water

While we use ionomer membranes as our model systems, we want to contribute to a broader knowledge of confined liquid dynamics, especially the dynamics of nanoconfined water. Water is the most abundant molecular species on the surface of Earth. While most liquid water is present as bulk water, nanoconfinement of water molecules has rich implications for various fields such as inorganic porous materials,[61-63] water desalination technologies,[64-65] and biological systems.[66-68] Confining water molecules to a few nanometers changes the physical properties of water compared to those of bulk water.[69-70] Physical properties of confined water have received intense studies over the past few decades. These properties include phase transitions,[65, 70-71] density profile,[72-73] energy landscapes,[72] structural features,[48, 65, 74-75] and dynamics.[72, 76] Specifically, the dynamics of water in nanoporous materials impacts a wide range of interests, such as, water transport in biological systems,[72, 77-78] water flow through inorganic materials such as nanoporous silica and cement,[79-83] and water diffusion in synthetic polymer membranes such as ion exchange membranes and reverse osmosis membranes.[15-16, 24-25, 37, 84]

When studying confinement effects on water dynamics, the confinement size and water-surface interactions are the most important factors.[22, 85] Confinement size determines the population of water molecules in direct contact with the confining surface. With smaller confinement size, more water molecules will be in the first surface layer next to the confining wall,

which significantly alters the structure and dynamics of confined water.[23] The water-surface interactions depend on the nature of the confinement medium. Two major categories of confining surfaces exist in terms of water-surface interactions: hydrophilic and hydrophobic confinement. Additionally, the confinement surface may either be ionic or neutral. Our goal is to understand water dynamics under hydrophobic confinement with ionic groups on the surface, which will best parallel the interior of an ionomer membrane. Moreover, as we will see in later sections, different confining surfaces may pose similar confinement effects on water dynamics.

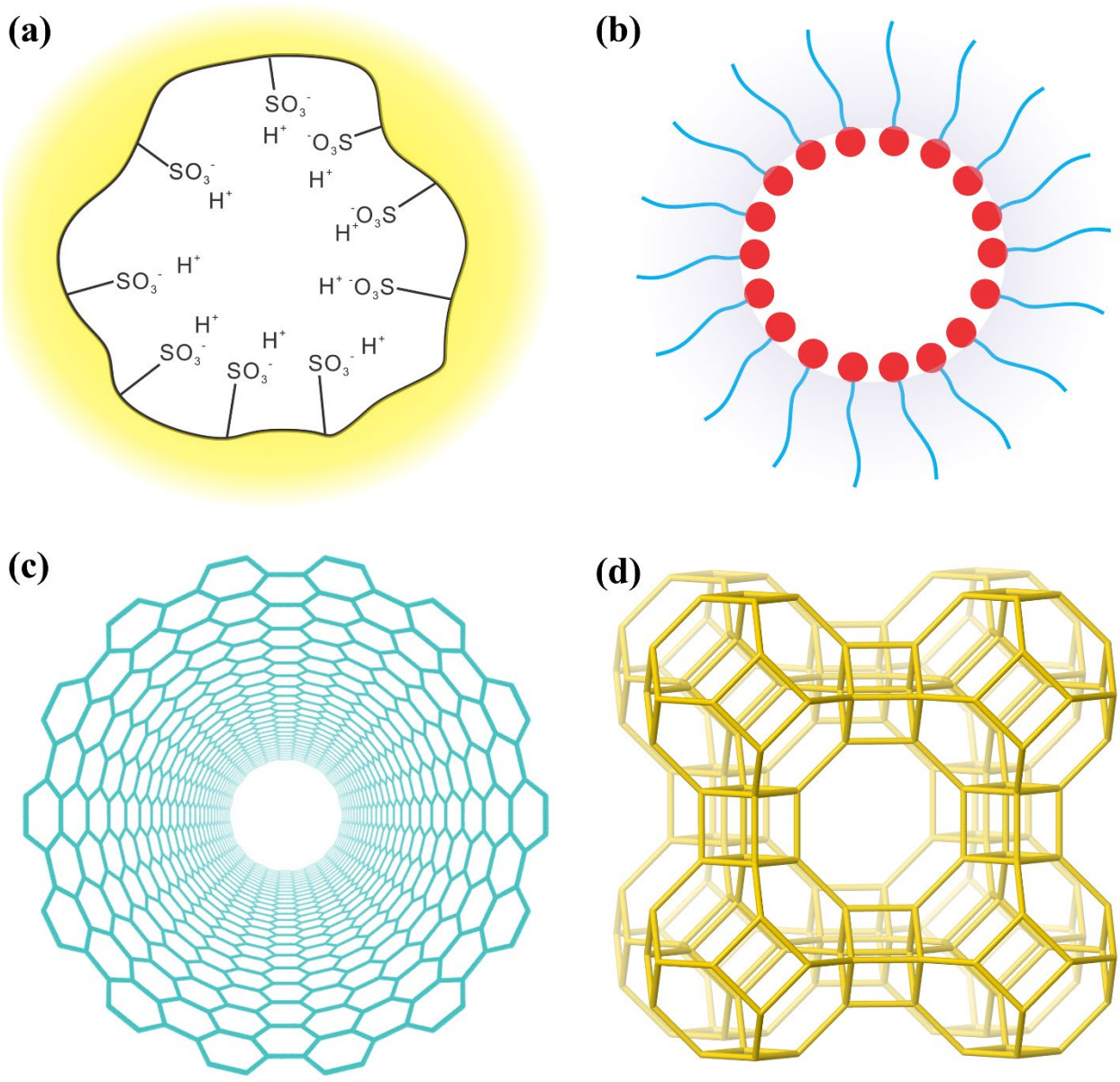

Figure 1.5 Common model systems to study the dynamics of nanoconfined liquids. The pore/channel sizes of all these systems range from one to several nanometers. Panel (a) represents the hydrophilic channel in a PFSA membrane. Panel (b) represents a reverse micelle with hydrophilic core. Panel (c) shows an axial view of a carbon nanotube (CNT). Panel (d) shows the structure of zeolite A. The PFSA membrane is a suitable model system to study the effect of confinement size since the size of the hydrophilic channels changes with hydration. The reverse micelle with tunable head groups provides an excellent model system for studying water-surface

interactions. CNTs and zeolites are popular simulation models due to their structural regularity and tunable pore size in the nanometer range.

1.3.1 Water under Hydrophilic Confinement

For water confined in a hydrophilic environment, the interactions between water molecules and the confining surface result in water adsorption. Water molecules tend to experience long associations with the hydrophilic surface.[86] Consequently, retarded water dynamics dominate under hydrophilic confinement, especially when the confinement size is ~1 nm.[80, 87-89] Gallo et al.[88] reported glass-like water under ultrathin hydrophilic confinement. Youssef et al.[87] also observed glass-like water molecules within sub-nanometer hydrophilic nanopores and recognized that the water under hydrophilic confinement behaves as if it is at lower temperature. Tan et al.[90] reported slowed reorientational dynamics of water confined in reverse micelles. Major et al.[89] reported the viscosity of confined water is millions of times higher than the bulk-water viscosity.

When the confinement size is substantially larger than 1 nm, the dynamical behavior of confined water is similar to bulk water.[91-93] Based on the confinement size, researchers have defined two regimes to describe water dynamics under hydrophilic confinement.[92] In the first regime, where the confinement size is larger than 2nm, the confined water molecules separate into two groups: surface water and central water.[91, 94] The central water is bulk-like and behaves similarly to it. The surface water interacts directly with the hydrophilic surface and possesses vastly different behaviors than the central water. Overall, even though the contributions from surface water are not negligible, the central water dominates the water dynamics in this first regime. In the second regime, where the size of confinement is smaller than 2 nm, the population of surface water becomes dominant,[95] and the dynamics of confined water vastly differs from that of bulk

water.

Due to the strong water-surface interactions, ordering of confined water happens near the hydrophilic surface.[96] The structure of surface water may differ significantly from that of bulk water, while water molecules further away from the hydrophilic surface have a similar structure as bulk water.[97] In bulk water, water molecules experience a tetrahedral structure locally. Under 1-nm confinement, researchers have observed a distorted tetrahedral water structure.[85, 87] Additionally, the structure of surface water may also be similar to bulk water when the confinement size is larger than 2 nm.[92] Overall, water in hydrophilic confinement exhibits a multiphase structure.[98-99] The confined water can transit from fluid-like to solid-like with changing confinement size. Multiple water phases may also coexist under hydrophilic confinement.[99]

1.3.2 Water under Hydrophobic Confinement

Confining water molecules in a hydrophobic environment leads to mixed results on the dynamics of water molecules. Similar to hydrophilic confinement, water dynamics under hydrophobic confinement separates into two regimes. In the first regime, with a confinement size above 2 nm, bulk-like and sometimes enhanced water dynamics dominate. Majumder[100] et al. reported enhanced water flow through a carbon nanotube of 7 nm in diameter. Holt et al.[76] apparently measured water flow through 2-nm carbon nanotubes and also observed an enhancement of water flow as compared to bulk water. Zaragoza et al.[73] simulated water diffusion inside carbon nanotubes and between graphene walls, with both tube diameter and wall separation beyond 2 nm, and found enhanced diffusion coefficient in both structures. Layfield et al.[101] conducted simulations of water confined between hydrophobic alkanethiol monolayers and observed enhanced water diffusion till 1.5 nm away from the hydrophobic surface. In the second regime, where the confinement size is of order 1 nm, retarded water diffusion is dominant. Fogarty

et al.[102] reported retarded reorientational dynamics of water confined in zeolites with pore size ~1 nm. Choudhury et al.[103-104] simulated water confined between parallel graphene sheets and observed retarded diffusion as well as slowed reorientational dynamics when the separation between graphene sheets was less than 1.3 nm. Liu et al.[105] and Farimani et al.[106] simulated the diffusion coefficient of water confined in a carbon nanotube with varying diameters and observed retarded water dynamics when tube diameter was below 2 nm. These results suggest a change of confinement effect on water dynamics when the size of confinement reaches a "critical" value. Once again, the population of surface water may be key in explaining the change of behavior. *One should notice a key difference between hydrophilic and hydrophobic confinement, though.* In hydrophilic confinement, the surface water differs from bulk water because of the strong water-surface interactions. In hydrophobic confinement, the water-surface interactions are weak and should not affect as strongly the dynamics of water molecules. Thus, the slowdown of water dynamics under hydrophobic confinement may mainly results from *geometric confinement*, and we will delve deeply into this confinement effect in chapter 4.

When under hydrophobic confinement, the weak water-surface interactions tend to depopulate water molecules from the confining surface.[107] The excluded volume between the water molecules and the hydrophobic surface leads to a reduced mass density of confined water compared to bulk water.[108-109] Hydrophobic confinement also gives rise to the formation of ordered water structures when the confinement size is small enough. For example, water molecules form stacked hexagons and pentagons in CNTs when the tube diameter ranges between 1.1 and 1.3 nm.[110] Water molecules form a squared-ice structure when confined between graphene sheets that are 0.7 nm apart.[49] The ordered structure under hydrophobic confinement likely forms in the process of adapting to the confinement geometry. With larger hydrophobic confinement size, water

molecules are more disordered, approaching the local structure of bulk water.

1.3.3 Geometric Confinement vs. Water-Surface Interactions

Concerning the dynamics of confined water, a debated question is whether geometric confinement or water-surface interactions have a dominant effect.[22-23] The answer certainly depends on the nature of the confining surface. In hydrophobic confinement, the water-surface interactions are weak, so geometric confinement tends to be more influential regarding the confined water dynamics. Zhou et al.[111] studied the dynamics of water confined in hydrophobic zeolites and concluded that geometric confinement contributes to more than two-thirds of the overall confinement effect. In hydrophilic confinement, the exact water-surface interactions often dominate the behavior of confined water. Renou et al.[112] simulated water confined in nanoporous silica and found vastly different water structures and dynamics between the protonated surface and deprotonated surface.

In addition to hydrophilic/hydrophobic surfaces, a confinement surface can also either be neutral or ionic. Understanding water dynamics at neutral and ionic interfaces attracts numerous studies. Moilanen et al.,[22] Fenn et al.,[113] and Park et al.[114] studied orientational dynamics of water confined in reverse micelles with neutral and ionic head groups and found that the confinement slows down water molecules more than the ionic groups. Through simulations, both enhanced and retarded water dynamics have been observed near hydrophobic surfaces with added charges. Kumar et al.[115] reported enhanced water dynamics near charged hydrophobic walls and attributed the enhancement to the disruption of ordered water structure near the confinement surface. Harrach et al.[85] reported retarded water dynamics in hydrophobic pores with charged groups, which was attributed to a rough energy landscape. We will present complementary observations in Chapter 6 and further explain the effect of ions/charges in nanoconfinement.

1.4 Summary

Understanding of confined liquid dynamics is not only beneficial to the field of polymer membranes but also poses broad impact across various fields and materials. In the remaining chapters, utilizing both NMR experiments and MD simulations, we will explore how confining matrices and liquid-surface interactions impact dynamics of confined liquid.

1.5 References

1. Geise, G. M.; Paul, D. R.; Freeman, B. D. Fundamental water and salt transport properties of polymeric materials. *Prog. Polym. Sci.* **2014,** *39*, 1-42.
2. Kusoglu, A.; Weber, A. Z. New Insights into Perfluorinated Sulfonic-Acid Ionomers. *Chem. Rev.* **2017,** *117*, 987-1104.
3. Mauritz, K. A.; Moore, R. B. State of understanding of Nafion. *Chemical Reviews* **2004,** *104*, 4535-4586.
4. Perez-Hernandez, N.; Luong, T. Q.; Perez, C.; Martin, J. D.; Havenith, M. Pore size dependent dynamics of confined water probed by FIR spectroscopy. *Phys. Chem. Chem. Phys.* **2010,** *12*, 6928-6932.
5. Gierke, T. D.; Munn, G. E.; Wilson, F. C. The Morphology in Nafion Perfluorinated Membrane Products, as Determined by Wide-Angle and Small-Angle X-Ray Studies. *J. Polym. Sci. Pol. Phys.* **1981,** *19*, 1687-1704.
6. Roche, E. J.; Pineri, M.; Duplessix, R.; Levelut, A. M. Small-Angle Scattering Studies of Nafion Membranes. *J. Polym. Sci. Pol. Phys.* **1981,** *19*, 1-11.
7. Rubatat, L.; Gebel, G.; Diat, O. Fibrillar Structure of Nafion: Matching Fourier and Real Space Studies of Corresponding Films and Solutions. *Macromolecules* **2004,** *37*, 7772-7783.
8. Rubatat, L.; Rollet, A. L.; Gebel, G.; Diat, O. Evidence of Elongated Polymeric Aggregates in Nafion. *Macromolecules* **2002,** *35*, 4050-4055.
9. Allen, F. I.; Comolli, L. R.; Kusoglu, A.; Modestino, M. A.; Minor, A. M.; Weber, A. Z. Morphology of Hydrated As-Cast Nafion Revealed through Cryo Electron Tomography. *ACS Macro Lett.* **2015,** *4*, 1-5.
10. Dorenbos, G.; Suga, Y. Simulation of equivalent weight dependence of Nafion morphologies and predicted trends regarding water diffusion. *J. Membrane Sci.* **2009,** *330*, 5-20.
11. Elliott, J. A.; Hanna, S.; Elliott, A. M. S.; Cooley, G. E. Interpretation of the small-angle X-ray scattering from swollen and oriented perfluorinated ionomer membranes. *Macromolecules* **2000,** *33*, 4161-4171.
12. Kreuer, K. D.; Portale, G. A Critical Revision of the Nano-Morphology of Proton Conducting Ionomers and Polyelectrolytes for Fuel Cell Applications. *Adv Funct Mater* **2013,** *23*, 5390-5397.
13. Kidd, B. E.; Li, X. L.; Piemonte, R. C.; Cooksey, T. J.; Singh, A.; Robertson, M. L.; Madsen, L. A. Tuning Biocompatible Block Copolymer Micelles by Varying Solvent Composition: Dynamics and Populations of Micelles and Unimers. *Macromolecules* **2017,** *50*, 4335-4343.
14. Li, X. L.; Cooksey, T. J.; Kidd, B. E.; Robertson, M. L.; Madsen, L. A. Mapping Coexistence Phase Diagrams of Block Copolymer Micelles and Free Unimer Chains. *Macromolecules* **2018,** *51*, 8127-8135.

15. Chang, K.; Korovich, A.; Xue, T. Y.; Morris, W. A.; Madsen, L. A.; Geise, G. M. Influence of Rubbery versus Glassy Backbone Dynamics on Multiscale Transport in Polymer Membranes. *Macromolecules* **2018,** *51*, 9222-9233.
16. Thieu, L. M.; Zhu, L.; Korovich, A. G.; Hickner, M. A.; Madsen, L. A. Multiscale Tortuous Diffusion in Anion and Cation Exchange Membranes. *Macromolecules* **2019,** *52*, 24-35.
17. Wang, Y.; Chen, Y.; Gao, J.; Yoon, H. G.; Jin, L.; Forsyth, M.; Dingemans, T. J.; Madsen, L. A. Highly Conductive and Thermally Stable Ion Gels with Tunable Anisotropy and Modulus. *Adv. Mater.* **2016,** *28*, 2571.
18. Fujimura, M.; Hashimoto, T.; Kawai, H. Small-Angle X-Ray-Scattering Study of Perfluorinated Ionomer Membranes .2. Models for Ionic Scattering Maximum. *Macromolecules* **1982,** *15*, 136-144.
19. Crothers, A. R.; Radke, C. J.; Weber, A. Z. Impact of Nano- and Mesoscales on Macroscopic Cation Conductivity in Perfluorinated-Sulfonic-Acid Membranes. *J. Phys. Chem. C* **2017,** *121*, 28262-28274.
20. Zhu, L.; Peng, X.; Shang, S. L.; Kwasny, M. T.; Zimudzi, T. J.; Yu, X. D.; Saikia, N.; Pan, J.; Liu, Z. K.; Tew, G. N.; Mustain, W. E.; Yandrasits, M.; Hickner, M. A. High Performance Anion Exchange Membrane Fuel Cells Enabled by Fluoropoly(olefin) Membranes. *Adv Funct Mater* **2019,** *29*, 1902059.
21. Zhu, L.; Yu, X. D.; Peng, X.; Zimudzi, T. J.; Saikia, N.; Kwasny, M. T.; Song, S. F.; Kushner, D. I.; Fu, Z. S.; Tew, G. N.; Mustain, W. E.; Yandrasits, M. A.; Hickner, M. A. Poly(olefin)-Based Anion Exchange Membranes Prepared Using Ziegler-Natta Polymerization. *Macromolecules* **2019,** *52*, 4030-4041.
22. Moilanen, D. E.; Levinger, N. E.; Spry, D. B.; Fayer, M. D. Confinement or the nature of the interface? Dynamics of nanoscopic water. *J. Am. Chem. Soc.* **2007,** *129*, 14311-14318.
23. Zhang, R.; Chen, Y.; Troya, D.; Madsen, L. A. Relating Geometric Nanoconfinement and Local Molecular Environment to Diffusion in Ionic Polymer Membranes. *Macromolecules* **2020,** *53*, 3296-3305.
24. Lingwood, M. D.; Zhang, Z.; Kidd, B. E.; McCreary, K. B.; Hou, J.; Madsen, L. A. Unraveling the local energetics of transport in a polymer ion conductor. *Chem. Commun.* **2013,** *49*, 4283-4285.
25. Kidd, B. E.; Forbey, S. J.; Steuber, F. W.; Moore, R. B.; Madsen, L. A. Multiscale Lithium and Counterion Transport in an Electrospun Polymer-Gel Electrolyte. *Macromolecules* **2015,** *48*, 4481-4490.
26. Berrod, Q.; Lyonnard, S.; Guillermo, A.; Ollivier, J.; Frick, B.; Gebel, G. QENS investigation of proton confined motions in hydrated perfluorinated sulfonic membranes and self-assembled surfactants. *EPJ Web Conf.* **2015,** *83*, 02002.
27. Li, J.; Park, J. K.; Moore, R. B.; Madsen, L. a. Linear coupling of alignment with transport in a polymer electrolyte membrane. *Nat. Mater.* **2011,** *10*, 507-511.
28. Schmidt-Rohr, K.; Chen, Q. Parallel cylindrical water nanochannels in Nafion fuel-cell membranes. *Nat. mater.* **2008,** *7*, 75-83.
29. Guvelioglu, G. H.; Stenger, H. G. Flow rate and humidification effects on a PEM fuel cell performance and operation. *J. Power Sources* **2007,** *163*, 882-891.
30. Pan, J.; Chen, C.; Zhuang, L.; Lu, J. T. Designing Advanced Alkaline Polymer Electrolytes for Fuel Cell Applications. *Acc. Chem. Res.* **2012,** *45*, 473-481.
31. Wang, Y. J.; Qiao, J. L.; Baker, R.; Zhang, J. J. Alkaline polymer electrolyte membranes for fuel cell applications. *Chem. Soc. Rev.* **2013,** *42*, 5768-5787.
32. Marino, M. G.; Melchior, J. P.; Wohlfarth, A.; Kreuer, K. D. Hydroxide, halide and water transport in a model anion exchange membrane. *J. Membr. Sci.* **2014,** *464*, 61-71.
33. Varcoe, J. R.; Atanassov, P.; Dekel, D. R.; Herring, A. M.; Hickner, M. A.; Kohl, P. A.; Kucernak, A. R.; Mustain, W. E.; Nijmeijer, K.; Scott, K.; Xu, T. W.; Zhuang, L. Anion-exchange membranes in electrochemical energy systems. *Energy Environ. Sci.* **2014,** *7*, 3135-3191.
34. Arges, C. G.; Zhang, L. Anion Exchange Membranes' Evolution toward High Hydroxide Ion Conductivity and Alkaline Resiliency. *ACS Appl. Energ. Mater.* **2018,** *1*, 2991-3012.

35. McDaniel, J. G.; Mantha, S.; Yethiraj, A. Dynamics of Water in Gemini Surfactant-Based Lyotropic Liquid Crystals. *J. Phys. Chem. B* **2016,** *120*, 10860-10868.
36. Li, J.; Wilmsmeyer, K. G.; Madsen, L. A. Anisotropic diffusion and morphology in perfluorosulfonate ionomers investigated by NMR. *Macromolecules* **2009,** *42*, 255-262.
37. Hou, J. B.; Li, J.; Madsen, L. A. Anisotropy and Transport in Poly(arylene ether sulfone) Hydrophilic-Hydrophobic Block Copolymers. *Macromolecules* **2010,** *43*, 347-353.
38. Yin, C. S.; Li, J. J.; Zhou, Y. W.; Zhang, H. N.; Fang, P. F.; He, C. Q. Phase Separation and Development of Proton Transport Pathways in Metal Oxide Nanoparticle/Nafion Composite Membranes during Water Uptake. *J. Phys. Chem. C* **2018,** *122*, 9710-9717.
39. Kristensen, M. B.; Catalano, J.; Haldrup, S.; Belsky, P.; Tomas, M.; Bentien, A. Tuning the ion channel network of perfluorosulfonated membranes via a facile sacrificial porogen approach. *J. Membr. Sci.* **2018,** *545*, 275-283.
40. Kamcev, J.; Paul, D. R.; Manning, G. S.; Freeman, B. D. Predicting Salt Permeability Coefficients in Highly Swollen, Highly Charged Ion Exchange Membranes. *ACS Appl. Mater. Inter.* **2017,** *9*, 4044-4056.
41. Pan, Y.; Zhong, Z. Modeling the Ion Transport Restriction in Mechanically Strained Separator Membranes. *J. Electrochem. Soc.* **2014,** *161*, A583-A586.
42. Majewski, P. W.; Gopinadhan, M.; Osuji, C. O. Understanding anisotropic transport in self-assembled membranes and maximizing ionic conductivity by microstructure alignment. *Soft Matter* **2013,** *9*, 7106-7116.
43. Suresh, G.; Pandey, A. K.; Goswami, A. Self-diffusion coefficients of water in Nafion-117 membrane with multivalent counterions. *J. Membr. Sci.* **2006,** *284*, 193-197.
44. Callaghan, P. *Translational Dynamics and Magnetic Resonance: Principles of Pulsed Gradient Spin Echo NMR*. Oxford University Press: New York, 2011.
45. Hou, J. B.; Li, J.; Mountz, D.; Hull, M.; Madsen, L. A. Correlating morphology, proton conductivity, and water transport in polyelectrolyte-fluoropolymer blend membranes. *J. Membr. Sci.* **2013,** *448*, 292-299.
46. Grundy, L. S.; Sethi, G. K.; Galluzzo, M. D.; Loo, W. S.; Maslyn, J. A.; Teran, A. A.; Thelen, J. L.; Timachova, K.; Reimer, J. A.; Madsen, L. A.; Balsara, N. P. Detection of the Order-to-Disorder Transition in Block Copolymer Electrolytes Using Quadrupolar Li-7 NMR Splitting. *ACS Macro Lett.* **2019,** *8*, 107-112.
47. Park, J. K.; Li, J.; Divoux, G. M.; Madsen, L. A.; Moore, R. B. Oriented Morphology and Anisotropic Transport in Uniaxially Stretched Perfluorosulfonate Ionomer Membranes. *Macromolecules* **2011,** *44*, 5701-5710.
48. Koga, K.; Gao, G. T.; Tanaka, H.; Zeng, X. C. Formation of ordered ice nanotubes inside carbon nanotubes. *Nature* **2001,** *412*, 802-805.
49. Algara-Siller, G.; Lehtinen, O.; Wang, F. C.; Nair, R. R.; Kaiser, U.; Wu, H. A.; Geim, A. K.; Grigorieva, I. V. Square ice in graphene nanocapillaries. *Nature* **2015,** *519*, 443-445.
50. Zhang, X. L.; Shi, Q.; Chen, P.; Zhou, J. F.; Li, S. S.; Xu, H.; Chen, X. B.; An, Z. W. Block poly(arylene ether sulfone) copolymers tethering aromatic side-chain quaternary ammonium as anion exchange membranes. *Polym. Chem.* **2018,** *9*, 699-711.
51. Erdogan, T.; Unveren, E. E.; Inan, T. Y.; Birkan, B. Well-defined block copolymer ionomers and their blend membranes for proton exchange membrane fuel cell. *J. Membr. Sci.* **2009,** *344*, 172-181.
52. Saito, M.; Arimura, N.; Hayamizu, K.; Okada, T. Mechanisms of ion and water transport in perfluorosulfonated ionomer membranes for fuel cells. *J. Phys. Chem. B* **2004,** *108*, 16064-16070.
53. Suresh, G.; Scindia, Y. M.; Pandey, A. K.; Goswami, A. Self-diffusion coefficient of water in Nafion-117 membrane with different monovalent counterions: a radiotracer study. *J. Membr. Sci.* **2005,** *250*, 39-45.
54. Sodaye, S.; Suresh, G.; Pandey, A. K.; Goswami, A. Interdiffusion of Exchanging Counterions in Poly(perfluorosulfonic acid) Membrane. *J. Phys. Chem. B* **2009,** *113*, 12482-12488.

55. Berrod, Q.; Hanot, S.; Guillermo, A.; Mossa, S.; Lyonnard, S. Water sub-diffusion in membranes for fuel cells. *Sci. Rep.* **2017,** *7*, 8326.
56. Habenicht, B. F.; Paddison, S. J. Ab Initio Simulations of the Effects of Nanoscale Confinement on Proton Transfer in Hydrophobic Environments. *J. Phys. Chem. B* **2011,** *115*, 10826-10835.
57. Habenicht, B. F.; Paddison, S. J.; Tuckerman, M. E. Ab initio molecular dynamics simulations investigating proton transfer in perfluorosulfonic acid functionalized carbon nanotubes. *Phys. Chem. Chem. Phys.* **2010,** *12*, 8728-8732.
58. Clark, J. K.; Habenicht, B. F.; Paddison, S. J. Ab initio molecular dynamics simulations of aqueous triflic acid confined in carbon nanotubes. *Phys. Chem. Chem. Phys.* **2014,** *16*, 16465-16479.
59. Clark, J. K.; Paddison, S. J. Ab initio molecular dynamics simulations of water and an excess proton in water confined in carbon nanotubes. *Phys. Chem. Chem. Phys.* **2014,** *16*, 17756-17769.
60. Goldsmith, J.; Martens, C. C. Effect of boundary conditions on the structure and dynamics of nanoscale confined water. *J. Phys. Chem. A* **2009,** *113*, 2046-2052.
61. Karaborni, S.; Smit, B.; Heidug, W.; Urai, J.; van Oort, E. The swelling of clays: Molecular simulations of the hydration of montmorillonite. *Science* **1996,** *271*, 1102-1104.
62. Cailliez, F.; Trzpit, M.; Soulard, M.; Demachy, I.; Boutin, A.; Patarin, J.; Fuchs, A. H. Thermodynamics of water intrusion in nanoporous hydrophobic solids. *Phys. Chem. Chem. Phys.* **2008,** *10*, 4817-4826.
63. Bordallo, H. N.; Aldridge, L. P.; Desmedt, A. Water dynamics in hardened ordinary Portland cement paste or concrete: From quasielastic neutron scattering. *J. Phys. Chem. B* **2006,** *110*, 17966-17976.
64. Wang, Y. H.; He, Z. J.; Gupta, K. M.; Shi, Q.; Lu, R. F. Molecular dynamics study on water desalination through functionalized nanoporous graphene. *Carbon* **2017,** *116*, 120-127.
65. Hummer, G.; Rasaiah, J. C.; Noworyta, J. P. Water conduction through the hydrophobic channel of a carbon nanotube. *Nature* **2001,** *414*, 188-190.
66. Pratt, L. R.; Pohorille, A. Hydrophobic effects and modeling of biophysical aqueous solution interfaces. *Chem. Rev.* **2002,** *102*, 2671-2692.
67. Luo, P. Z.; Baldwin, R. L. Interaction between water and polar groups of the helix backbone: An important determinant of helix propensities. *PNAS* **1999,** *96*, 4930-4935.
68. Israelachvili, J.; Wennerstrom, H. Role of hydration and water structure in biological and colloidal interactions. *Nature* **1996,** *379*, 219-225.
69. Christenson, H. K. Confinement effects on freezing and melting. *J. Phys.-Condens. Mat.* **2001,** *13*, R95-R133.
70. Gelb, L. D.; Gubbins, K. E.; Radhakrishnan, R.; Sliwinska-Bartkowiak, M. Phase separation in confined systems. *Rep. Prog. Phys.* **1999,** *62*, 1573-1659.
71. Zhang, J.; Liu, G.; Jonas, J. Effects of Confinement on the Glass-Transition Temperature of Molecular Liquids. *J. Phys. Chem.* **1992,** *96*, 3478-3480.
72. Beckstein, O.; Sansom, M. S. P. Liquid-vapor oscillations of water in hydrophobic nanopores. *PNAS* **2003,** *100*, 7063-7068.
73. Zaragoza, A.; Gonzalez, M. A.; Joly, L.; Lopez-Montero, I.; Canales, M. A.; Benavides, A. L.; Valeriani, C. Molecular dynamics study of nanoconfined TIP4P/2005 water: how confinement and temperature affect diffusion and viscosity. *Phys. Chem. Chem. Phys.* **2019,** *21*, 13653-13667.
74. Mashl, R. J.; Joseph, S.; Aluru, N. R.; Jakobsson, E. Anomalously immobilized water: A new water phase induced by confinement in nanotubes. *Nano Lett.* **2003,** *3*, 589-592.
75. Cicero, G.; Grossman, J. C.; Schwegler, E.; Gygi, F.; Galli, G. Water confined in nanotubes and between graphene sheets: A first principle study. *J. Am. Chem. Soc.* **2008,** *130*, 1871-1878.
76. Holt, J. K.; Park, H. G.; Wang, Y. M.; Stadermann, M.; Artyukhin, A. B.; Grigoropoulos, C. P.; Noy, A.; Bakajin, O. Fast mass transport through sub-2-nanometer carbon nanotubes. *Science* **2006,** *312*, 1034-1037.
77. Steudle, E.; Henzler, T. Water Channels in Plants - Do Basic Concepts of Water Transport Change. *J. Exp. Bot.* **1995,** *46*, 1067-1076.

78. Horner, A.; Pohl, P. Single-file transport of water through membrane channels. *Faraday Discuss.* **2018,** *209*, 9-33.
79. Mietner, J. B.; Brieler, F. J.; Lee, Y. J.; Froba, M. Properties of Water Confined in Periodic Mesoporous Organosilicas: Nanoimprinting the Local Structure. *Angew. Chem. Int.* **2017,** *56*, 12348-12351.
80. Hou, D. S.; Li, D. K.; Zhao, T. J.; Li, Z. J. Confined Water Dissociation in Disordered Silicate Nanometer-Channels at Elevated Temperatures: Mechanism, Dynamics and Impact on Substrates. *Langmuir* **2016,** *32*, 4153-4168.
81. Briman, I. M.; Rebiscoul, D.; Diat, O.; Zanotti, J. M.; Jollivet, P.; Barboux, P.; Gin, S. Impact of Pore Size and Pore Surface Composition on the Dynamics of Confined Water in Highly Ordered Porous Silica. *J. Phys. Chem. C* **2012,** *116*, 7021-7028.
82. Sattig, M.; Reutter, S.; Fujara, F.; Werner, M.; Buntkowsky, G.; Vogel, M. NMR studies on the temperature-dependent dynamics of confined water. *Phys. Chem. Chem. Phys.* **2014,** *16*, 19229-19240.
83. Manzano, H.; Moeini, S.; Marinelli, F.; van Duin, A. C. T.; Ulm, F. J.; Pellenq, R. J. M. Confined Water Dissociation in Microporous Defective Silicates: Mechanism, Dipole Distribution, and Impact on Substrate Properties. *J. Am. Chem. Soc.* **2012,** *134*, 2208-2215.
84. Hou, J., Transport and Anisotropy inside Ionic Polymer Membranes. 2012; p 158.
85. Harrach, M. F.; Klameth, F.; Drossel, B.; Vogel, M. Effect of the hydroaffinity and topology of pore walls on the structure and dynamics of confined water. *J. Chem. Phys.* **2015,** *142*, 034703.
86. Sendner, C.; Horinek, D.; Bocquet, L.; Netz, R. R. Interfacial Water at Hydrophobic and Hydrophilic Surfaces: Slip, Viscosity, and Diffusion. *Langmuir* **2009,** *25*, 10768-10781.
87. Youssef, M.; Pellenq, R. J. M.; Yildiz, B. Glassy Nature of Water in an Ultraconfining Disordered Material: The Case of Calcium-Silicate-Hydrate. *J. Am. Chem. Soc.* **2011,** *133*, 2499-2510.
88. Gallo, P.; Rovere, M.; Ricci, M. A.; Hartnig, C.; Spohr, E. Evidence of glassy behaviour of water molecules in confined states. *Philos. Mag. B* **1999,** *79*, 1923-1930.
89. Major, R. C.; Houston, J. E.; McGrath, M. J.; Siepmann, J. I.; Zhu, X. Y. Viscous water meniscus under nanoconfinement. *Phys. Rev. Lett.* **2006,** *96*.
90. Tan, H. S.; Piletic, I. R.; Fayer, M. D. Orientational dynamics of water confined on a nanometer length scale in reverse micelles. *J. Chem. Phys.* **2005,** *122*, 174501.
91. Brubach, J. B.; Mermet, A.; Filabozzi, A.; Gerschel, A.; Lairez, D.; Krafft, M. P.; Roy, P. Dependence of water dynamics upon confinement size. *J. Phys. Chem. B* **2001,** *105*, 430-435.
92. Bourg, I. C.; Steefel, C. I. Molecular Dynamics Simulations of Water Structure and Diffusion in Silica Nanopores. *J. Phys. Chem. C* **2012,** *116*, 11556-11564.
93. Kerisit, S.; Liu, C. X. Molecular Simulations of Water and Ion Diffusion in Nanosized Mineral Fractures. *Environ. Sci. Technol.* **2009,** *43*, 777-782.
94. Gruener, S.; Hofmann, T.; Wallacher, D.; Kityk, A. V.; Huber, P. Capillary rise of water in hydrophilic nanopores. *Phys. Rev. E* **2009,** *79*, 067301.
95. Li, T. D.; Gao, J. P.; Szoszkiewicz, R.; Landman, U.; Riedo, E. Structured and viscous water in subnanometer gaps. *Phys. Rev. B* **2007,** *75*, 115415.
96. Thompson, W. H. Perspective: Dynamics of confined liquids. *J. Chem. Phys.* **2018,** *149*, 170901.
97. Wang, J. W.; Kalinichev, A. G.; Kirkpatrick, R. J. Molecular modeling of water structure in nano-pores between brucite (001) surfaces. *Geochim. Cosmochim. Acta* **2004,** *68*, 3351-3365.
98. Pertsin, A.; Grunze, M. Quasistatic computer simulation study of the shear behavior of Bi- and trilayer water films confined between model hydrophilic surfaces. *Langmuir* **2008,** *24*, 4750-4755.
99. Shaat, M.; Zheng, Y. M. Fluidity and phase transitions of water in hydrophobic and hydrophilic nanotubes. *Sci. Rep.* **2019,** *9*, 5689.
100. Majumder, M.; Chopra, N.; Andrews, R.; Hinds, B. J. Nanoscale hydrodynamics: enhanced flow in carbon nanotubes. *Nature* **2005,** *438*, 44.
101. Layfield, J. P.; Troya, D. Molecular simulations of the structure and dynamics of water confined between alkanethiol self-assembled monolayer plates. *J. Phys. Chem. B* **2011,** *115*, 4662-4670.

102. Fogarty, A. C.; Coudert, F. X.; Boutin, A.; Laage, D. Reorientational Dynamics of Water Confined in Zeolites. *ChemPhysChem* **2014,** *15*, 521-529.
103. Choudhury, N.; Pettitt, B. M. Dynamics of water trapped between hydrophobic solutes. *J. Phys. Chem. B* **2005,** *109*, 6422-6429.
104. Choudhury, N. Orientational dynamics of water trapped between two nanoscopic hydrophobic solutes: A molecular dynamics simulation study. *J. Chem. Phys.* **2010,** *133*, 154515.
105. Liu, Y. C.; Wang, Q.; Wu, T.; Zhang, L. Fluid structure and transport properties of water inside carbon nanotubes. *J. Chem. Phys.* **2005,** *123*, 234701.
106. Farimani, A. B.; Aluru, N. R. Spatial Diffusion of Water in Carbon Nanotubes: From Fickian to Ballistic Motion. *J. Phys. Chem. B* **2011,** *115*, 12145-12149.
107. Rasaiah, J. C.; Garde, S.; Hummer, G. Water in nonpolar confinement: from nanotubes to proteins and beyond. *Annu. Rev. Phys. Chem.* **2008,** *59*, 713-740.
108. Wang, G. J.; Hadjiconstantinou, N. G. Why are fluid densities so low in carbon nanotubes? *Phys. Fluids* **2015,** *27*, 052006.
109. Doshi, D. A.; Watkins, E. B.; Israelachvili, J. N.; Majewski, J. Reduced water density at hydrophobic surfaces: Effect of dissolved gases. *PNAS* **2005,** *102*, 9458-9462.
110. Thomas, J. A.; McGaughey, A. J. H. Water Flow in Carbon Nanotubes: Transition to Subcontinuum Transport. *Phys. Rev. Lett.* **2009,** *102*, 184502.
111. Zhou, T. C.; Bai, P.; Siepmann, J. I.; Clark, A. E. Deconstructing the Confinement Effect upon the Organization and Dynamics of Water in Hydrophobic Nanoporous Materials: Lessons Learned from Zeolites. *J. Phys. Chem. C* **2017,** *121*, 22015-22024.
112. Renou, R.; Szymczyk, A.; Ghoufi, A. Water confinement in nanoporous silica materials. *J. Chem. Phys.* **2014,** *140*, 044704.
113. Fenn, E. E.; Wong, D. B.; Fayer, M. D. Water dynamics at neutral and ionic interfaces. *PNAS* **2009,** *106*, 15243-15248.
114. Park, S.; Moilanen, D. E.; Fayer, M. D. Water dynamics - The effects of ions and nanoconfinement. *J. Phys. Chem. B* **2008,** *112*, 5279-5290.
115. Kumar, P.; Han, S. H. Dynamics of two-dimensional monolayer water confined in hydrophobic and charged environments. *J. Chem. Phys.* **2012,** *137*, 114510.

Chapter 2 Probing Diffusion with NMR Diffusometry and MD Simulations

2.1 Diffusion Basics

2.1.1 Theory and Concepts in Self-Diffusion

In this dissertation, we focus on the self-diffusion of liquid molecules both in bulk and under nanoconfinement. Here, we review the concepts involved in self-diffusion and the techniques, NMR diffusometry and MD simulations, to probe self-diffusion behavior. During self-diffusion, the center of mass of all the diffusing species (mostly water molecules and ions in this dissertation) does not change with time. Instead, individual particles tend to fluctuate away from their original positions over time. The diffusion propagator describes the collective displacement of diffusing species[1-2]

$$P(x,t) = (4\pi D_x t)^{-\frac{1}{2}} \exp(-\frac{x^2}{4D_x t}) \tag{2.1.1}$$

where $P(x)$ is the diffusion propagator along the x direction, D_x is the diffusion coefficient along the x direction, and t is the diffusion time. Diffusion propagators along y and z directions take the same form

$$P(y,t) = \left(4\pi D_y t\right)^{-\frac{1}{2}} \exp\left(-\frac{y^2}{4D_y t}\right), \;\; P(z,t) = (4\pi D_z t)^{-\frac{1}{2}} \exp(-\frac{z^2}{4D_z t}) \tag{2.1.2}$$

where D_y and D_z are the diffusion coefficients along y and z directions. In three-dimensional diffusion of bulk liquids, the diffusion is isotropic, meaning that the diffusion coefficient would be the same in all directions. The diffusion propagator follows a Gaussian distribution (**Figure 2.1**). The standard deviation of this Gaussian distribution is the root-mean-square displacement (RMSD) of the diffusing species

$$\sqrt{\langle x^2 \rangle} = \text{RMSD} = \sqrt{2D_x t} \tag{2.1.3}$$

where $\sqrt{\langle x^2 \rangle}$ is the standard deviation of the diffusion propagator $P(x,t)$, D_x is the diffusion coefficient along the x direction, and t is the diffusion time. The RMSD carries the meaning of the average displacement of diffusing species as observed over the diffusion time t. Equation 2.1.3 represents the RMSD for one-dimensional diffusion. In terms of isotropic two-dimensional or three-dimensional diffusion, the RMSD scales to $\sqrt{4Dt}$ and $\sqrt{6Dt}$ accordingly. Based on equation 2.1.3, the mean square displacement (MSD) of molecules is proportional to the diffusion time.

$$\text{MSD} = 2Dt \tag{2.1.4}$$

Equation 2.1.4 serves as the basis for the measurements or calculations of diffusion coefficients from NMR diffusometry experiments or MD simulations.

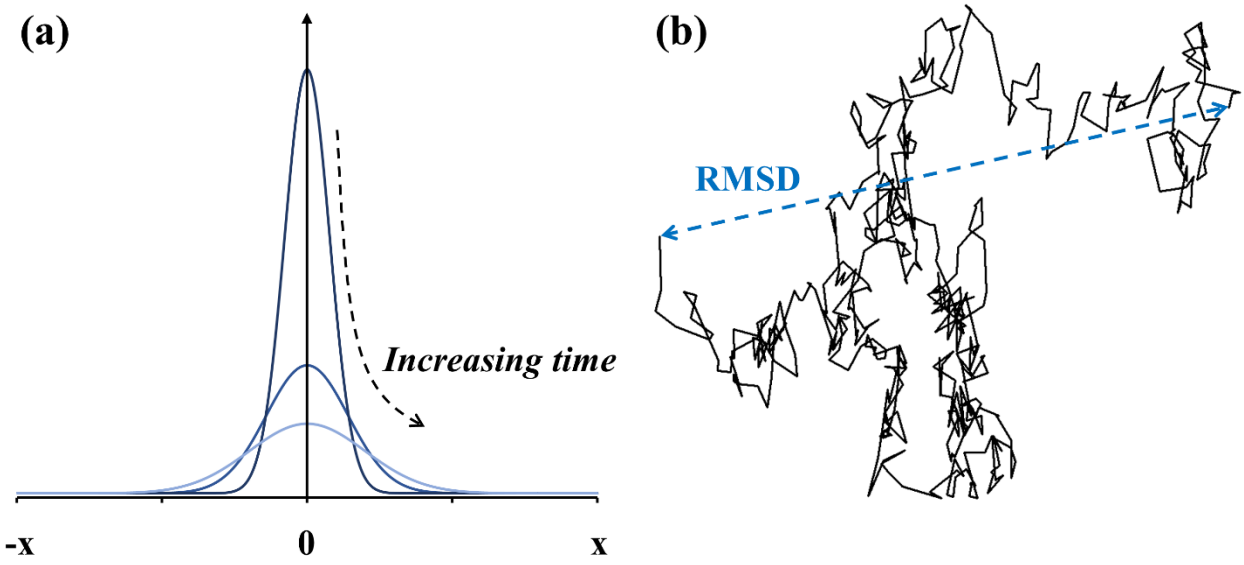

Figure 2.1. Panel (a) illustrates the change of diffusion propagator over time. The average displacement always remains equal to zero in self-diffusion, while the distribution of the displacement broadens over time. Panel (b) shows the random Brownian motions of a molecule. The trajectory of the Brownian motion is conceptualized as a series of random jumps. The displacement of the molecule is the straight-line distance (the dotted line) between the beginning and ending positions, which should be distinguished from the trajectory length. RMSD is a

property of the ensemble of water molecules undergoing diffusion.

One should note that equation 2.1.4 is not always valid. This linear relationship usually stands in the long-time limit (beyond tens of picoseconds) but not in the short-time limit (within several picoseconds or subpicosecond). Before the motion of a molecule becomes diffusive, a pre-diffusive regime exists (**Figure 2.2**).

The Langevin equation gives another approach to the relation between MSD and diffusion time[2]

$$\mathrm{MSD} = \frac{2k_B T}{\zeta}\left[t - t_\zeta\left(1 - \exp\left(-t/t_\zeta\right)\right)\right] \tag{2.1.5}$$

where k_B is the Boltzmann constant, T is the absolute temperature, ζ is a friction coefficient to describe the frictional forces between neighboring molecules, $t_\zeta = m/\zeta$ is the average collision time between molecules, and m is the mass of the diffusing species. When the diffusion time is much shorter than the collision time ($t \ll \mathrm{t}_\zeta$), the motions of molecules are in the ballistic (inertial motion) regime, and equation 2.1.5 becomes

$$\lim_{t \ll \mathrm{t}_\zeta} \mathrm{MSD} = \frac{k_B T}{m} t^2 \tag{2.1.6}$$

Here, equation 2.1.6 shows the MSD is proportional to t^2, and thus the RMSD is proportional to t. These relations indicate that the molecules are moving without changing velocity during the ballistic regime. Another characteristic of the ballistic regime is that the MSD only depends on the temperature and the mass of the diffusing species. When the diffusion time is much longer than the collision time, the motions of molecules enter the diffusive regime ($t \gg \mathrm{t}_\zeta$), and equation 2.1.5 becomes

$$\lim_{t \gg t_\zeta} \text{MSD} = \frac{2k_B T}{\zeta} t \tag{2.1.7}$$

In the diffusive regime, the MSD is proportional to t, which agrees with Equation 2.1.4. By comparing equation 2.1.7 and equation 2.1.4, one can establish the relationship between D and the collision time t_ζ

$$D = \frac{k_B T}{\zeta} = \frac{k_B T t_\zeta}{m} \tag{2.1.8}$$

By rearranging equation 2.1.8, the collision time t_ζ equals

$$t_\zeta = \frac{mD}{k_B T} = \frac{MD}{RT} \tag{2.1.9}$$

where M is the molar mass of the diffusing species. As an example, we can estimate the collision time of water molecules. The diffusion coefficient of liquid water is on the magnitude of 10^{-9} m^2/s. Based on the molar mass of water, the collision time of water molecules is on the timescale of femtoseconds at room temperature. Due to the short timescale, it is challenging to observe the ballistic regime experimentally. Fortunately, MD simulations provide the ability to calculate diffusion behavior on the timescale of femtoseconds. **Figure 2.2** shows the MSD and RMSD of water molecules in lithium triflate solutions (details of this simulation system can be found in section 3.2.3). From these plots, we observe a ballistic regime within the first tens of femtoseconds where the RMSD increases linearly with time. Additionally, the MSD and RMSD of water molecules in chemically different solutions are the same during the ballistic regime, matching the prediction from equation 2.1.6. Furthermore, **Figure 2.2** shows that a transition regime exists between the ballistic and diffusive regimes, before diffusion dominates the molecular motion. While the transition regime only lasts for ~1 ps, its behavior is complicated and has not been successfully described by any explicit equation. Here, we refer to the combination of the ballistic

regime and the transition regime as the *pre-diffusive* regime.

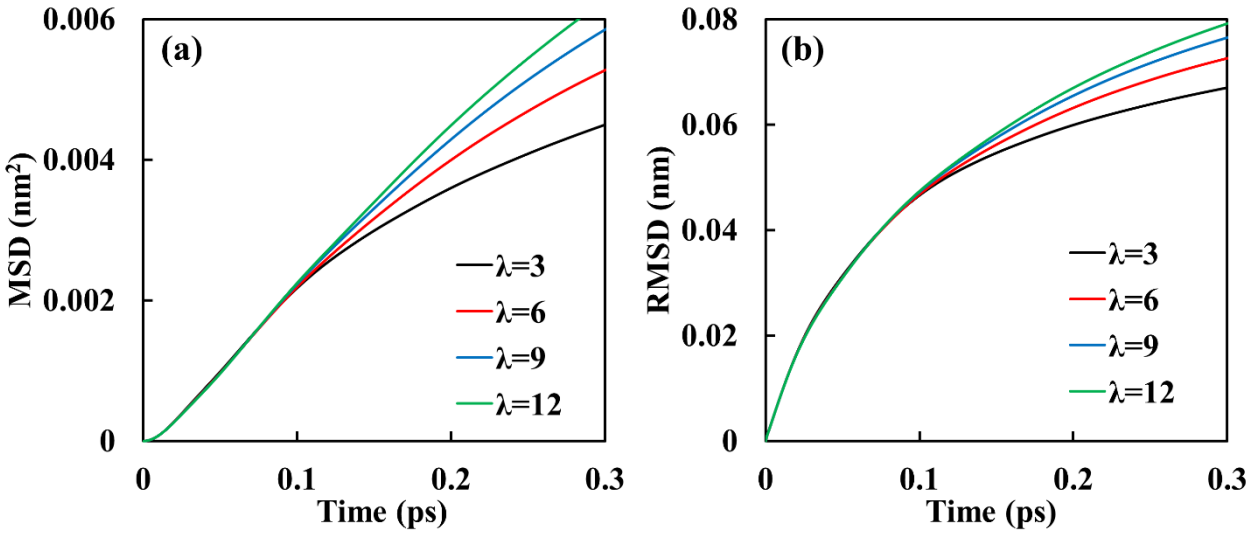

Figure 2.2. Generated from MD simulations, the calculated MSD and RMSD of water molecules in lithium triflate solutions as a function of diffusion time t at temperature = 300 K. The symbol λ denotes the concentration of the salt solutions (mole ratio of water to ion pairs - see section 3.2.3 for details). We observe the ballistic regime when diffusion time is smaller than 10 fs, within which the RMSD increases linearly with diffusion time. Here, the diffusive regime barely starts at the end of 0.5 ps. Salt solutions of different concentrations exhibit different water diffusion coefficients. More concentrated solutions (smaller λ) show slower diffusion coefficients. Despite differences in diffusion coefficients, displacements of water molecules are the same in the ballistic regime, which agrees with the predictions from Langevin dynamics. The prediffusive regime extends from tens of femtoseconds to ~1 ps. During the prediffusive regime, the slope of the MSD *vs.* time plots gradually decreases until diffusive motions dominate.

Without boundary conditions, the diffusion propagator follows the Gaussian distribution, also known as the normal distribution. When the MSD follows equation 2.1.4, the diffusion

behavior is referred to as normal diffusion. Since the slope of the MSD vs. time plot is directly proportional to the diffusion coefficient, normal diffusion will exhibit a constant diffusion coefficient over time. In addition to normal diffusion, there exists "anomalous" diffusion behavior in which the MSD of molecules no longer follows a linear relationship with diffusion time but may instead follow a generalized relation

$$MSD \propto t^{\kappa} \tag{2.1.10}$$

where κ is a coefficient that can deviate from unity. This anomalous diffusion often happens when boundary conditions for diffusive motion exist. In general, there are two types of anomalous diffusion. In the first scenario, the diffusion propagator is no longer Gaussian. The distortion of the diffusion propagator may happen when there is geometric confinement on a similar lengthscale as the diffusion length.[3] The geometric confinement limits the freedom of diffusing species to perform random motions. Thus, the diffusion propagator, which follows a normal distribution with random motions, is no longer Gaussian when the diffusing species experiences structural confinement. The characteristic behavior of molecular diffusion under geometric confinement is restricted diffusion, which has $\kappa < 1$.[2] When restricted diffusion happens, the MSD vs. time plot is concave downward, which means the diffusion coefficient decreases with increasing diffusion time.[3-4] In the second scenario, the diffusion propagator remains Gaussian; however, the standard deviation of the propagator is not proportional to time. For example, in single-file diffusion, the diffusion propagator still satisfies a Gaussian distribution, while the relation between MSD and diffusion time follows[5]

$$\text{MSD} \propto t^{1/2} \tag{2.1.11}$$

2.1.2 Activation Energy of Diffusion

When studying the temperature dependence of diffusion coefficients,[6-8] we often observe

diffusion coefficients that follow the Arrhenius equation

$$D = D_0 e^{-\frac{E_a}{RT}} \tag{2.1.12}$$

where E_a is the activation energy of diffusion, and D_0 is the pre-exponential factor.[6] One can extract the activation energy of diffusion from the Arrhenius fit

$$E_a = -\frac{\partial(lnD)}{\partial\left(\frac{1}{RT}\right)} = RT^2\frac{\partial(lnD)}{\partial T} \tag{2.1.13}$$

In previous work, our group has demonstrated that E_a is the same between bulk liquid and confined liquid with confinement size as small as a few nanometers.[6-8] A direct assumption based on this observation is that E_a mainly depends on the molecular-scale environment, including potentially both geometric confinement and intermolecular interactions. Thus, activation energy can serve as a suitable tool for studying the dynamics of nanoconfined liquids.

The linear relationship between lnD and $1/T$ in the Arrhenius equation is usually valid within a narrow temperature window (~40 K for liquids). With a temperature range as wide as 100 K, the Arrhenius plot usually becomes curved. In other words, the activation energy of diffusion changes with temperature. Activation energy commonly depends on temperature, which occurs not only in the diffusion process but also in other rate processes such as ionic conductivity and chemical reactions.[9-11] Thus, when comparing activation energies across different systems, we should study them over a similar temperature range.

Multiple equations exist to describe wide-temperature-range diffusion data, with the most popular one being the Vogel-Fulcher-Tamman (VFT) equation[12]

$$D = D_0 e^{-\left(\frac{A}{T-T_0}\right)} \tag{2.1.14}$$

where D_0, A, T_0 are the three fitting parameters (as opposed to two for simple Arrhenius fitting). In addition to the VFT equation, the Speedy-Angell power law[13] and a polynomial equation[14] can

also describe non-Arrhenius behavior of temperature-dependent diffusion coefficients

$$D = D_0[(T/T_S) - 1]^{\gamma} \quad (2.1.15)$$

$$lnD = a + b(1000/RT) + c(1000/RT)^2 \quad (2.1.16)$$

One should note that all of the above fitting equations are empirical or semi-empirical. Therefore, one should not overinterpret the physical meanings of the fitting parameters in these equations.

2.2 Nuclear Magnetic Resonance (NMR) Concepts and Experiments

2.2.1 General NMR Principles

In a nucleus, the combination of protons and neutrons gives rise to the inherent spin number. A nucleus that possesses an even number of both protons and neutrons would have a nuclear spin number of zero. Otherwise, the nucleus will have a non-zero spin number. Nuclei with non-zero spin numbers have multiple spin states

$$Number\ of\ spin\ states = 2I + 1 \quad (2.2.1)$$

where I is the spin number of the nucleus.

Without an external magnetic field, all nuclear spin states are degenerate. Under an external magnetic field, the nuclear spin states are no longer degenerate. Nuclear magnetic resonance (NMR) spectroscopy is a technique that takes advantage of the difference in energy between nuclear spin states to obtain a spectroscopic signal. Thus, a nucleus with a spin number of zero would only have one spin state and is not detectable by NMR techniques. For example, commonly probed NMR nuclei include ^{1}H and ^{13}C with a spin number of 1/2, ^{2}H with a spin number of 1, and ^{7}Li with a spin number of 3/2. Meanwhile, nuclei with a spin number of 0, such as ^{12}C and ^{16}O, show no NMR signal. In an NMR spectrometer, a strong external magnetic field permeates the sample region. In the direction of the external magnetic field, the nuclear spins in the sample

precess with the Larmor frequency (ω_0)[15]

$$\omega_0 = \gamma B_0 \tag{2.2.2}$$

where γ is the gyromagnetic ratio of the nucleus, and B_0 is the magnetic field strength. The energy separation between spin states is directly proportional to the Larmor frequency

$$\Delta E = h\omega_0 = h\gamma B_0 \tag{2.2.3}$$

where ΔE is the energy difference between two spin states, h is the Planck constant. Taking ^{1}H as an example, ^{1}H has two spin states, one that aligns parallel (low energy state) with the direction of the external magnetic field, and one that aligns antiparallel (high energy state) with the magnetic field. **Figure 2.3** illustrates the splitting pattern, also known as the Zeeman diagram, of the proton. Due to the energy difference, a population difference (of nuclei) exists among different spin states. The Boltzmann distribution evaluates the population difference between two spin states

$$\frac{P_i}{P_j} = \frac{n_i}{n_j} exp^{-\Delta E/k_B T} \tag{2.2.4}$$

where P_i and P_j are the population of nuclei in the upper spin state and lower spin state, and n_i and n_j are the degeneracy of the two spin states. The signal intensity of an NMR spectrum is directly proportional to the population difference between spin states. We can infer from equations 2.2.3 and 2.2.4 that a higher external magnetic field always leads to higher NMR signal intensity. Based on equation 2.2.4, there exist 1,000,096 proton nuclei in the lower spin state per 1,000,000 proton nuclei in the upper spin state at a temperature of 298 K for an instrument operating at 600 Mhz (B_0 = 14 T). The small population difference of nuclear spin states along with the small value of the intrinsic magnetic moment of each nucleus lead to the relatively low sensitivity of NMR techniques.

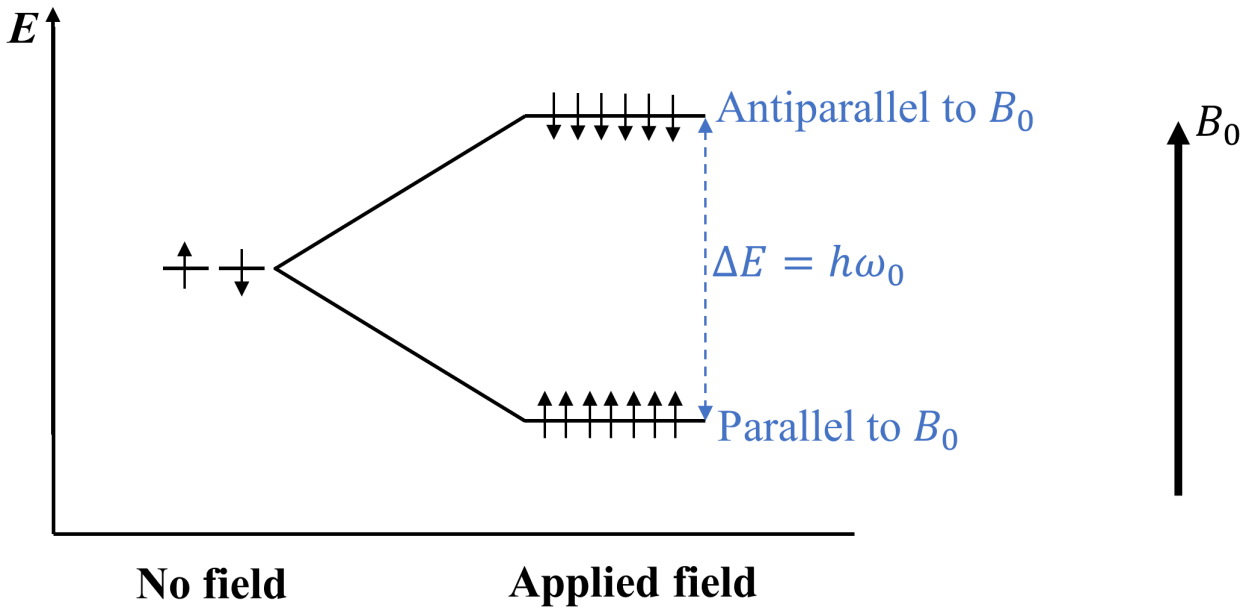

Figure 2.3 Zeeman diagram for a spin-1/2 nucleus. A spin-1/2 nucleus has two spin states, which are degenerate without an external magnetic field. In an external magnetic field B_0, the two spin states split into upper and lower spin states. The spins that align parallel to B_0 have lower energy than those aligned antiparallel to B_0. The energy difference between the two spin states is directly proportional to the strength of B_0. Due to the state energy difference, the lower spin state has a slightly higher population than the upper spin state.

2.2.2 1D NMR experiments and Relaxation Times

The 1D NMR experiment gives a spectrum in the frequency domain. As previously mentioned, the lower spin state has a slightly larger population than the upper spin state. As a result, there is a net spin magnetization M_z along the direction of the external magnetic field, which is by tradition called the z-direction or the longitudinal direction. **Figure 2.4** describes the pulse sequence of a 1D NMR experiment. At the beginning of a 1D experiment, a radiofrequency pulse rotates the z-direction magnetization by 90°, putting the net magnetization into the xy-plane or the

transverse plane. The photon energy of this 90° pulse is the same as the energy separation between spin states. Thus, the 90° pulse excites the nuclear spins from the lower spin state to the upper spin state.

After the 90° pulse, the net magnetization M_{xy} precesses in the transverse plane at the Larmor frequency, during which two relaxation processes happen concurrently. The spin-spin relaxation, which happens in the transverse plane, results from the dephasing of spins. Individual spins precess at the Larmor frequency corresponding to their local magnetic field. Due to the inhomogeneities of the external magnetic field and the fluctuations of the local magnetic environment, individual spins do not feel exactly the same magnetic field strength and will precess at slightly different frequencies. As a result, the spins phase out in the transverse plane, and the intensity of net magnetization decreases with time

$$M_{xy}(t) = M_{eq}e^{-t/T_2} \tag{2.2.5}$$

where $M_{xy}(t)$ is the net magnetization in xy-plane at time t, $t = 0$ is the time at which the magnetization lies in the xy-plane just after the 90° pulse, M_{eq} is the magnitude of the equilibrium net magnetization (originally along the z-axis), and T_2 is the spin-spin or transverse relaxation time that characterizes the decay rate of $M_{xy}(t)$. Another relaxation process, spin-lattice or longitudinal relaxation, is the relaxation of magnetization from the transverse plane back to the longitudinal direction. In other words, the spin-lattice relaxation is the thermodynamic re-equilibration of the spin state populations. During spin-lattice relaxation, M_z gradually grows back to its equilibrium

$$M_z(t) = M_{eq}\left(1 - e^{-t/T_1}\right) \tag{2.2.6}$$

where $M_z(t)$ is the net magnetization along the z-direction at time t, and T_1 is the spin-lattice relaxation time. The spin-lattice relaxation happens at the same time as spin-spin relaxation, while the spin-spin relaxation is typically faster than the spin-lattice relaxation ($T_2 < T_1$). During the

relaxation process, the NMR signal detector detects the magnetization along one direction in the transverse plane. The signal in the transverse plane is oscillating back and forth with a decaying intensity, thus leading to the free-induction decay (FID) pattern. The FID is the NMR signal in the time domain. A Fourier transform (FT) converts the FID into the frequency domain spectrum

$$S(\omega) = \int_0^{\infty} S(t)\, e^{-i\omega t} dt \tag{2.2.7}$$

where $S(\omega)$ is the NMR signal (spectrum) in the frequency domain and $S(t)$ is the signal (FID) in the time domain.

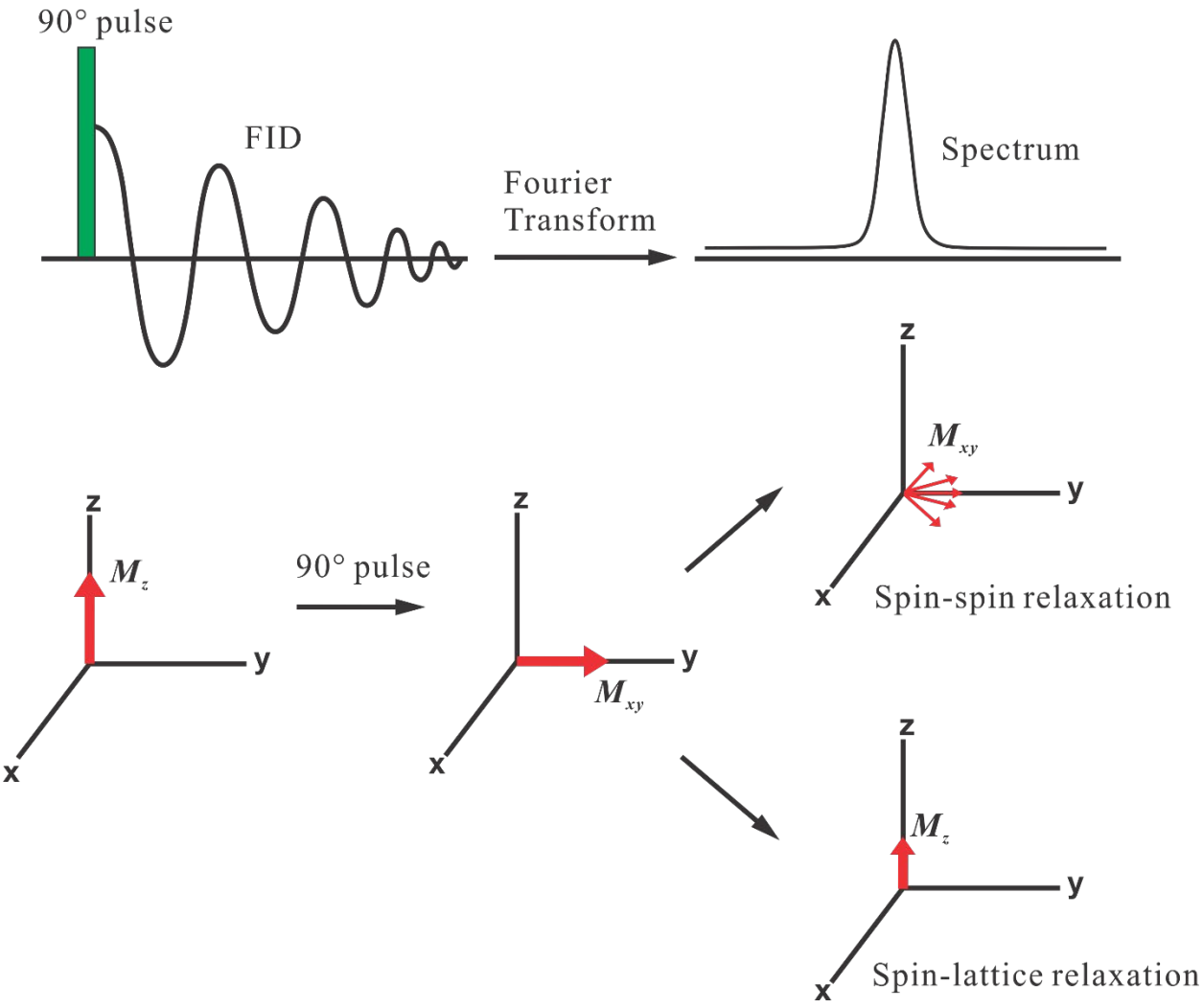

Figure 2.4 Scheme of a single-pulse 1D NMR experiment. A 90° radiofrequency pulse rotates the net magnetization from the z-direction to the xy-plane. After the 90° pulse, the transverse magnetization precesses in the xy-plane while going through two relaxation processes. The spin-lattice relaxation is the relaxation of nuclear spins back to equilibrium along the z-axis. The spin-spin relaxation is the dephasing of the nuclear spins in the xy-plane. The dephasing leads to attenuation of magnetization in the xy-plane with a decay time of T_2. An NMR signal detector detects the magnetization from one direction in the xy-plane, and records the FID signal in the time domain. Through Fourier transformation, the FID generates the NMR spectrum.

2.2.3 NMR Diffusometry

NMR diffusometry, sometimes known as diffusion-ordered spectroscopy (DOSY) or pulsed-field-gradient (PFG) NMR, is a class of 2D NMR experiments that measures the diffusion coefficients of NMR-active nuclei. In NMR diffusometry, a magnetic field gradient pulse alters the local magnetic field profile.[2, 16] Varying the strength of the gradient pulse provides the second dimension in the NMR diffusometry experiment. The gradient pulses add to the local magnetic field strength along a given direction based on the following equation:[17]

$$B(r) = B_0 + gr \tag{2.2.8}$$

where $B(r)$ is the local magnetic field strength as a function of position r during the gradient pulse, B_0 is the static magnetic field strength, and g is the gradient strength. The pulse sequence of an NMR diffusometry experiment not only depends on the field gradient but also incorporates the spin-echo pulse sequence.[18] To illustrate the idea of NMR diffusometry, we present one of its pulse sequences, the pulsed-gradient stimulated spin-echo (PGSTE) method,[19] in **Figure 2.5**. The PGSTE pulse sequence contains two subsequences: the radiofrequency pulses that change the state of the nuclear spins and the gradient pulses that create a spatially varying local magnetic field

strength. After the first 90° radiofrequency pulse, the net spin magnetization goes from the z-direction down to the xy-plane, and all the spins are in phase at this point. The first gradient pulse comes right after the first radiofrequency pulse. During the first gradient pulse, the Larmor frequency $\omega(r)$ at which the spins precess will vary with position:

$$\omega(r) = \gamma B(r) = \gamma B_0 + \gamma g r \tag{2.2.9}$$

Consequently, the spin magnetic moments along the gradient direction become out of phase during the gradient pulse. After the first gradient pulse, the second 90° pulse reverts the spin magnetic moments to the z-axis. Before the second gradient pulse, the third 90°pulse brings the magnetic moments again to the xy-plane. This three successive 90° pulse sequence is called the stimulated echo,[19] which gives constructive interference of magnetic moments and increases the signal intensity. The time between the two gradient pulses, denoted as Δ, is the diffusion time. The second gradient pulse is able to reverse the spin dephasing if the positions of the nuclei do not change during the diffusion time. When diffusion happens, the dephasing cannot be fully reversed at the end of the PGSTE pulse sequence, which leads to attenuation of NMR signal intensity. The Stejskal-Tanner equation[19-20] describes the relation between PGSTE signal attenuation, the NMR experimental parameters, and the diffusion coefficient.

$$I/I_0 = e^{-\gamma^2 D g^2 \delta^2 (\Delta - \frac{\delta}{3})} \tag{2.2.10}$$

I is the signal intensity at gradient strength g, I_0 is the signal intensity at zero gradient strength, δ is the duration of the gradient pulse. During a PGSTE experiment, the diffusion time, Δ, and gradient pulse duration, δ, are both kept constant while the gradient strength, g, is varied in steps. By plotting I/I_0 against gradient strength, one can extract the diffusion coefficient.

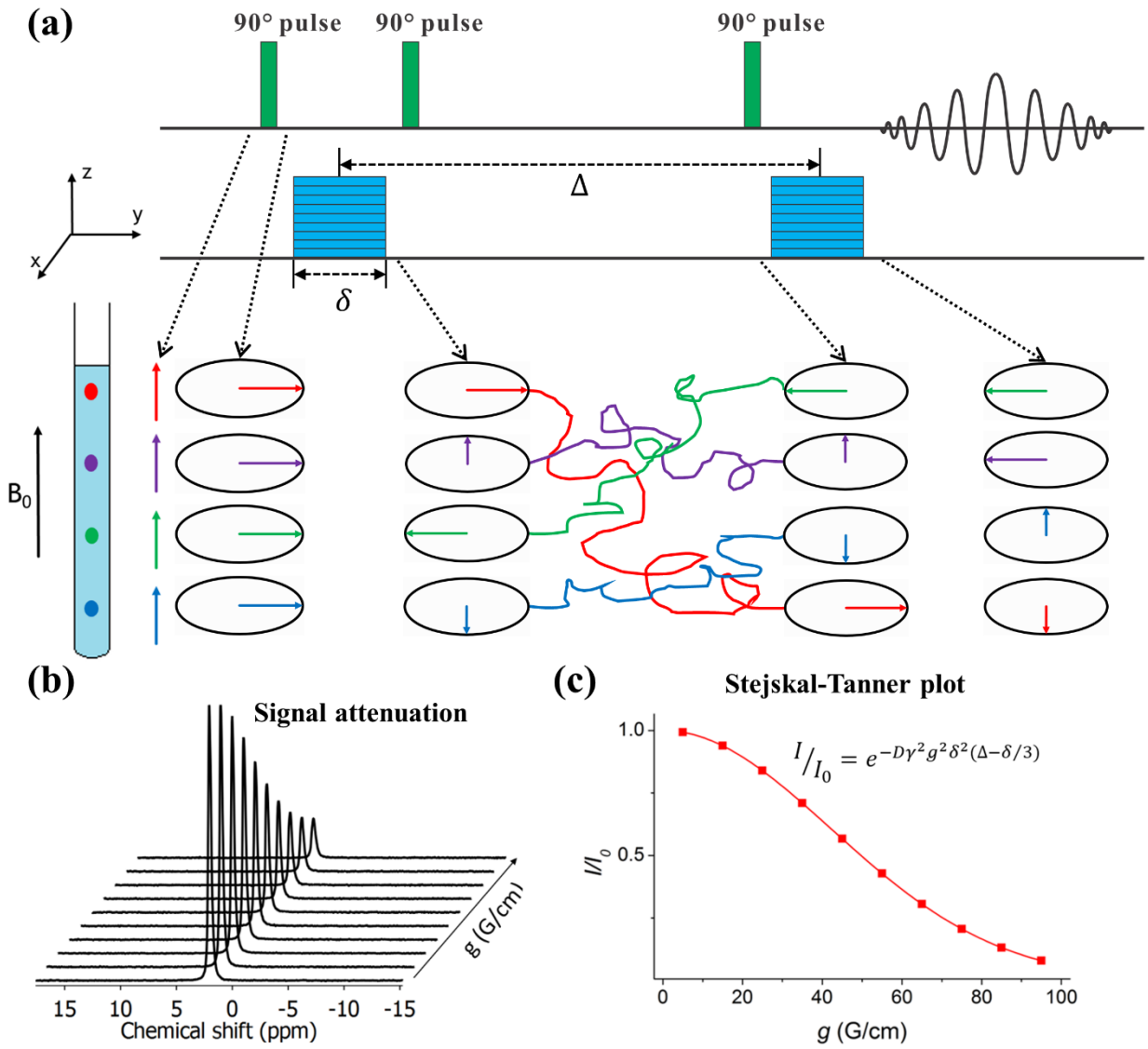

Figure 2.5. Panel (a) shows the pulse sequence of a PGSTE experiment and the change of spin magnetization due to the pulse sequence and diffusion of nuclei. The green pulses are the three 90° pulses, and blue pulses represent the gradient pulses. The scheme here corresponds to a field gradient along the z-direction. The four different dots inside a tube represent nuclear spins at different positions along z. The circles with arrows inside each represent a slice (or cylindrical band) of nuclear spins in the xy-plane. The direction of the arrows denotes the phase of the precessing nuclear spins. Panel (b) shows NMR spectra that show signal attenuation with increasing gradient strength. Panel (c) shows a representative Stejskal-Tanner plot, where each

point is formed from the integral of each spectrum in panel (b) normalized by the integral of the first (tallest) spectrum taken at $g = 0$.

In a PGSTE experiment, the diffusion time Δ needs to be comparable to or less than the longitudinal (spin-lattice) relaxation time (T_1) of the moving species. T_1 ranges between 10 ms and 2000 ms for most mobile species in soft materials like ionomer membranes. Considering that the diffusion coefficient of mobile species such as water molecules and ions in bulk or under confinement may range from 10^{-14} to 10^{-9} m^2/s, NMR diffusometry probes RMSD of diffusing species ranging from 100 nm to 10 μm based on equation 2.1.3. In NMR diffusometry, the field gradient can only be applied in one direction for a given experiment. Thus, the diffusion coefficient measured by NMR diffusometry is always one-dimensional along the direction of the gradient. NMR diffusometry has been effective in studying various materials such as polymer membranes,[4, 7, 21-25] ionic liquids,[26-28] and micelles.[29-30]

2.3 Molecular Dynamics (MD) Simulations

2.3.1 Algorithms

MD is a classical-mechanics simulation tool that affords insight into various dynamical and energetic properties of a model system. **Figure 2.6** describes the overall algorithms of MD simulations. The primary inputs for MD simulations are the coordinates, velocities, and masses of the atoms, and the force-field describing the interactions between the atoms. With the input parameters, MD simulations calculate the intermolecular and intramolecular interactions between atoms based on classical force field. In MD simulations, the intermolecular interactions are composed of two subcategories: Lennard-Jones (LJ) interactions and Coulombic interactions. The

Lennard-Jones potential (V_{LJ})[31] is an approximation of the interaction between two neutral atoms that contains a repulsion term and an attraction term

$$V_{LJ} = 4\varepsilon[(\frac{\sigma}{r_{ij}})^{12} - (\frac{\sigma}{r_{ij}})^{6}] \quad (2.3.1)$$

where V_{LJ} is the Lennard-Jones potential, r_{ij} is the distance between atom i and atom j, ε is the scaling factor of the potential energy, and σ is the distance at which the potential energy reaches zero. The Coulombic potential (V_{Coul}) describes the interaction between two charged atoms

$$V_{Coul} = k\frac{q_i q_j}{r_{ij}} \quad (2.3.2)$$

where V_{LJ} is the Coulombic potential, k is Coulomb's constant, and q_i and q_j are the charges of the two atoms. To efficiently calculate the intermolecular interactions, MD simulations incorporate two methods: periodic boundary conditions, which will be explained later, and a cut-off distance scheme. The purpose of setting a cut-off distance in the calculation of intermolecular interactions is to improve the time efficiency of MD simulations. Beyond the cut-off distance (typically 1.2 nm), the simulations no longer calculate the pairwise Lennard-Jones potential. The basis for this approximation is that the LJ potential decays quickly with increasing distance. The cut-off scheme saves time when calculating LJ interactions and is especially economical for large simulation systems. The Coulombic potential, however, is much longer-range than the Lennard-Jones potential. Within the cut-off distance, the Coulombic potential is calculated based on equation 2.3.2. To facilitate the calculation of long-range Coulombic interactions beyond the cut-off distance, a common approach is the particle-mesh Ewald summation, which calculates long-range Coulombic interactions in reciprocal space.[32]

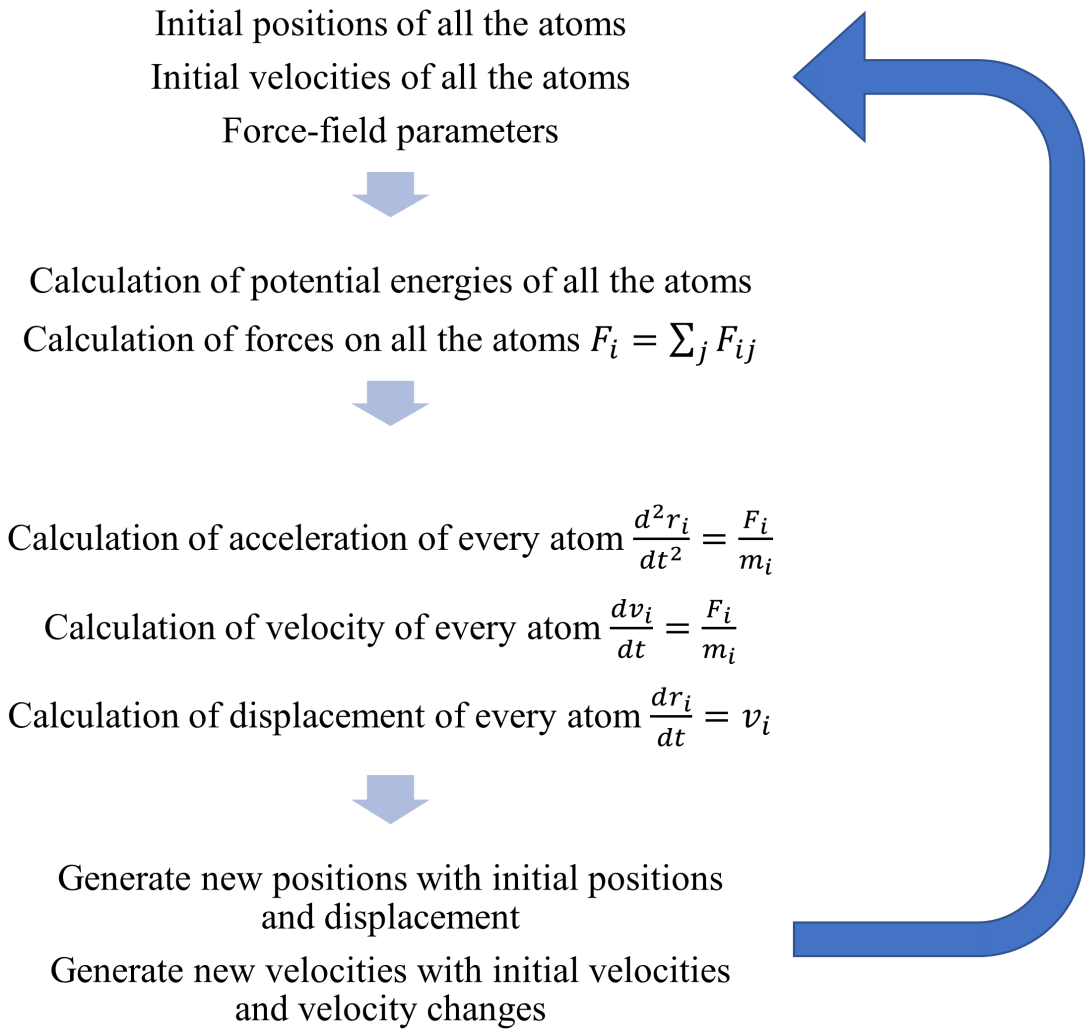

Figure 2.6 Scheme of the algorithm used in MD simulations. MD simulations start with input files that contain the coordinates and velocities of all atoms in the system. With the input files, the force-field parameters (more details in section 2.3.2), and the masses of atoms, the simulation generates new coordinates and velocities after a short timestep (typically 1 fs). The output is recursively used as the input to repeat the whole process.

In MD simulations, the intramolecular interactions have three subcategories: bond potentials, bond angle potentials, and dihedral potentials. There is often more than one approach to describe each kind of intramolecular interaction. For simplicity, only one common approach

will be described for each category below. Between bonded atoms, the harmonic potential is a common approximation of the bond energy

$$V_b = \frac{1}{2} k^b (r_{ij} - r_e)^2 \tag{2.3.3}$$

where V_b is the bond potential, k^b is the force constant of the bond, r_{ij} is the bond length, and r_e is the equilibrium bond length. Similarly, the energy of bond angles can also be approximated by a harmonic potential

$$V_a = \frac{1}{2} k^\theta (\theta_{ij} - \theta_e)^2 \tag{2.3.4}$$

where V_a is the angular potential, k^θ is the force constant of angle vibration, θ_{ij} is the bond angle, and θ_e is the equilibrium bond angle. The Ryckaert-Bellemans function describes the dihedral potential

$$V_d = \sum_{n=0}^{5} C_n (\cos(\theta))^n \tag{2.3.5}$$

where C_n are the coefficients specific to the atoms of the dihedral, and θ is the dihedral angle.

The overall potential energy on an atom is the summation of intermolecular and intramolecular interactions. And the force on an atom is calculated by

$$F_{ij} = -\frac{\partial [V_{intra} + V_{inter}]}{\partial r_{ij}} \tag{2.3.6}$$

where F_{ij} is the force of atom j on atom i, and V_{intra} and V_{inter} are the interactions between atom i and atom j.

In MD simulations, it is assumed that the forces are pair-additive. Thus, the total force upon an atom i is the summation of the forces from all the interacting atoms:

$$F_i = \sum_j F_{ij} \tag{2.3.7}$$

With the total force, one can calculate the displacement of the atom based on Newton's equation of motion

$$\frac{d^2 r_i}{dt_s^2} = \frac{F_i}{m_i} \tag{2.3.8}$$

where r_i is the displacement of atom i within time t_s, and m_i is the mass of atom i. The time t_s is the timestep in MD simulations. The length of one timestep is typically very short (1 fs) to avoid large changes to the molecular environment during a timestep divergence in the simulation. With the displacement of every atom, the simulation generates a new set of coordinates and velocities at the end of each timestep. Furthermore, the new coordinates serve as the input for the force calcuation for the next timestep. MD simulations are based on the recursive calculations of timesteps, and the number of timesteps can be as high as 10^6 or even 10^8 for desired simulations. The coordinates, forces, velocities, and potential energies of all the atoms are the main outputs of MD simulations.

2.3.2 Force-Field Parameters

To calculate the potential energy of a molecular system, researchers have explicitly defined force-field parameters for individual atoms and groups of atoms. The force-field parameters include, but are not limited to, Lennard-Jones parameters, the charge of an atom, the mass of an atom, equilibrium bond lengths/angles, and force constants for the bonds/bond angles. Take the water molecule as an example. While several models exist to describe water molecules, the SPC/E water model[33] and TIP4P/2005 water model[34] are among the models that best predict the self-diffusion coefficient of water.[35]

The SPC/E model is a three-site model with each site defining one atom in a water molecule. The oxygen site carries a charge of -0.8476 e, while the two hydrogen sites both carry a charge of 0.4238 e. The oxygen-hydrogen bond length is 1.0000 Å, while the bond angle is 109.47°.[33] Moreover, the SPC/E model is a rigid model in which the bond length and bond angle are constrained to remain constant during simulations. In SPC/E water, only the oxygen atom bears the Lennard Jones parameters of water (refer to **Table 2.1**), which is also a common practice in other water models. Notice the geometric parameters of the SPC/E model are not the same as experimental values. Intentionally adjusting force-field parameters can offset part of the errors introduced by the approximations and provide better simulation results when calculating specific properties.

The TIP4P/2005 model is a rigid four-site model. In addition to the hydrogen and oxygen atoms, there is also a "virtual site" in the TIP4P/2005 model for added flexibility. [34] The virtual site separates the charge of an oxygen atom from the LJ interactions. In the TIP4P/2005 model, the oxygen atom has zero charge but carries the LJ parameters. The virtual site carries no LJ parameters while bearing the negative charge to balance the positive charges of hydrogen atoms. There are numerous simulation models exclusively for water. However, force fields for molecules other than water are less abundant. In this dissertation, we utilize the generic force field, OPLS-AA,[36] to describe non-water molecules.

In the force fields, the ε and σ terms of LJ interactions (equation 2.3.1) are explicitly defined for every atom. When LJ interactions are defined between two atoms, the combination rules generate the specific ε and σ terms. The combination rule for the OPLS-AA force field is

$$\varepsilon_{ij} = \sqrt{\varepsilon_i \varepsilon_j} \qquad \sigma_{ij} = \sqrt{\sigma_i \sigma_j} \tag{2.3.9}$$

where σ_i and ε_i are the LJ parameters of atom i, σ_j and ε_j are the LJ parameters of atom j, and the

combined σ_{ij} and ε_{ij} are the LJ parameters to calculate the LJ interactions between atom i and atom j.

Table 2.1 Force-field parameters for SPC/E and TIP4P/2005 water models

	SPC/E	TIP4P/2005
σ (nm)	0.316557	0.31589
ε (kJ/mol)	0.650194	0.7749
Charge of oxygen atom	-0.8476	0
Charge of hydrogen atom	0.4238	0.5564
H-O-H angle (°)	109.47	104.52
O-H bond length (Å)	1.0000	0.9572
Charge of virtual site	NA	-1.1128

For time efficiency, classical force fields treat atoms as point charges. The point charges do not polarize according to neighboring species, which often leads to overestimation of electrostatic interactions.[37] To account for the polarizability of molecules, researchers have developed polarizable force fields such as the fluctuating charge model,[38] Drude particle model,[39] and charge transfer model.[40] In the fluctuating charge model, atoms are still treated as point charges while the magnitudes of the charges are allowed to fluctuate with respect to the electronegativity of the atom. If the instantaneous electronegativity of the atom is larger than its average electronegativity, the charge on the atom is reduced; otherwise, the charge on the atom is increased.[38] The Drude particle model gets its name from the Drude model proposed by Paul Drude in 1900.[41] In the Drude particle model, a zero-mass and charged particle (the Drude particle) attaches to one or several atoms in the molecule through a harmonic spring.[39] The Drude particle oscillates in reaction to the change of the surrounding electrostatic environment. Through displacement, the Drude particle changes the dipole moment of the molecule therefore making the molecule polarizable. In the fluctuating charge model and the Drude particle model, the total

charge of a neutral molecule always stays at zero. In the charge transfer model, neutral molecules may carry instantaneous positive/negative charges. Charge transfer describes the transfer of partial charges between molecules. Quantum simulations have shown nontrivial charge transfer between neighboring molecules/ions.[42-43] In MD simulations, charge transfer is often implemented by defining a distance-dependent amount of charge transferred.[40, 44] All polarizable force fields are much more performance-hungry than simple fixed-charge force fields, and a unified approach to the polarizable force field is still lacking.

2.3.3 Periodic Boundary Conditions

In practice, the simulation systems in MD cannot be macroscopically large. The finite size of a simulation system is usually represented by a simulation box (shown in **Figure 2.7**). If a molecule exists at the center of the simulation box, it will see neighboring molecules in all directions. However, when a particle exists at the edge of the box, it will see neighboring molecules only on one side while seeing a vacuum on the other side. Consequently, the interactions felt by the molecules at the edge will be significantly different from the interior molecules, which is not realistic when calculating bulk average properties. Additionally, the finite size of a simulation box creates difficulties in calculating long-range electrostatic interactions. To alleviate the edge effect and better model long-range interactions, researchers introduce periodic boundary conditions (PBC) into MD simulations. PBC replicate the simulation box in the direction of interest (all three directions for bulk simulations). With PBC, the particles near the edge of the box are in a similar environment as interior particles, removing the edge effect. PBC also allows the particles traveling out of the simulation box to enter the box from the opposite, keeping constant composition.

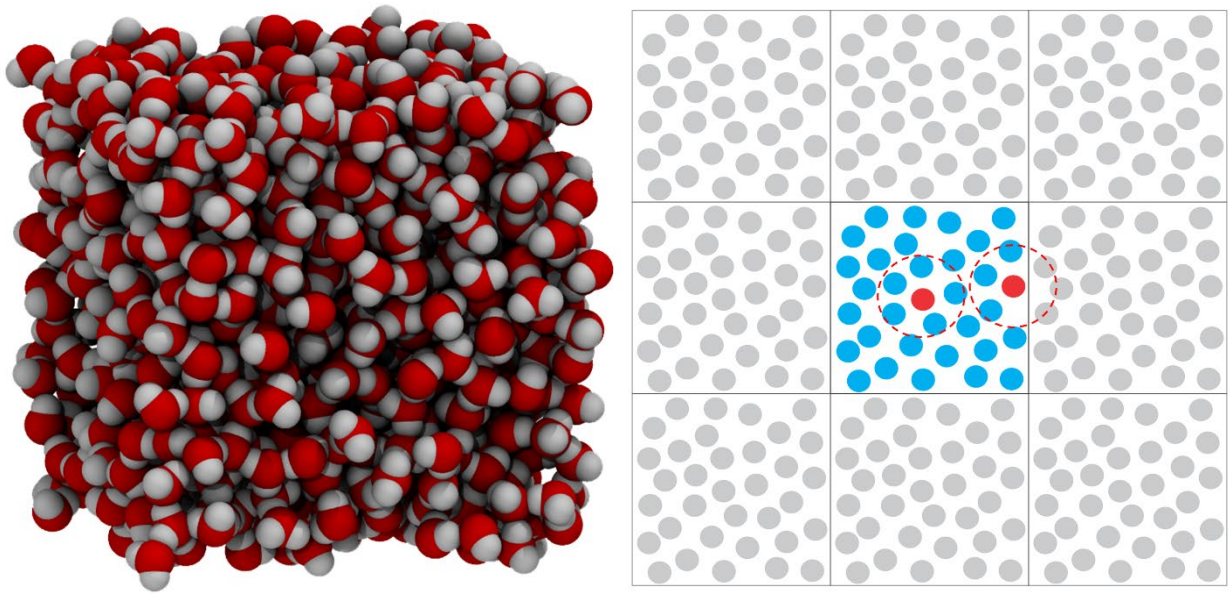

Figure 2.7. The left panel shows an example simulation box with only water molecules inside. The cubic and cuboid shapes are the most common shapes for a simulation box. The right panel shows a description of the periodic boundary conditions. For simplicity, we describe PBC with a two-dimensional scheme. Note that the simulation box can replicate itself in all three dimensions. The red bubbles highlight molecules at the center and the edge of a simulation box. With PBC, the center molecule and the molecule at the edge experience a similar potential energy environment.

2.3.4 Analysis of MD Simulations

Here we review a few typical analyses that we utilize in later chapters. The main outputs from MD simulations include coordinates and velocities of all atoms as a function of simulation time. These outputs serve as the basis for further analysis of a given simulation system. The coordinates provide a way to calculate the displacement and diffusion coefficients of molecules

$$D_x = \frac{\langle [x_i(t_0 + t) - x_i(t_0)]^2 \rangle}{2t} \tag{2.3.10}$$

where D_x is the diffusion coefficient along the x-direction, $x_i(t_0 + t)$ is the x-direction coordinate

of the atom i at time $t_0 + t$, and $x_i(t_0)$ is the coordinate of the atom i at time t_0. The $\langle[x(t_0 + t) - x(t_0)]^2\rangle$ term calculates the mean square displacement of the probe atoms during the period t. In the calculation of diffusion coefficients, multiple restarting points are chosen throughout the trajectory. In other words, the value of t_0 varies in the process of averaging. Alternatively, the diffusion coefficient can also be obtained from velocities by the Green-Kubo relations[45-46]

$$D = \frac{1}{3}\int_0^\infty \langle v_i(t_0 + t) \cdot v_i(t_0)\rangle dt \tag{2.3.11}$$

where D is the three-dimensional diffusion coefficient, $v_i(t_0 + t)$ is the velocity of atom i at time $t_0 + t$, and $v_i(t_0)$ is the velocity of atom i at time t_0. The $\langle v_i(t_0 + t) \cdot v_i(t_0)\rangle$ term is the velocity autocorrelation function (**Figure 2.8a**).

Radial distribution functions (RDFs) can also be calculated from the coordinates of atoms. An RDF, also known as a pair correlation function, evaluate the number density of particle B around particle A (A and B can be identical or different) as a function of distance

$$g(r) = \frac{\rho_B(r)}{\langle\rho_B\rangle} \tag{2.3.12}$$

where $g(r)$ is the conventional notation for an RDF, $\langle\rho_B\rangle$ is the average number density of particle B in the simulation system, and $\rho_B(r)$ is the number density of particle B when the distance between A and B is within r and $r + dr$ (dr is a small value, e.g. 1 pm). An RDF illustrates the distribution of particle B around particle A (**Figure 2.8b**). In addition, one can extract the coordination number from the RDF[47]

$$N_{co}(x) = 4\pi\rho\int_0^x r^2 g(r) dr \tag{2.3.13}$$

where $N_{co}(x)$ is the coordination number of particle B around particle A within a specified

distance x, ρ is the number density of particle B, and $g(r)$ is the RDF of particle B around particle A.

Hydrogen-bonding analysis is also useful in MD simulations of aqueous systems. The hydrogen-bonding analysis is based on definitions of hydrogen-bond donors and hydrogen acceptors (Figure 2.8c). For aqueous systems, the hydrogen-bond donor is the oxygen atom of the water molecule that donates an O-H bond. The hydrogen-bond acceptor is the oxygen atom of the water molecule that accepts hydrogen bond. For two water molecules to establish a hydrogen bond, the donor-acceptor distance needs to be less than 0.35 nm, and the hydrogen-donor-acceptor angle needs to be smaller than 30°.

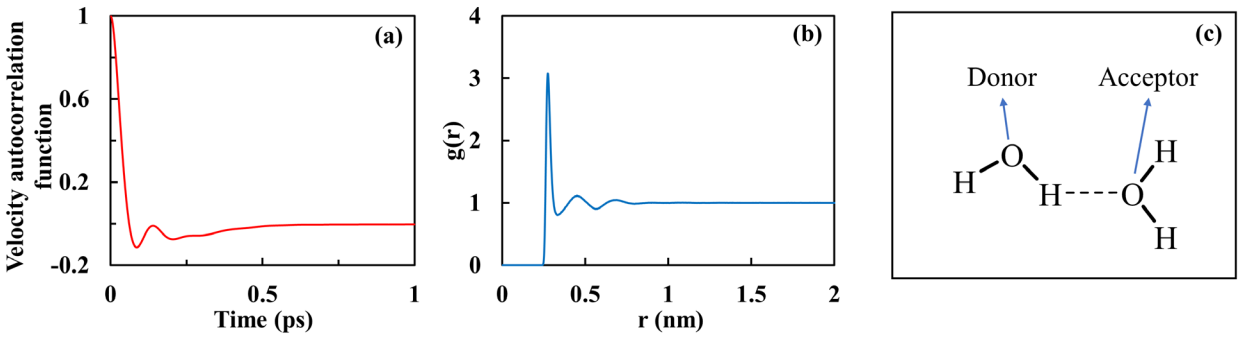

Figure 2.8 Example plots of the velocity autocorrelation function (a) and radial distribution function (b) in an aqueous solution. Panel (c) illustrates the definition of donor and acceptor in the hydrogen-bonding analysis.

2.4 Summary

Activation energy of diffusion provides a desirable probe to investigate confined liquid dynamics on the lengthscale of ~1 nm. With NMR diffusometry experiments and MD simulations, we can extract/calculate activation energies in both experimental and computational model systems. In the remaining chapters, we are going to look at the liquid dynamics in materials such

as polymer membranes and simulation models such as carbon nanotubes with the techniques described in this chapter. The combination of experiments and simulations provide unique perspectives and new insights into the dynamics of confined liquid.

2.5 References

1. Einstein, A. The theory of the Brownian Motion. *Ann. Phys.* **1906,** *19*, 371-381.
2. Callaghan, P. *Translational Dynamics and Magnetic Resonance: Principles of Pulsed Gradient Spin Echo NMR*. Oxford University Press: New York, 2011.
3. Appel, M.; Fleischer, G.; Karger, J.; Fujara, F.; Siegel, S. NMR evidence of anomalous molecular diffusion due to structural confinement. *Epl-Europhys Lett* **1996,** *34*, 483-487.
4. Thieu, L. M.; Zhu, L.; Korovich, A. G.; Hickner, M. A.; Madsen, L. A. Multiscale Tortuous Diffusion in Anion and Cation Exchange Membranes. *Macromolecules* **2019,** *52*, 24-35.
5. Kärger, J.; Stallmach, F., PFG NMR Studies of Anomalous Diffusion. In *Diffusion in Condensed Matter: Methods, Materials, Models*, Heitjans, P.; Kärger, J., Eds. Springer Berlin Heidelberg: Berlin, Heidelberg, 2005; pp 417-459.
6. Kidd, B. E.; Forbey, S. J.; Steuber, F. W.; Moore, R. B.; Madsen, L. A. Multiscale Lithium and Counterion Transport in an Electrospun Polymer-Gel Electrolyte. *Macromolecules* **2015,** *48*, 4481-4490.
7. Lingwood, M. D.; Zhang, Z.; Kidd, B. E.; McCreary, K. B.; Hou, J.; Madsen, L. A. Unraveling the local energetics of transport in a polymer ion conductor. *Chem. Commun.* **2013,** *49*, 4283-4285.
8. Zhang, R.; Chen, Y.; Troya, D.; Madsen, L. A. Relating Geometric Nanoconfinement and Local Molecular Environment to Diffusion in Ionic Polymer Membranes. *Macromolecules* **2020,** *53*, 3296-3305.
9. Weingartner, H.; Haselmeier, R.; Holz, M. Effect of xenon upon the dynamical anomalies of supercooled water. A test of scaling-law behavior. *J. Phys. Chem.* **1996,** *100*, 1303-1308.
10. Murugavel, S. Origin of non-Arrhenius conductivity in fast ion conducting glasses. *Phys Rev B* **2005,** *72*, 134204.
11. Silva, V. H. C.; Aquilanti, V.; de Oliveira, H. C. B.; Mundim, K. C. Uniform description of non-Arrhenius temperature dependence of reaction rates, and a heuristic criterion for quantum tunneling vs classical non-extensive distribution. *Chem. Phys. Lett.* **2013,** *590*, 201-207.
12. Smith, R. S.; Kay, B. D. The existence of supercooled liquid water at 150 K. *Nature* **1999,** *398*, 788-791.
13. Speedy, R. J.; Angell, C. A. Isothermal Compressibility of Supercooled Water and Evidence for a Thermodynamic Singularity at -45 degrees. *J. Chem. Phys.* **1976,** *65*, 851-858.
14. Easteal, A. J.; Price, W. E.; Woolf, L. A. Diaphragm Cell for High-Temperature Diffusion Measurements - Tracer Diffusion-Coefficients for Water to 363-K. *J. Chem. Soc. Faraday Trans.* **1989,** *85*, 1091-1097.
15. H. Levitt, M. Spin dynamics: basics of nuclear magnetic resonance. **2001**.
16. Price, W. S. *NMR studies of translational motion*. Cambridge University Press: Cambridge ; New York, 2009.
17. Stejskal, E. O. Use of Spin Echoes in a Pulsed Magnetic-Field Gradient to Study Anisotropic Restricted Diffusion and Flow. *J. Chem. Phys.* **1965,** *43*, 3597-3603.
18. Hahn, E. L. Spin Echoes. *Phys. Rev.* **1950,** *80*, 580-594.
19. Tanner, J. E. Use of Stimulated Echo in NMR-Diffusion Studies. *J. Chem. Phys.* **1970,** *52*, 2523-2526.

20. Stejskal, E. O.; Tanner, J. E. Spin Diffusion Measurements: Spin Echoes in the Presence of a Time-Dependent Field Gradient. *J. Chem. Phys.* **1965,** *42*, 288-292.
21. Hou, J. B.; Li, J.; Madsen, L. A. Anisotropy and Transport in Poly(arylene ether sulfone) Hydrophilic-Hydrophobic Block Copolymers. *Macromolecules* **2010,** *43*, 347-353.
22. Hou, J. B.; Li, J.; Mountz, D.; Hull, M.; Madsen, L. A. Correlating morphology, proton conductivity, and water transport in polyelectrolyte-fluoropolymer blend membranes. *J. Membr. Sci.* **2013,** *448*, 292-299.
23. Li, J.; Wilmsmeyer, K. G.; Madsen, L. A. Hydrophilic channel alignment modes in perfluorosulfonate ionomers: Implications for proton transport. *Macromolecules* **2008,** *41*, 4555-4557.
24. Li, J.; Wilmsmeyer, K. G.; Madsen, L. A. Anisotropic diffusion and morphology in perfluorosulfonate ionomers investigated by NMR. *Macromolecules* **2009,** *42*, 255-262.
25. Chang, K.; Korovich, A.; Xue, T. Y.; Morris, W. A.; Madsen, L. A.; Geise, G. M. Influence of Rubbery versus Glassy Backbone Dynamics on Multiscale Transport in Polymer Membranes. *Macromolecules* **2018,** *51*, 9222-9233.
26. Wang, Y.; Chen, Y.; Gao, J. W.; Yoon, H. G.; Jin, L. Y.; Forsyth, M.; Dingemans, T. J.; Madsen, L. A. Highly Conductive and Thermally Stable Ion Gels with Tunable Anisotropy and Modulus. *Adv. Mater.* **2016,** *28*, 2571-2578.
27. Wang, Y.; Gao, J.; Dingemans, T. J.; Madsen, L. A. Molecular alignment and ion transport in rigid rod polyelectrolyte solutions. *Macromolecules* **2014,** *47*, 2984-2992.
28. Wang, Y.; He, Y.; Yu, Z.; Gao, J.; Ten Brinck, S.; Slebodnick, C.; Fahs, G. B.; Zanelotti, C. J.; Hegde, M.; Moore, R. B.; Ensing, B.; Dingemans, T. J.; Qiao, R.; Madsen, L. A. Double helical conformation and extreme rigidity in a rodlike polyelectrolyte. *Nat. Commun.* **2019,** *10*, 801.
29. Kidd, B. E.; Li, X. L.; Piemonte, R. C.; Cooksey, T. J.; Singh, A.; Robertson, M. L.; Madsen, L. A. Tuning Biocompatible Block Copolymer Micelles by Varying Solvent Composition: Dynamics and Populations of Micelles and Unimers. *Macromolecules* **2017,** *50*, 4335-4343.
30. Li, X. L.; Cooksey, T. J.; Kidd, B. E.; Robertson, M. L.; Madsen, L. A. Mapping Coexistence Phase Diagrams of Block Copolymer Micelles and Free Unimer Chains. *Macromolecules* **2018,** *51*, 8127-8135.
31. Jones, J. E. On the determination of molecular fields - II From the equation of state of a gas. *Proc. R. Soc. A* **1924,** *106*, 463-477.
32. Darden, T.; York, D.; Pedersen, L. Particle Mesh Ewald - an N.Log(N) Method for Ewald Sums in Large Systems. *J. Chem. Phys.* **1993,** *98*, 10089-10092.
33. Berendsen, H. J. C.; Grigera, J. R.; Straatsma, T. P. The Missing Term in Effective Pair Potentials. *J. Phys. Chem.* **1987,** *91*, 6269-6271.
34. Abascal, J. L. F.; Vega, C. A general purpose model for the condensed phases of water: TIP4P/2005. *J. Chem. Phys.* **2005,** *123*, 234505.
35. Rozmanov, D.; Kusalik, P. G. Transport coefficients of the TIP4P-2005 water model. *J. Chem. Phys.* **2012,** *136*, 044507.
36. Jorgensen, W. L.; Maxwell, D. S.; TiradoRives, J. Development and testing of the OPLS all-atom force field on conformational energetics and properties of organic liquids. *J. Am. Chem. Soc.* **1996,** *118*, 11225-11236.
37. Schroder, C. Comparing reduced partial charge models with polarizable simulations of ionic liquids. *Phys. Chem. Chem. Phys.* **2012,** *14*, 3089-3102.
38. Rick, S. W.; Stuart, S. J.; Berne, B. J. Dynamical Fluctuating Charge Force-Fields - Application to Liquid Water. *J. Chem. Phys.* **1994,** *101*, 6141-6156.
39. Lamoureux, G.; Harder, E.; Vorobyov, I. V.; Roux, B.; MacKerell, A. D. A polarizable model of water for molecular dynamics simulations of biomolecules. *Chem. Phys. Lett.* **2006,** *418*, 245-249.
40. Yao, Y.; Kanai, Y.; Berkowitz, M. L. Role of Charge Transfer in Water Diffusivity in Aqueous Ionic Solutions. *J. Phys. Chem. Lett.* **2014,** *5*, 2711-2716.
41. Drude, P. On the electron theory of metals. *Ann Phys-Berlin* **1900,** *1*, 566-613.

42. Zhao, Z.; Rogers, D. M.; Beck, T. L. Polarization and charge transfer in the hydration of chloride ions. *J. Chem. Phys.* **2010,** *132*, 014502.
43. Dal Peraro, M.; Raugei, S.; Carloni, P.; Klein, M. L. Solute-solvent charge transfer in aqueous solution. *Chemphyschem* **2005,** *6*, 1715-1718.
44. Schroder, C.; Lyons, A.; Rick, S. W. Polarizable MD simulations of ionic liquids: How does additional charge transfer change the dynamics? *Phys. Chem. Chem. Phys.* **2020,** *22*, 467-477.
45. Green, M. S. Markoff Random Processes and the Statistical Mechanics of Time-Dependent Phenomena .2. Irreversible Processes in Fluids. *J. Chem. Phys.* **1954,** *22*, 398-413.
46. Kubo, R. Statistical-Mechanical Theory of Irreversible Processes .1. General Theory and Simple Applications to Magnetic and Conduction Problems. *J. Phys. Soc.* **1957,** *12*, 570-586.
47. Kumar, P.; Kulkarni, A. D.; Yashonath, S. Influence of a Counterion on the Ion Atmosphere of an Anion: A Molecular Dynamics Study of LiX and CsX (X = F-, Cl-, I-) in Methanol. *J. Phys. Chem. B* **2015,** *119*, 10921-10933.

Chapter 3 Relating Geometric Nanoconfinement and Local Molecular Environment to Diffusion in Ionic Polymer Membranes

This chapter is reprinted from the following publication with permission from the following reference: Zhang, R.; Chen, Y.; Troya, D.; Madsen, L. A., Relating Geometric Nanoconfinement and Local Molecular Environment to Diffusion in Ionic Polymer Membranes. *Macromolecules* **2020**, *53*, 3296. Copyright (2019) American Chemical Society. Section 3.4.2 also includes further studies.

3.1 Introduction

In this work, we aim to contribute to the fundamental understands of ionomer membranes by revealing the relationship between ionomer nanostructure and the dynamics of water moving through it via the interpretation of the E_a of diffusion.[1-3] We would like to focus on the effect of nanoconfinement without the interference of water-surface interactions. Thus, we employ NMR diffusometry and molecular dynamics (MD) simulations to investigate diffusion coefficients and activation energies of diffusion (E_a) for both a lithium-form PFSA membrane and aqueous solutions of lithium triflate. The lithium triflate solutions have a similar chemical composition as the ionic domain of lithium form Nafion. Thus, the water-ion interactions are similar between the two systems. By comparing the E_a between confined water in the membrane and bulk water in the solutions, we eliminate the contribution from water-surface interactions, and the difference between the two systems would likely a result of the confined environment of water molecules. NMR shows that, at high water/ion molar ratio (λ), E_a for water diffusion is slightly lower in the membrane than in the solution. Conversely, membrane transport exhibits much higher E_a at low hydration as compared to solutions. MD simulations of a model system consisting of carbon

nanotubes with varying diameters reveal that E_a of diffusion clearly relates to both the geometric nanoconfinement of the hydrophilic pathways in the membrane as well as the local molecular environment. These results demonstrate that E_a of diffusion can serve as a revelatory tool for the study of molecular transport processes and the coupling of morphology with transport at the nanoscale. These understandings thus provide new insights and new experimental and computational models for understanding transport in a wide range of polymer membranes, such as those used in molecular separations applications.

3.2 Experimental and Computational Methods

3.2.1 Sample Preparation

Lithium triflate (LiOTf) was purchased from Strem Chemicals (USA) with 99% purity and used as received to make aqueous solutions. Solution concentrations were determined by mass ratios. Solutions with λ values (molar ratio of water molecules to lithium ions) of 3.0, 4.0, 5.0, 6.1, 9.0, 12, 17, and 20 were prepared. The solutions were flame-sealed into NMR tubes to maintain concentration. Ammonium-form Nafion 117 (PFSA) obtained from GasHub (Singapore) was pretreated using the following procedures. The membrane was washed in 3% H_2O_2 at 80°C for 1 hour, followed by another hour in lightly boiling HPLC H_2O. The yellowish membrane turned colorless during this process. Then, the membrane was treated with 0.5 M H_2SO_4 at 80°C for 1 hour, followed by three rinses in lightly boiling HPLC H_2O. To fully transform the ammonium-form membrane into the lithium-form membrane, the membrane was placed in 1 M LiOH aqueous solution at 80°C for 2 hours, followed by rinsing in lightly boiling HPLC H_2O for another 2 hours. This process was repeated twice to ensure the exchange of ammonium ions with lithium ions. The membrane was cut into small slices (2.5 mm x 10 mm), and 6-8 layers were stacked together to

enable rapid NMR measurements with a high signal-to-noise ratio (SNR). The membrane stack was placed in HPLC water for at least 48 hours to achieve full hydration. To attain variable hydration (λ), the fully hydrated membrane was dried in air for varying times, followed by mass determination. For NMR measurements, the membrane stack was tightly wrapped in plastic film and Teflon tape before placing it into a plastic cell manufactured in-house from Delrin.[4] The Delrin cell was machined to fit the size of the stacked PFSA sample so that the dead volume was minimal. The Delrin cell was sealed by silicone grease after loading the membrane, which was subsequently equilibrated in the sealed cell for 2 – 6 hours before measurements. The membrane was weighed again after measurements. At the end of all measurements, a dehydrated membrane was obtained by heating the membrane at 105 °C under vacuum for two days. The mass of membrane after measurements ($m_{hydrated\ membrane}$) and the mass of dehydrated membrane ($m_{dehydrated\ membrane}$) were used in the determination of λ. The water/ion molar ratio, denoted by λ, was determined by the following equation:

$$\lambda = \frac{m_{hydrated\ membrane} - m_{dehydrated\ membrane}}{m_{dehydrated\ membrane}} \times \frac{EW_{Nafion}}{M_{w,H_2O}} \tag{3.1}$$

where EW_{Nafion} is the equivalent weight of PFSA (Nafion 117 - 1100 grams dry polymer/mole sulfonate groups), and M_{w,H_2O} is the molecular weight of water. λ values ranging from 3.0 to 20 were prepared for the membrane measurements.

3.2.2 NMR Experiments

NMR measurements for both aqueous lithium triflate solutions and lithium-form PFSA were performed on a 400 MHz Bruker Avance III (9.4 T) spectrometer, and the Diff60 diffusion probe (Bruker Biospin, Billerica, MA) using a maximum gradient strength of 2400 G/cm. *D* of water was measured with a 5 mm ^{1}H coil and the pulsed-gradient stimulated echo (PGSTE) sequence. The PGSTE pulse sequence measures NMR signal intensity as a function of magnetic

field gradient parameters. In these experiments, the normalized signal intensity I/I_0 as a function of varying field gradient strength g, was fitted with the Stejskal-Tanner equation[5-6]

$$I/I_0 = e^{-\gamma^2 D g^2 \delta^2 (\Delta - \frac{\delta}{3})} \tag{3.2}$$

where γ is the gyromagnetic ratio of the probe nucleus, D is the self-diffusion coefficient (diffusion will be used interchangeably with self-diffusion throughout this article), δ is the duration of the gradient pulse, and Δ is the time between gradient pulses, also called the diffusion time. For lithium triflate solutions, gradient pulse durations δ of 1.5 – 2 ms, diffusion times Δ of 20 – 40 ms, PGSTE experiment repetition times of 1 – 4 s, and maximum gradient strengths g of 40 – 100 G/cm were applied to achieve over 80% attenuation in signal intensity, and with 8 – 32 scans per gradient step to obtain sufficient SNR. For diffusion measurements of lithium form PFSA, δ = 1.5 ms, Δ = 20 ms, repetition times of 0.3 – 0.5 s, and maximum g of 200 – 1800 G/cm were used. Temperature calibration was done with neat ethylene glycol. Pure ethylene glycol exhibits two peaks in proton NMR, and the chemical shift difference ($\Delta\delta$) between the two peaks is related to the absolute temperature by[7]

$$T = -99.00 \times \Delta\delta + 463.00 \tag{3.3}$$

E_a of diffusion is determined by measuring D as a function of temperature. Five temperatures were used for each membrane measurement. The temperature range for the measurements of lithium-form PFSA was 300 K to 310 K. The temperature range was chosen to minimize any effect of the dependence of E_a on temperature. Measurements for lithium triflate solutions were performed over a slightly expanded temperature range (300 – 330 K, five temperatures within 300 – 310 K, and another five temperatures between 310 K and 330 K) to facilitate comparison with both experimental and computational results.

3.2.3 Simulation Systems

Simulation systems involved in this chapter are shown in **Figure 3.1**. The model designed to probe nanoconfinement consists of a 20 nm single-wall carbon nanotube (CNT) (**Figure 3.1a**). The CNT is hydrated by 4 nm cubic water reservoirs containing all rigid three-site SPC/E[8] water molecules. A graphene sheet prevents the hydration of the CNT outer wall. The diameter of the CNT was varied from 1.2 to 2.5 nm to explore the confinement dimension. Aqueous lithium triflate solutions (**Figure 3.1b**) were modeled with the TIP4P/2005 rigid four-site water model.[9] The level of hydration was adjusted by fixing the number of ions (800 LiOTf ion pairs) and varying the number of water molecules to obtain λ values of 3, 4, 5, 6, 9, 12, and 17. The diffusion coefficients calculated with this model were directly compared to experimental NMR measurements to validate the force field. The CNT model only probes the confinement effect. However, there are other differences between the nanoscale ionic domains and the lithium triflate solutions. The effect of sidechain dynamics and nano-scale phase separation on water diffusion through PFSA membranes was investigated with an aqueous solution of PFSA sidechains and lithium counterions (**Figure 3.1c**). The number of TIP4P water molecules was varied while maintaining a fixed number of ions to obtain λ values of 3, 4, 5, 6, 9, 12, and 15. The effect of sidechain dynamics was probed by either fixing the anchor sidechain atoms to random points in the simulation box or by allowing full freedom of motion. To study the influence of nanoscale phase separation, solutions were created in which the sidechains were aggregated into domains or uniformly dispersed in water.

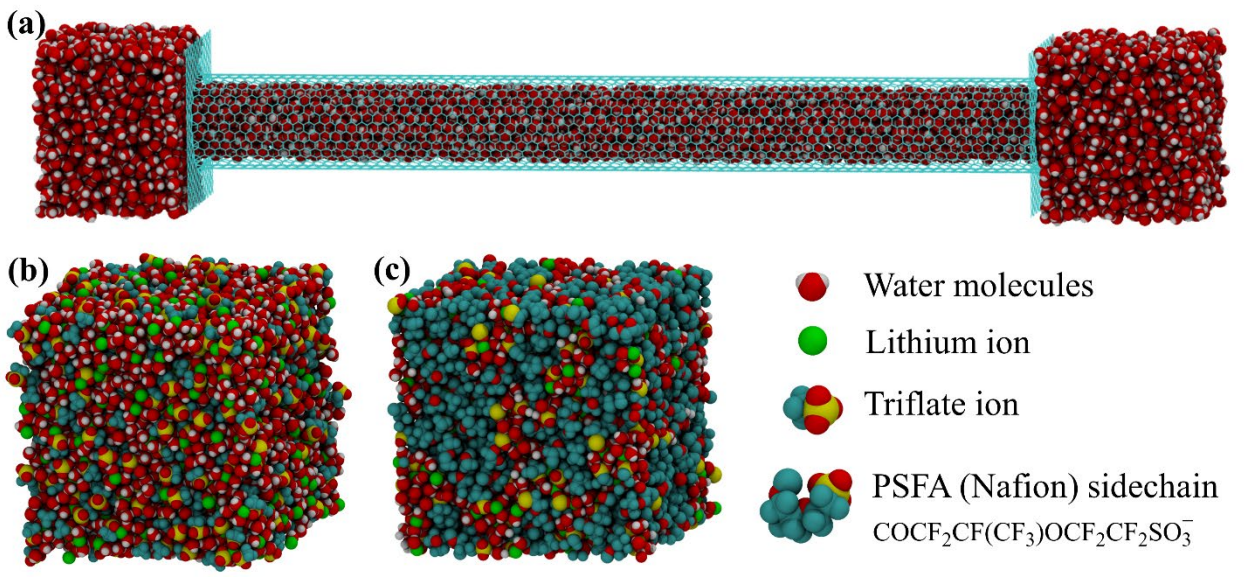

Figure 3.1 Simulation models involved in this work. The model shown in (a) consists of a hydrated carbon nanotube with diameters varying from 1.2 – 2.5 nm, designed to probe the effects of nanoconfinement. Model in (a) was used to explore nanoconfinement effects. Model in (b) represents an aqueous lithium triflate solution, which was used in force field optimization and to probe intermolecular effects. An aqueous solution of PFSA sidechains and Li counterions ($\lambda = 4$) is displayed in (c), which was designed to additionally investigate the effect of molecular environment.

3.2.4 Simulation Details

All the simulations are conducted with the GROMACS 5.0.5 package.[10] All models were equilibrated with NPT ensemble (1 bar) for 1 – 5 ns before production NVT calculations were run for 4 – 20 ns. Periodic boundary conditions are turned on at all three directions x, y, and z. The cut-off distance is set to 1.2 nm. PME is used for calculating long-range electrostatic interactions. The combination rule described in chapter 2.3.2 is used. A timestep of 1 fs is used for both NPT and NVT simulations. The velocity-rescale scheme is used for temperature coupling in NPT

simulations, while the Nose-Hoover algorithm is used for temperature coupling in NVT simulations. The type of pressure coupling depends on the simulation systems. In the CNT model, a compressibility of 4.5×10^{-5} bar^{-1}, which corresponds to the compressibility of bulk water at 300 K, is applied through the axial direction of the CNT, while the other directions are assumed non-compressible to avoid compression of the CNT and graphene plates. In the other models, isotropic pressure coupling is applied. Diffusion coefficients for all systems were computed from 300 K to 340 K at 10 K intervals. Fits of the diffusion coefficients to an Arrhenius equation (Equation 2.1.13) provided E_a of diffusion. Diffusion coefficients were extracted from the linear region of mean square displacement (MSD) plot vs. time[11]

$$D = \frac{\langle|\vec{r}(t_0 + t) - \vec{r}(t_0)|^2\rangle}{2nt} \tag{3.4}$$

where D is the diffusion coefficient, t is the diffusion time, n is the dimension factor (2 for one-dimensional diffusion, 4 for two-dimensional diffusion, and 6 for three-dimensional diffusion), and $|\vec{r}(t_0 + t) - \vec{r}(t_0)|$ is the displacement of a molecule from time t_0 to time $t_0 + t$, which can be extracted from the trajectory of the simulation system. MSD is calculated with a 1 ps time interval and at least 1 ns trajectory length. In the CNT model, one-dimensional diffusion coefficients are calculated only from the water molecules inside the CNT along the axial direction. In the other models, three-dimensional diffusion coefficients are calculated from all the molecules. A prolonged pre-diffusive region is observed in certain systems, and diffusion coefficients are extracted from the linear region of MSD vs. t plots.

3.2.5 Force Field Optimization

Sample calculations that used standard force-field parameters for lithium triflate solutions showed large deviations between calculated and measured diffusion coefficients. In order to improve the accuracy of the force-field parameters, NMR diffusometry measurements on the

lithium triflate solutions were used to benchmark and optimize the simulations. A number of force fields exist for water molecules, and some of them, such as TIP4P/2005 and OPC models,[9, 12] are well tailored for predicting diffusion properties at ambient conditions. Taking the OPLS-AA force field directly for the bonding interactions in triflate,[13] comparisons with NMR diffusometry measurements in lithium triflate aqueous solutions were used to optimize the non-bonding terms. Starting with literature values,[14-15] a set of partial charges for triflate were developed that nicely reproduced NMR experiments using a trial-and-error approach. **Figure 3.2** shows the comparison between simulated diffusion coefficients and experimentally measured diffusion coefficients. Detailed force-field parameters can be found in Appendix A.

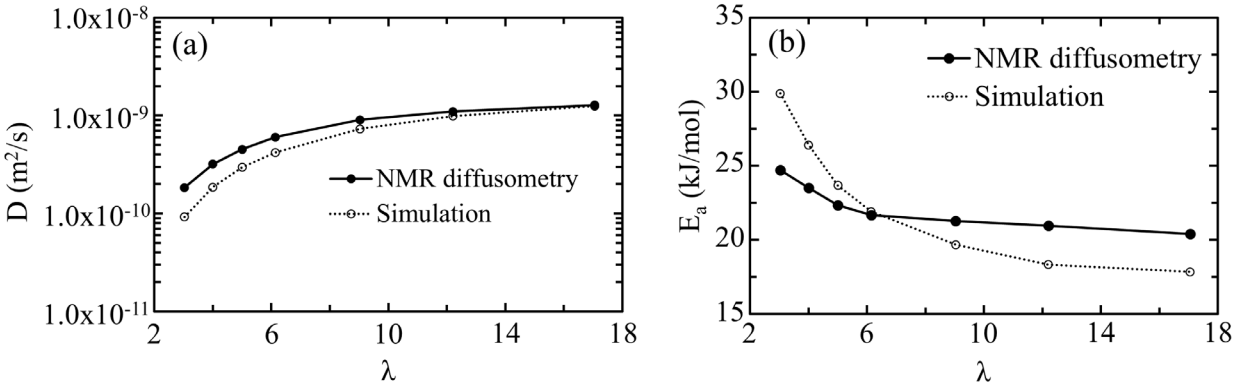

Figure 3.2 Parallel comparison between NMR and simulation results. D_{water} in LiOTf solutions at 300 K (a) and E_a of diffusion (b) as a function of hydration level. The range of λ is based on the hydration range of Nafion membrane and the solubility of LiOTf. We focused on fixed-charged force fields in this work. These results display optimum diffusion coefficients obtained from our optimization approach. The simulations predict slightly larger activation energies and lower diffusion coefficients at low λ, which is consistent with the overestimation of electrostatic interactions by fixed-charged MD simulations.[16] All attempts to better match the low-λ region of the activation energy curve resulted in a degradation of the agreement with experimental diffusion coefficients at intermediate and high hydration levels. Even though the experimental activation

energy as a function of hydration is not quantitatively matched by the calculations, the force field nicely reproduces the trend, which lends confidence to the qualitative insight we gained from the rest of the simulations.

3.3 Dynamical Properties of Water Under Carbon Nanotube (CNT) Confinement

3.3.1 Water Diffusion Measurements in Bulk and under Nanoconfinement

We measured the diffusion coefficient of water (D_{water}) in both lithium-form PFSA and in lithium triflate solutions over the same range of water-ion mole ratio (λ). D_{water} in the bulk salt solutions serves as a hydration-dependent chemical sibling of the PFSA hydrophilic channels, but without the geometric confinement imposed by the nm-scale channels in the membrane. The measured D_{water} values in the membrane are 3 – 20 times smaller than those in the aqueous solutions over the hydration-level range probed (**Figure 3.3a**). Based on the diffusion time of the NMR experiment, the diffusion length (root-mean-square displacement) of water molecules in the membrane is 1 – 10 μm. Thus, D_{water} in the membrane is sensitive to not only the local molecular environment but also the long-range membrane morphology.[2, 17] We note that we have previously shown that the PFSA membrane shows no variation of D_{water} as a function of the accessible diffusion times and lengths, [2] and that we verified this diffusion-time independence for the present membrane.

Two regions are evident in the E_a of water plots as a function of hydration for the two materials (**Figure 3.3b**). At high λ (7 – 20), E_a of water is very similar for the membrane and the solutions. This similarity indicates that water within the membrane is behaving locally as it does in bulk at high hydration. Note that, in the high-λ region, E_a measured in the membrane is slightly lower than that of salt solutions and approaches that of liquid water, which is consistent with

previous work on acid-form PFSA.[18] Another behavior appears at low λ (3 – 7), where E_a of diffusion in the membrane becomes substantially larger than in the bulk salt solutions.

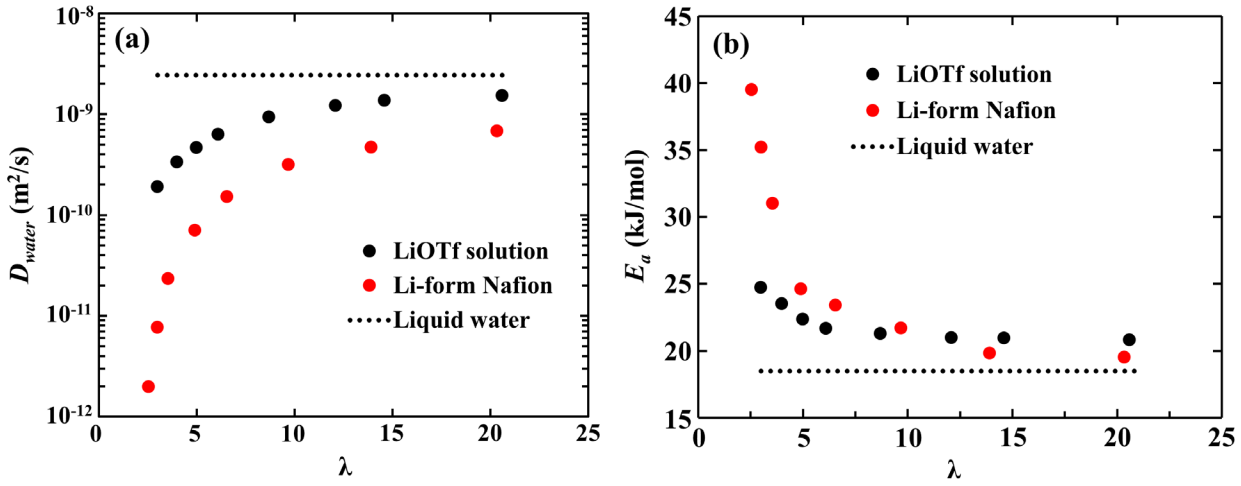

Figure 3.3 D_{water} at 30 °C (a) and E_a of water (b) in LiOTf solution and in Li^+-form PFSA as a function of water/ion ratio λ. D_{water} in the membrane is always lower than that in LiOTf solution. E_a in the membrane is substantially higher than that in the salt solution at low λ, and slightly lower at high λ. Errors in D_{water} are *ca.* $\pm$ 3%, and errors in E_a are *ca.* $\pm$ 5%.

Examining the environmental details in the LiOTf solutions and the hydrophilic domains of lithium form PFSA, we identify a few major differences. First, the transport of water and ions is nanoconfined in the membrane but free in aqueous solutions. Second, the polymer's ionic sidechains in the ionomer membrane are phase-separated on the nanometer scale, while the ionic groups are fully mixed in bulk solutions. The difference in the E_a variation with hydration behaviors likely results from these structural differences. As previously mentioned, nanoconfinement in a liquid will lead to unique properties as compared to the bulk state. To delve deeper into the influence of nanoconfinement on E_a of diffusion, and to try to separate this effect from the molecular environment that diffusing molecules encounter, we turn to molecular

simulations.

3.3.2 Simulation of Water Diffusion under Nanoconfinement

We simulate the effect of geometric restriction on the D_{water} and E_a by confining water molecules in the nanometer-scale environment of the carbon nanotube (CNT) shown in **Figure 3.1a**. We vary the CNT diameter in order to mimic the changing ionic domain size with water content in the PFSA.[19] **In Figure 3.4**, the D_{water} and E_a plots show two distinctive regions, similar to the trend seen in the membrane experiments. The first region appears when the tube diameter is above 1.3 nm. In this region, simulations of the CNT model and bulk water show nearly identical E_a of diffusion while the diffusion coefficient of the confined water is slightly lower than in bulk liquid. The minor difference in D_{water} and similar E_a indicates that the confined water can behave *locally* like bulk water even when the confinement dimension is a few nanometers. Nevertheless, the behavior of water in the CNT becomes distinctively different from that of liquid water as the tube diameter drops below 1.3 nm. In this region, D_{water} in the CNT sharply decreases while E_a of the confined water sharply increases with respect to liquid water.

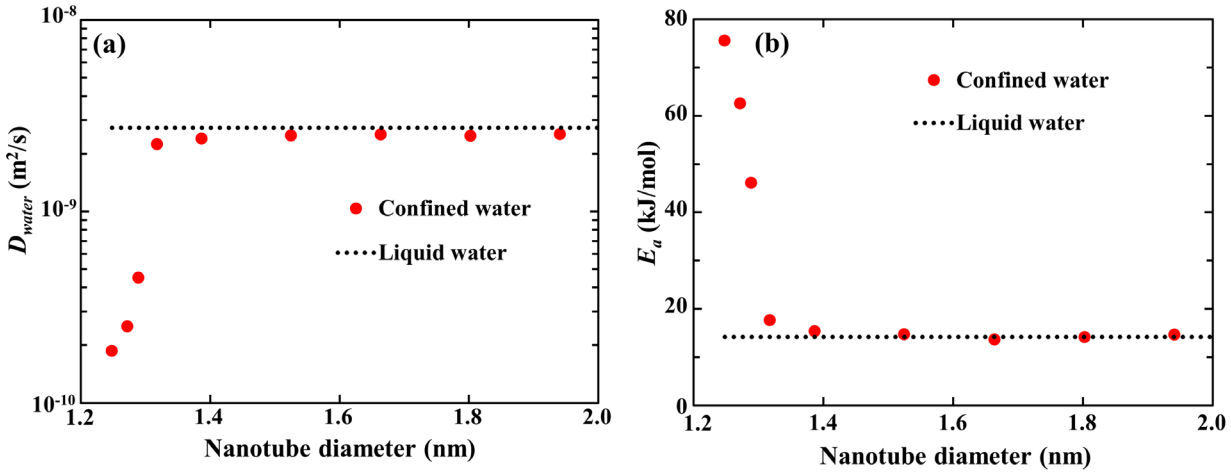

Figure 3.4 D_{water} (a) and E_a of water (b) from MD simulation of the CNT model in **Figure 3.1a**. Water diffusion in the CNT mimics that of free liquid when the CNT diameter is above 1.3 nm.

We observe the ordering of water molecules in the CNT when the tube diameter reaches 1.3 nm, below which both the D_{water} and E_a change drastically.

Further analysis of the simulations reveals that water molecules become ordered at low tube diameters (**Figure 3.5**). As previously mentioned, the formation of ordered water under nanoconfinement has been recognized both experimentally[20-22] and computationally,[21, 23-24] not only in the cylindrical geometry[24] imposed by the CNT but also in a planar geometry.[21] Thus, nanoconfinement may, in general, lead to the formation of slow-diffusing, solid-like water. Even though the ordering of water in the CNT is similar to that in a solid, the ordered water still exhibits relatively fast diffusion: D_{water} is less than a factor of 10 smaller than that of liquid water. We hypothesize that as the water molecules experience increasing confinement in the CNT or in the membrane, the potential energy governing water molecule motion becomes more *orientationally dependent*. That is, the potential energy minima vary as a function of the water molecule orientation. The potential energy minima localize the water molecules in energy minima flanked by steep energy surfaces, which have the effect of restricting their random diffusion. A similar potential-energy argument was presented by Horstmann et al.[25] for water under neutral confinement. We include an initial discussion of this effect below.

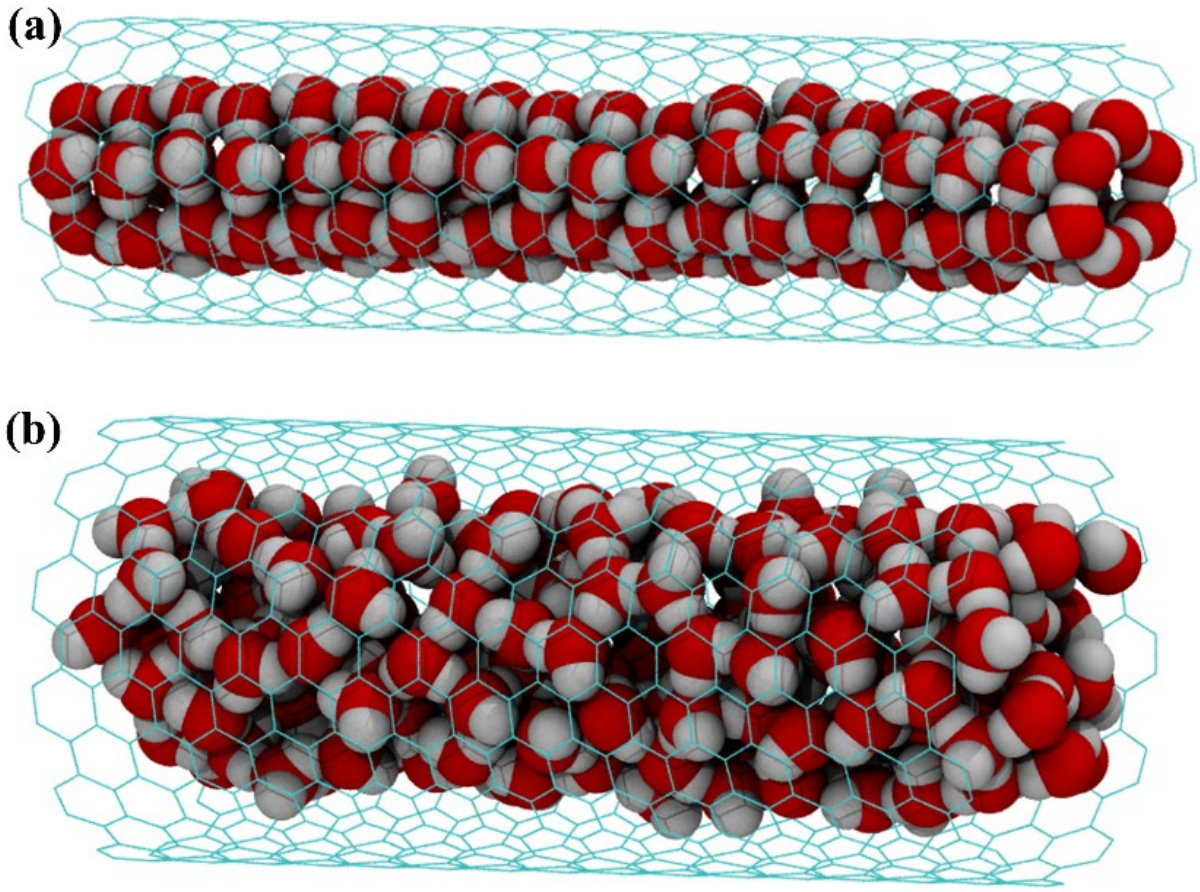

Figure 3.5 Ordered water (a) and disordered water (b) in a carbon nanotube. Panel (a) corresponds to a tube diameter of 1.248 nm, and panel (b) corresponds to a tube diameter of 1.664 nm. Water molecules form a hexagonal structure in (a) while distributing randomly in (b).

To validate this hypothesis regarding an anisotropic potential energy surface, we calculated the potential energy of water molecules in the CNT model (**Figure 3.6**) as a function of the z-axis coordinate of molecules. We compute potential energy based on short-range intermolecular interactions with a 2.4 nm cut-off distance while we ignore long-range electrostatic interactions. The water in a 1.248 nm-diameter CNT model, which shows the highest E_a in **Figure 3.4b**, shows the lowest potential energy. Thus, the ordered water is in a low-energy configuration. Although we cannot directly compare potential energies to E_a values, we note that the difference in potential

energy between ordered water and disordered liquid-like water is much smaller in magnitude than the difference in E_a values, reinforcing that E_a of diffusion probes the energetics of water dynamics through the surrounding molecular medium. We believe the E_a of diffusion relates to the energy required to disrupt the local interactions and move beyond the instantaneous hydration shell of a given diffusing molecule. For liquid water, the hydration shell of a water molecule is fleeting, signifying a relatively isotropic interaction potential and low E_a of diffusion. For a water molecule ordered inside a narrow CNT or a slightly hydrated ionomer membrane, the hydration shell is more permanent, suggesting a more stable configuration and a larger E_a of diffusion.

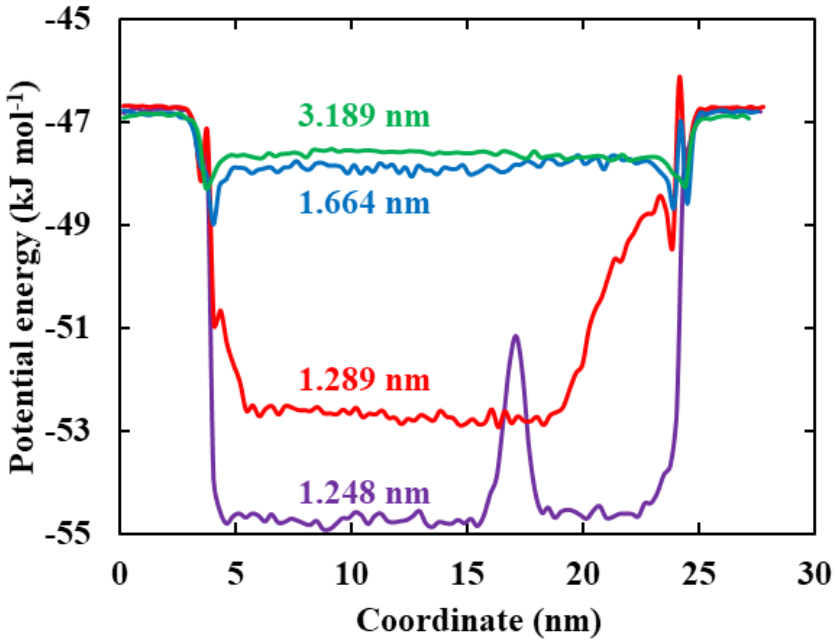

Figure 3.6 Potential energy of water molecules inside the CNT as a function of z-axis coordinate. The potential energy plots correspond to CNT models of different diameters as labeled on the plots. Potential energy is calculated by adding up intermolecular interactions with a cut-off distance of 2.4 nm. Long-range electrostatic interactions, which do not contribute significantly to the total potential energy in these systems, are ignored. The two "arms" on each side of every plot

correspond to the potential energy of the water reservoir. Ordered water is present in the CNTs with diameters of 1.248 nm and 1.289 nm. The potential energy of ordered water is smaller than that of disordered water. Note that the potential energy of the ordered water in CNT is not homogeneous. In the 1.248-nm case, a sharp increase in potential energy presents at ~17 nm on the z-axis, which corresponds to a defect in the ordered water inside the CNT. Defects also present in the 1.289-nm CNT. The existence of these imperfections, which destabilize the ice-like structure, is responsible for the non-zero diffusion coefficient of ordered water.

We now discuss these results in the context of diffusion in real ionic polymer membranes. The hydrophilic domains in hydrated PFSA are around 1 – 3 nm in size,[18-19] and this diameter varies with λ. We expect that confinement will affect the experimental E_a of diffusion in membranes at low λ. The sharper and steeper upturn in the E_a of diffusion for the CNT simulations compared to the trend seen in the membrane most likely is a consequence of the geometric homogeneity of the CNT model. This uniformity of diameter is undoubtedly not present in the more tortuous and irregular hydrophilic channels of PFSA membranes (**Figure 3.7a**). We propose that this geometric inhomogeneity of hydrophilic domains gives rise to a *distribution of water configurations on the lengthscale of nanometers*, including some that are analogous to the ordered configurations present in the CNT model, as well as liquid-like configurations (**Figure 3.8b**). Note the lengthscale probed by NMR diffusometry is ~1 μm. Thus, the measured diffusion coefficient becomes the average of all configurations, which makes the variation in the E_a of diffusion with λ (and nanochannel size) more gradual than in the CNT model, which probes lengthscales significantly smaller.

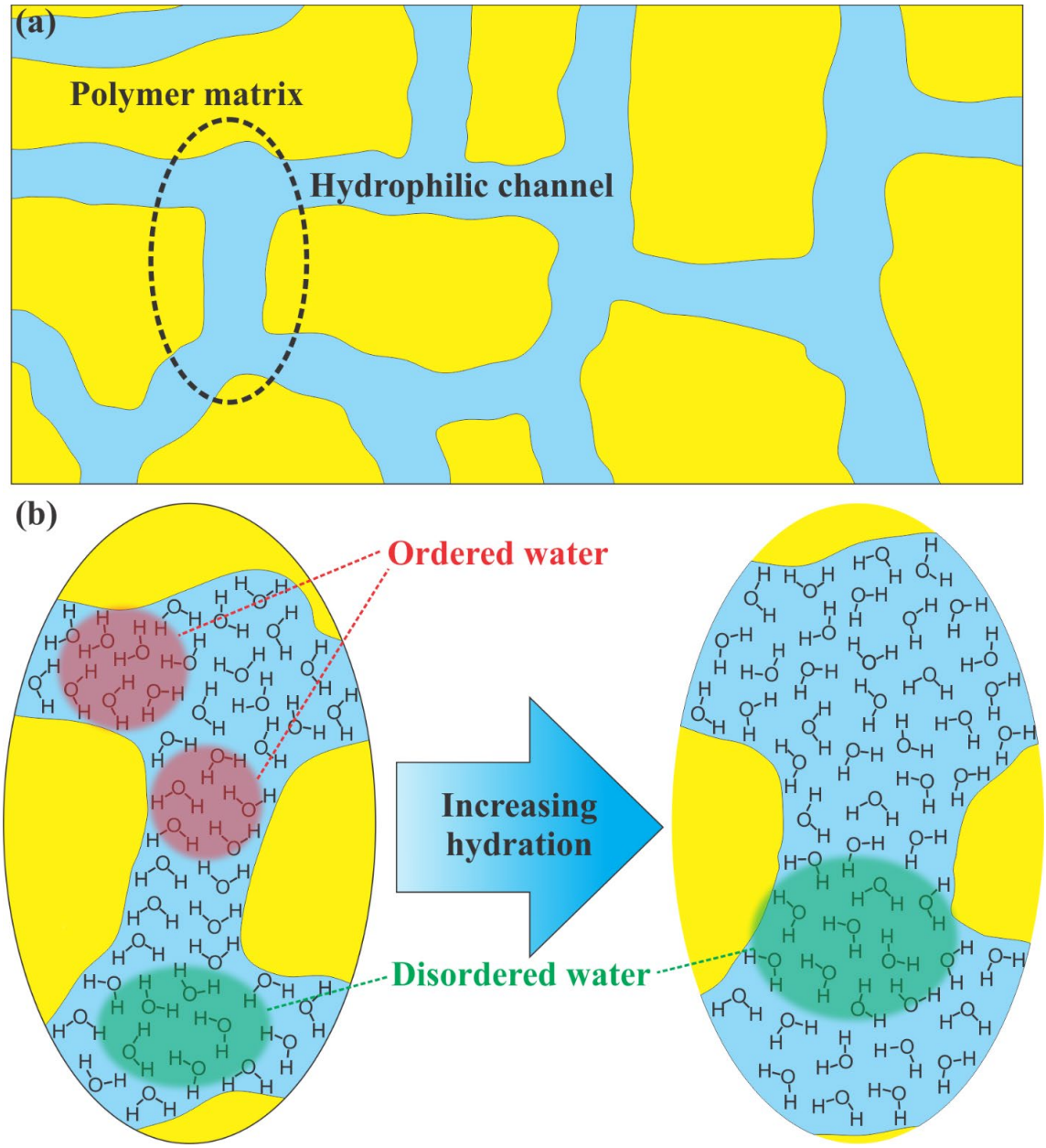

Figure 3.7 (a) Tortuous hydrophilic domains in PFSA membranes on the lengthscale of nanometers. Blue represents the hydrophilic domains, while yellow represents the polymer matrix. The size of hydrophilic domains varies from region to region. Part (b) highlights the oval region in panel (a), showing that ordered (solid-like) water and disordered (liquid-like) water can coexist in the hydrophilic domains. At high hydration, solid-like water becomes less abundant due to the expansion of all hydrophilic domains.

3.3.3 Effects of Molecular Environment on Diffusion

We now turn our attention to probing the effects of the local molecular environment on D_{water}. Two characteristic features of the hydrophilic domains in ionomer membranes are their nanoscale phase separation and the fact that the sidechains with pendant ions are anchored to the backbones. To understand the effect of both of these features on water transport, we employ the salt solution simulation model shown in **Figure 3.1c**. This model consists of a solution of lithium ions and sidechains of PFSA ((C)O-CF_2-$CF(CF_3)$-O-CF_2-CF_2-SO_3^-). To gain further insight using this model, we conduct a range of simulations in which we control both the level of phase separation and the physical anchoring of the sidechain.

Figure 3.8 depicts the various simulation schemes adopted with these models. We first create a simulation box containing randomly dispersed water molecules, lithium ions, and PFSA sidechains at varying λ values. We subsequently restrict the sidechain motion by immobilizing (at arbitrary locations in the box) the carbon atom that would anchor the sidechain to the polymer backbone in the membrane. In order to achieve a nanoscale phase-separated model, the randomly dispersed system (with free sidechains) is equilibrated (NPT ensemble) for sufficient time (10 – 20 ns) to ensure that the density and energy of the system reach equilibrium. The amphiphilic nature of the sidechains leads to phase-separated systems, which are more thermodynamically favorable than the randomly dispersed system.

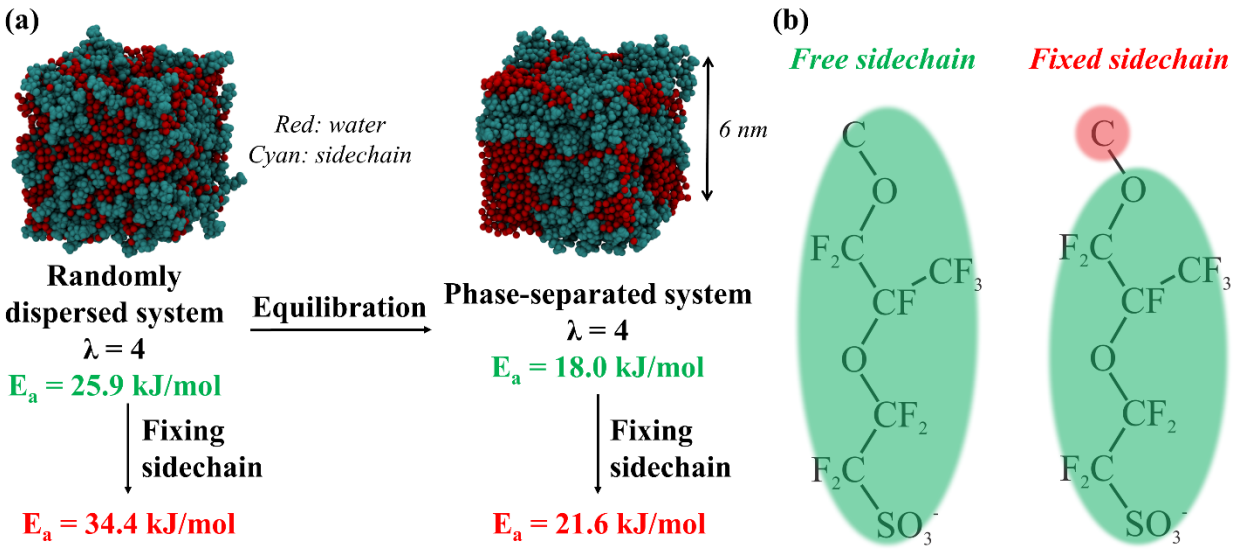

Figure 3.8 (a) Simulations of randomly dispersed and phase-separated models of ionomer sidechain solutions. Equilibration of the dispersed system (NPT ensemble) leads to a phase-separated system. The E_a values shown in panel (a) correspond to $\lambda = 4$. Higher λ values yield similar trends, but with smaller differences in E_a. (b) shows the difference between a fixed sidechain and a free sidechain. In the fixed-sidechain scenario, we immobilize the anchored carbon (shaded in red) in the sidechain while keeping all other atoms (shaded in green) free. Errors in computed E_a values are *ca.* ± 2 kJ/mol.

Figure 3.9 shows D_{water} and E_a of diffusion for the randomly dispersed and phase-separated models corresponding to **Figure 3.8a** with both free and fixed sidechains. Within the dispersed systems, limiting the dynamics of the sidechain by fixing the sidechain anchor atom increases E_a compared to the free sidechain scenario. While the effect diminishes as λ increases, we still observe substantial differences in E_a at $\lambda = 15$. In the phase-separated system, the E_a is consistently lower than that of the randomly dispersed system. The dispersed system has the same composition and nearly identical density as the phase-separated system, yet their E_a values are distinctly

different.

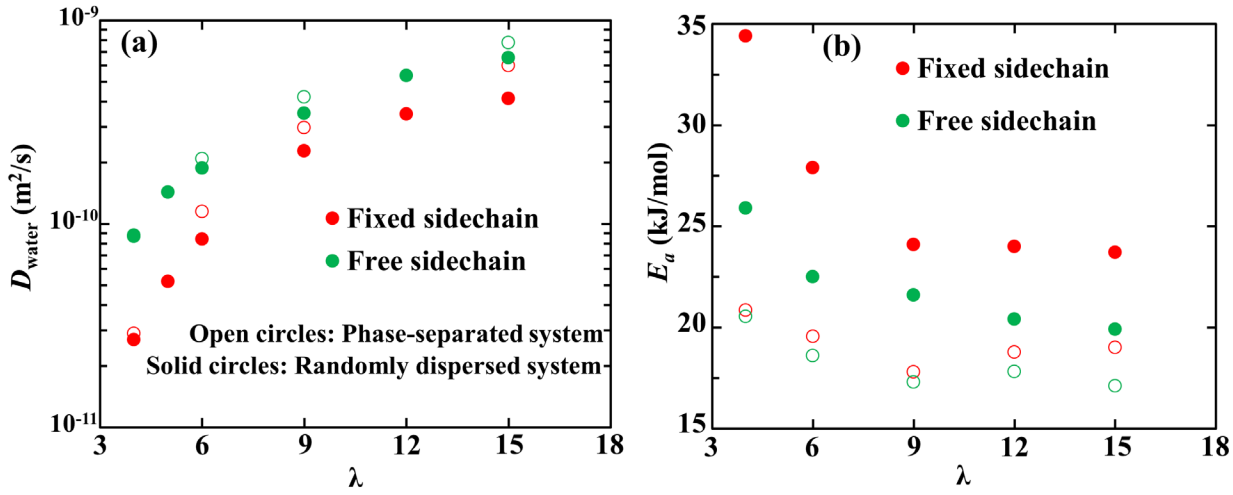

Figure 3.9 D_{water} (a) and E_a (b) from MD simulations of aqueous solutions of Li^+ and membrane sidechains (the model in **Figure 3.1c**). Solid circles represent results for the randomly dispersed model, while open circles are for the phase-separated model. Phase-separation leads to the elevation of D_{water} and the decrement of E_a. Note that the E_a difference between free and fixed sidechain scenarios, which is distinct in randomly dispersed systems, becomes much weaker in the phase-separated system.

To understand why E_a in the phase-separated system is significantly lower than in the randomly dispersed model, we analyzed radial distribution functions (RDFs) for both systems. The RDFs in **Figure 3.10** reveals that the local environment of water varies markedly for the phase-separated and randomly dispersed systems, with the phase-separated system showing an increased density of neighboring water molecules in the hydrophilic phase compared to water in the dispersed system. Comparing these two systems in terms of both RDFs (local molecular environment) and E_a (transport energetics), we see that a water-rich neighboring environment correlates with a lower E_a of water diffusion as compared to a local environment with an increased

average presence of membrane sidechains. Based on these results, we see that the E_a of water diffusion critically depends on the immediate neighbors (molecules or ions). The differences in RDFs between phase-separated and randomly dispersed systems diminish with λ, which is nicely correlated with a reduction in the differences between the E_a for phase-separated and randomly dispersed models at high λ.

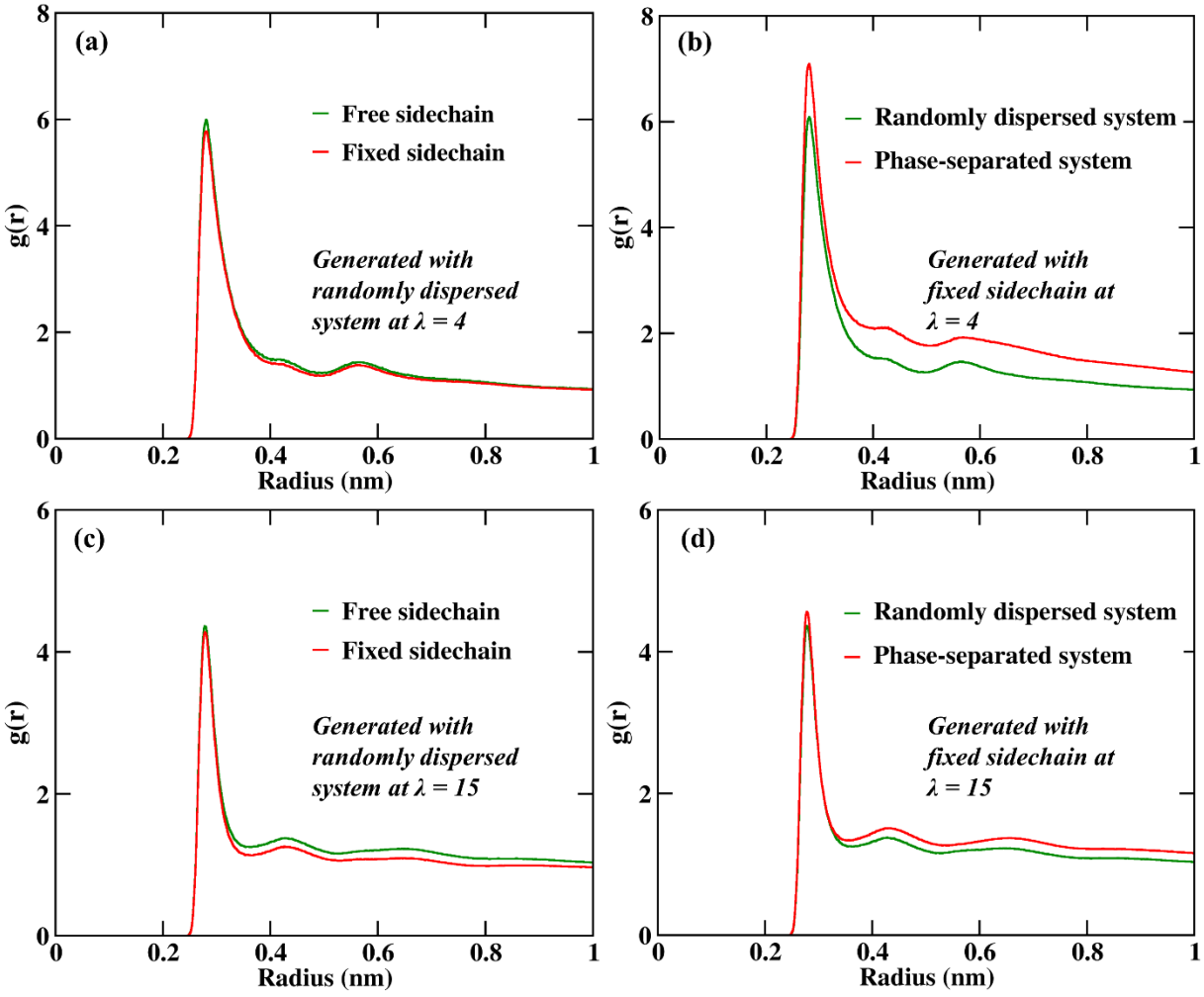

Figure 3.10 Radial distribution functions (RDFs) of the O_w-O_w distance (oxygen atoms between water molecules) in the model of **Figure 3.1c**. Panel (a) and (b) correspond to $\lambda = 4$ while panel (c) and (d) correspond to $\lambda = 15$. Panel (a) and (c) correspond to randomly dispersed systems,

while panels (b) and (d) correspond to fixed-sidechain systems. In the phase-separated system, a water molecule sees more water molecules (higher intensity in RDF) in its immediate neighborhood than in the randomly dispersed system. After 10 – 20 ns simulations of free sidechains in the dispersed system, the system shifts to a phase-separated system.

By comparing both D_{water} and E_a of diffusion, we notice that E_a provides very different information as compared to the diffusion coefficient. Taking $\lambda = 4$ as an example, one can see D_{water} is almost identical between randomly dispersed and phase-separated systems, either in the free- or fixed-sidechain cases (**Figure 3.9a**), but the E_a of diffusion is significantly different (**Figure 3.9b**). In the phase-separated systems, water molecules do not distribute as uniformly as in the randomly dispersed model. Instead, water-rich and water-poor environments coexist. We anticipate that water molecules in the water-rich region behave more like bulk liquid water, similar to the liquid-like water in the CNT, and water molecules in the water-poor environment diffuse slower and have higher E_a of diffusion. For this phase-separated system, the average of different environments results in similar D_{water} as in the dispersed system, but the overall E_a is much lower than that in the dispersed system. The reasoning here is that the E_a of diffusion in the phase-separated system is more weighted toward the water-rich regions. For clarity, we present the derivation of average E_a in a multi-component system here. Component 1 and component 2 (which correspond to the fast- and slow-diffusing water) are diffusing at different D and possess different E_a. Their Arrhenius equations are

$$D_1 = D_{0,1} e^{-\frac{E_{a,1}}{RT}} \tag{3.5}$$

$$D_2 = D_{0,2} e^{-\frac{E_{a,2}}{RT}} \tag{3.6}$$

Here D is the diffusion coefficient, D_0 is the pre-exponential factor, and E_a is the activation energy of diffusion. Quantities with subscript 1 correspond to component 1, and quantities with subscript 2 correspond to component 2. Assuming the components have n_1 and n_2 molecules, the average diffusion coefficient is

$$D_{average} = \frac{n_1 D_1 + n_2 D_2}{n_1 + n_2} = (\frac{n_1}{n_1 + n_2})D_1 + (\frac{n_2}{n_1 + n_2})D_2 = \frac{n_1 D_{0,1} e^{-\frac{E_{a,1}}{RT}} + n_2 D_{0,2} e^{-\frac{E_{a,2}}{RT}}}{n_1 + n_2} \quad (3.7)$$

Based on the Arrhenius equation, the activation energy can be expressed as

$$E_a = -\frac{\partial(lnD)}{\partial(\frac{1}{RT})} \quad (3.8)$$

Substituting equation (8) into equation (9), the activation energy for the average diffusion coefficient would be

$$\begin{aligned} E_{a,average} &= -\frac{\partial(lnD_{average})}{\partial\left(\frac{1}{RT}\right)} = \frac{n_1 D_1 E_{a,1} + n_2 D_2 E_{a,2}}{n_1 D_1 + n_2 D_2} \\ &= \left(\frac{n_1 D_1}{n_1 D_1 + n_2 D_2}\right) E_{a,1} + (\frac{n_2 D_2}{n_1 D_1 + n_2 D_2}) E_{a,2} \end{aligned} \quad (3.9)$$

Thus, while the average D is only weighted by the population of different components (in a heterogeneous system), the weights for the average E_a are the product of the population and the diffusion coefficient of each component. This means that the component with a faster diffusion coefficient has an increased influence on the average E_a. This explains the experimental trend observed at high λ in the ionomer membrane (**Figure 3.4**). Due to the phase-separated nature of PFSA membranes, a bulk-like water region will form in the center of the hydrophilic domains at high hydration. The bulk-like water region, which possesses a faster diffusion coefficient, also becomes more populated with increasing hydration, which tilts the overall E_a in the membrane to nearly that of bulk liquid water.

Another striking result in the phase-separated system is that the difference in E_a between fixed- and free-sidechain scenarios is notably smaller than in the randomly dispersed model. This phenomenon also likely results from the different molecular environments for water molecules in the two models. As mentioned above, phase segregation leads to water-rich and sidechain-rich regions. Consequently, the number of water molecules with sidechains in their immediate neighborhood is smaller in the phase-separated system than in the dispersed system, and therefore sidechain dynamics are less influential. This observation has important implications for water diffusion in PFSA membranes. With nanoscale phase separation, the fixed sidechains within PFSA membranes should not heavily influence E_a of diffusion, especially at high hydration.

3.3.4 Emerging Picture of Activation Energy of Diffusion in Ionomer Membranes

The results of this work advance the nanoscale picture of water diffusion in the hydrophilic domains of PFSA membranes. Both geometric confinement and molecular environment are related to E_a of diffusion. In order for nanoconfinement to significantly alter E_a of diffusion, the size of the confinement needs to be small enough (~1 nm based on simulations). When water molecules are in confining structures of this size, the potential energy surface governing water molecule motion is such that water molecules become trapped in potential energy minima and acquire partial ordering. The correlated motion of ordered water creates a larger energy penalty for a water molecule to move out of the shell of its neighbors, significantly increasing the E_a for diffusion. The nontrivial difference in E_a between lithium-form PFSA and lithium triflate solutions at low λ, as shown in **Figure 3.4**, likely results from the formation of partially ordered, slow-diffusing water under membrane nanoconfinement. This effect cannot exist in fully dispersed and well-mixed salt solutions. In addition, the fixed nature of the polymer sidechains may contribute to the elevation of the E_a of diffusion, although this effect is minimized under the phase-separated environment of

PFSA membranes. At high hydration, we observe a characteristic feature in the experiments: The E_a of water diffusion in PFSA becomes lower than that in salt solutions. We suggest that this feature results from nanoscale phase separation and the formation of bulk-like water regions. As discussed in the previous section, E_a disproportionately weights toward the fast diffusing species in a multi-component system. In the hydrophilic domains of PFSA membranes, there exist water molecules closely associated with the sidechains as well as bulk-like water molecules surrounded by only water molecules. While the average D_{water} depends on the molar ratio of the two components, the average E_a depends on the product of the molar ratio *and* the diffusion coefficient of the two components. The fast diffusing bulk-like water molecules, therefore, contribute more heavily to the overall diffusion process, making the resulting E_a closer to that of bulk liquid water. We cannot observe this effect in the aqueous LiOTf solutions due to the lack of phase heterogeneity. When the membrane becomes highly hydrated (**Figure 3.11**), bulk-like water dominates the overall water population, which makes the aforementioned effect even stronger. As a result, E_a in the membrane drops below that of aqueous salt solutions and approaches that of liquid water.

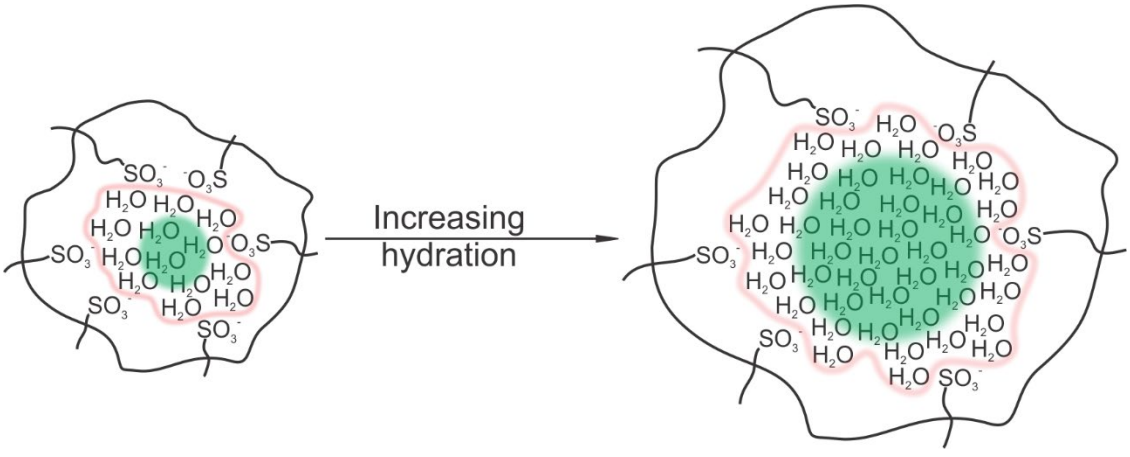

Figure 3.11 Conceptual figure of water channels in the PFSA membrane. At low hydration, the size of water regions reaches the critical value for nanoconfinement effects to take place, markedly increasing E_a for diffusion. With increasing hydration, the hydrophilic domain expands. Nanoscale

phase separation leads to the formation of bulk-like water in the hydrophilic domain, which gives rise to low E_a.

3.4 Structural Analysis of Confined Water in CNT Model

3.4.1 Tetrahedricity of Confined Water in CNT

In bulk water, a water molecule forms a tetrahedral structure with its four immediate neighbors. The order parameter, tetrahedricity, evaluates the local ordering of water molecules[26-27]

$$\mathcal{T} = 1 - \frac{3}{8}\sum_{j=1}^{3}\sum_{k=j+1}^{4}\left(\cos(\psi_{jk}) + \frac{1}{3}\right)^2 \tag{3.10}$$

where $\mathcal{T}$ is the tetrahedricity, j and k are the indexes of the two neighboring water molecules of the center water molecule, ψ_{jk} is the angle formed by the oxygen atoms of molecule j, molecule k, and the center molecule. When water molecules form regular tetrahedron with their four nearest neighbors, the angle ψ_{jk} equals to 109.5°, and $\cos(\psi_{jk})$ equals to $-\frac{1}{3}$. Thus, the tetrahedricity $\mathcal{T} = 1$ with regular tetrahedron structure (which is the structure of ice I_h). When the local ordering of water molecules is entirely random, the angle ψ_{jk} can take any value between 0° and 180°, the tetrahedricity equals zero

$$\mathcal{T} = 1 - \frac{3}{8}\int_0^{\pi}\left(\cos(\psi_{jk}) + \frac{1}{3}\right)^2 d\psi_{jk} = 0 \tag{3.11}$$

In liquid water, the hydrogen-bonding interactions lead to preferred orientations locally, and the tetrahedricity would always be non-zero for liquid water. **Figure 3.12a** shows the tetrahedricity of two bulk water models, SPC/E and TIP4P/2005, as a function of temperature. The TIP4P/2005 water model is more ordered than the SPC/E water model, which matches with the literature

observation.[37] In both water models, the tetrahedricity decreases as temperature increases. In **Figure 3.12b**, we generate plots for confined water in CNTs of different diameters at 300 K. In all plots, the two plateaus on both ends correspond to the tetrahedricity of the water reservoir, which is the same as that of bulk water at 300 K (~0.63). Note the drop of tetrahedricity in the 1.248-nm CNT correlates nicely with the potential energy drop we show in **Figure 3.6**. When enlarging tube diameter from 1.3 nm to 3.2 nm, the tetrahedricity increases toward that of bulk water (~0.63), which likely originates from the increasing amount of bulk-like water in the center of the nanotube. Below a tube diameter of 1.3 nm, the tetrahedricity increases, signifying the formation of ordered water. **Figure 3.12c** shows the correlation between tetrahedricity and activation energy. It seems that the tetrahedricity is strongly dependent on surface water. When the amount of surface water increases, the tetrahedricity of confined water decreases rapidly (except for when ordered water forms). The activation energy of the surface water depends weakly on confinement size; thus, we observe weak correlations between E_a and tetrahedricity.

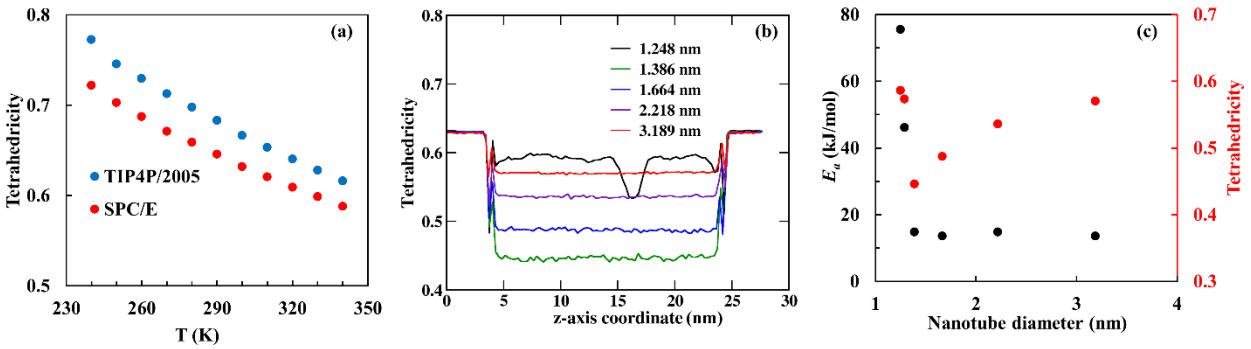

Figure 3.12 Panel (a) plots the tetrahedricity of the SPC/E water model and the TIP4P/2005 water model as a function of time. Panel (b) corresponds to the tetrahedricity of water molecules at 300 K in the CNT model as a function of the coordinate along the tube axis direction (z-axis direction). Panel (c) presents the E_a and average tetrahedricity (averaged over water molecules located between 6 nm and 22 nm along the z-axis) of confined water as a function of the tube diameter.

3.4.2 Hydrogen-Bond Analysis

Analysis of hydrogen bonds in terms of MD simulations is described in **Chapter 2.3.4**. A water molecule can both act as a hydrogen donor and a hydrogen acceptor. Thus, a water molecule at most can have four hydrogen bonds. **Figure 3.13** shows the hydrogen-bonding analysis on bulk SPC/E water and ice. Results on bulk water are sampled on a simulation box containing 4097 SPC/E water molecules, while results on ice are a sample on an icebox containing 867 SPC/E water molecules. In **Figure 3.13a**, we plot the average number of hydrogen bonds per water molecule (N_{HB}) and the average number of neighboring water molecules within 0.35 nm (N_{CO}) as a function of temperature for both liquid water and ice systems. Unsurprising, both N_{HB} and N_{CO} are nearly identical to 4 in the ice system, echoing the highly structured ice geometry. The coordination number, N_{CO}, of bulk water is weakly dependent on temperature, with a maximum at 300 K. The N_{HB} in bulk water continuously decreases with increasing temperature, pointing to a more random structure locally. The ratio between N_{HB} and N_{CO} signified the possibility (shown in **Figure 3.13b**) of a water molecule to form hydrogen bonds with its neighboring molecules. In addition to the number of hydrogen bonds, the hydrogen-donor-acceptor angle distribution and donor-acceptor distance distribution are typical analyses of the hydrogen-bonding network as well. **Figures 3.13e**,**f** compare the angle/distance distribution of hydrogen bonds between water and ice. Ice is showing a narrow distribution in both angle distribution and distance distribution, which agrees with the ordered ice structure. **Figures 3.13c**,**d** plot the angle/distance distribution of hydrogen bonds in bulk water as a function of temperature. The increasing temperature always broadens these distribution curves, again confirming a more disordered water structure with increasing temperature.

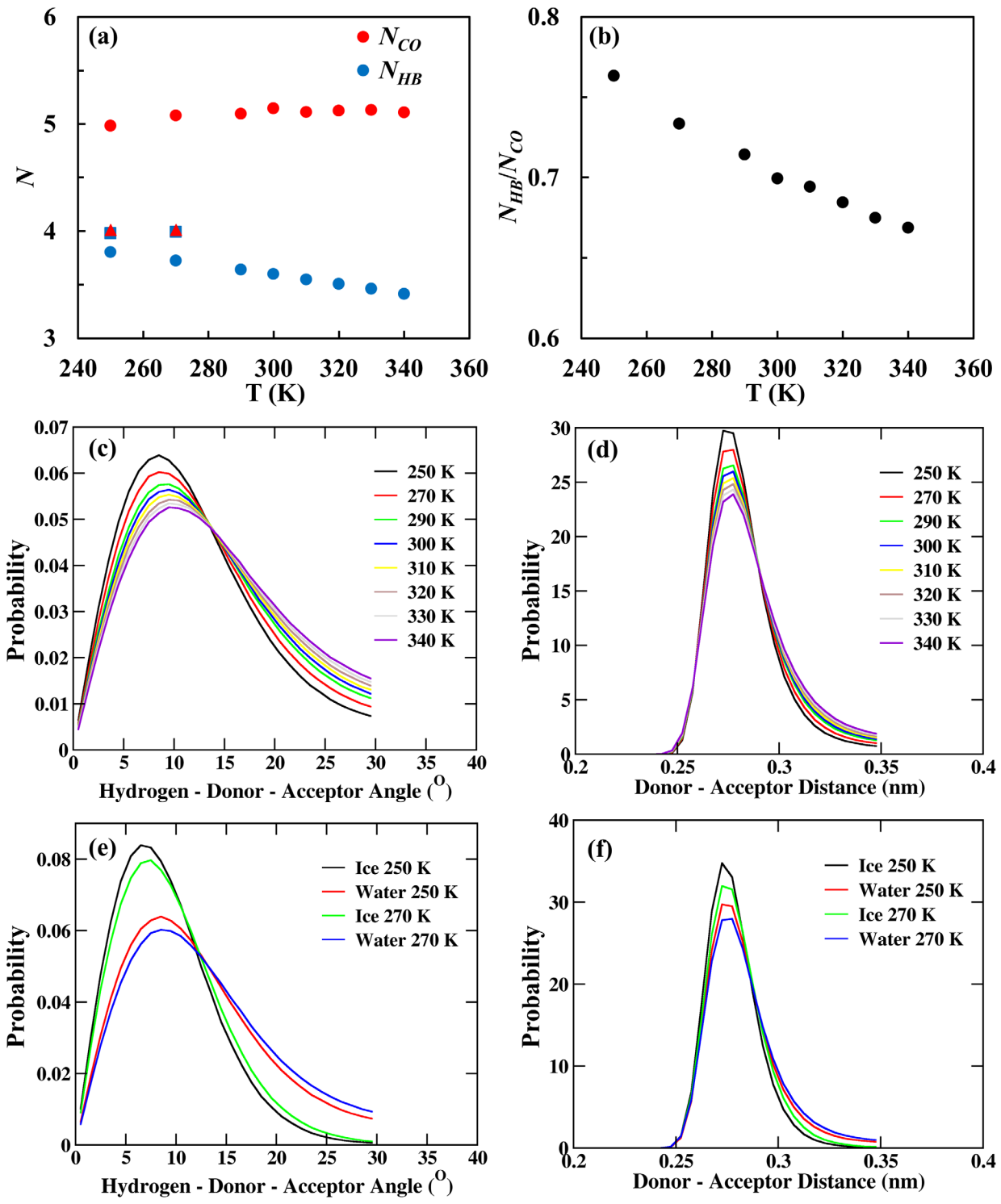

Figure 3.13 Hydrogen-bonding analysis of bulk SPC/E water/ice. Panel (a) plots the average number of hydrogen bonds per molecule (N_{HB}) and the coordination number (N_{CO}) as a function of temperature. Note that the triangles and squares represent the data points of ice while the circles

represent the data points of liquid water. Panel (b) shows the ratio between N_{HB} and N_{CO} with varying temperatures. Panel (c) and (d) show the angle distribution and distance distribution of the hydrogen-bonding network in bulk water. Panel (e) and (f) compare the angle/distance distribution of water to that of ice at the same temperatures.

The previous paragraph summarizes the hydrogen-bond analysis of bulk water. Here we explore the hydrogen-bond properties in confined water. **Figure 3.14a** shows the N_{HB} and N_{CO} of water confined in the CNT model. The coordination number decreases with decreasing tube diameters, which is probably due to the increasing amount of surface water with smaller confinement. With decreasing tube diameter, the number of hydrogen bonds decreases initially and starts to increase when the tube diameter is smaller than 1.3 nm. **Figure 3.14b** shows the ratio between N_{HB} and N_{CO}. At large tube diameters, N_{HB}/N_{CO} of confined water is similar to that of bulk water and is almost independent of the tube diameter. This means the decrease of N_{HB} with tube diameter is merely a result of a decreasing number of neighbors. When ordered water forms below a tube diameter of 1.3 nm, N_{HB}/N_{CO} of confined water increases by almost 20%, signaling the formation of a locally more ordered water structure. The N_{HB}/N_{CO} plot confirms two regimes of water structure in CNT. Beyond 1.3 nm, the structure of confined water molecules is dominated by bulk-like water. Below 1.3 nm, most water molecules exclusively become the surface water, and a more ordered structure forms locally. The angle/distance distribution of confined water is similar to bulk water (shown in **Figures 3.14c,d**). The distributions are slightly narrower when confined water becomes more ordered.

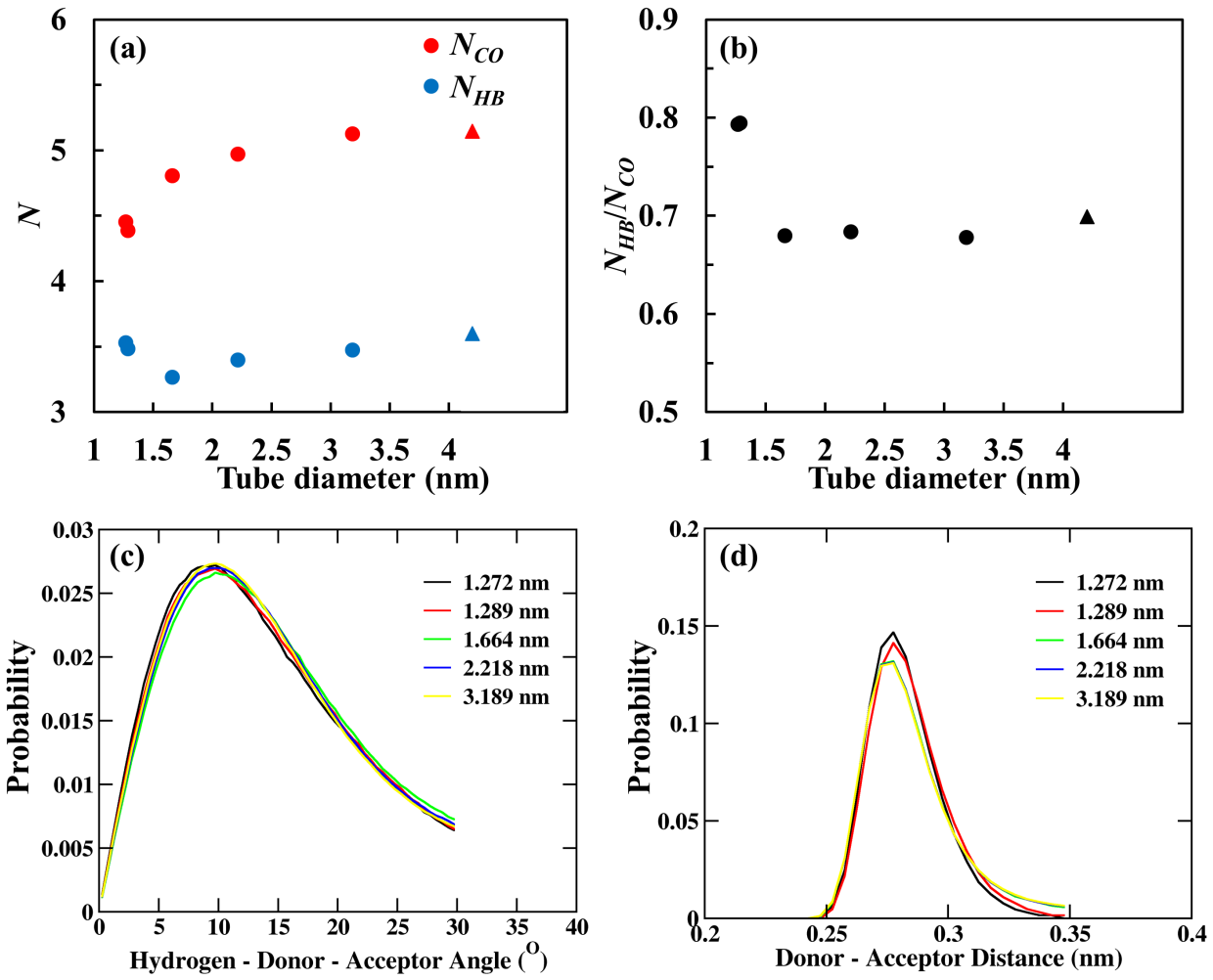

Figure 3.14 Panel (a) and (b) show the N_{HB}, N_{CO}, and N_{HB}/N_{CO} as a function of nanotube diameter. Note the triangles represent the data points of bulk water. Panel (c) and (d) show the angle/distance distribution of the hydrogen-bonding network of confined water at 300 K.

3.5 Conclusions

In summary, we have shed light on how the nanoscopic effects in a PFSA membrane are related to the E_a of water diffusion through its conducting hydrophilic domains. The main experimental results show two distinctive regimes of behavior for the E_a of diffusion. At high hydration, E_a is lower in the membrane than in salt solutions with identical water/ion ratio, but the trend strongly reverses at low hydration. This pattern results from a combination of geometric

nanoconfinement and local molecular environment, and each of these effects influences water diffusion behavior over different λ regimes. At low hydration, MD simulations show the size of the hydrophilic domains might reach the critical value beyond which water becomes ordered and solid-like. The ordered water has a much higher E_a than bulk water and is responsible for the steep elevation of E_a at low λ. In the heterogeneous PFSA membrane, there will be a distribution of sizes of hydrophilic domains. Thus, water molecules may be ordered in some regions of the membrane but remain disordered in other regions. The transition from ordered to disordered water likely happens smoothly over decreasing λ values, and the E_a consequently increases gradually. At high hydration, the hydrophilic domain sizes are dominantly above the critical size, so the formation of ordered water is limited. Meanwhile, the population of bulk-like water becomes dominant due to nanoscale phase separation of ionic sidechains. We believe that E_a weights more toward fast diffusing species, bulk-like water in this case, so the ensemble average E_a approaches that of liquid water at high λ.

We would like to emphasize here the rich implications and general applicability of the E_a of diffusion for understanding local diffusion processes. We have managed to show that E_a of diffusion serves as a probe for the local molecular environment, which includes both a confinement effect and intermolecular interactions between water and confining medium. The confinement effect on water dynamics becomes dominant only when the size of the confinement is close to the size of the molecules undergoing transport. The fact that water at the nanoscale can have an E_a close to that of liquid water illustrates the importance of water-rich domains in membranes. Creating regions for transport that are larger than 1 nm in size seems crucial to obtain fast water and ion transport with a low activation energy of diffusion. We can apply the same reasoning to diffusing ions in membranes, which are more challenging to measure and simulate due to their low

density, but we are exploring ongoing work. While these results and understandings are based on polymer membranes, we can obtain E_a of diffusion for any diffusive process. Thus, we can use E_a of diffusion to study transport not only in polymer membranes but also in other nanoporous materials such as metal-organic frameworks and porous silica.

3.6 References

1. Kidd, B. E.; Forbey, S. J.; Steuber, F. W.; Moore, R. B.; Madsen, L. A. Multiscale Lithium and Counterion Transport in an Electrospun Polymer-Gel Electrolyte. *Macromolecules* **2015,** *48*, 4481-4490.
2. Lingwood, M. D.; Zhang, Z.; Kidd, B. E.; McCreary, K. B.; Hou, J.; Madsen, L. A. Unraveling the local energetics of transport in a polymer ion conductor. *Chem. Commun.* **2013,** *49*, 4283-4285.
3. Zhang, R.; Chen, Y.; Troya, D.; Madsen, L. A. Relating Geometric Nanoconfinement and Local Molecular Environment to Diffusion in Ionic Polymer Membranes. *Macromolecules* **2020,** *53*, 3296-3305.
4. Hou, J. B.; Li, J.; Madsen, L. A. Anisotropy and Transport in Poly(arylene ether sulfone) Hydrophilic-Hydrophobic Block Copolymers. *Macromolecules* **2010,** *43*, 347-353.
5. Stejskal, E. O.; Tanner, J. E. Spin Diffusion Measurements: Spin Echoes in the Presence of a Time-Dependent Field Gradient. *J. Chem. Phys.* **1965,** *42*, 288-292.
6. Tanner, J. E. Use of Stimulated Echo in NMR-Diffusion Studies. *J. Chem. Phys.* **1970,** *52*, 2523-2526.
7. Ammann, C.; Meier, P.; Merbach, A. A simple multinuclear NMR thermometer. *J. Magn. Reson.* **1982,** *46*, 319-321.
8. Berendsen, H. J. C.; Grigera, J. R.; Straatsma, T. P. The Missing Term in Effective Pair Potentials. *J. Phys. Chem.* **1987,** *91*, 6269-6271.
9. Abascal, J. L. F.; Vega, C. A general purpose model for the condensed phases of water: TIP4P/2005. *J. Chem. Phys.* **2005,** *123*, 234505.
10. Abraham, M. J.; Murtola, T.; Schulz, R.; Pall, S.; Smith, J. C.; Hess, B.; Lindahl, E. GROMACS: High performance molecular simulations through multi-level parallelism from laptops to supercomputers. *SoftwareX* **2015,** *1-2*, 19-25.
11. Einstein, A. The theory of the Brownian Motion. *Ann. Phys.* **1906,** *19*, 371-381.
12. Izadi, S.; Anandakrishnan, R.; Onufriev, A. V. Building Water Models: A Different Approach. *J. Phys. Chem. Lett.* **2014,** *5*, 3863-3871.
13. Jorgensen, W. L.; Maxwell, D. S.; TiradoRives, J. Development and testing of the OPLS all-atom force field on conformational energetics and properties of organic liquids. *J. Am. Chem. Soc.* **1996,** *118*, 11225-11236.
14. Sunda, A. P.; Venkatnathan, A. Molecular Dynamics Simulations of Triflic Acid and Triflate Ion/Water Mixtures: A Proton Conducting Electrolytic Component in Fuel Cells. *J. Comput. Chem.* **2011,** *32*, 3319-3328.
15. Sunda, A. P.; Venkatnathan, A. Molecular dynamics simulations of side chain pendants of perfluorosulfonic acidpolymer electrolyte membranes. *J. Mater. Chem. A* **2013,** *1*, 557-569.
16. Schroder, C. Comparing reduced partial charge models with polarizable simulations of ionic liquids. *Phys. Chem. Chem. Phys.* **2012,** *14*, 3089-3102.
17. Thieu, L. M.; Zhu, L.; Korovich, A. G.; Hickner, M. A.; Madsen, L. A. Multiscale Tortuous Diffusion in Anion and Cation Exchange Membranes. *Macromolecules* **2019,** *52*, 24-35.

18. Mauritz, K. A.; Moore, R. B. State of understanding of Nafion. *Chem. Rev.* **2004,** *104*, 4535-4586.
19. Kreuer, K. D.; Portale, G. A Critical Revision of the Nano-Morphology of Proton Conducting Ionomers and Polyelectrolytes for Fuel Cell Applications. *Adv Funct Mater* **2013,** *23*, 5390-5397.
20. Agrawal, K. V.; Shimizu, S.; Drahushuk, L. W.; Kilcoyne, D.; Strano, M. S. Observation of extreme phase transition temperatures of water confined inside isolated carbon nanotubes. *Nat. Nanotechnol.* **2017,** *12*, 267-273.
21. Algara-Siller, G.; Lehtinen, O.; Wang, F. C.; Nair, R. R.; Kaiser, U.; Wu, H. A.; Geim, A. K.; Grigorieva, I. V. Square ice in graphene nanocapillaries. *Nature* **2015,** *519*, 443-445.
22. Singla, S.; Anim-Danso, E.; Islam, A. E.; Ngo, Y.; Kim, S. S.; Naik, R. R.; Dhinojwala, A. Insight on Structure of Water and Ice Next to Graphene Using Surface-Sensitive Spectroscopy. *Acs Nano* **2017,** *11*, 4899-4906.
23. Cicero, G.; Grossman, J. C.; Schwegler, E.; Gygi, F.; Galli, G. Water confined in nanotubes and between graphene sheets: A first principle study. *J. Am. Chem. Soc.* **2008,** *130*, 1871-1878.
24. Mashl, R. J.; Joseph, S.; Aluru, N. R.; Jakobsson, E. Anomalously immobilized water: A new water phase induced by confinement in nanotubes. *Nano Lett.* **2003,** *3*, 589-592.
25. Horstmann, R.; Sanjon, E. P.; Drossel, B.; Vogel, M. Effects of confinement on supercooled tetrahedral liquids. *J. Chem. Phys.* **2019,** *150*, 214704.
26. Errington, J. R.; Debenedetti, P. G. Relationship between structural order and the anomalies of liquid water. *Nature* **2001,** *409*, 318-321.
27. Layfield, J. P.; Troya, D. Molecular simulations of the structure and dynamics of water confined between alkanethiol self-assembled monolayer plates. *J. Phys. Chem. B* **2011,** *115*, 4662-4670.

Chapter 4 Prolonged Associations between Water Molecules under Hydrophobic Nanoconfinement

This chapter is under preparation for submission to Journal of Physical Chemistry B with authors Rui Zhang, Diego Troya, and Louis Madsen.

4.1 Introduction

Water dynamics under nano-size confinement differ significantly from bulk. Interest in the dynamics of confined water has stimulated studies in both hydrophilic and hydrophobic confinement. On the one hand, retarded water dynamics are usually observed under hydrophilic confinement.[1-4] On the other hand, confining water molecules to a hydrophobic environment gives mixed results on the dynamics of water molecules, depending on the geometry of the confinement medium.[5-10] To understand the observed slowdown of water dynamics under hydrophobic confinement, we investigate water in various confining structures with molecular dynamics simulations. We observe that water molecules under hydrophobic confinement behave as if they are under lower temperatures, which has only been shown with hydrophilic confinement before.[4] We quantify the effect of confinement and temperature on water dynamics by determining the residence time of water around itself under changing confinement size/temperatures, and we learn that both decreasing confinement size and lowering temperature prompt longer association among water molecules.[11] We notice that the residence time, which evaluates the timescale of associations between water molecules, is closely related to both diffusion coefficients and activation energy of diffusion. This observation opens up possibilities to predict the diffusion coefficient and activation energy of diffusion of a liquid system by just calculating its residence time. Additional studies consider the effect of the level of hydrophobicity of the confinement medium and the presence of

ions. Overall, this study reveals the physical origin of retarded water dynamics under hydrophobic confinement and the relationship between residence time and diffusion behavior.

4.2 Computational Methods

4.2.1 Simulation Systems and Force Fields

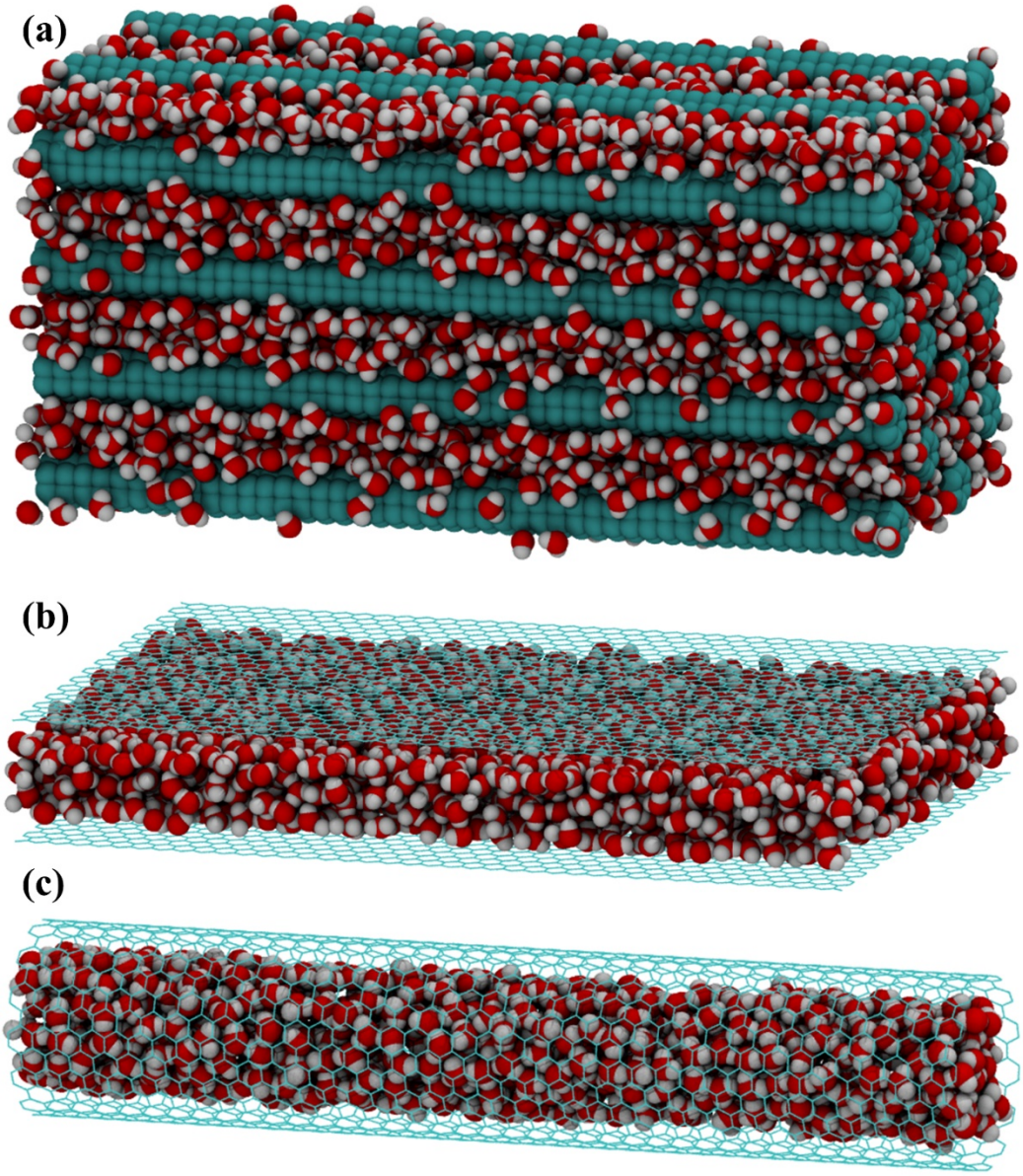

Figure 4.1 Schematic representations of simulation models involved in this work. Panel (a) represent the rigid-rod model. The rod-rod distance in the figure is 1.2 nm. Sixteen 16.8 nm-long

rigid rods are present in all the rigid-rod models. All rigid rods are equal in distance to each other and are in a hexagonal packing pattern. Two water reservoirs with a length of 3 nm along the axial direction of the rigid rods are present on each end of the carbon rods. Panel (b) represents the parallel-sheet model. The layer-to-layer distance shown in the figure is 1 nm. The graphene layers are 16 nm in length and 6 nm in width. Panel (c) is the CNT model adapted from our previous work.[10]

We performed all MD simulations using the GROMACS 5.0.5 package.[12-14] **Figure 4.1** exhibits the geometry of simulation models involved in this work. **Figure 4.1a** showcases the rigid rods model. In this model, we place rigid carbon rods in a hexagonal pattern. Each rod consists of stacked carbon-atom rings with 6 atoms in each ring. Following the literature,[15] the distance between carbon-atom layers is 0.21 nm while the distance between adjacent carbon atoms on each layer is 0.173 nm. The length of each rod is 16.8 nm with 40 layers of carbon rings. We vary the distance between carbon rods between 1.2 nm and 2.8 nm to give different sizes of confinement of the solvating water. Notice the rod-rod distance here is the distance from the center of one rod to the center of an adjacent rod. Two water reservoirs are present at each end of the rods. The total number of solvating water molecules ranges from 11000 to 42000 in this rigid-rod model. **Figure 4.1b** represents the parallel-sheet model. This model consists of two graphene sheets, which are 16 nm long and 6 nm wide. We vary the layer-to-layer distance from 0.7 nm to 1.8 nm to get different confinement sizes in this model. We immerse the parallel sheets in a larger water reservoir whose size is about 4 nm × 8 nm × 18 nm. The total number of water molecules in the parallel-sheet model is around 16000. **Figure 4.1c** represents the CNT model. The length of the nanotube is 20 nm, while the diameter of the nanotube ranges from 1.4 nm to 3.2 nm. We put two water reservoirs on both ends of the CNTs. The total number of molecules in the CNT model ranges

from 4000 to 8000.

We use SPC/E water[16] in these models for most of the production runs. Nonetheless, results with TIP4P/2005 water[17] are also presented for a few representative models. The simulations considered periodic boundary conditions in all three directions. The cut-off distance for Lennard-Jones interactions is 1.2 nm. We immobilize the confinement structure using position restrains and assigning a large mass (1×10^{20} amu) to the carbon atoms. We overwrite the Lennard-Jones interactions between carbon atoms in the confinement medium to zero. We apply Particle-mesh Ewald summations to calculate long-range electrostatic interactions. The force field parameters for carbon atoms and lithium triflate are adapted from our previous publication.[10] For calculation of diffusion coefficients, the timestep is 1 fs while the output frequency is one per 1000 steps. We equilibrate all the systems with at least 1 ns NPT (isobaric-isothermal) simulations followed by multiple 4 – 8 ns NVT (canonical) production runs.

4.2.2 Calculated Quantities

We calculate mean squared displacement (MSD) and diffusion coefficient (D)[18] from the NVT simulations (Equation 3.4). For all the confined simulation models, we calculate MSD of only water molecules moving within the confined region and ignore water molecules in the reservoirs. We calculate MSD up to 2 – 3 ns and extract diffusion coefficients from the linear region of MSD *vs.* t plots. We run simulations from 300 K to 340 K at 10-K intervals and extract activation energy of diffusion from the Arrhenius equation (Equation 2.1.13) using the calculated diffusion coefficients.

To determine the residence time of water, we utilize the residence time correlation function $S(t)$:[19]

$$S(t) = \langle h(t)h(0)\rangle/\langle h\rangle \tag{4.1}$$

where $h(t)$ is unity if a pair of water molecules are located within a certain cut-off distance of target molecules/atoms at time 0 and remain continuously in that region through time t; otherwise, $h(t)$ equals 0. We evaluate $\langle h(t)h(0)\rangle$ by taking 1000 different starting points throughout the simulations and average it by the number of starting points. $\langle h\rangle$ is the normalization factor whose absolute value does not change the values of residence times. In the calculation of residence time of water around water, we assign $\langle h\rangle$ a value so that $S(0)$ gives the average number of water molecules around a center molecule within the cut-off distance, which is around 4 for both bulk and confined water. $S(t)$ evaluates the timescale of water molecules continuously within the cut-off distance of the target molecule. We notice that $S(t)$ not only quantifies residence time of water molecules[11, 20-22] but also evaluates the timescale of ionic association.[23-24] In the present study, we set the cut-off distance of water association to 0.33 nm based on the radius of the first solvation shell of bulk water. Nevertheless, we discuss the effect of using alternative cut-off distances on the values of $S(t)$ in section 4.4.4. Additionally, we use $S(t)$ to evaluate the associations between water molecules and the hydrophobic rigid rods.

Our calculations reveal that the $S(t)$ of this work can be well fit to a double exponential decay model

$$S(t) = Ae^{-t/\tau_s} + Be^{-t/\tau_l} \quad (4)$$

where A and B are fitting parameters, and τ_s and τ_l stand for short and long residence time, respectively.[22] This model has been used in previous studies.[20, 22, 25] In the stepwise calculation of $S(t)$, the length of the time interval affects the decay time. The correlation function $S(t)$ will fail to capture certain association/dissociation events if the time interval is too long, but the calculation becomes computationally intensive if the time step is too short. After significant testing, we were able to balance computational cost and accuracy evaluating $S(t)$ along 20 – 80 ps trajectories every

10 fs.

4.3 Residence Time of Water and Its Connection to Water Diffusion Behavior

4.3.1 Diffusion Anisotropy and Retarded Water Dynamics in the Rigid-Rod Model

In the rigid-rod model, we calculated both the diffusion coefficient parallel to the axial direction of the rods ($D_{\parallel}$) and the diffusion coefficient perpendicular to the axial direction of the rods ($D_{\perp}$). **Figure 4.2** shows the temperature dependence of $D_{\parallel}$ and $D_{\perp}$ as well as the average diffusion coefficient $D_{average}$ for simulations with various rod-rod distances. Since $D_{\perp}$ is a two-dimensional coefficient, it contributes twice as much to the average diffusion coefficient, $D_{average}$. In all the cases, $D_{\parallel}$ is larger than $D_{\perp}$, which is expected considering that the rods are physically restricting diffusive motions perpendicular to them. This diffusion anisotropy grows more prominent with shorter rod-rod distances. Remarkably, the activation energies obtained from the temperature dependence of $D_{\parallel}$ and $D_{\perp}$ are the same, even if the diffusion coefficients are different, which agrees with our conclusion in prior work that the activation energy of diffusion arises from immediate molecular interactions and is not sensitive to long-range structure features.[10, 26-27]

Figures 4.2c,d present the $D_{average}$ and the E_a extracted from $D_{average}$ as a function of rod-rod distance. We observe retarded water dynamics at all rod-rod distances as $D_{average}$ is lower than the bulk water diffusion coefficient. The slowdown of water molecules becomes more significant as the confinement size decreases. The increase of E_a with decreasing rod-rod distances reveals that the retarded water dynamics in this model originates not only from physical restrictions (repulsion from the confining surface) but also increased energy barriers for diffusion. This observation again confirms that nanoconfinement affects the energetics of molecules, consistent with our previous work on the confinement effect.[10] A major difference between the phenomenon

here and what we observed previously in the carbon nanotube (CNT) model is the trend of E_a. We observe a gradual increase in water E_a with decreasing rod-rod distance here while seeing a much sharper increase of E_a with decreasing CNT diameter. We would also like to emphasize that the ordered water we saw in CNT does not appear to form in this rigid-rod model. We propose that the water molecules are also becoming more structured with smaller rod-rod distances here. However, the structure happens at an immediate molecular scale rather than at a long-range scale. To shed light on the structuring of water in the rod-rod model, we present an analysis of the hydrogen bonding in section 4.5. We focus for now on the residence time of confined water.

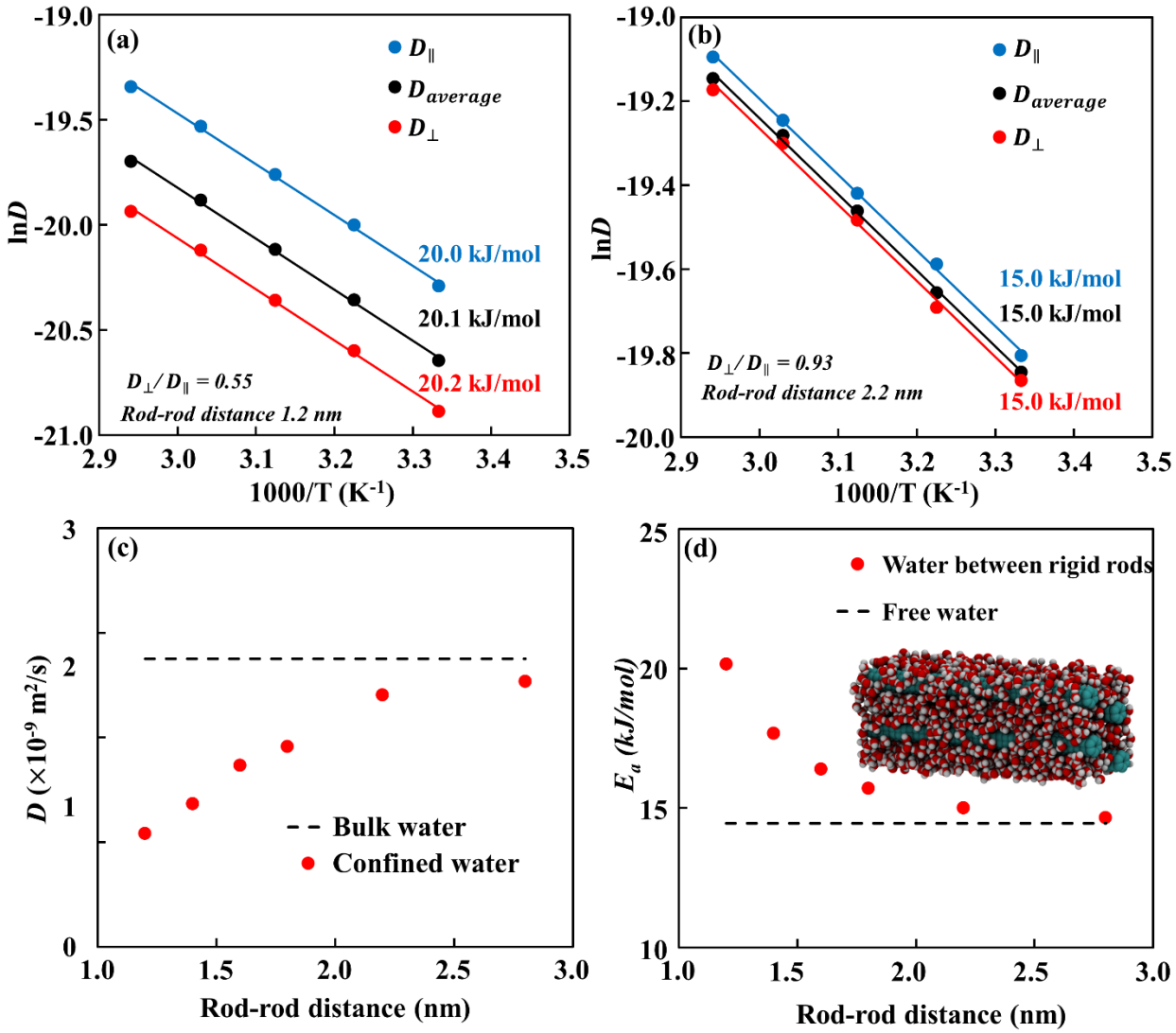

Figure 4.2 Anisotropic diffusion in the rigid-rod model and the change of E_a with rod-rod distance. Panel (a) and (b) correspond to variable-temperature diffusion under rod-rod distances of 1.2 nm and 2.2 nm, respectively. The temperature ranges from 300 K to 340 K with a 10 K interval. The difference between $D_{\parallel}$ and $D_{\perp}$ progressively lowers as the rod-rod distance increases. Importantly, the activation energies labeling the Arrhenius plots are not sensitive to the diffusion direction. Panel (c) and (d) respectively show the evolution of $D_{average}$ and E_a with rod-rod distance. With decreasing confinement size, the $D_{average}$ decreases while E_a increases, suggesting retarded water dynamics in heavily confined media.

4.3.2 Parallels between Confinement and Temperature in the Rigid-Rod Model

Figure 4.3a shows the temperature dependence of all diffusion coefficients in the rigid-rod model at varying rod-rod distances compared to the diffusion coefficients for bulk water. In **Figure 4.3b**, we artificially offset the temperatures of the rigid-rod model results to match the D of pure water. Remarkably, most of the data points fit very well after the shifting. Driven by the curiosity of underlying relationships, we plot the offset of reciprocal temperature (δ_{rt}) vs. rod-rod distance, porosity, and the surface-to-volume ratio of water in **Figures 4.3c,d**. In the calculation of porosity and surface-to-volume ratio, we hypothesize the interface between water and rods to be independent of rod-rod distance and estimate the volume of confined water by assuming an effective radius (0.42 nm) of the rigid rods.[28-29] As shown in Figs. 4.3c,d, the δ_{rt} appears to scale linearly with rod-rod distance, but the scaling is not linear with respect to the surface-to-volume ratio. Notwithstanding, this parallel between the effect of narrowing confinement and decreasing temperature implies that hydrophobically confined molecules behave as if they are under lower effective temperatures. In other words, the confinement effect is similar to the effect of lowing

temperature, which suggests one can gain insight into the confinement effect by studying the effect of temperature.

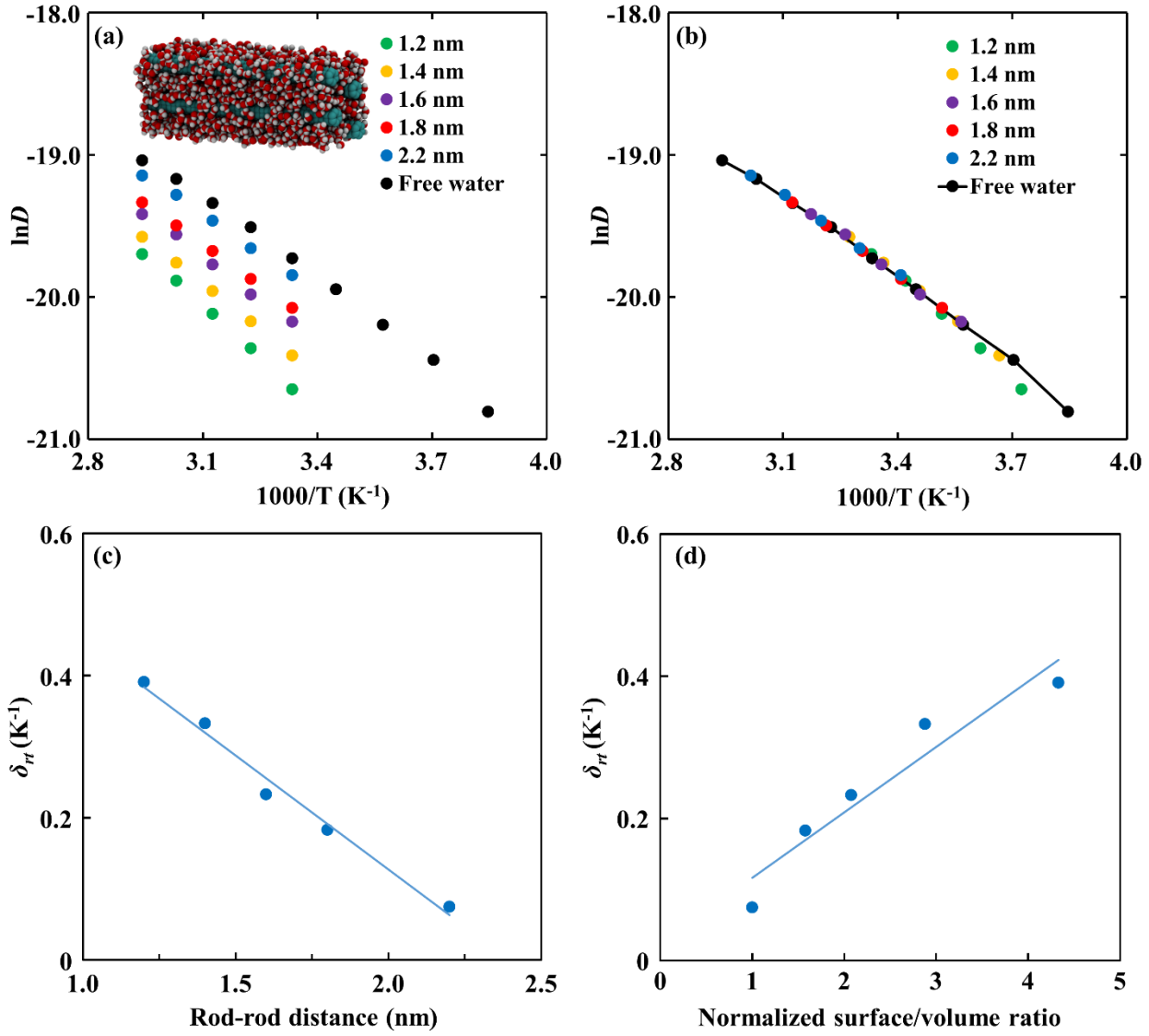

Figure 4.3. Arrhenius plots of confined SPC/E water in the rigid-rod model (the legends represent the rod-rod distance) as well as free SPC/E water. Panel (a) represents the original data of diffusion coefficients at varying temperatures. The temperature range for confined water is 300 K – 340 K with 10 K intervals while being 260 K – 340 K with 10 K intervals for free water. Panel (b) represents shifted plots of the same data series as in panel (a). We shift the data series of confined water until they overlap with the plot of free water. The shifted data series of confined water mostly

follows the trend of bulk water except when the rod-rod distance is 1.2 nm. Panel (c) and (d) plot the shift factors of the Arrhenius plots in terms of reciprocal temperature obtained from panel (b) as a function of rod-rod distance and surface/volume ratio. In both plots, the five data points correspond to five rod-rod distances ranging between 1.2 nm and 2.2 nm. The surface/volume ratio is normalized to 1 at a rod-rod distance of 1.2 nm.

We note the Arrhenius plot for the diffusion coefficient of water in **Figure 4.3b** is non-linear, signaling an expected variation of E_a with temperature. While the dependence of E_a on temperature is usually weak, we believe that it connects with a change in the local environment due to changing temperature.[10] In the next few sections, we quantify the connection between the molecular environment experienced by water and the residence time of water around water. We will show that both a lowered temperature and a smaller confinement size increase residence time. Consequently, we propose that the association between water molecules is the origin of retarded water dynamics under hydrophobic confinement.

4.3.3 Associations between Water Molecules in the Bulk

We now examine the residence time between water molecules in bulk SPC/E water with temperatures ranging between 260 K and 340 K. We perform bulk water simulation with 4096 SPC/E water molecules and calculate the residence time correlation function $S(t)$ at varying temperatures. **Figure 4.4a** shows the $ln(S(t))$ as a function of t at a few selected temperatures. We notice two regions from these plots, a fast-decaying region at short times and a slower-decaying region at longer times. This behavior can be nicely fit with the double exponential model of Eqn. (4). **Figure 4.4b** represents the short and long residence times, τ_s and τ_l, obtained from the fit, as a function of temperature. Both residence times increase with decreasing temperature.

In other words, lowering temperature prompts extended associations between water molecules in the bulk state.

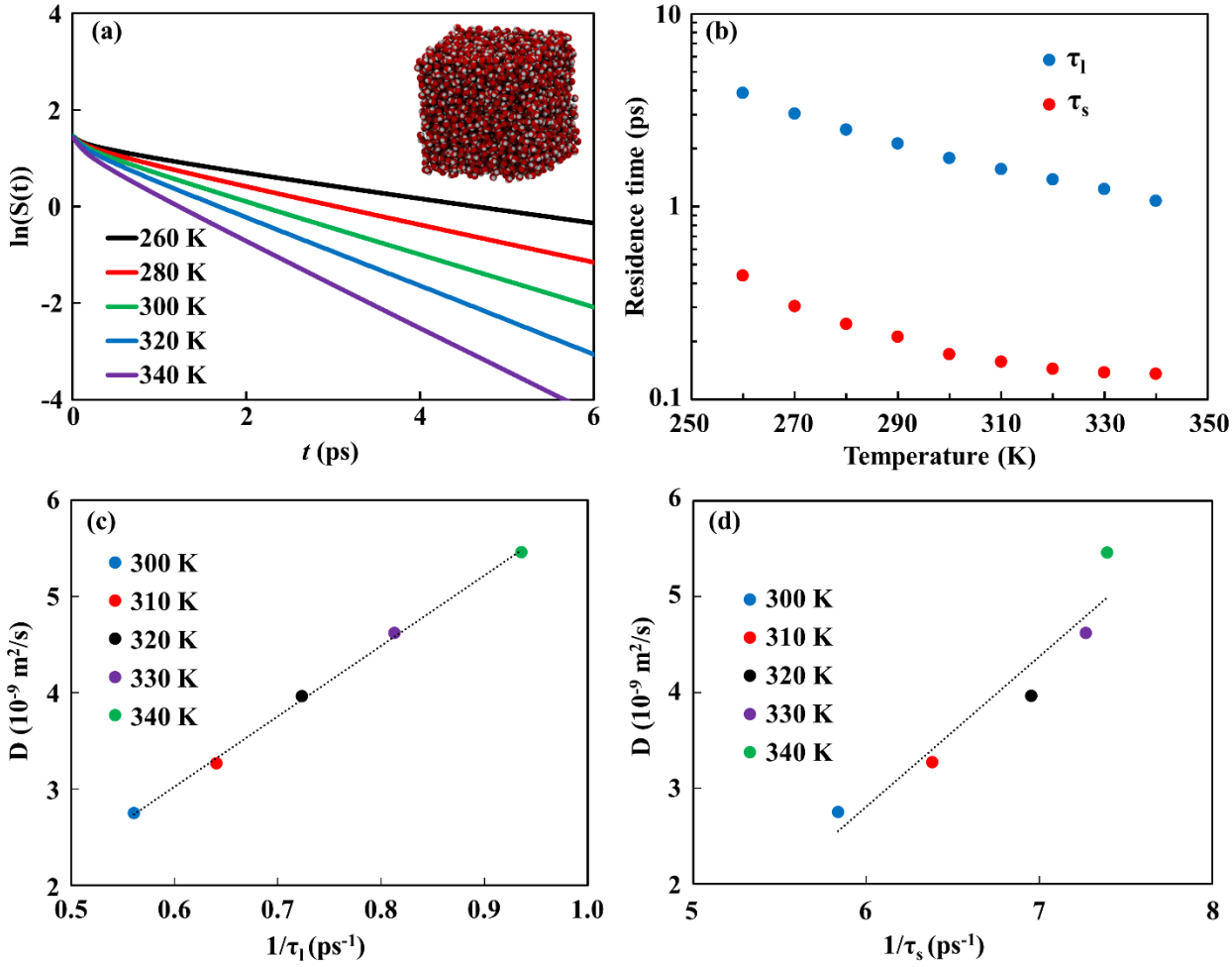

Figure 4.4 Panel (a) shows representative $\ln(S(t))$ $vs.\, t$ plots generated from free SPC/E water at varying temperatures. $S(t)$ evaluates the timescale of associations between neighboring water molecules. The decay indicates the loss of associations between neighboring water molecules. As temperature rises, the association between adjacent molecules becomes increasingly shorter-lived. (b) shows the long and short residence times as a function of temperature. Both τ_s and τ_l show a monotonic decrease with increasing temperature. The errors in τ_s and τ_l are estimated to be ± 0.02 ps and ± 0.05 ps, respectively. Panels (c) and (d) plot diffusion coefficients of bulk water as a

function of $1/\tau$. Diffusion coefficients scale linearly with $1/\tau_l$, but they do not with $1/\tau_s$, which supports the notion that τ_s and τ_l may carry different physical meanings.

When comparing residence time to diffusion properties, D and E_a, of bulk water, longer residence time correlates with lower diffusion coefficients and higher activation energies. We argue that with longer timescale associations, it is more difficult for water molecules to escape the shell formed by their immediate neighbors, so the diffusion becomes slower. Similar reasoning applies to the activation energy as well. We notice that the lengthened associations between water molecules are responsible for increased activation energy in supercooled liquids,[30-31] which is analogous to what we observe here.

The diffusion coefficients scale linearly with $1/\tau_l$ (**Figure 4.4c**). This linearity highlights the connection between water dynamics resulting in long residence times and the diffusion coefficients. Water molecules transition from ballistic to diffusive motion in the picosecond timescale.[32] Ballistic motion involves collisions with immediate neighboring molecules, while diffusive motion occurs after molecules exit their initial environment. Towards the end of τ_l, neighboring molecules are starting to separate from each other. Thus, τ_l signals the timescale for diffusive motions to become dominant. (We include a more in-depth analysis of the relation between D and τ_l in section 4.4.6.) Contrary to the long residence-time behavior, the diffusion coefficients scale nonlinearly with $1/\tau_s$ (**Figure 4.4d**), which indicates τ_s may report on a different metric of molecular dynamics from D. The molecular association process related with τ_s is much shorter than 1 ps. At such timescales, the motions of molecules have not entered the diffusive regime and are therefore squarely in the pre-diffusive, ballistic stage.[27, 33] In previous work, we showed that the activation energy of diffusion, E_a, arises from molecular interactions and motions

on the picosecond timescale.[10, 27] Thus, we can hypothesize τ_s is likely correlated with E_a, and we discuss this correlation in the next section.

4.3.4 Associations between Water Molecules in the Rigid-Rod Model

In the previous section, we quantified the effect of temperature on water dynamics by calculating the residence time of bulk water. In this section, we turn our attention to examining the dynamics of water molecules in a confined state using the same metric. **Figure 4.5** provides insight on the residence time of water around water in the rigid-rod model. There is an apparent increase in the residence time with decreasing rod-rod distance, resembling what we see with decreasing temperature. The trend in residence time of confined water supports the notion that nanoconfinement prompts longer associations between water molecules. Thus, the observed retarded water dynamics under hydrophobic confinement correlates with longer-lived associations among water molecules; in other words, the water molecules are slowing themselves down.

While the effects of reduced temperature and hydrophobic confinement on the residence time are similar, we believe the mechanisms behind the two effects are different. Lowering the temperature reduces thermal motion, limiting the energy available for a molecule to escape the attractive potential provided by neighboring molecules. Hydrophobic nanoconfinement, on the other hand, physically limits the molecules' freedom of motion, resulting in longer aggregation. **Figures 4.5c,d** plot diffusion coefficients of confined water in this model to $1/\tau_l$, where we observe a linear relationship reminiscent of that in bulk water. We also note that, much as with bulk water, the diffusion coefficients scale nonlinearly with $1/\tau_s$ for confined water (see **Figures 4.5e,f**).

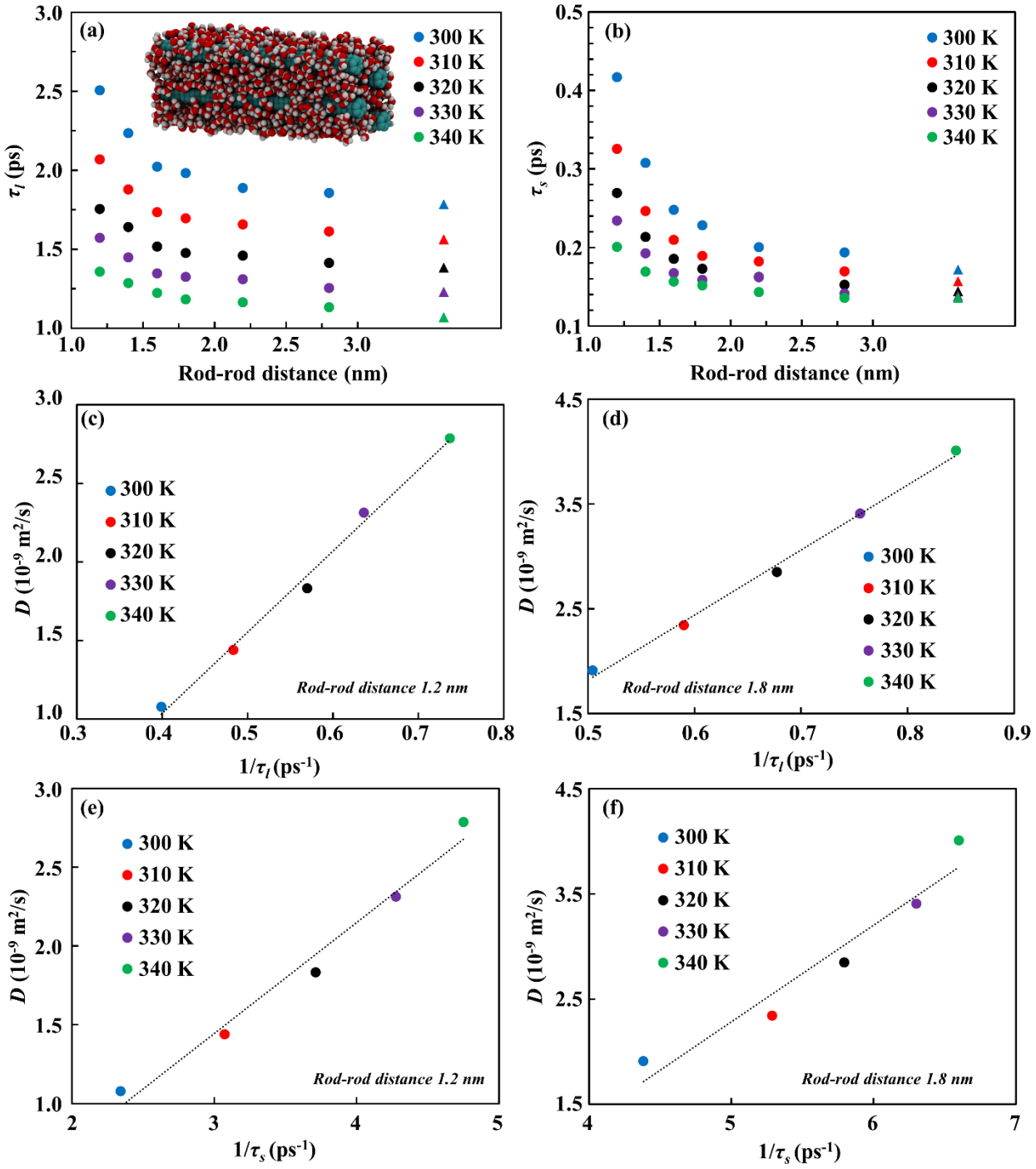

Figure 4.5 Residence time calculated from confined SPC/E water in the rigid-rod model and comparison between confined and free water. Panel (a) plots τ_l as a function of rod-rod distance while panel (b) plots τ_s as a function of rod-rod distance. At each rod-rod distance, τ_s at five temperatures from 300 K and 340 K are present. Note that the triangular symbol represents the

residence time of bulk water. The residence time of confined water steadily decreases with increasing confinement size and converges to those of bulk water. Errors in τ_l and τ_s are estimated to be $\pm$0.05 ps and $\pm$0.02 ps, respectively. Panel (c) and (d) plot diffusion coefficients of confined water as a function of $1/\tau_l$. The linear relationship between D and $1/\tau_l$ stays valid for confined water. Panel (e) and (f) plot diffusion coefficients of confined water as a function of $1/\tau_s$. Similar to observed in the bulk water, D is nonlinear with $1/\tau_s$. Panel (c), (e) corresponds to a rod-rod distance of 1.2 nm while panel (d), (f) corresponds to a rod-rod distance of 1.8 nm.

There are subtle differences in the variation of τ_s and τ_l with confinement size and temperature in **Figures 4.5a,b** that merit further discussion. First, the relative increase in τ_l with decreasing rod-rod distances is smaller than that of τ_s, which indicates that the τ_s is more sensitive to confinement size. Second, the temperature dependence of τ_s is more sensitive to the rod-rod distance than that of τ_l (**Figure 4.6**). When comparing E_a of diffusion to the activation energy of the residence times, the E_a of τ_s agrees with the E_a of diffusion better. This is another indication that τ_s is more correlated with E_a than τ_l.

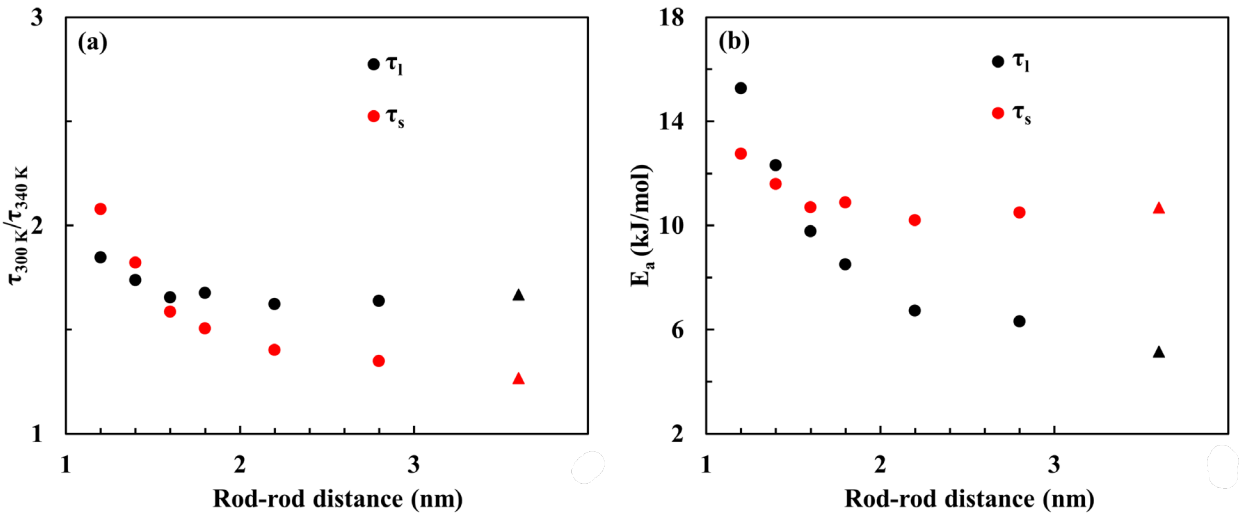

Figure 4.6 Panel (a) shows the ratio between residence time at 300 K and 340 K for both the long

and short residence times of water around water in the rigid-rod model. Panel (b) shows the Arrhenius activation energies (follow the equation $\tau = \tau_0 e^{E_a/RT}$) of the two residence times as a function of rod-rod distances. The triangles stand for the value calculated from bulk water. For τ_l, the temperature dependence drops slightly when the rod-rod distance increases from 1.2 nm to 1.6 nm but stays almost constant afterward. For τ_s, the temperature dependence decreases continuously towards that of bulk water. When comparing the trends of τ_l and τ_s to the reliance of E_a of diffusion on the rod-rod distance (**Figure 4.2d**), the size dependence of τ_s is more similar to the size dependence of E_a, suggesting that τ_s is more correlated with E_a.

4.3.5 Association of Water Molecules in the Parallel-Sheet and CNT Models

We now discuss the dynamics of water confined between the two parallel graphene sheets. Within the confined region, the diffusion coefficient of water perpendicular to the sheets is zero. Thus, we only consider water diffusion parallel to the graphene sheets. **Figure 4.7a** shows the Arrhenius plots of the diffusion coefficients of confined water in this model compared to bulk water. Note that the temperature range for a layer-to-layer distance of 0.7 nm is different from the rest. At 300 K and 310 K, we observe that water molecules form a "squared ice" structure[34-35] when confined between parallel sheets 0.7 nm apart. This structured water no longer exists beyond 320 K. Thus, we use a slightly different temperature range, 320 K and 360 K, when the layer-to-layer distance is 0.7 nm.

In this parallel-sheet model, we also observe an increase of E_a with a smaller confinement size, reaching a maximum at a layer-to-layer distance of 0.7 nm. **Figure 4.7b** shows the τ_l of confined water in the parallel-sheet model. Much as with diffusion coefficients and activation energies of diffusion, the residence time of confined water is slightly different from that of bulk

water at the largest layer-to-layer distance of 1.8 nm, implying confinement can be experienced within that range.

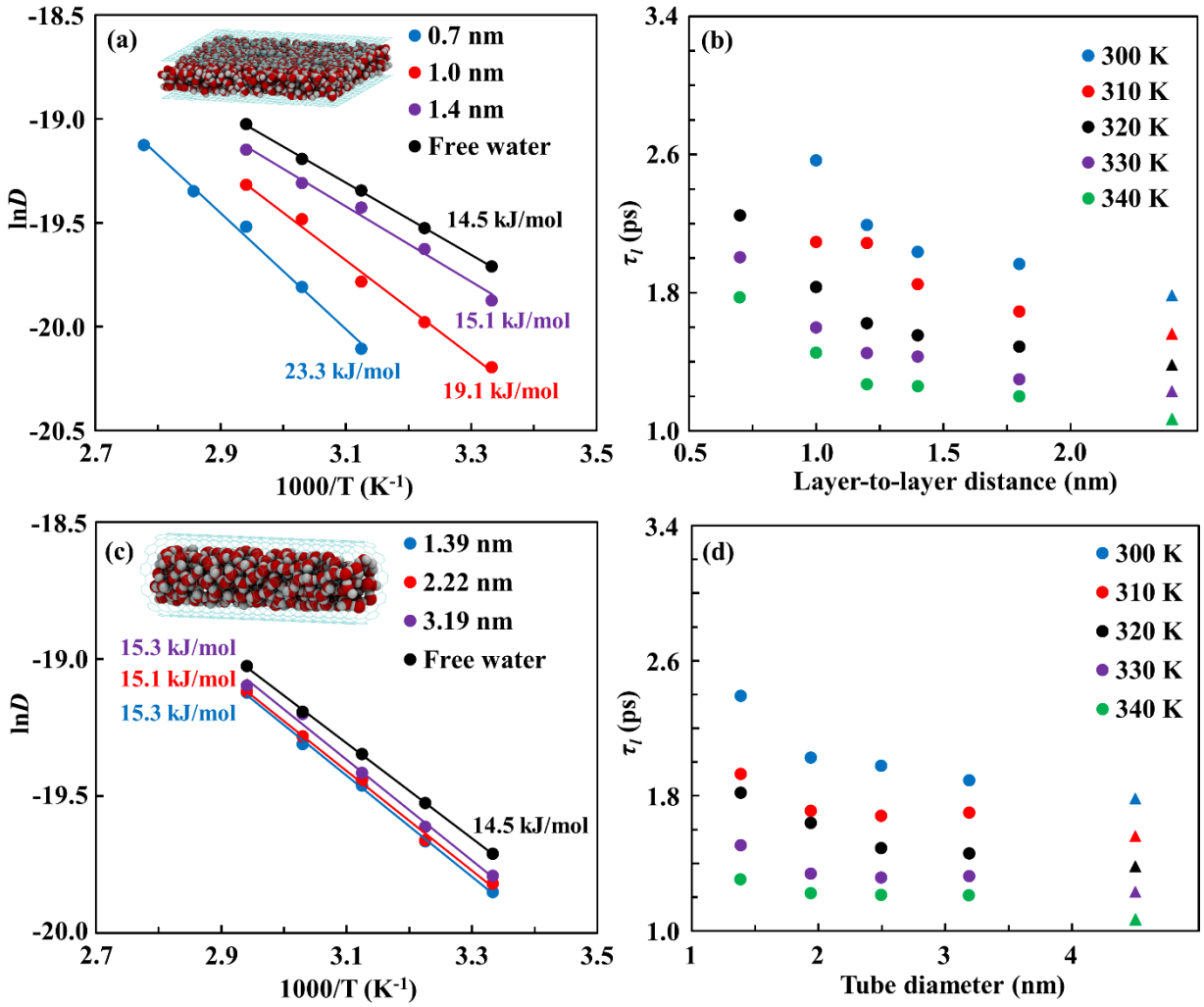

Figure 4.7. Panel (a) shows the Arrhenius plots of bulk SPC/E water and confined SPC/E water in the parallel-sheet model at varying layer-to-layer distances. Note we cannot extract diffusion coefficient at 300K and 310 K at a layer-to-layer distance of 0.7 nm because water molecules freeze and form squared ice-like structures at these temperatures. Panel (b) shows the τ_l of confined water (circle) in the parallel-sheet model as a function of layer-to-layer distance. The triangles are the residence time of bulk water. Panel (c) and (d) corresponds to Arrhenius plots and residence time of water in the CNT model as a function of the tube diameter. Note the diffusion

coefficient calculated in the CNT model is one-dimensional along the tube axis, and the diffusion coefficient calculated in the parallel-sheet model is two-dimensional parallel to the graphene sheets.

In addition to the parallel-sheet model, we have also examined carbon nanotube (CNT) simulations. As some previous work has shown, water molecules inside CNTs form a long-range ordered structure when tube diameter is close to 1.2 nm,[10, 36] which strongly affects the water dynamics.[9-10] For simplicity, we discuss the scenario when the tube diameter is larger than 1.3 nm, such that ordered water does not form inside the CNT. **Figure 4.7c** shows the diffusion coefficients of water in the CNT model as a function of the tube diameter. While there is little dependence of diffusion coefficients on tube diameter, we observe an increase in residence time with decreasing tube diameters. The insensitivity of the diffusion coefficients with tube diameter is different from what we observe in the rigid-rod and parallel-sheet models because, in the CNT model, the diffusion is just one-dimensional (along the axial direction). An important emerging trend is that regardless of the model of hydrophobic nanoconfinement, tighter confinement volumes lead to longer associations between water molecules. The prolonged association between water molecules induced by nanoconfinement is responsible for the slowdown of molecular diffusion and the increase in the activation energy of diffusion.

4.3.6 Association between Water Molecules and a Confining Surface

So far, we have investigated the dynamical association between water molecules subject to confinement. We now describe the association between water molecules and the confinement medium. For simplicity, we focus on the rigid-rod model in this section, and we calculate $S(t)$ based on distance from the water molecules to the center of the nearest rod. By examining density profiles around the rods, we determined that 0.55 nm from the center of the rod is a proper cut-off

distance in the residence-time analysis to probe the dynamics of water molecules within the first surface layer of a rigid rod. In the calculation of the residence of water around rods, we normalize all correlation functions so that $S(0) = 1$. **Figure 4.8** displays the residence time of water around rods. We notice the decay of $S(t)$ at a rod-rod distance of 1.2 nm is distinctively slower than the others, and $S(t)$ and the residence times are almost independent of rod-rod distances for 1.4 nm rod-rod distance and beyond. **Figures 4.8b,c** also demonstrate that the residence time at a rod-rod distance of 1.2 nm is uniquely longer than the others. Visual inspection of the structure of water in the rigid-rod model (the insert in **Figure 4.8a**), shows a "ring" of water around the 1.2-nm distanced rods. Judging from the residence time of water around rods, this "ring" water structure is most stable at a rod-rod distance of 1.2 nm. At 1.4 nm and beyond, the "ring" structure becomes less distinctive/stable, and we also observe lower residence time of water around rods that is rather insensitive to inter-rod distance. Considering the weak interactions between water molecules and carbon rods, the "ring" structure of water observed within the 1.2-nm distanced rods are likely a result of confinement size.

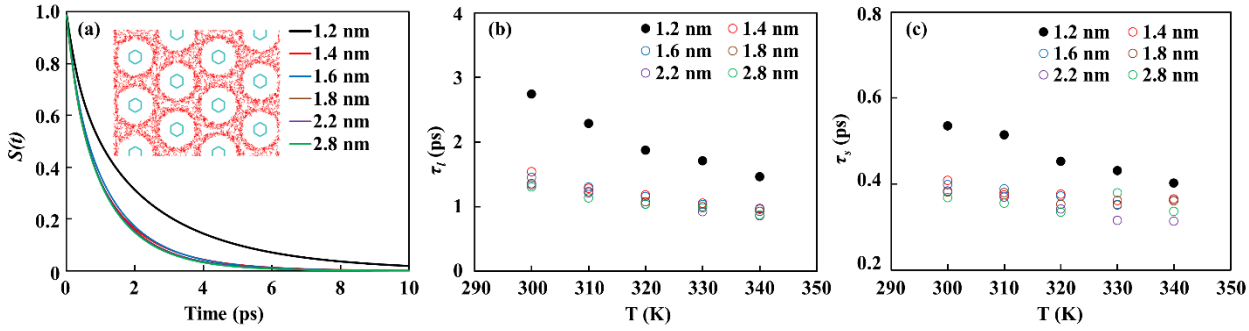

Figure 4.8 Panel (a) shows the residence time correlation functions, $S(t)$, of water-rod associations for varying rod-rod distances. The inset of panel (a) shows a snapshot of the water structure in the rigid-rod model at a rod-rod distance of 1.2 nm. All plots in (a) correspond to a temperature of 300 K. Panel (b) and (c) plots the residence time of water around rods as a function

of temperature. The residence here corresponds to a cut-off distance of 0.55 nm between water molecules and center of rods. We observe the errors in τ_l and τ_s are higher here (estimated to be $\pm$0.1 ps) due to a smaller number of sampling,

4.3.7 Modified Water-Surface Lennard-Jones Interactions in the Rigid-Rod Model

We now explore how the interaction potential between the atoms forming the confinement medium and water affects the dynamics of confined water. We conduct simulations on the rigid-rod model with 1.2-nm and 1.8-nm rod-rod distances using varying Lennard-Jones parameters of the rod carbon atoms to modify the interaction between the rigid rods and water molecules. We present the results for two C-atom Lennard-Jones attraction well depths that are 2 and 4 times greater than in the original simulation, without changing the location of the well (parameters shown in **Table 4.1**). This force-field parameter modification can be used to shed rich light on water dynamics under enhanced attraction with the confinement medium.

Table 4.1. Modified Lennard-Jones parameters of the carbon atom

	σ_c (nm)	ε_c (kJ/mol)
Original	0.355	0.293
Modification 1	0.355	0.586
Modification 2	0.355	1.172

The two new sets of carbon Lennard-Jones parameters give stronger interactions between the water molecules and the rigid rods but keep the interactions between water molecules unchanged. **Figures 4.9a,b** show the Arrhenius plots of water diffusion under the two new sets of force fields. As the water-rod interactions increases, the diffusion of water slows down while activation energy increases slightly. **Figure 4.9d** plots the residence time of water around rods for

the same systems. Unsurprisingly, water molecules become more associated with rigid rods when water-rod interactions grow stronger. **Figure 4.9c** plots the residence time of water around water with modified and original force fields. Interestingly, the associations between water molecules increase when water-rod interactions become stronger. Calculations reveal that the increased associations between water molecules still persist at a rod-rod distance of 1.8 nm. An explanation for the increased water associations even when the water-water potential remains unchanged is the stabilization of the surface water. The increased rod-water Lennard-Jones attractions localize the water molecules within the rod surface layer, and those water molecules consequently become associated with each other for longer times. Considering that the Lennard-Jones interactions are short-range interactions and decay quickly with increased distance, we expect the increase of the carbon-water Lennard-Jones attractive well will mostly lengthen the associations of water molecules in the first surface layer while having a limited impact on the water molecules further away.

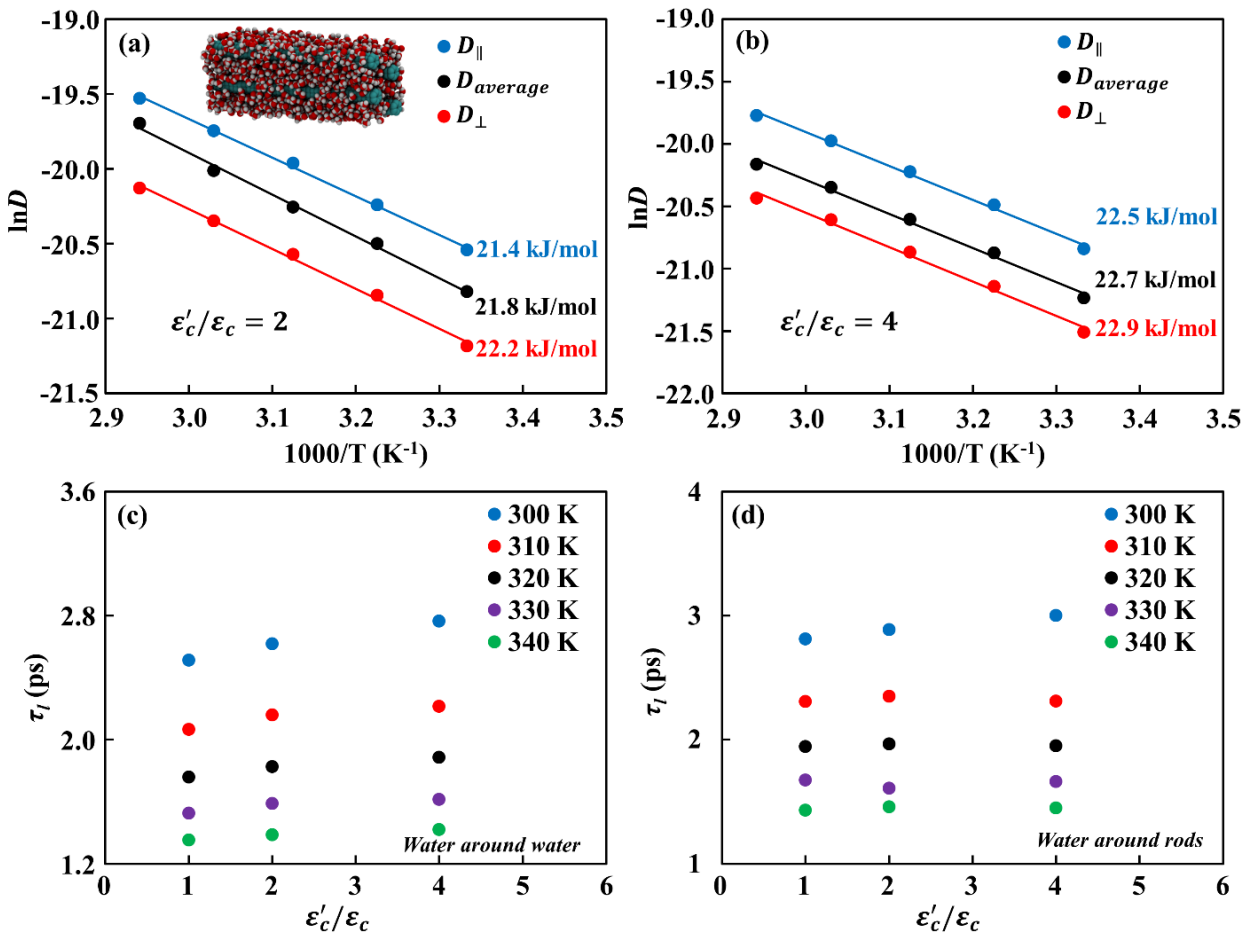

Figure 4.9 Impact of changing hydrophobicity on diffusion and residence time. Panel (a) and (b) present the Arrhenius plots of confined water in the rigid-rod models with a rod-rod distance of 1.2 nm and modified hydrophobicity. In panel (a), the modified Lennard-Jones parameter of the carbon atom (ε_c') are twice as strong as the original parameter (ε_c). In panel (b), ε_c' is four times as high as ε_c. Note the average E_a with the original force field is about 20.1 kJ/mol (shown in **Figure 4.2a**). Panel (c) shows the τ_l of water around water with both original force fields and modified force fields. Panel (d) shows the τ_l of water around rods with both original force fields and modified force fields

4.3.8 Associations of Water in Confined Salt Solutions

The simulation systems discussed so far contain no ions. For the sake of completeness and in an effort to target ionic transport through hydrophilic channels of membranes, we have also incorporated lithium triflate (LiOTf) ion pairs into the rigid-rod model. The addition of 1000 lithium triflate ion pairs to the water solvating the rigid-rod model with 1.2 nm and 1.8 nm rod-rod distances result in H_2O/Li^+ molar ratios (λ) of 6.8 in the 1.2-nm model and 16.8 in the 1.8-nm model. In parallel, we created bulk aqueous LiOTf solutions with λ values of 6.8 and 16.8 to compare with the models under confinement. The methodology described previously to calculate $S(t)$ and residence time is maintained for the ionic solutions for consistency, including the 0.33-nm cut-off distance.

Figures 4.10a,b show the Arrhenius plots of water and lithium ions under both confined and bulk environments. As with the non-ionic solutions, the confined solutions in general exhibit lower *D* and higher E_a as compared to the bulk model. **Figures 4.10c**,**d** show the τ_l of water around water in the confined solution, bulk ionic solution, and bulk liquid water. Water molecules in bulk ionic solutions are more associated than in pure water, which we attribute to the strong ion-water associations. The residence time of water around ions is much longer than the residence time of water around water,[37] which lengthens the associations between water molecules solvating the same ion. When comparing the τ_l between confined and bulk ionic solutions, the confinement further increases the residence time of water around water. Moreover, we also observe the confinement effect to be particularly noticeable at the smaller inter-rod distances. Both the change in diffusion behavior and the change of residence time are more significant with smaller rod-rod distance when going from the free to confined ionic solutions.

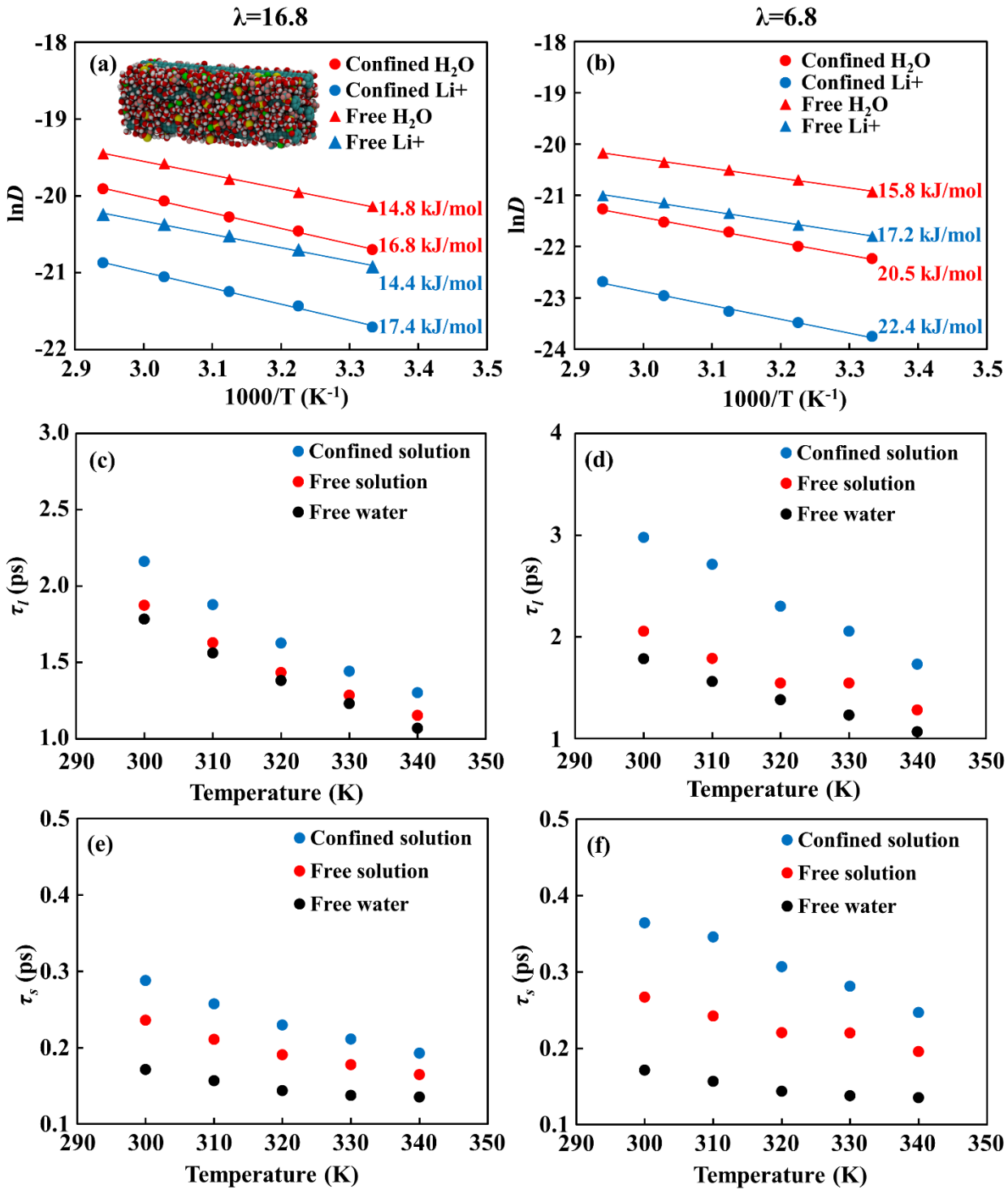

Figure 4.10 Panels (a) and (b) show the Arrhenius plots of lithium ions and water molecules in both confined LiOTf solutions (circle) and bulk LiOTf solutions (triangle). Panels (c) and (d) plots the long residence time of water in confined LiOTf solutions, bulk LiOTf solutions, and bulk water.

Panels (e) and (f) plot the short residence time of water in the aforementioned systems. The left column corresponds to a water/lithium molar ratio (λ) of 16.8, while the right column corresponds to a λ of 6.8. Note that the diffusion coefficients of confined solutions are $D_{average}$. The existence of ions increases associations between water molecules, and the confinement effect still persists in the presence of ions.

4.4 Residence-Time Dependence on Density, Temperature, Force Fields, and Cut-off Distance

4.4.1 Dependence of the Residence Time of Bulk Water on Changing Temperatures and Densities

In section 4.3.3, we attribute the decrease of residence times to the temperature increase. However, with changing temperature, the density of the system is also changing, although not to a significant extent (less than 5%). To evaluate the impact of density on residence time, we recalculate the residence time of water around water with the same density at varying temperatures. To achieve the same density, we start from the output coordination file of the 300-K NPT simulation and run NVT simulations of varying temperatures. We present the results in **Table 4.2**. After constraining the density, the changes of both τ_s and τ_l are within uncertainties with respect to the simulations with varying density. We can thus conclude that the residence time is dependent on the temperature alone, and not density.

Table 4.2 Residence times of bulk SPC/E water with temperature-equilibrated density (τ_s, τ_l) and unequilibrated 300 K density ($\tau_{s,sd}$, $\tau_{l,sd}$). The change of density with temperature appears to have little effect on the residence time, at least within this temperature range.

Temperature (K)	τ_s (ps)	$\tau_{s,sd}$ (ps)	τ_l (ps)	$\tau_{l,sd}$ (ps)
260	0.44	0.42	3.88	3.76
270	0.30	0.31	3.03	3.00
280	0.25	0.26	2.50	2.52
290	0.21	0.21	2.12	2.13
300	0.17	0.17	1.78	1.78
310	0.16	0.15	1.56	1.56
320	0.14	0.15	1.38	1.39
330	0.14	0.14	1.23	1.23
340	0.14	0.13	1.07	1.12

4.4.2 Residence Times and Associations of Water Molecules in the Simulations of TIP4P/2005 Water Model

In the previous simulations, we use the SPC/E water model in the calculation of residence time. Here we explore another water model to see if the behaviors observed with the SPC/E water are model-dependent. **Figure 4.11** compares the τ_s and τ_l of water around water in bulk TIP4P/2005 water and bulk SPC/E water. Overall, TIP4P/2005 water gives slightly longer residence times than SPC/E water, signaling more extended associations between TIP4P water molecules. The difference here is consistent with the fact that bulk TIP4P/2005 water has lower diffusion coefficients and higher activation energies than bulk SPC/E water.

The general trends observed in the residence time of SPC/E water are also observed in the TIP4P/2005 water. Increasing temperatures always lead to shorter associations between neighboring water molecules (**Figure 4.11a**). Similar to SPC/E water, we found that the diffusion coefficients of TIP4P/2005 water correlate better to $1/\tau_l$ than to $1/\tau_s$ (**Figures 4.11c,d**). We also looked at the residence times of confined TIP4P/2005 water in the rigid-rod model. **Figure 4.12** summarizes the diffusion behaviors and residence times of TIP4P/2005 water confined in the rigid-rod model. For efficiency, we only looked at two rod-rod distances, 1.2 nm and 1.8 nm. One

corresponds to extremely confined water, while the other corresponds to coarsely confined water. TIP4P/2005 water appears to be more sensitive to confinement than SPC/E water. At a rod-rod distance of 1.2 nm, the E_a of TIP4P/2005 water increases to over 30 kJ/mol, which is almost 10 kJ/mol higher than that of confined SPC/E water. At a rod-rod distance of 1.8 nm, the E_a of TIP4P/2005 water is similar to that of bulk TIP4P/2005 water. The calculation of residence of confined TIP4P/2005 water also gives similar trends as those observed with SPC/E water. Smaller confinement prompts longer associations between water molecules, while larger confinement leads to a residence time similar to that of bulk water. These observations confirm that the behavior of residence time and its connection with confinement are not model-dependent.

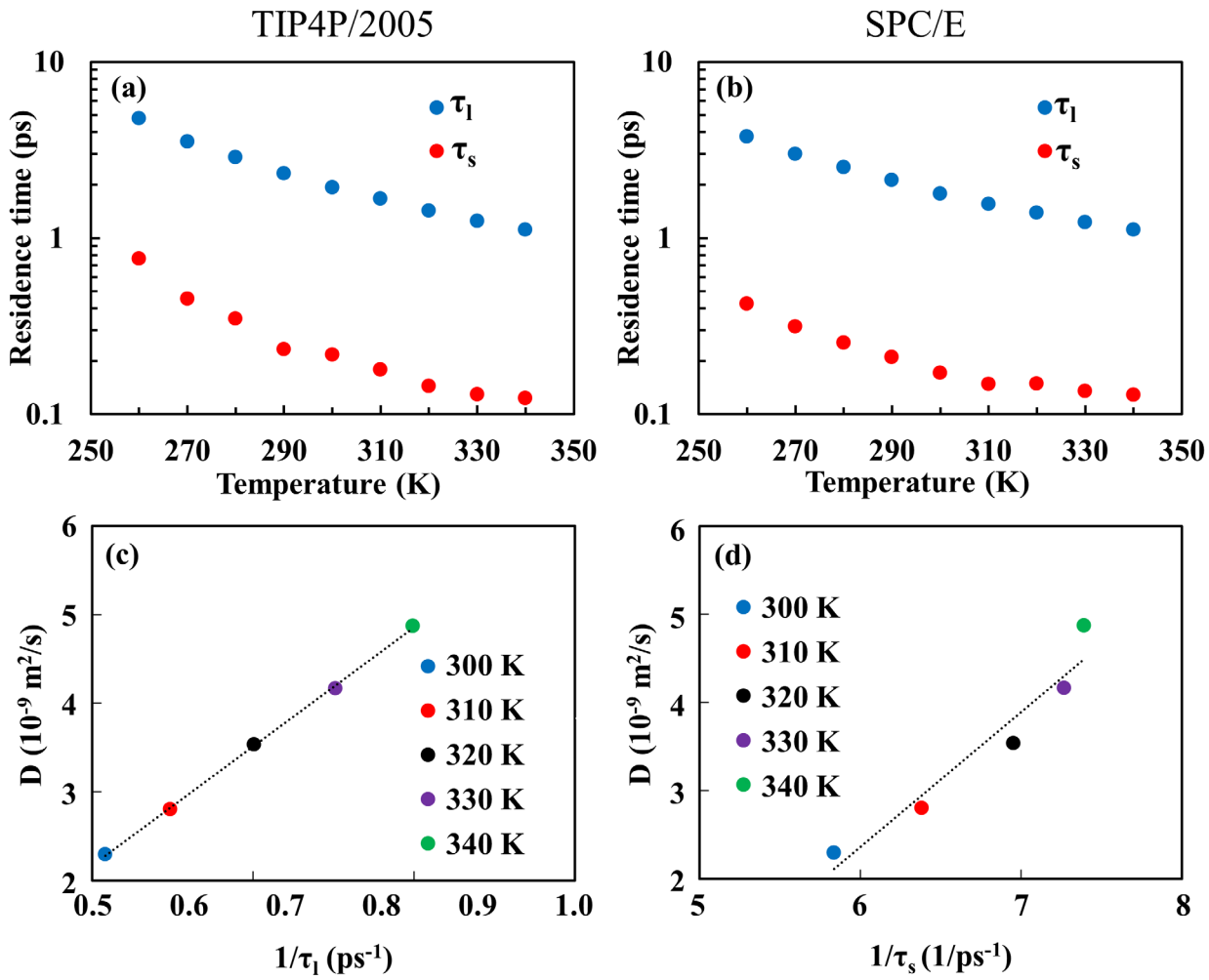

Figure 4.11 Comparing residence time of water around water between (b) bulk SPC/E water and (a) bulk TIP4P/2005 water. The TIP4P/2005 water shows slightly higher residence time than SPC/E water, especially at lower temperatures. Panel (c) and (d) plot diffusion coefficients of bulk TIP4P/2005 water as a function of $1/\tau_l$ and $1/\tau_s$.

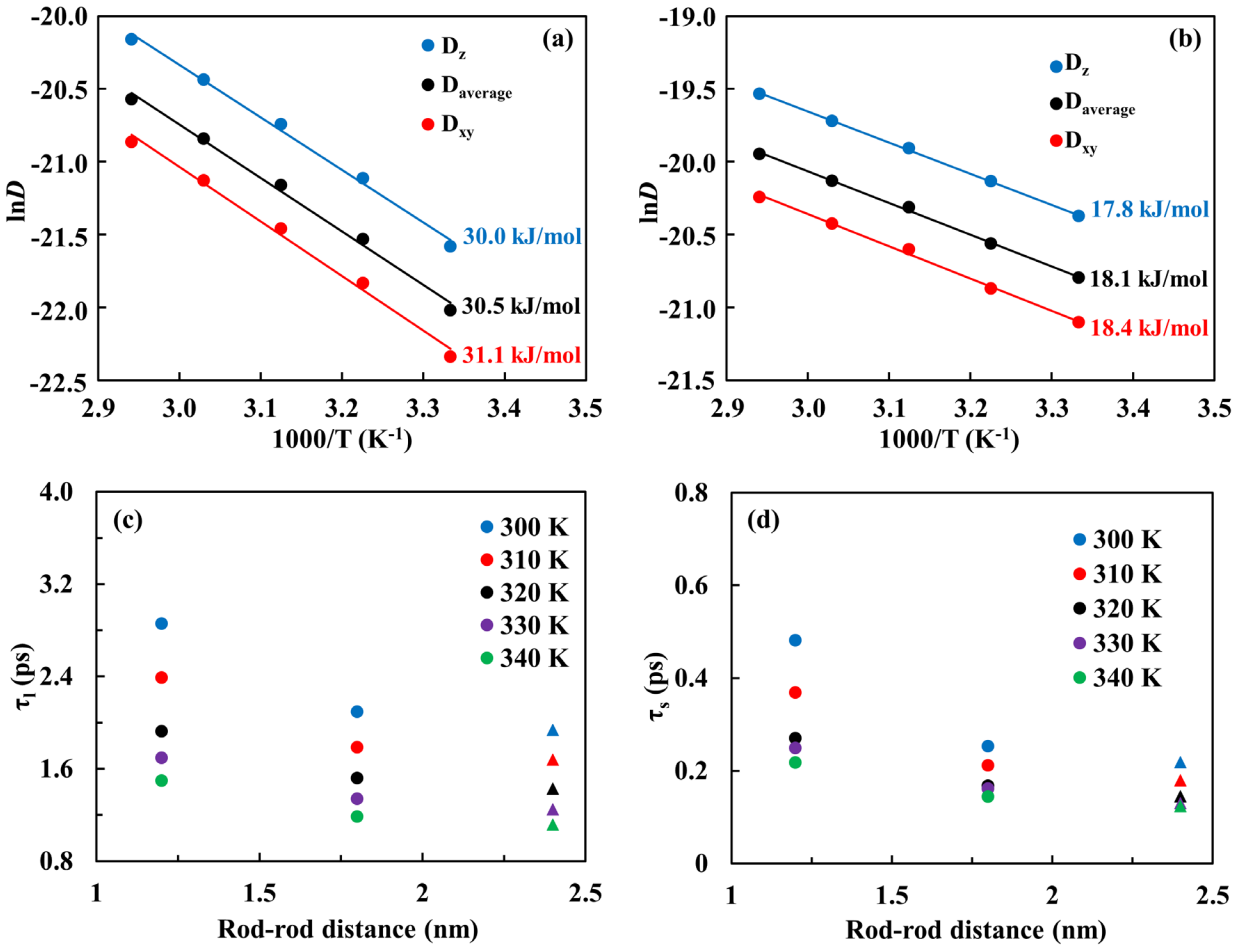

Figure 4.12 Panels (a) and (b) show the Arrhenius plots of confined TIP4P/2005 water in the rigid-rod model with rod-rod distances of 1.2 nm and 1.8 nm. The temperature range is 300 K – 340 K with a 10 K interval. E_a of bulk TIP4P/2005 water at the same temperature range is 16.2 kJ/mol. Panels (c) and (d) summarize the residence time for confined (circle) and bulk (triangle) TIP4P/2005 water. We observe similar trends as in those of confined SPC/E water.

4.4.3 Dependence of the Residence Time on the Cut-off Distance

In the calculation of the residence time of water around water, we define a cut-off distance of 0.33 nm. There is, however, no consensus on how to determine the exact cut-off distance. We choose this cut-off distance based on the RDFs of water around water (shown in **Figure 4.13**). The first peak in the RDFs signifies the distance of neighboring water molecules. We look for the first minimum after the first peak and use that as the standard for cut-off distance. However, as shown in the RDF plots, the first minimum can shift slightly with either changing temperatures or changing confinement size.

In an effort to find out the dependence of residence time on cut-off distance, we turned to the rigid-rod model with a rod-rod distance of 1.2 nm and calculated the residence time of water with varying cut-off distance. **Figure 4.14** shows the dependence of residence time on cut-off distance in the rigid-rod model. The long residence time, τ_l, appears to increases linearly with increasing cut-off distances, and the rate of increment is faster with lower temperatures. The short residence time, τ_s, also appears to increases linearly with increasing cut-off distances. Interestingly, the rate of increase in τ_s is slower with lower temperatures, contrary to what we observe in τ_l. Overall, the dependence of τ_l on cut-off distance is stronger than that of τ_s. With a change of 0.01 nm in the cut-off distance, τ_l changes by over 20% while τ_s changes by less than 10%. By reducing the cut-off distance to 0.32 nm, the τ_l of highly confined water is already similar to the τ_l of bulk water at a cut-off distance of 0.33 nm. This dependence emphasizes the importance of keeping the cut-off distance consistent. Throughout our trials, we found out that the cut-off distance can change the absolute values of residence time but not the general dependence of residence time on temperature/confinement. For simplicity, we kept the cut-off distance at 0.33 nm for all the simulation models and calculations.

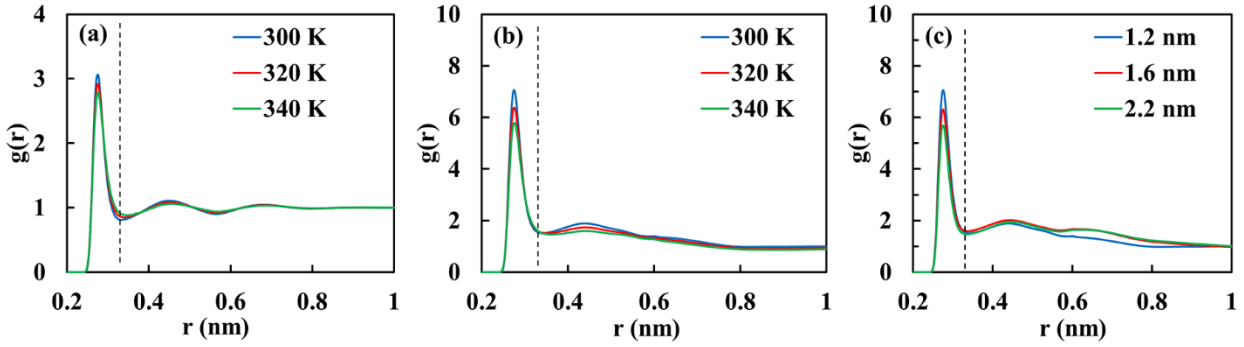

Figure 4.13 Radial distribution functions (RDFs) of water around water in bulk water (a), confined water in rigid-rod model with a rod-rod distance of 1.2 nm (b), and confined water at 300 K in the rigid-rod model (c). The dashed line represents the cut-off distance at 0.33 nm. We select the cut-off distance based on the first minimal in RDFs. This cut-off distance works reasonably well with both confined and bulk water.

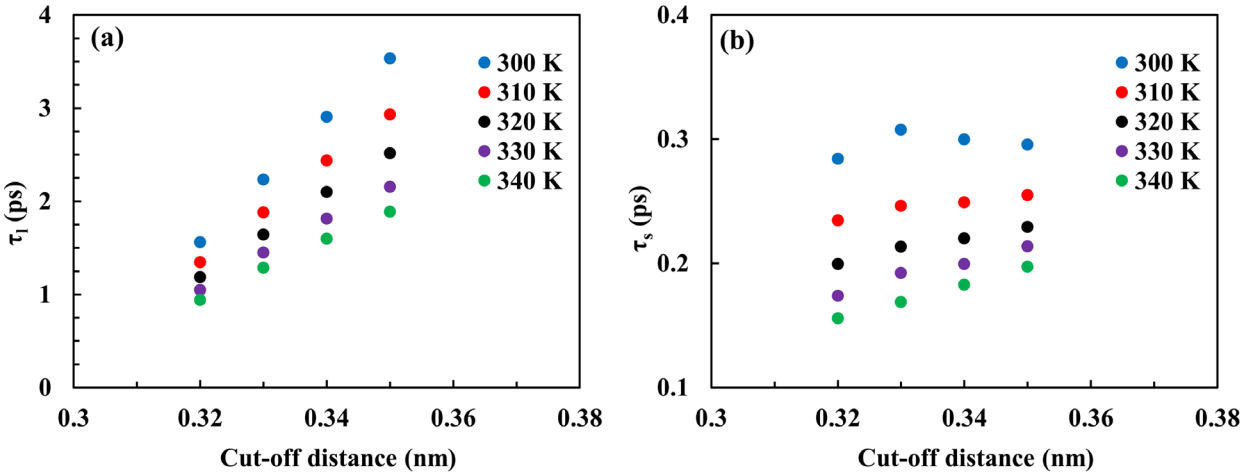

Figure 4.14 Residence time of water around water in the rigid-rod model at varying cut-off distances. All the data points correspond to the same rod-rod distance of 1.2 nm. τ_l is strongly dependent on the cut-off distance while τ_s is not nearly as dependent on the cut-off distance. This emphasizes the importance of consistent cut-off distances as well as the inherent difference between τ_l and τ_s. We would also like to mention that the linear dependence of D on $1/\tau_l$ stands

in all the cut-off distances.

4.4.4 Physical Implications of τ_l and the Correlation between τ_l and Diffusion Coefficient

We start from the random walk picture (**Figure 4.15**) to explain τ_l and its relation to the diffusion coefficient. The long residence time τ_l stands for the average time it takes for associated molecules to separate from each other. In other words, a molecule exits the vicinity of its initial neighbors at the end of τ_l. Thus, the displacement of a molecule within τ_l is a random step. We discover that the displacement during τ_l is not strongly dependent on the temperature when looking at the same system. **Figure 4.15b** represents the mean squared displacement (MSD) of bulk water as a function of diffusion time at varying temperatures. The MSD of water molecules at τ_l ranges between 0.030 nm^2 and 0.039 nm^2 at these temperatures. Thus, the molecules travel similar displacement within τ_l at varying temperatures. Assuming there are n random steps, the total diffusion time equals to $n\tau_l$, and the MSD equals $6Dn\tau_l$ (three-dimensional diffusion). We can assume that MSD is directly proportional to the number of random steps when d is a constant, providing there are enough time and number averaging. Thus, $D\tau_l$ is a constant, and D is proportional to $1/\tau_l$. The calculation of residence times supports that D is linear with $1/\tau_l$ with a small deviation from the proportional relationship.

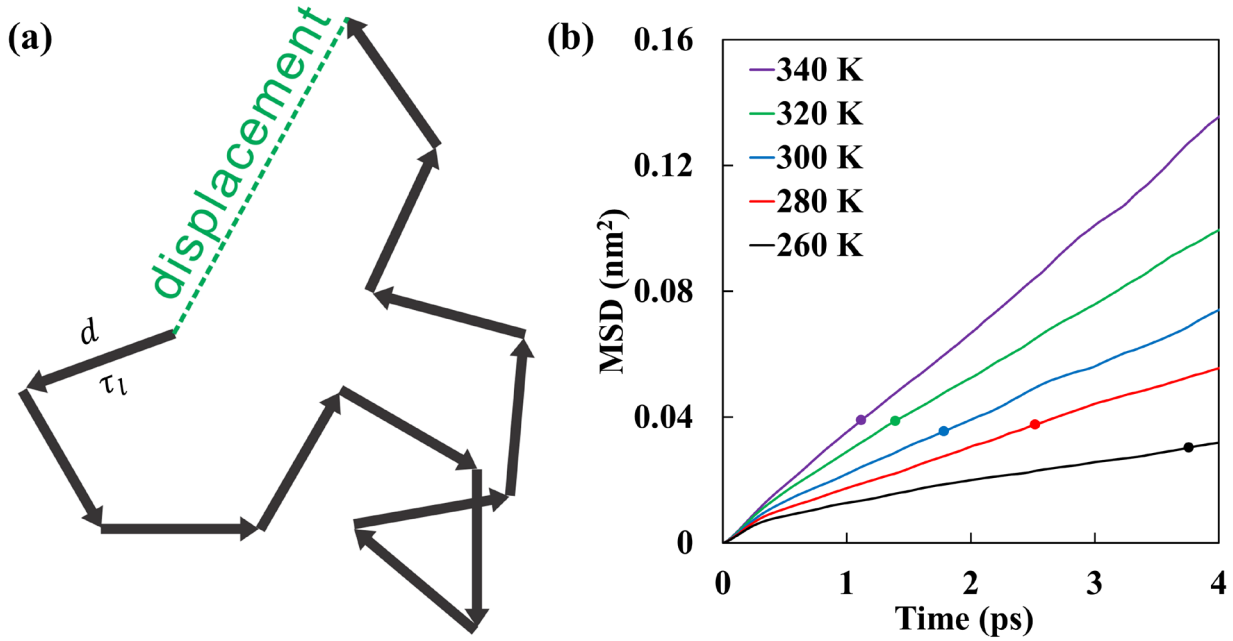

Figure 4.15 Panel (a) depicts a random walk picture of diffusive motions, which consists of a series of random steps. Assuming an infinite amount of number and time averaging, the average displacement within one random step (with a fixed amount of time) is a constant. Panel (b) plots the mean squared displacement of bulk SPC/E water vs. time at varying temperatures. Within the 4 ps time window, the MSD is initially nonlinear with time and becomes linear with time after around 1 ps. The fluctuations of plots originate from not enough averaging and the small displacement of molecules in such a short time. The circles on the plots represent the long residence time τ_l at respective temperatures.

4.5 Structural Water under Rigid-Rod Confinement

4.5.1 Structure of Confined Water in the Rigid-Rod Model

We present a snapshot of confined water in the rigid-rod model in Figure 4.17. We clearly observe a "ring" structure of surface layer water when the rod-rod distance is 1.2 nm. The density of water between the "ring" structures is visibly lower than within the "ring" structure. This "ring" structure is less apparent when the rod-rod distance is higher than 1.2 nm. The interactions between

the hydrophobic carbon rods and the water molecules are weak, which means the water molecules do not naturally get adsorbed onto the confining surface. Thus, the formation of this structured water is likely a result of small confinement size. When the confinement size continues to go lower than the 1.2 nm, we observe more interesting structures of confined water. At rod-rod distances of 1.1 nm and 1 nm, the water rings around adjacent rods overlap. As a result, the confined water forms a honeycomb-like structure. At a rod-rod distance of 0.9 nm, the confined water does no longer occupy all the volume between the rods. Some of the regions between two rods become a vacuum at this rod-rod distance.

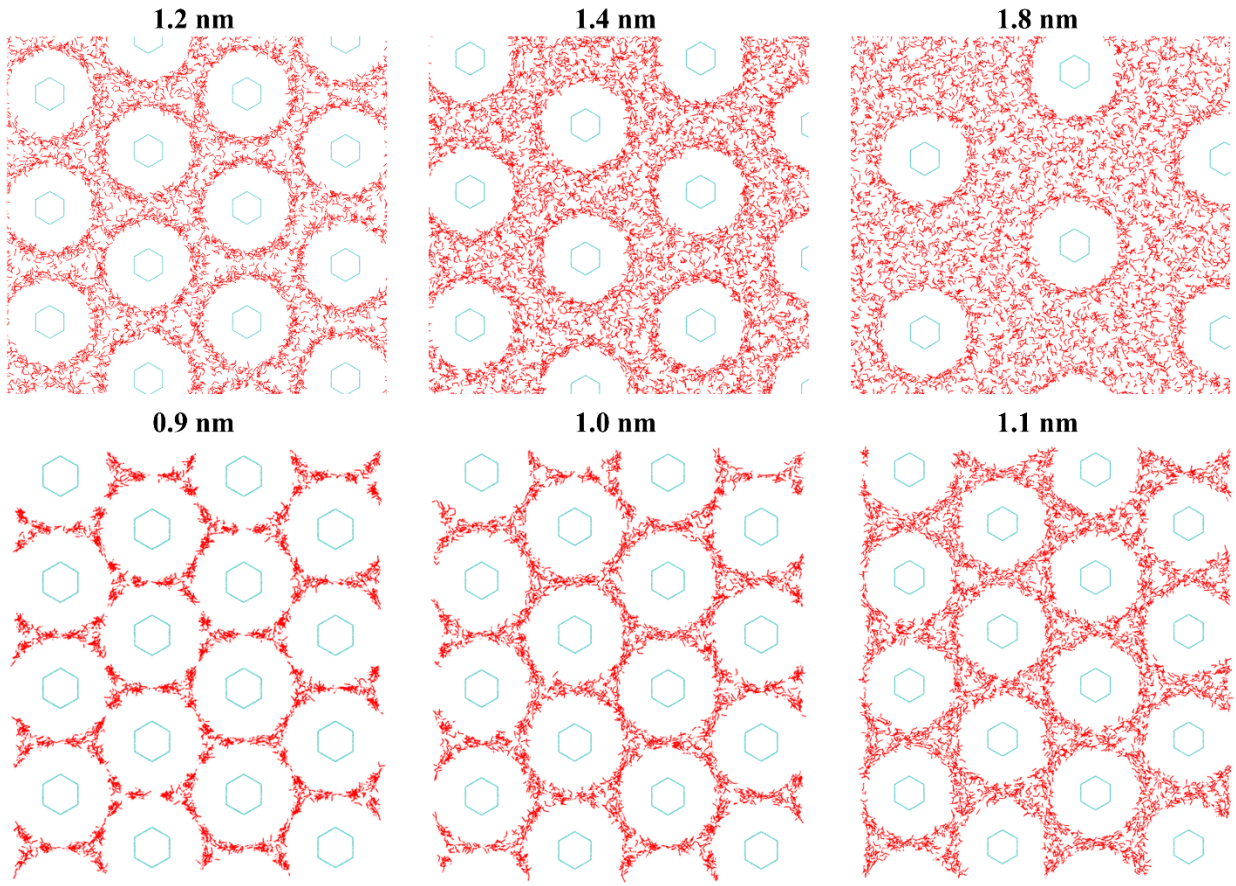

Figure 4.16 Snapshots of confined water in the rigid-rod model with varying rod-rod distances. In the top panels, from left to right, the rod-rod distances are 1.2 nm, 1.4 nm, and 1.8 nm. In the bottom panels, from left to right, the rod-rod distances are 0.9 nm, 1.0 nm, and 1.1 nm.

At rod-rod distances smaller than 1.2 nm, the diffusion coefficient of water continues to decrease. Interestingly, the activation energy of diffusion also starts to decrease slightly with smaller rod-rod distances. The most plausible explanation for this unusual phenomenon is the dehydration of water molecules from the confinement surface. With rod-rod distances smaller than 0.9 nm, the water molecules can no longer enter some of the space between the rigid rods, likely due to the inability of a water molecule to be efficiently stabilized between two carbon walls. At a rod-rod distance of 0.9 nm, we are directly observing partial dehydration (i.e. cavitation) of the confined water molecules. While the dehydration may not be visible at rod-rod distances of 1.0 nm and 1.1 nm, the density of confined water significantly decreased. Measurements and calculations on the density of hydrophobically confined water consistently find that the density of confined water is lower than bulk water and decreases with smaller confinement size.[38-41] This is the reason why in the previous sections we refrained from going below 1.2 nm. We learn from the observations here that confinement can also prompt the formation of structured water in the rigid-rod model. The ordered structure here is different from what we observed inside a CNT due to the differences in the geometries of the confinement matrix. The commonality is that the confined water will adapt to the surface of confinement and form ordered structures specific to the medium.

4.5.2 Hydrogen-Bonding Analysis of Confined Water in the Rigid-Rod Model

Figure 4.17 presents the hydrogen-bonding properties of confined water in the rigid-rod model. Details of the analysis can be found in section 2.3.4. Both the number of hydrogen bonds per molecule, N_{HB}, and the coordination number, N_{CO}, decrease with decreasing confinement size, which is similar to what is observed in the CNT model (section 3.4.2). Again, we observe two

regions from the N_{HB}/N_{CO} plot. At relatively long rod-rod distances, the N_{HB}/N_{CO} ratio of confined water is very similar to that of bulk water, signaling the bulk-like water behavior. At shorter rod-rod distances, the ratio starts to increase more significantly. The increase of N_{HB}/N_{CO} with shorter rod-rod distances indicates that N_{HB} is not decreasing as fast as N_{CO} with increased confinement. We argue that the angular orientation between neighboring molecules might be more suited for the formation of hydrogen bonds at smaller confinement sizes. In other words, the water molecules are becoming more ordered locally with decreasing confinement size. This is consistent with what we have seen in the previous section and in the CNT model.

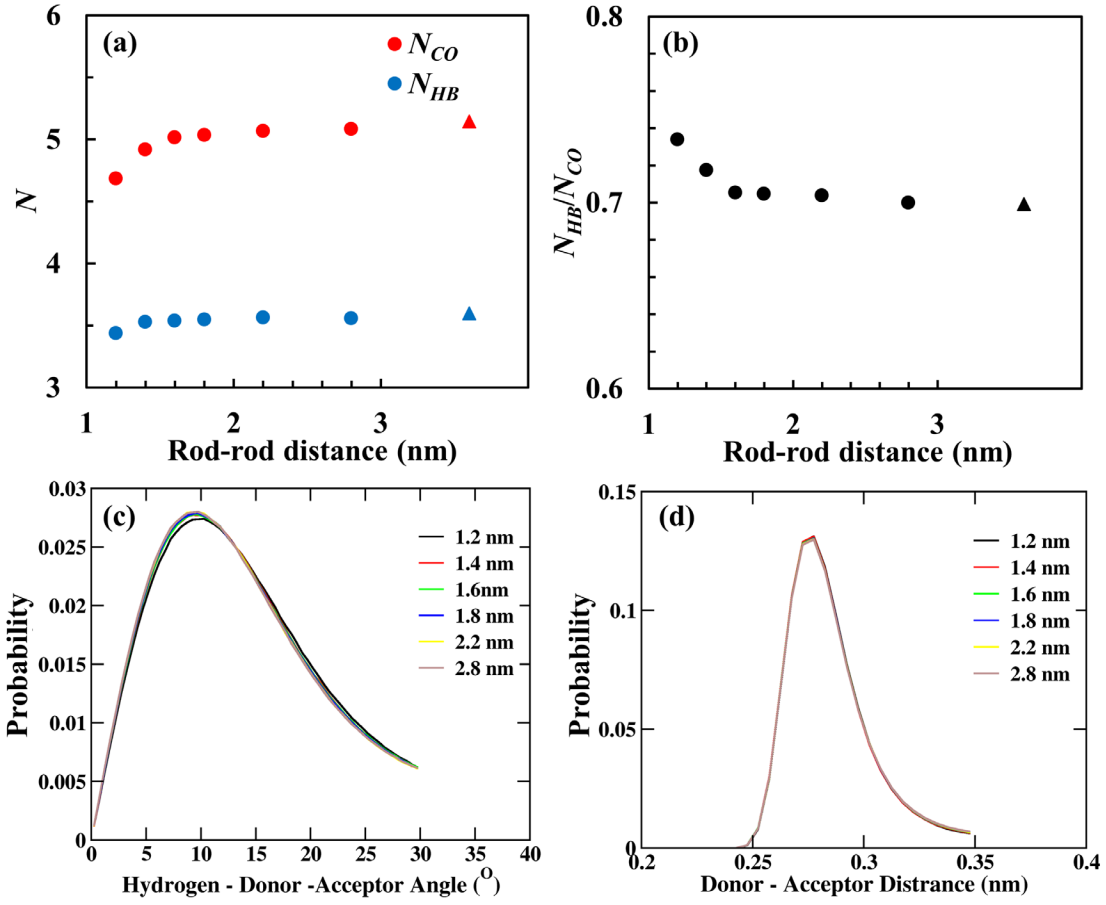

Figure 4.17 Hydrogen-bonding analysis of water molecules within the confinement region of the rigid-rod model. Panel (a) and (b) plot the N_{HB}, N_{CO}, and N_{HB}/N_{CO} as a function of rod-rod distance. Note the triangular symbols represent the values of bulk water. Panel (c) and (d) show the

angle/distance distribution of the hydrogen-bonding network.

4.5.3 Tetrahedricity of Confined Water in the Rigid-Rod Model

Figure 4.18 presents the tetrahedricity of water confined in the rigid-rod model. We calculate the tetrahedricity of all the water molecules based on their location along the direction parallel to the rigid rods. The tetrahedricity of the water reservoirs is close to that of bulk water. The tetrahedricity of the confined water appears to be always smaller than that of bulk and decreases with smaller confinement size. The trend here supports that the tetrahedricity of surface layer water is much lower than that of bulk. With a rod-rod distance of 1.2 nm, most water molecules are within the surface layer of the rigid rods. As the rod-rod distance increases, the increasing amount of bulk-like water shifts the average tetrahedricity closer to that of bulk. This tetrahedricity analysis shows an opposite trend to the hydrogen-bonding analysis in the previous section. While the surface layer water shows a higher tendency to form hydrogen bonds with its immediate neighbors as it becomes increasingly confined, it becomes less likely to form a regular tetrahedron with its four nearest neighbors. We would like to point out the difference between hydrogen-bonding formation and the tetrahedricity here. Hydrogen-bonding analysis, based on its definition, emphasizes the atomic arrangements (including both hydrogen and oxygen atoms) between two neighboring water molecules. Tetrahedricity, however, emphasizes the spatial ordering of only the oxygen atoms of water molecules. The confinement surface here distorts the spatial ordering of the surface layer water but does not compromise the hydrogen bonds between two water molecules. Thus, we see different behavior between hydrogen-bonding and tetrahedricity.

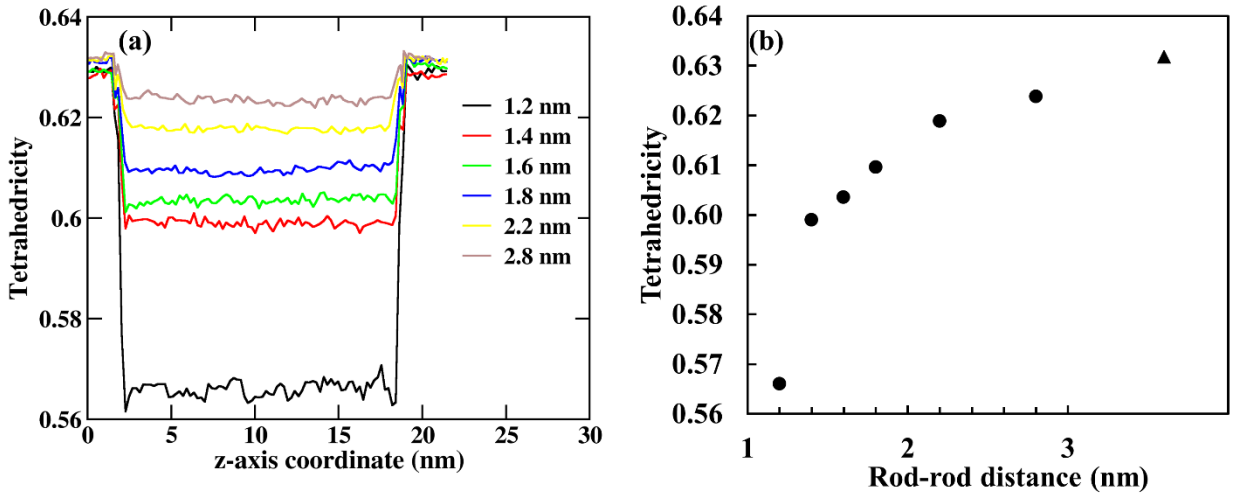

Figure 4.18 Tetrahedricity of water molecules in the rigid-rod model at 300 K. Panel (a) plots tetrahedricity of water as a function of z-axis coordinate. The stepped structure at the extrema is due to the water reservoirs capping the rigid-rod model. The confinement region ranges between 2.5 nm and 18.5 nm along the z-axis. Panel (b) plots the average tetrahedricity of the confinement region as a function of rod-rod distance. The sudden drop of tetrahedricity at a rod-rod distance of 1.2 nm emphasizes the unique water structure at this confinement size.

4.6 Conclusions

A pivotal observation in this work is that hydrophobic confinement retards water motion as long as the confinement size is small enough (around 1 nm). The dynamics of confined water molecules parallels that under an effective lower temperature. We examine this parallel via examination of the residence time of water around water. We show that such residence time increases with either lowering temperature or decreasing confinement size, revealing prolonged associations between water molecules under several hydrophobic confinements, including CNT, parallel plates, and hexagonally packed rigid-rod models. We argue that the associations between water molecules in the confined systems result from the physical restriction of the confinement

medium, which reduces the number of possible pathways for molecular motion. The associated molecular motions correlate with the retarded water dynamics, shown by lower diffusion coefficients and increased diffusive energy barriers. The nanoconfinement effect becomes more prominent at smaller confinement sizes due to an increased fraction of surface water, which is subject to more impact from the confinement surface than the molecules further away.

We also reveal that the residence time of water around water is closely related to water diffusion. The long residence time (τ_l) is inversely proportional to the diffusion coefficient. Remarkably, molecules travel a similar distance within τ_l regardless of temperature, suggesting that molecules would travel a similar distance before they forget their initial positions. The short residence time (τ_s) falls into the timescale of the ballistic regime and relates more with the activation energy of diffusion. Indeed, we show that the activation energy of τ_s has a similar dependence on confinement size as the activation energy of diffusion. Additional insight is provided via examination of the association between water molecules and the confinement surface. Due to the short-range nature of the weak interactions between water molecules and hydrophobic surface, changes to the water dynamics mostly affect molecules in the first surface layer. We also observe that the surface water layer forms a "ring" structure in the rigid-rod model. This ring structure is uniquely more stable when the rod-rod distance is 1.2 nm. The prolonged water associations under confinement persist under modified water-surface interactions and the presence of ions.

Overall, we show that the residence time of water around water is strongly correlated with the diffusion behavior of water molecules, either in bulk or in confinement. The residence time of water around water can therefore serve as an essential tool to study the diffusive behavior of water under various conditions. In summary, we observe increased residence time of water around water

under various kinds of confinement and reveal the origin of retarded water dynamics under hydrophobic confinement.

4.7 References

1. Hou, D. S.; Li, D. K.; Zhao, T. J.; Li, Z. J. Confined Water Dissociation in Disordered Silicate Nanometer-Channels at Elevated Temperatures: Mechanism, Dynamics and Impact on Substrates. *Langmuir* **2016,** *32*, 4153-4168.
2. Gallo, P.; Rovere, M.; Ricci, M. A.; Hartnig, C.; Spohr, E. Evidence of glassy behaviour of water molecules in confined states. *Philos. Mag. B* **1999,** *79*, 1923-1930.
3. Major, R. C.; Houston, J. E.; McGrath, M. J.; Siepmann, J. I.; Zhu, X. Y. Viscous water meniscus under nanoconfinement. *Phys. Rev. Lett.* **2006,** *96*.
4. Youssef, M.; Pellenq, R. J. M.; Yildiz, B. Glassy Nature of Water in an Ultraconfining Disordered Material: The Case of Calcium-Silicate-Hydrate. *J. Am. Chem. Soc.* **2011,** *133*, 2499-2510.
5. Majumder, M.; Chopra, N.; Andrews, R.; Hinds, B. J. Nanoscale hydrodynamics: enhanced flow in carbon nanotubes. *Nature* **2005,** *438*, 44.
6. Holt, J. K.; Park, H. G.; Wang, Y. M.; Stadermann, M.; Artyukhin, A. B.; Grigoropoulos, C. P.; Noy, A.; Bakajin, O. Fast mass transport through sub-2-nanometer carbon nanotubes. *Science* **2006,** *312*, 1034-1037.
7. Zaragoza, A.; Gonzalez, M. A.; Joly, L.; Lopez-Montero, I.; Canales, M. A.; Benavides, A. L.; Valeriani, C. Molecular dynamics study of nanoconfined TIP4P/2005 water: how confinement and temperature affect diffusion and viscosity. *Phys. Chem. Chem. Phys.* **2019,** *21*, 13653-13667.
8. Choudhury, N.; Pettitt, B. M. Dynamics of water trapped between hydrophobic solutes. *J. Phys. Chem. B* **2005,** *109*, 6422-6429.
9. Farimani, A. B.; Aluru, N. R. Spatial Diffusion of Water in Carbon Nanotubes: From Fickian to Ballistic Motion. *J. Phys. Chem. B* **2011,** *115*, 12145-12149.
10. Zhang, R.; Chen, Y.; Troya, D.; Madsen, L. A. Relating Geometric Nanoconfinement and Local Molecular Environment to Diffusion in Ionic Polymer Membranes. *Macromolecules* **2020,** *53*, 3296-3305.
11. Ding, Y.; Hassanali, A. A.; Parrinello, M. Anomalous water diffusion in salt solutions. *PNAS* **2014,** *111*, 3310-3315.
12. Van Der Spoel, D.; Lindahl, E.; Hess, B.; Groenhof, G.; Mark, A. E.; Berendsen, H. J. GROMACS: fast, flexible, and free. *J. Comput. Chem.* **2005,** *26*, 1701-1718.
13. Hess, B.; Kutzner, C.; van der Spoel, D.; Lindahl, E. GROMACS 4: Algorithms for Highly Efficient, Load-Balanced, and Scalable Molecular Simulation. *J. Chem. Theory Comput.* **2008,** *4*, 435-447.
14. Abraham, M. J.; Murtola, T.; Schulz, R.; Pall, S.; Smith, J. C.; Hess, B.; Lindahl, E. GROMACS: High performance molecular simulations through multi-level parallelism from laptops to supercomputers. *SoftwareX* **2015,** *1-2*, 19-25.
15. Yu, Z.; He, Y. D.; Wang, Y.; Madsen, L. A.; Qiao, R. Molecular Structure and Dynamics of Ionic Liquids in a Rigid-Rod Polyanion-Based Ion Gel. *Langmuir* **2017,** *33*, 322-331.
16. Berendsen, H. J. C.; Grigera, J. R.; Straatsma, T. P. The Missing Term in Effective Pair Potentials. *J. Phys. Chem.* **1987,** *91*, 6269-6271.
17. Abascal, J. L. F.; Vega, C. A general purpose model for the condensed phases of water: TIP4P/2005. *J. Chem. Phys.* **2005,** *123*, 234505.
18. Einstein, A. The theory of the Brownian Motion. *Ann. Phys.* **1906,** *19*, 371-381.

19. Brunne, R. M.; Liepinsh, E.; Otting, G.; Wuthrich, K.; van Gunsteren, W. F. Hydration of proteins. A comparison of experimental residence times of water molecules solvating the bovine pancreatic trypsin inhibitor with theoretical model calculations. *J. Mol. Biol.* **1993,** *231*, 1040-1048.
20. Hua, L.; Huang, X.; Zhou, R.; Berne, B. J. Dynamics of water confined in the interdomain region of a multidomain protein. *J. Phys. Chem. B* **2006,** *110*, 3704-3711.
21. Li, T.; Hassanali, A. A.; Singer, S. J. Origin of slow relaxation following photoexcitation of W7 in myoglobin and the dynamics of its hydration layer. *J. Phys. Chem. B* **2008,** *112*, 16121-16134.
22. Bizzarri, A. R.; Cannistraro, S. Molecular Dynamics of Water at the Protein−Solvent Interface. *J. Phys. Chem. B* **2002,** *106*, 6617-6633.
23. Mogurampelly, S.; Keith, J. R.; Ganesan, V. Mechanisms Underlying Ion Transport in Polymerized Ionic Liquids. *J. Am. Chem. Soc.* **2017,** *139*, 9511-9514.
24. Zhao, W.; Leroy, F.; Heggen, B.; Zahn, S.; Kirchner, B.; Balasubramanian, S.; Muller-Plathe, F. Are There Stable Ion-Pairs in Room-Temperature Ionic Liquids? Molecular Dynamics Simulations of 1-n-Butyl-3-methylimidazolium Hexafluorophosphate. *J. Am. Chem. Soc.* **2009,** *131*, 15825-15833.
25. Makarov, V. A.; Andrews, B. K.; Smith, P. E.; Pettitt, B. M. Residence times of water molecules in the hydration sites of myoglobin. *Biophys. J.* **2000,** *79*, 2966-2974.
26. Kidd, B. E.; Forbey, S. J.; Steuber, F. W.; Moore, R. B.; Madsen, L. A. Multiscale Lithium and Counterion Transport in an Electrospun Polymer-Gel Electrolyte. *Macromolecules* **2015,** *48*, 4481-4490.
27. Lingwood, M. D.; Zhang, Z.; Kidd, B. E.; McCreary, K. B.; Hou, J.; Madsen, L. A. Unraveling the local energetics of transport in a polymer ion conductor. *Chem. Commun.* **2013,** *49*, 4283-4285.
28. Kohler, M. H.; Bordin, J. R.; da Silva, L. B.; Barbosa, M. C. Breakdown of the Stokes-Einstein water transport through narrow hydrophobic nanotubes. *Phys. Chem. Chem. Phys.* **2017,** *19*, 12921-12927.
29. Sadeghi, M.; Parsafar, G. A. Density-induced molecular arrangements of water inside carbon nanotubes. *Phys. Chem. Chem. Phys.* **2013,** *15*, 7379-7388.
30. Bauer, T.; Lunkenheimer, P.; Loidl, A. Cooperativity and the Freezing of Molecular Motion at the Glass Transition. *Phys. Rev. Lett.* **2013,** *111*, 225702.
31. Bennemann, C.; Donati, C.; Baschnagel, J.; Glotzer, S. C. Growing range of correlated motion in a polymer melt on cooling towards the glass transition. *Nature* **1999,** *399*, 246-249.
32. Callaghan, P. *Translational Dynamics and Magnetic Resonance: Principles of Pulsed Gradient Spin Echo NMR*. Oxford University Press: New York, 2011.
33. Chandler, D. *Introduction to Modern Statistical Mechanics* Oxford University Press: New York, 1987.
34. Algara-Siller, G.; Lehtinen, O.; Wang, F. C.; Nair, R. R.; Kaiser, U.; Wu, H. A.; Geim, A. K.; Grigorieva, I. V. Square ice in graphene nanocapillaries. *Nature* **2015,** *519*, 443-445.
35. Singla, S.; Anim-Danso, E.; Islam, A. E.; Ngo, Y.; Kim, S. S.; Naik, R. R.; Dhinojwala, A. Insight on Structure of Water and Ice Next to Graphene Using Surface-Sensitive Spectroscopy. *Acs Nano* **2017,** *11*, 4899-4906.
36. Mashl, R. J.; Joseph, S.; Aluru, N. R.; Jakobsson, E. Anomalously immobilized water: A new water phase induced by confinement in nanotubes. *Nano Lett.* **2003,** *3*, 589-592.
37. Nguyen, M.; Rick, S. W. The influence of polarizability and charge transfer on specific ion effects in the dynamics of aqueous salt solutions. *J. Chem. Phys.* **2018,** *148*, 222803.
38. Knight, A. W.; Kalugin, N. G.; Coker, E.; Ilgen, A. G. Water properties under nano-scale confinement. *Sci. Rep.* **2019,** *9*, 8246.
39. Wang, G. J.; Hadjiconstantinou, N. G. Why are fluid densities so low in carbon nanotubes? *Phys. Fluids* **2015,** *27*, 052006.
40. Kohler, M. H.; da Silva, L. B. Size effects and the role of density on the viscosity of water confined in carbon nanotubes. *Chem. Phys. Lett.* **2016,** *645*, 38-41.
41. Doshi, D. A.; Watkins, E. B.; Israelachvili, J. N.; Majewski, J. Reduced water density at hydrophobic surfaces: Effect of dissolved gases. *PNAS* **2005,** *102*, 9458-9462.

Chapter 5 Observation of Concentration-Temperature Superposition in the Water Dynamics Salt Solutions: The Effect of Ions

This chapter is under preparation for submission to Journal of Physical Chemistry B with authors Rui Zhang, Louis Madsen, and Diego Troya.

5.1 Introduction

In the previous two chapters, we focused on the effect of geometric confinement on water dynamics. In addition to geometric confinement, the interactions between water molecules and the confining surface also affect the dynamics of confined water.[1-5] In ionomer membranes, mobile species are under membrane confinement with fixed ionic head groups and counterions. In this chapter and the next, we will delve deeper into the effects of water-ion interactions.

In previous studies, infrared spectroscopy[6] has shown that the ions alter the bond-stretching dynamics of neighboring water molecules. Depending on the type of ions, experimental results reveal both enhanced and retarded water dynamics.[7] Through MD simulations, Yethiraj et al.[8-9] interpret the effects of ions from two perspectives: disruption of the hydrogen-bonding network and interactions with neighboring water molecules. In addition, polarization[10] and charge transfer in aqueous solutions[11-12] contribute to ion-specific water dynamics in aqueous solutions. Understanding the dynamics of water under the presence of ions adds valuable information to the knowledge gained in the previous two chapters. In this chapter, we start with the dynamics of bulk-state water under the presence of ions, in other words, water in aqueous solutions. Remarkably, we notice a temperature-concentration superposition behavior from Arrhenius diffusion plots of water molecules and ions in the solutions. Researchers have reported the temperature-concentration superposition on various properties concerning polymeric materials.[13-17] However,

observation of this superposition behavior in the diffusion of bulk solutions is unprecedented. Inspired by the concept of residence time in chapter 4, we again calculate the residence time of water around water in the aqueous solutions. We observe an increased residence time when either increasing the concentrations or decreasing the temperatures of lithium triflate solutions. The temperature-concentration superposition points to a unique perspective: the effect of ions on water dynamics may be similar to the effect of changing temperature.

5.2 Experimental and Computational Methods

5.2.1 NMR Diffusometry Experiments

Lithium triflate (LiOTf) was purchased from Strem Chemicals (USA) with 99% purity and used as received to make aqueous solutions. Lithium triflate is highly soluble in water, with a solubility limit occurring around $\lambda = 3$, so it provides a wide range of data to be comparable to simulations. Details of sample preparation are included in section 3.2.1. NMR measurements are conducted in the same way as described in section 3.2.2. In this chapter, we have expanded the temperature range slightly to better compare with simulations. For calibration of temperature lower than 300 K, pure methanol is used. Depending on the chemical shift difference (δ) between the two peaks of methanol, three different equations are used for temperature calibration

$$T_{sample} = -108.6 * \delta + 468.1 \quad (if\ \delta \leq 1.824\ ppm) \tag{5.1}$$

$$T_{sample} = -124.98 * \delta + 498.4 \quad (if\ 1.824\ ppm < \delta < 2.1474\ ppm) \tag{5.2}$$

$$T_{sample} = -142.8 * \delta + 537.4 \quad (if\ \delta \geq 2.1474\ ppm) \tag{5.3}$$

where T_{real} stands for the temperature of pure methanol. In all the LiOTf solution samples, capillary tubes with 0.5-mm inner diameter are put into the solutions inside the NMR tubes to alleviate convection at non-ambient temperatures.

5.2.2 Simulation Details

All simulations were conducted with the GROMACS 5.0.5 package. Aqueous lithium triflate solutions were modeled with the TIP4P/2005 rigid four-site water model.[18] Detailed force-field parameters can be found in Appendix A. With the TIP4P/2005 water model, 400 LiOTf ion pairs are used with a varying number of water molecules to create an H_2O/Li^+ molar ratio (λ) ranging from 2 to 17. Details of the simulation parameters can be found in section 3.2.4. Comparing to previous simulations in chapter 3, a much wider temperature range is used here. Simulations are conducted from 280 K to 420 K for the solution at $\lambda = 3$, 240 K to 380 K for the solution at $\lambda = 6$, and 220 K to 350 K for the solution at $\lambda = 12$. We must mention that the solutions in all the simulations remain in the liquid state at any temperatures since the force fields do not lead to phase transitions in the simulation timescale.

5.3 Temperature-Concentration Superposition (TCS) in Bulk Solutions

5.3.1 TCS behaviors of Water and Ion Diffusion in MD Simulations

Inspired by the parallel between confinement and temperature in chapter 4.3.2, we shift the Arrhenius plots of LiOTf solutions at varying concentrations to the same reference plot. **Figure 5.1** summarizes the original data sets and shifted data sets. **Figure 5.1a** plots the wide temperature diffusion coefficients of solutions with $\lambda = 3$, 6, and 12. In **Figure 5.1b**, we shift the plots in **Figure 5.1a** horizontally to the reference $\lambda = 6$ plot. We observe a nearly perfect match between different plots after shifting. In **Figure 5.1c**, we construct a master curve similar to the time-temperature superposition (TTS). We put together the Arrhenius plots of water in LiOTf solutions of all concentrations from 300 K to 340 K. We then shift the Arrhenius plots horizontally to the reference concentration at $\lambda = 6$. Over several orders of magnitude of diffusion coefficients, we

observe a clean fit between the master curve and the wide temperature reference plot. Based on the previous observations, the TCS principle in diffusion is instrumental in predicting diffusion coefficients of water or ions at a non tabulated concentration or temperature. In addition to water molecules, we observe the same behavior from the Arrhenius plots of lithium ions. **Figure 5.2**summarizes the TCS behavior of the lithium ions in LiOTf solutions. Arrhenius plots of both lithium ions and water molecules at any concentration match the wide-temperature coefficients after shifting.

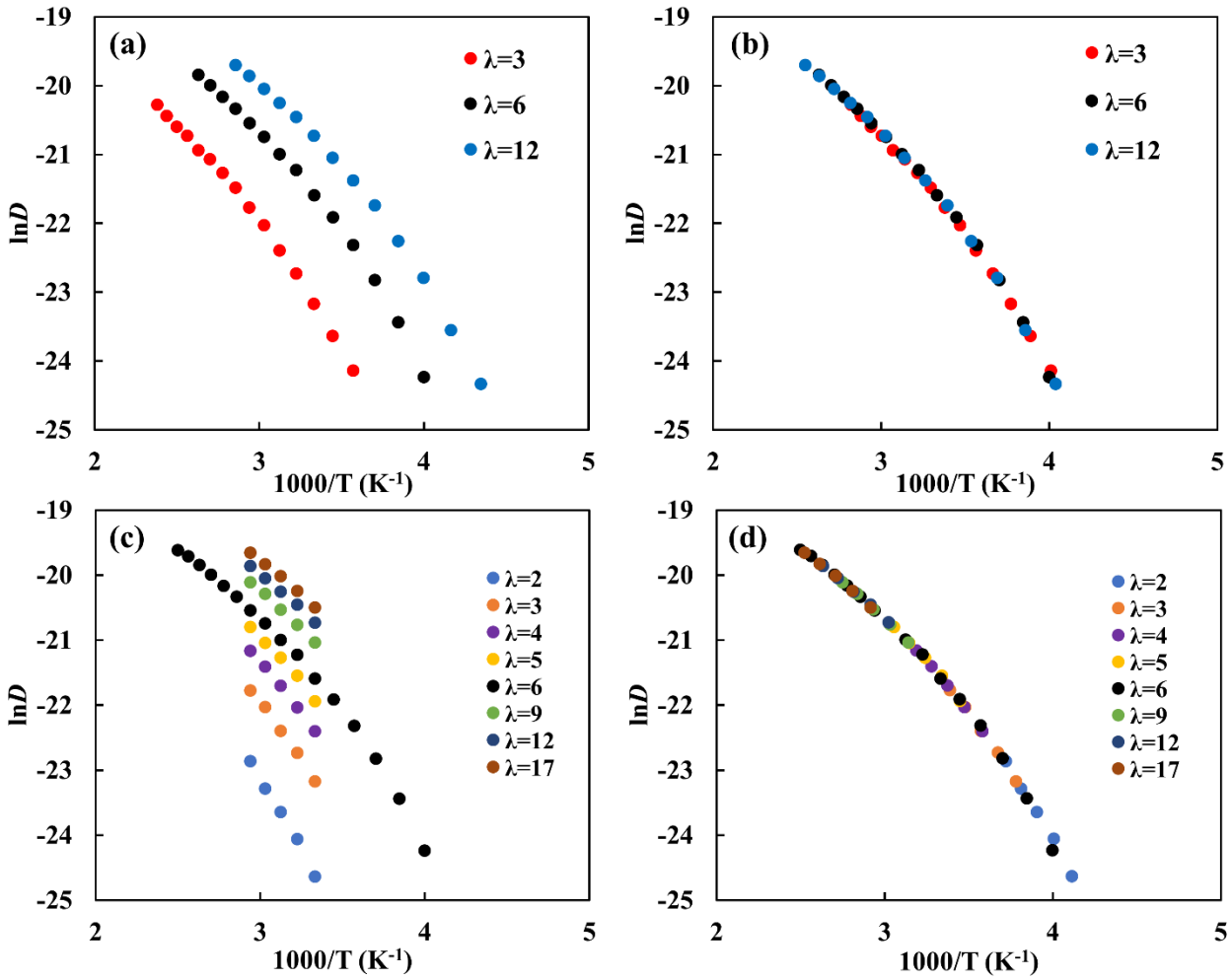

Figure 5.1 TCS behavior of TIP4P/2005 water molecules in the LiOTf solutions. Panel (a) presents wide temperature range Arrhenius plots of water diffusion coefficients in $\lambda = 6$ solution

(from 240 K to 380 K), $\lambda = 3$ solution (from 280 K to 420 K), and $\lambda = 12$ solutions (from 220 K to 350 K). In panel (b), the Arrhenius plots of $\lambda = 3$ and $\lambda = 12$ solutions are shifted horizontally to match with the Arrhenius plot of $\lambda = 6$ solution. Panel (c) shows both wide temperature range Arrhenius plot of $\lambda = 6$ solution and narrow temperature range (300 K to 340 K) Arrhenius plots of all other solutions. In panel (d), we construct a master curve by horizontally shifting the narrow temperature range Arrhenius plots to the reference Arrhenius plot at $\lambda = 6$. The master curve overlaps nicely with the wide temperature diffusion data.

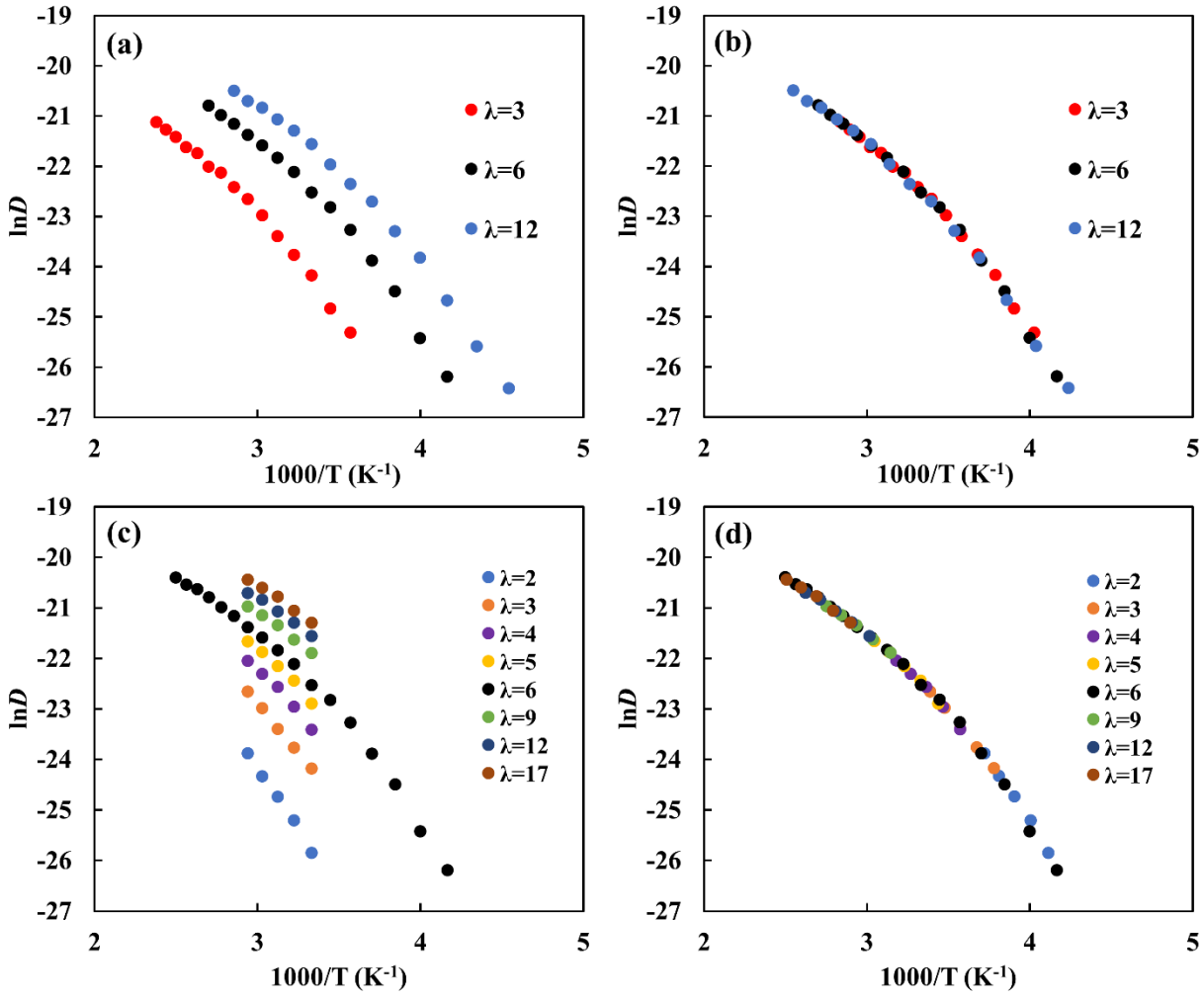

Figure 5.2 TCS behavior of lithium ions in LiOTf solutions. The temperature range of data points and the construction of master curves are the same as in **Figure 5.1** for water. We observe almost

the same behavior with lithium ions as with water molecules.

5.3.2 Implications of TCS on the Activation Energy

By definition, the slope of an Arrhenius diffusion plot is proportional to the activation energy of diffusion. Usually, we observe the Arrhenius plots to be nonlinear at a broad-temperature range. Thus, the activation energy is temperature-dependent and is proportional to the tangent slope of the Arrhenius plot. When horizontally shifting the Arrhenius plots, the tangent slope remains unchanged. Thus, the TCS behavior means that the activation energy of diffusion is similar between solutions at different concentrations when the diffusion coefficients are similar.

Figure 5.3a compares the E_a of water diffusion in LiOTf solutions with $\lambda = 3$, 6, and 12. To enable calculation of activation energy at any temperatures, we fit the diffusion data with Vogel-Fulcher-Tamman (VFT) equation[19]

$$D = D_0 e^{-(\frac{A}{T-T_0})} \tag{5.4}$$

where D is the diffusion coefficient, and D_0, A, T_0 are the fitting parameters. We can extract the activation energy in Arrhenius definition from the VFT equation as

$$E_a = -\frac{\partial(lnD)}{\partial(1/RT)} = BRT^2/(T-T_0)^2 \tag{5.5}$$

Based on the concentration-temperature superposition, we should also be able to shift E_a plots and obtain a similar overlap between different concentrations. And indeed, we observe in **Figure 5.3b** that the E_a plots from the three different concentrations overlap well with each other after horizontal shifting. Similarly, we present the same plots for E_a of lithium ions in **Figures 5.3d,e,f**. The trends in the lithium-ion E_a are very similar to those in the water E_a, suggesting a possible coordinated motion of water molecules and ions in the aqueous solutions.

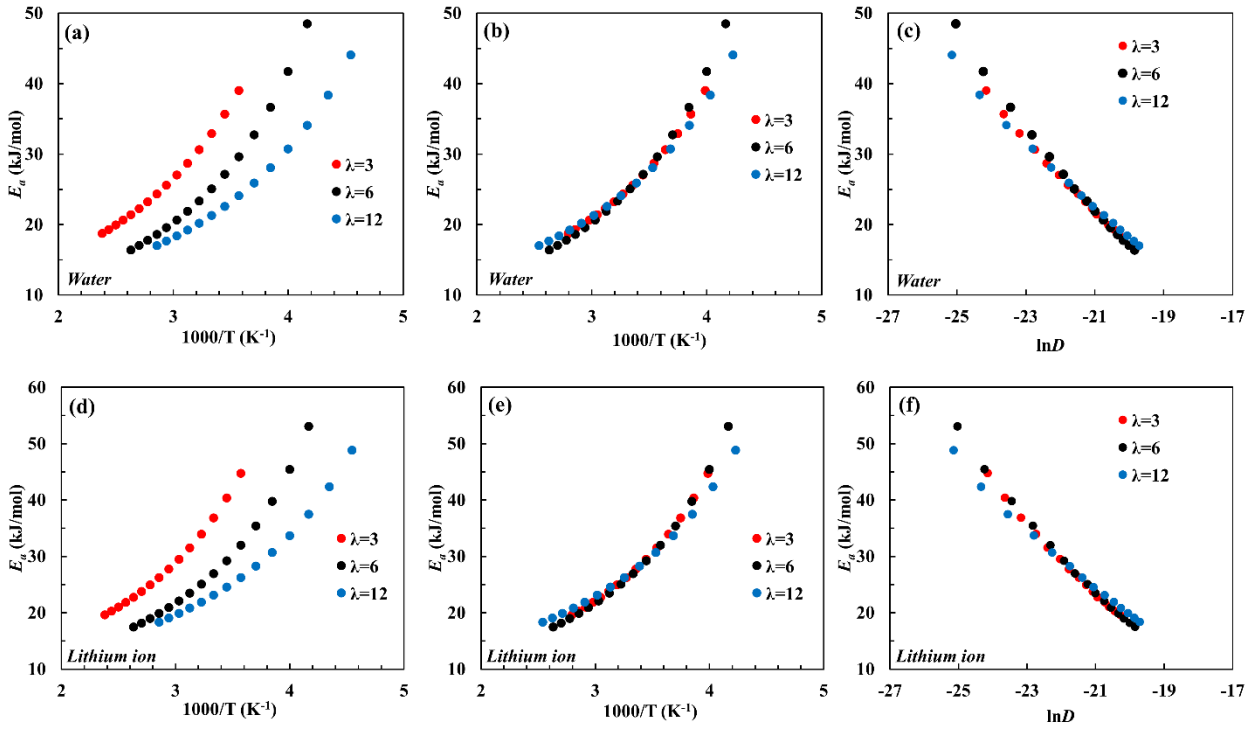

Figure 5.3 VFT activation energy plots of water molecules and lithium ions as a function of inverse temperature and diffusion coefficient. Panel (a) plots wide temperature range E_a of water diffusion for $\lambda = 6$ (from 240 K to 380 K), $\lambda = 3$ (from 280 K to 420 K), and $\lambda = 12$ (from 220 K to 350 K) solutions as a function of inverse temperature. In panel (b), E_a plots are shifted to overlap. Panel (c) plots E_a of water as a function of the natural log of D of water. The matching of E_a is generally better at higher temperatures. Panels (d), (e), and (f) show the same kind of plots as in panels (a), (b), and (c) and are based on the VFT fit of lithium-ion diffusion coefficients.

We also plot E_a as a function of diffusion coefficients in **Figure 5.3c**. As expected, E_a of solutions at different concentrations also match each other when the diffusion coefficients are similar. The deviations happen at relatively low diffusion coefficients, which corresponds to the low-temperature regime. In order to reach the same E_a at the same diffusion coefficients, the front factor D_0 needs to compensate for the change in temperatures. Here we look at two different

concentrations as an example. The Arrhenius equations in solutions of two different concentrations would be

$$lnD_1 = lnD_{0,1} - \frac{E_{a,1}}{RT_1} \tag{5.6}$$

$$lnD_2 = lnD_{0,2} - \frac{E_{a,2}}{RT_2} \tag{5.7}$$

where the subscript 1 and 2 represent the two solutions with different concentrations. In the context of TCS, $E_{a,1} = E_{a,2}$ when $D_1 = D_2$. Assuming we are at the temperatures where $D_1 = D_2$ and $E_{a,1} = E_{a,2} = E_a$, we have

$$lnD_{0,1} - \frac{E_a}{RT_1} = lnD_{0,2} - \frac{E_a}{RT_2} \tag{5.8}$$

$$lnD_{0,1} - lnD_{0,2} = \frac{E_a}{RT_1} - \frac{E_a}{RT_2} = \frac{E_a}{R}\left(\frac{1}{T_1} - \frac{1}{T_2}\right) = \frac{E_a}{R}\delta_{rt} \tag{5.9}$$

Note $T_1 \neq T_2$ and $D_{0,1} \neq D_{0,2}$ here. Note also $\frac{1}{T_1} - \frac{1}{T_2}$ is the offset of reciprocal temperature (refer to section 5.3.3 below) and is a constant. Thus, equation 5.9 states that $lnD_{0,1} - lnD_{0,2}$ is directly proportional to E_a.

We notice that equation 5.9 fits into the theory of compensation effect, which proposes a linear relationship between E_a and the natural log of the preexponential factor[20]

$$lnD_0 = \mathcal{A} - \frac{E_a}{RT_c} \tag{5.10}$$

where $\mathcal{A}$ and T_c are fitting parameters. The compensation effect exists in the rates of various processes, including diffusion of gas in polymers,[21-22] nucleation processes,[23] and ionic conductivity.[24] To date, there is no consensus on the physical origin of the compensation effect. One plausible explanation is the enthalpy-entropy compensation, which relates the preexponential factor and activation energy to the entropy and enthalpy, respectively.[25] Another possible

explanation of the compensation effect is purely mathematical. When E_a increases, the slope of the Arrhenius plot will increase, thus leading to the increase in the intercept, lnD_0. For molecular diffusion, the compensation effect exists in two different scenarios: first, it can be observed in the same system with the same diffusing species;[22, 26] second, it also exists with the same species diffusing in different systems.[27-28] The first scenario builds upon the fact that activation energy is temperature-dependent, and shows that when performing Arrhenius fits at different temperature ranges, one obtains a series of different E_a and D_0 that follow the compensation rule. The second scenario connects activation energy and preexponential factor between different systems at the same temperature range. We consider both scenarios with the LiOTf solutions and show the compensation effects in **Figure 5.4**.

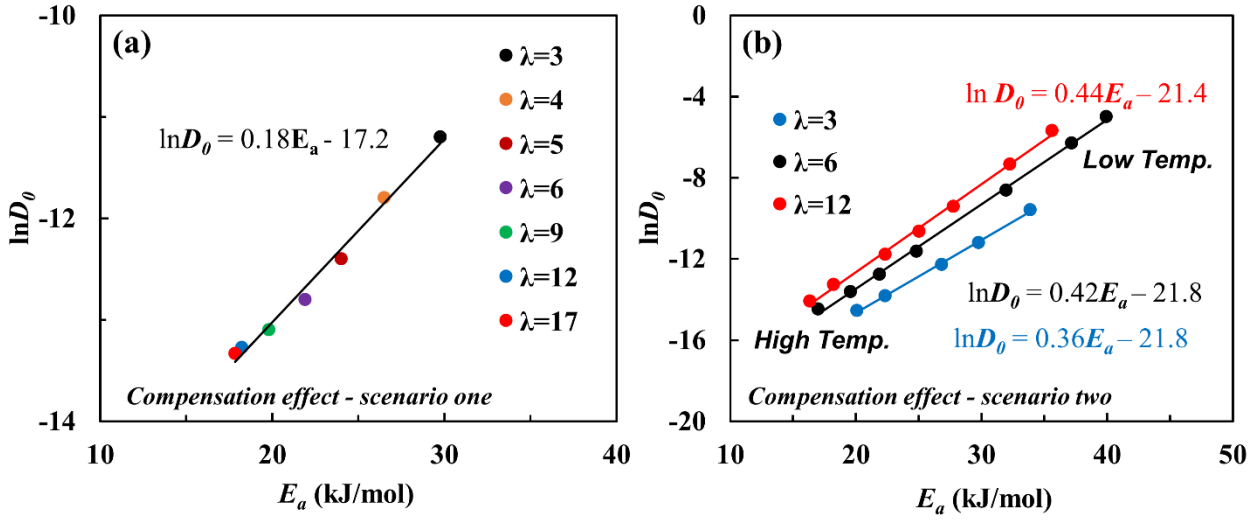

Figure 5.4 Plots of lnD_0 vs. E_a extracted from simulation results of LiOTf solutions. Panel (a) plots lnD_0 vs. E_a in solutions of different concentrations under the same temperature range (300K – 340 K). Panel (b) plots lnD_0 vs. E_a in solutions of the same concentrations under different fitting temperature ranges. We observe an apparent compensation effect in panel (b). The linear relation between lnD_0 and E_a also stands in panel (a). However, panel (a) appears to show two regimes ($\lambda \geq 6$ and $\lambda < 6$) where the slopes of lnD_0 vs. E_a are different.

To go from the compensation effect (Equation 5.10) to the prediction of temperature-concentration superposition (Equation 5.9), the fitting parameter $\mathcal{A}$ in **Figure 5.4b** needs to be similar between solutions at different concentrations. When the fitting parameter $\mathcal{A}$ is the same, the differences between lnD_0 at two different concentrations is proportional to E_a, matching the expectation from equation 5.9. From the fits in **Figure 5.4b**, we see $\mathcal{A}$ is indeed similar across different concentrations. Note the compensation effect does not necessarily explain the TCS behavior.

The previous discussions show that the compensation effect leads to the same conclusion as the TCS. The TCS remains an observation in our current state of study, but, as we will present in the next few sections, the TCS shows highly similar behavior to the time-temperature superposition and is worth further investigation.

5.3.3 The Offset of Reciprocal Temperature and a WLF-Type Fitting Equation

Inspired by the time-temperature superposition (TTS), we present the temperature-concentration superposition as

$$D\left(\lambda_r, \frac{1}{T_0} + \delta_{rt}\right) = D(\lambda_1, \frac{1}{T_1}) \tag{5.11}$$

where $D\left(\lambda_r, \frac{1}{T_0}\right)$ is the diffusion coefficient of the mobile species at a temperature T_0 and at the reference concentration λ_r, $D(\lambda_1, \frac{1}{T_1})$ is the diffusion coefficient of the mobile species at a temperature of T_1 and a concentration of λ_1, δ_{rt} (the offset of inverse temperature) is the horizontally shifting of diffusion data between solutions at concentrations of λ_1 and λ_r, and T_1 is the temperature at which the solution at a concentration of λ_1 would have the same diffusion coefficient as the solution at the reference concentration and a temperature T_0. **Table 5.1** lists δ_{rt}

of LiOTf solutions at $\lambda_r = 3$ reference concentration. Note that changing reference concentration will give a different set of δ_{rt}.

Table 5.1 Extracted δ_{rt} from Arrhenius plots of water diffusion in the simulations LiOTf solutions. Reference concentration $\lambda_r = 3$

λ_1	3	4	5	6	9	12	17
δ_{rt} ($\times 10^{-4}$ K^{-1})	0	1.99	3.32	4.49	6.40	7.57	8.65

The Williams-Landel-Ferry (WLF) equation in TTS describes the relationship between offset and temperatures. Similarly, drawing inspiration from the WLF formalism, we construct a fitting equation for δ_{rt} in the TCS

$$\delta_{rt} = -\frac{C_1 * (\lambda_1 - \lambda_r)}{C_2 + (\lambda_1 - \lambda_r)} \tag{5.12}$$

where C_1 and C_2 are fitting parameters. Interestingly, the extracted δ_{rt} from the simulation data fits well with equation 5.12 (example fitting curves in **Figure 5.5**), which suggests that the TCS phenomenon may have some similaries to the TTS behaivor. The exact relations betwwn TCS and TTS requires further exploration.

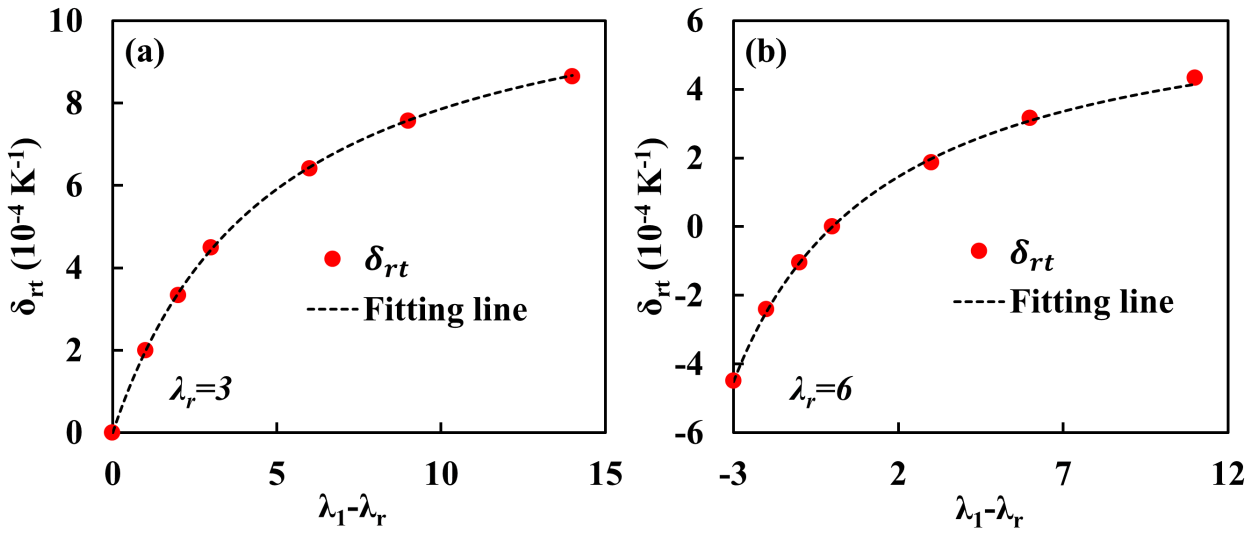

Figure 5.5 Example plots of δ_{rt} as a function of $\lambda_1 - \lambda_r$. The red circles represent the offsets at respective $\lambda_1 - \lambda_r$ values. The dash lines represent the fitting curves using equation 5.12. Plot (a) utilizes a reference concentration $\lambda_r = 3$ while plot (b) utilizes a reference concentration $\lambda_r = 6$. We observe a nice match between fitting lines and the actual value of δ_{rt}, suggesting that δ_{rt} does follow the proposed WLF-type equation. Note that these plots only shift horizontally and vertically while maintaining the shape by changing reference concentrations.

Figure 5.5 shows the example fitting curves for the offsets generated from both water diffusion and lithium-ion diffusion data, while **Table 5.2** collects the fitting parameters at different reference concentrations (λ_r). We would like to mention that δ_{rt} is almost the same for both water and lithium ions. Consequently, the fitting parameters generated on water diffusion data are similar to those generated with lithium-ion diffusion data. With these fitting parameters, it is viable to calculate δ_{rt} and predict diffusion coefficients for non-tabulated concentrations. Furthermore, the correspondence between water and lithium-ion suggests highly correlated motion between them in solution.

Table 5.2 Fitting parameters, C_1 and C_2 in equation 5.12, with varying reference concentration λ_r generated from both water and lithium-ion diffusion data

	Water		**Lithium ion**	
λ_r	C_1 (x10^{-4} K^{-1})	C_2	C_1 (x10^{-4} K^{-1})	C_2
3	-11.7	4.90	-11.8	4.95
4	-9.65	5.88	-9.71	5.96
5	-8.52	7.12	-8.41	6.97
6	-7.04	7.68	-7.35	7.96
9	-5.29	11.0	-5.68	11.5

12	-4.13	13.9	-4.27	14.1
17	-3.03	18.9	-3.24	19.2

We notice from the literature[29] that, in the context of TTS, the fitting parameters C_1 and C_2 would follow the relations

$$C_1 C_2 = C_1' C_2' \tag{5.13}$$

$$C_2 = T_r + b \tag{5.14}$$

where C_1' and C_2' are the fitting parameters with a different reference temperature from T_r, and b is a fitting parameter. Equations 5.13 and 5.14 state that the product of C_1 and C_2 is a constant regardless of the reference temperature and that C_2 has a linear relationship with the reference temperature. Motivated by these relationships, we can construct similar relations for the fitting parameters in the context of TCS

$$C_1 C_2 = C_1' C_2' \tag{5.15}$$

$$C_2 = \lambda_r + b \tag{5.16}$$

In **Figure 5.6**, we plot $C_1 C_2$ and C_2 as a function of the reference concentration λ_r, and we do observe that they generally obey equations 5.15 and 5.16. These observations suggest that the TCS behaves similarly to the TTS. Future work into the parallel between TCS and TTS may help reveal the physical origin of TCS in aqueous solutions.

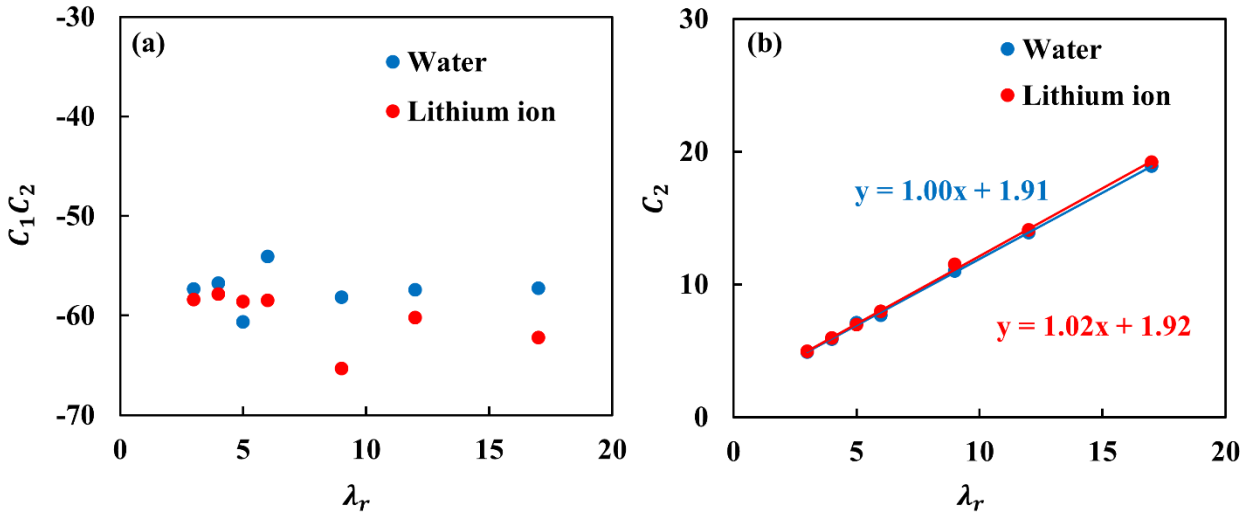

Figure 5.6 Plots of C_1C_2 and C_2, obtained from both water and lithium-ion diffusion data, as a function of the reference concentration λ_r. As observed from panel (a), the product of C_1C_2 stays consistent with varying λ_r, matching equation 5.15. Panel (b) plots the fitting parameter C_2 as a function of λ_r. The equations stand for the linear regression results of C_2 *vs.* λ_r, and again, the results match with equation 5.16.

5.3.4 Residence Time of Water around Water and Li^+ in LiOTf Solutions

The parallel between concentration and temperature implies that changing the ionic concentration may have a similar effect as varying temperature. Thus, we again calculate the residence time of water to understand the associations between water molecules in the LiOTf solutions. The methodology to calculate the residence time here is the same as described in section 4.2.2. With varying concentrations, the radial distribution functions (RDFs) of water around water show the first minimum at considerably different locations (**Figure 5.11**). It is thus more challenging to give a precise definition of cut-off distance from RDFs. In chapter 4, the calculation of residence time for bulk and confined water utilized a cut-off distance of 0.33 nm. To be consistent, we apply the same cut-off distance in calculating the residence time of water around

water in the LiOTf solutions. In calculations of the residence time of water around lithium ion, we use a cut-off distance of 0.3 nm based on the respective RDFs (**Figure 5.11b**). **Figures 5.7a,b** plot the τ_l and τ_s of water around water in the LiOTf solutions while **Figures 5.7e,f** present the τ_l and τ_s of water around lithium ions. The residence time of water around lithium ion is more than ten times longer than the residence time of water around water, consistent with literature values.[30] **Figures 5.7c,d** show the correlation between $1/\tau_l$ of water around water and the diffusion coefficient of water molecules. We again observe a linear relationship, suggesting the correlation between τ_l and diffusion coefficient still stands in an ionic aqueous solution.

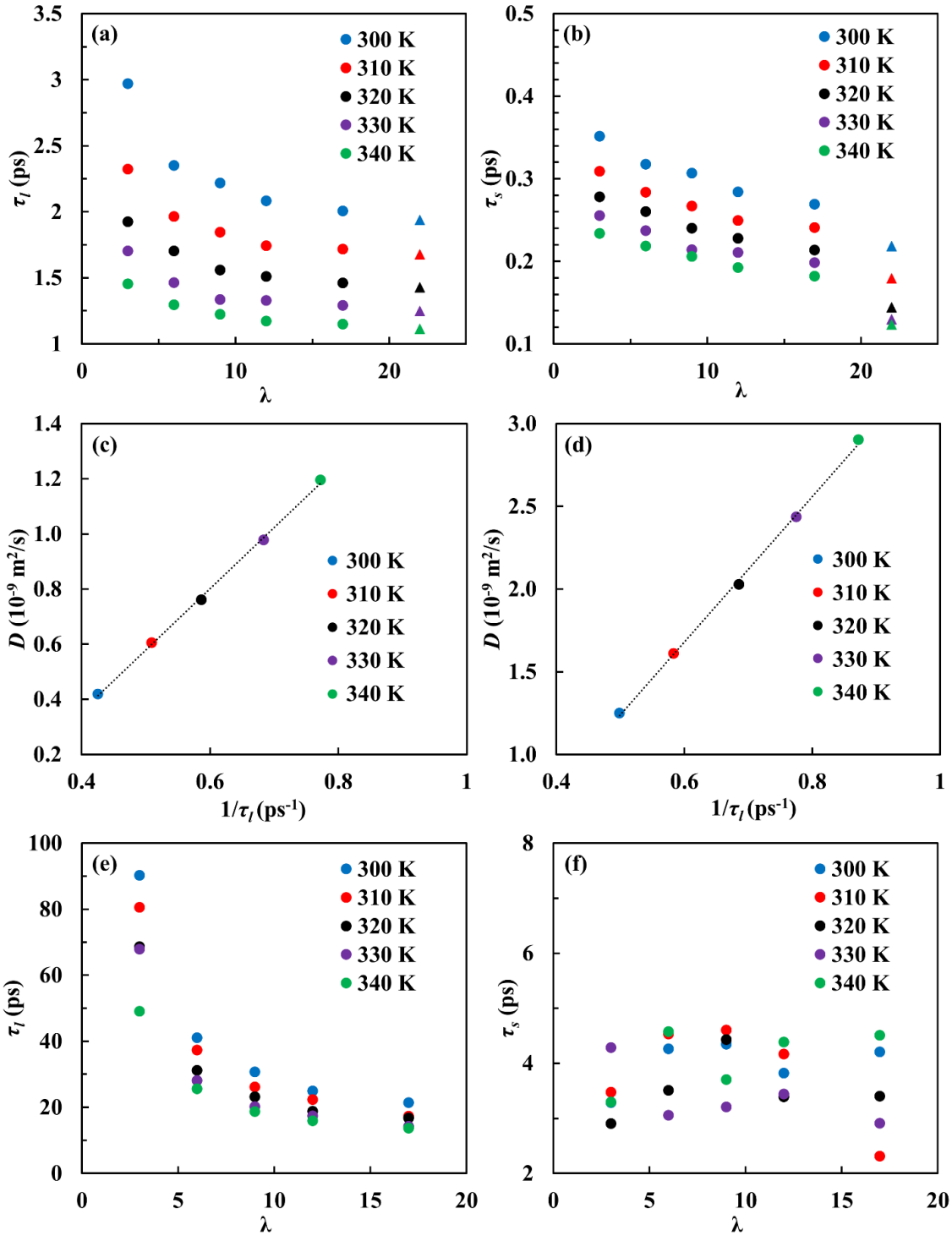

Figure 5.7 Panels (a) and (b) show the residence times (τ_l and τ_s) of water around water in LiOTf solutions as a function of H_2O/Li^+ molar ratio (λ). The errors in τ_s and τ_l of water are estimated to be $\pm$0.05 ps. The triangles represent residence times of bulk water. Panel (c) plots the diffusion

coefficients of water molecules in the $\lambda_1 = 3$ solution as a function of $1/\tau_l$ while panel (d) plots the diffusion coefficients of water molecules in the $\lambda_1 = 12$ solution as a function of $1/\tau_l$. We observe the linear relation between D and $1/\tau_l$, similar to the observed relationship in chapter 4 for nanoconfined water. Panels (e) and (f) show the τ_l and τ_s of water around lithium ions. Note that the uncertainty in the residence time of water around lithium ion is much larger than for water around water because the two-component exponential decay function does not fit well with residence time correlation function of water around lithium ions.

Based on our understanding of TCS, we anticipate that the presence of ions on water dynamics may have a similar effect to changing temperature. Both lowering temperature and increasing ion concentration would lengthen the associations between water molecules. However, we acknowledge that the mechanisms behind the two processes may be different. With lowered temperatures, the thermal energy of the water molecules becomes lower, which makes it more difficult for a water molecule to escape the shell formed by its neighboring molecules. With the presence of ions, water molecules neighboring the same ions would remain associated with the ions for a prolonged period due to increased intermolecular interactions. A further question would be how would the associations between water molecules that are not in the vicinity of ions change? This question is difficult to answer in this chapter for a few reasons. First, the concentrations of the LiOTf solutions here are high, which means few water molecules are not close to any ions. Second, there are fast exchanges between water molecules solvating the ions and water molecules that are not, and deconvoluting these two types of water molecules is difficult. In the next chapter, by restricting the mobility of ions/charges, we will explore further how ions change the dynamics of confined water molecules.

5.3.5 TCS in Diffusion Coefficients Measured by NMR

So far, we have presented TCS behavior in MD simulations. In this section, we present TCS based on the diffusion data collected from NMR diffusometry. Collecting wide temperature range diffusion data through NMR diffusometry is more challenging than with MD simulations. At both low and high temperatures, the convection in the liquid sample may bring significant errors to the diffusion coefficients.[31] Thus, the temperature range accessible by NMR experiments is much narrower than in MD. In **Figure 5.8a**, we present the Arrhenius plots of water diffusion in LiOTf solutions of varying λ. (We additionally measured lithium-ion diffusion in narrow temperature ranges and observed a similar behavior as that of water diffusion.) The $\lambda = 6$ data series carries a temperature range from 273 K to 330K. We shift the data at other concentrations horizontally using the $\lambda = 6$ data series as the reference to create a master curve in **Figure 5.8b**. Due to the narrow temperature range, it becomes difficult to know if the master curve would match the wide temperature range diffusion data at individual concentrations, but in the measured temperature range, the master curve fits impressively well all measurements.

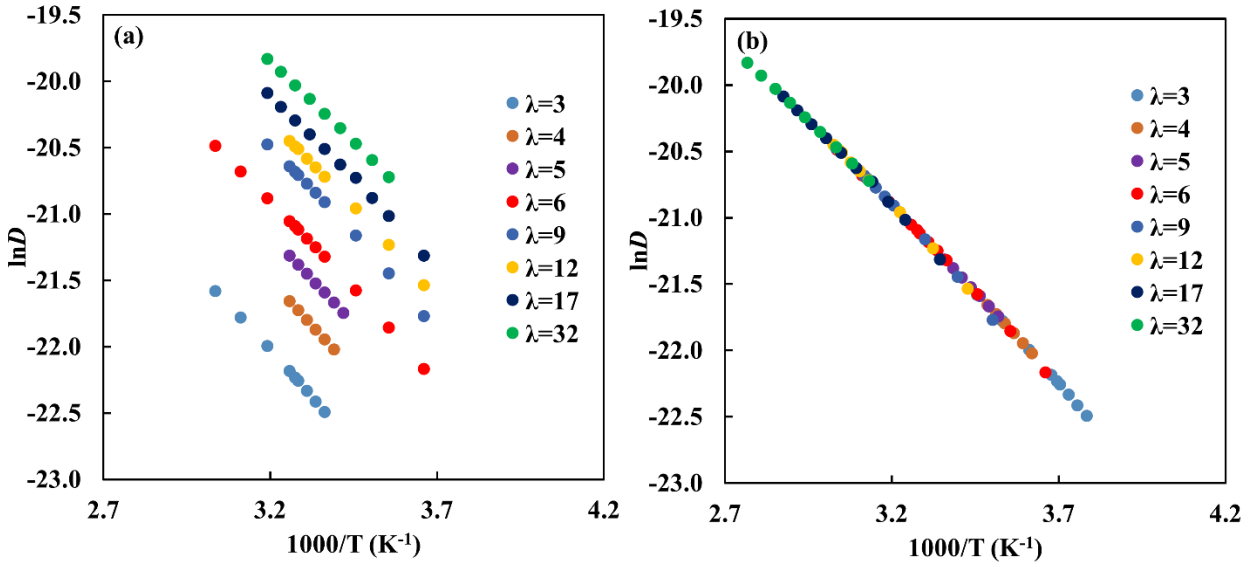

Figure 5.8 TCS behavior of water diffusion in LiOTf solutions measured from NMR diffusometry. Panel (a) corresponds to original Arrhenius plots of water diffusion coefficients at varying concentrations. In panel (b), we shift all the Arrhenius plots to match the reference plot at $\lambda = 6$.

An important trend to notice here is that the slopes of these plots, which are directly proportional to activation energies, are not as concentration-dependent as seen in simulations (activation energy of water in these solutions can be found in **Figure 3.2**). Thus, while the data sets appear to match each other after shifting, it may merely result from similar slopes. We also notice that the low-temperature diffusion coefficient, such as $\lambda = 6$ and $\lambda = 9$ at 273 K, does not fit into the master curve as smoothly as others, hinting that the diffusion data may deviate further with even lower temperatures. We argue that achieving wider-temperature range diffusion data will help justify and understand the TCS behavior in experiments.

Within the restrictions of the data, we have extracted δ_{rt} from these experimental diffusion data and find that they also obey equation 5.12. **Table 5.3** summarizes the fitting parameters from the water diffusion data. Similar to the MD simulations, we also observe a constant C_1C_2 value and a linear relationship between C_2 and λ_r. These results support that the temperature-concentration superposition is not an artifact from simulations. However, further investigation is essential to reveal the physical origin of this superposition behavior and its relationship to the TTS.

Table 5.3 Fitting results of equation 5.12, C_1 and C_2, with varying λ_r generated from water diffusion data collected from experiments

λ_1	C_1 (x10^{-4} K^{-1})	C_2
3.03	-9.44	3.88

4.01	-7.54	4.91
5.01	-6.25	5.91
6.14	-5.14	6.66
9.03	-3.64	9.77
12.2	-2.86	12.96
17.1	-1.93	17.73
32.2	-1.19	33.09

5.3.6 Bulk Water in the Picture of TCS

So far, we have shown the TCS behavior of water molecules and lithium ions in LiOTf solution both in simulations and in experiments. Using the WLF-type and VFT equations, we anticipate that we can predict the diffusion coefficients at any concentration or any temperature in these solutions. A question then is whether we may also be able to predict the diffusion coefficient of bulk water.

In **Figure 5.9a**, we put the calculated diffusion coefficients of bulk water and the master curve described above in the same plot. Then, in **Figure 5.9c**, we shift the Arrhenius plot of bulk water horizontally to match the master curve. Similarly, we present results from experiments in **Figures 5.9b,d**. In simulations, the temperature of bulk water diffusion ranges between 220 K and 360 K with a 10 K interval. In experiments, we take from the literature the diffusion coefficients of bulk water between 240 K and 373 K.[32-33] After shifting, the bulk water diffusion data only partially matches the master curves, either in experiments or in simulations, and the matching region occurs at relatively high temperatures. In the simulations, the deviation starts at 240 K and the experiments at 253 K. These deviations happen below the freezing point of water (the freezing point of TIP4P/2005 water[34] is around 250 K), suggesting phase changes are not involved in the deviation. Further investigation seems therefore essential to reveal the origin of deviations.

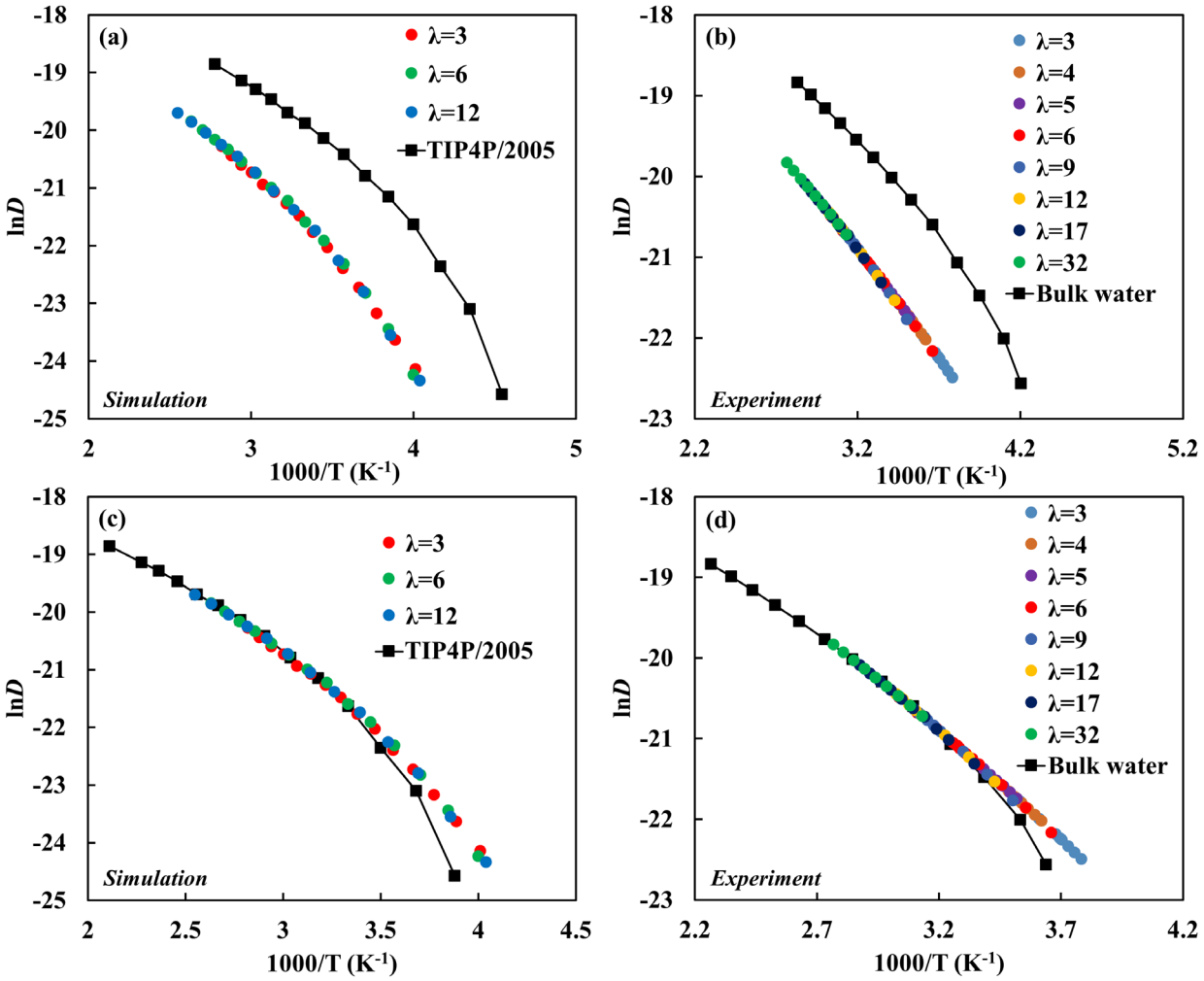

Figure 5.9 TCS behavior of bulk water in experiments and simulations. Panels (a) and (c) are for simulation, while panels (b) and (d) contain experimental data. In panels (a) and (b), we plot wide temperature range Arrhenius plots of bulk water diffusion with the master curves created from Arrhenius plots of LiOTf solutions. In panels (c) and (d), we shift the bulk water plots horizontally to match the master curves. After shifting, the high-temperature end of the bulk water plot can overlap with the master curve, and deviation happens at the low-temperature end.

In the context of equation 5.12, bulk water would carry a λ_1 value of ∞. Thus, to calculate δ_{rt} of bulk water, we have

$$\delta_{rt,bulk\ water} = \lim_{\lambda_1 \to \infty} -\frac{C_1 * (\lambda_1 - \lambda_r)}{C_2 + (\lambda_1 - \lambda_r)} = -C_1 \quad (3)$$

The δ_{rt} for bulk water plot to match with the reference plot is equal to $-C_1$, providing that bulk water also obeys the TCS behavior. As previously discussed, bulk water does not fully match the master curve created from LiOTf solutions. Thus, we extract δ_{rt} of bulk water based on the matching regime at the high-temperature end. Then, we can compare the $-C_1$value extracted from the fitting of δ_{rt} and the $\delta_{rt,bulk\ water}$ value extracted from the shifting of bulk-water Arrhenius plot. **Table 5.4** summarizes the comparison between fitting parameter C_1 and δ_{rt} of bulk water. In simulations, the δ_{rt} of bulk water is slightly lower than the $-C_1$ while the experiments seem to generate $\delta_{rt,bulk\ water}$ slightly higher than $-C_1$. Based on these observations, the high-temperature diffusion data of bulk water does follow equation 5.12.

Table 5.4 Comparison of the fitting parameter C_1 to the offset of bulk water

Simulations			**Experiments**		
λ_1	$-C_1$ (x10^{-4} K^{-1})	$\delta_{rt,bulk\ water}$ (x10^{-4} K^{-1})	λ_1	$-C_1$ (x10^{-4} K^{-1})	$\delta_{rt,bulk\ water}$ (x10^{-4} K^{-1})
3	11.7	11.1	3.03	9.49	9.85
4	9.65	9.15	4.01	7.61	7.94
5	8.52	7.82	5.01	6.30	6.65
6	7.04	6.65	6.14	5.20	5.65
9	5.29	4.74	9.03	3.69	4.08
12	4.13	3.74	12.2	2.91	3.33
17	3.03	2.49	17.1	1.98	2.50
			32.2	1.23	1.42

5.4 Structural Analysis of Water Molecules in LiOTf Solutions by MD Simulations

5.4.1 Hydrogen-Bonding Analysis

Figure 5.10 displays results of a hydrogen-bonding analysis (see details in section 2.3.4) of water molecules in the LiOTf solutions. We observe that both the average number of hydrogens bonds, N_{HB}, and the coordination number, N_{CO}, decrease with increasing ion concentration. The ratio between N_{HB} and N_{CO} also decreases with increasing λ. In other words, a water molecule is less likely to form hydrogen bonds with its neighboring water molecules in the presence of ions, supporting the disruption of the hydrogen-bonding network by the ions.

At a λ=17, N_{CO} is almost identical to that of bulk water, while N_{HB} is visibly lower. N_{CO} is a local quantity that evaluates the average number of neighboring water molecules. At a λ of 17, most water molecules are already seeing a bulk-like environment, leading to a coordination number similar to bulk. The fact that N_{HB} behaves differently from N_{CO} in dilute solutions points to the long-range impact of ions. The ions not only change the structure of their immediate neighboring water molecules but also impacts water molecules further away. Thus, we still see a nontrivial disruption to the hydrogen-bonding network at a λ of 17.

Figures 5.10c,d show the angle and distance distributions of hydrogen bonds in the LiOTf solutions. As the ion concentration increases, both the angle and distance distributions get broader, which aligns with the ionic disruption of water's hydrogen-bonding network.

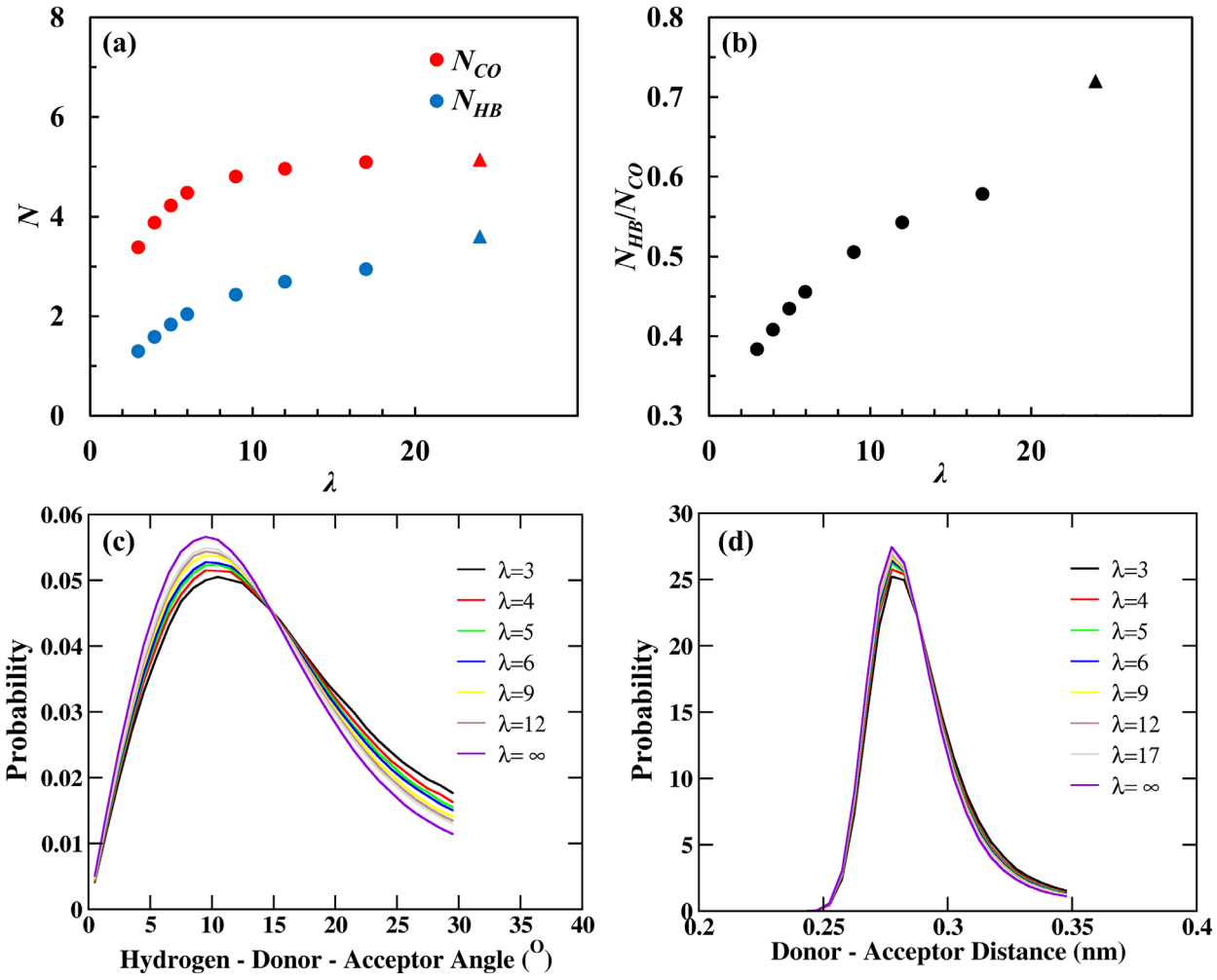

Figure 5.10 Hydrogen-bonding analysis of water molecules in LiOTf solutions at 300 K. Panels (a) and (b) plot the N_{HB}, N_{CO}, and N_{HB}/N_{CO} as a function of H_2O/Li^+ molar ratio (λ). The triangular symbols represent the values of bulk water. Panels (c) and (d) show the hydrogen-bond angle/distance distribution as a function of λ. The distribution curves are normalized to the area.

5.4.2 Radial Distribution Functions (RDFs)

Figure 5.11a shows the RDFs of water around water in LiOTf solutions as a function of λ. The presence of ions considerably changes the local structure of water. Comparing to the RDF of bulk water, the RDFs of water in the solutions have broader distributions in the first solvation shell.

The first minimum happens around 0.33 nm in the RDF of bulk water while ranging between 0.37 nm and 0.4 nm in the RDFs of LiOTf solutions. The broadened distributions indicate a more disordered local water structure. **Figure 5.11b** shows the RDFs of water around lithium ions. The first solvation shell of lithium ions is highly structured since all these RDFs reach zero at around 0.3 nm. As previously reported, the residence time of water around lithium ions is much longer than that of water around water because of the strong ion-dipole interactions. These interactions also stabilize the structure of the first solvation shell of water around the Li ions.

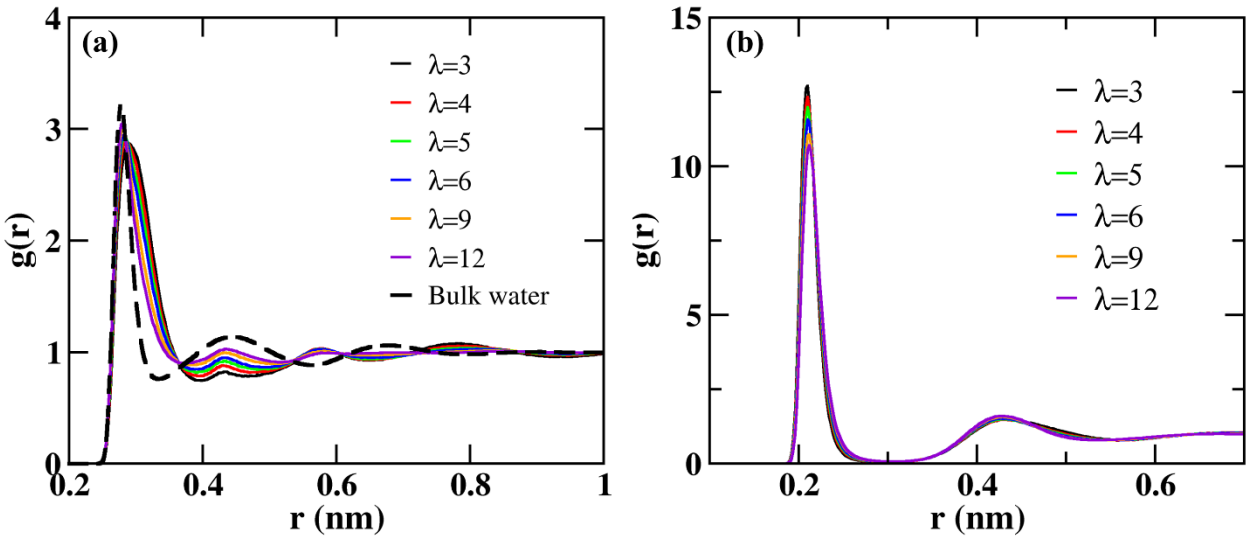

Figure 5.11 Normalized RDFs of water around water (a) and water around lithium ion (b) in LiOTf solutions at 300 K. Note the dashed line in panel (a) corresponds to the RDF of bulk water. In generating both plots, we consider the oxygen-oxygen distance or lithium-oxygen distance to align with the calculation of residence time correlation functions.

5.5 Conclusions

This chapter focuses on the observed temperature-concentration superposition (TCS) behavior of water/ion diffusion in bulk ionic solutions. By comparing TCS to TTS, we propose a WLF-type equation (Equation 5.12) in the context of TCS. We find that the offset of reciprocal

temperature, δ_{rt}, fits well with equation 5.12. Thus, it is possible to predict diffusion coefficients of water molecules and ions at any concentrations with that equation. We also notice that the δ_{rt} and fitting parameters are nearly identical between water molecules and lithium ions, suggesting the possibility to identify coupled and decoupled motions by studying the behavior of δ_{rt}.

Moreover, we find TCS behavior through experimentally measured diffusion coefficients in bulk LiOTf solutions. In all the systems above, δ_{rt} follows our proposed WLF-type equation. When going to the infinite high λ, which corresponds to bulk water, we notice deviations from the TCS behavior at low temperatures. The deviation likely results from the supercooling of bulk water. We propose that wider-temperature experiments on solutions with high solubility limit would help to justify the TCS behavior better.

Inspired by the calculations of residence times in chapter 4, we calculate the residence time of water around water and water around lithium ions in the LiOTf solutions. We find that the timescale of associations between water molecules and lithium ions to be more than ten times longer than the associations between water molecules. We propose that the associations between the water molecules surrounding the same lithium ions contribute to the increased residence time of water around water.

We have also examined the structural properties of water in the presence of ions. The ions disrupt the hydrogen-bonding network between water molecules. Water molecules in the aqueous ionic solutions are less likely to form hydrogen bonds with their neighbors as compared to the bulk. The local structure between water molecules is more disordered than bulk water, while the water structure around ions is highly ordered.

5.6 References

1. Moilanen, D. E.; Levinger, N. E.; Spry, D. B.; Fayer, M. D. Confinement or the nature of the interface? Dynamics of nanoscopic water. *J. Am. Chem. Soc.* **2007,** *129*, 14311-14318.
2. Zhou, T. C.; Bai, P.; Siepmann, J. I.; Clark, A. E. Deconstructing the Confinement Effect upon the Organization and Dynamics of Water in Hydrophobic Nanoporous Materials: Lessons Learned from Zeolites. *J. Phys. Chem. C* **2017,** *121*, 22015-22024.
3. Fenn, E. E.; Wong, D. B.; Fayer, M. D. Water dynamics at neutral and ionic interfaces. *PNAS* **2009,** *106*, 15243-15248.
4. Harrach, M. F.; Klameth, F.; Drossel, B.; Vogel, M. Effect of the hydroaffinity and topology of pore walls on the structure and dynamics of confined water. *J. Chem. Phys.* **2015,** *142*, 034703.
5. Renou, R.; Szymczyk, A.; Ghoufi, A. Water confinement in nanoporous silica materials. *J. Chem. Phys.* **2014,** *140*, 044704.
6. Kropman, M. F.; Bakker, H. J. Femtosecond mid-infrared spectroscopy of aqueous solvation shells. *J. Chem. Phys.* **2001,** *115*, 8942-8948.
7. Muller, K. J.; Hertz, H. G. A parameter as an indicator for water-water association in solutions of strong electrolytes. *J. Phys. Chem.* **1996,** *100*, 1256-1265.
8. Kim, J. S.; Wu, Z.; Morrow, A. R.; Yethiraj, A.; Yethiraj, A. Self-Diffusion and Viscosity in Electrolyte Solutions. *J. Phys. Chem. B* **2012,** *116*, 12007-12013.
9. Kim, J. S.; Yethiraj, A. A diffusive anomaly of water in aqueous sodium chloride solutions at low temperatures. *J. Phys. Chem. B* **2008,** *112*, 1729-1735.
10. Yu, H. B.; Whitfield, T. W.; Harder, E.; Lamoureux, G.; Vorobyov, I.; Anisimov, V. M.; MacKerell, A. D.; Roux, B. Simulating Monovalent and Divalent Ions in Aqueous Solution Using a Drude Polarizable Force Field. *J. Chem. Theory Comput.* **2010,** *6*, 774-786.
11. Yao, Y.; Kanai, Y.; Berkowitz, M. L. Role of Charge Transfer in Water Diffusivity in Aqueous Ionic Solutions. *J. Phys. Chem. Lett.* **2014,** *5*, 2711-2716.
12. Yao, Y.; Berkowitz, M. L.; Kanai, Y. Communication: Modeling of concentration dependent water diffusivity in ionic solutions: Role of intermolecular charge transfer. *J. Chem. Phys.* **2015,** *143*, 241101.
13. Mi, Y.; Zhou, S.; Stern, S. A. Representation of Gas Solubility in Glassy-Polymers by a Concentration Temperature Superposition Principle. *Macromolecules* **1991,** *24*, 2361-2367.
14. Hatzigrigoriou, N. B.; Vouyiouka, S. N.; Joly, C.; Dole, P.; Papaspyrides, C. D. Temperature-humidity superposition in diffusion phenomena through polyamidic materials. *J Appl Polym Sci* **2012,** *125*, 2814-2823.
15. Suarez-Martinez, P. C.; Batys, P.; Sammalkorpi, M.; Lutkenhaus, J. L. Time-Temperature and Time-Water Superposition Principles Applied to Poly(allylamine)/Poly(acrylic acid) Complexes. *Macromolecules* **2019,** *52*, 3066-3074.
16. Gornall, J. L.; Terentjev, E. M. Concentration-temperature superposition of helix folding rates in gelatin. *Phys. Rev. Lett.* **2007,** *99*, 028304.
17. Cramer, C.; De, S.; Schonhoff, M. Time-Humidity-Superposition Principle in Electrical Conductivity Spectra of Ion-Conducting Polymers. *Phys. Rev. Lett.* **2011,** *107*, 028301.
18. Abascal, J. L. F.; Vega, C. A general purpose model for the condensed phases of water: TIP4P/2005. *J. Chem. Phys.* **2005,** *123*, 234505.
19. Smith, R. S.; Kay, B. D. The existence of supercooled liquid water at 150 K. *Nature* **1999,** *398*, 788-791.
20. Mialhe, P.; Charles, J. P.; Khoury, A. The Thermodynamic Compensation Law. *J. Phys. D: Appl. Phys.* **1988,** *21*, 383-384.
21. Freeman, B. D. Basis of permeability/selectivity tradeoff relations in polymeric gas separation membranes. *Macromolecules* **1999,** *32*, 375-380.

22. Zheng, J. M.; Qiu, J.; Madeira, L. M.; Mendes, A. Polymer structure and the compensation effect of the diffusion pre-exponential factor and activation energy of a permeating solute. *J. Phys. Chem. B* **2007,** *111*, 2828-2835.
23. Khait, Y. L.; Weil, R. Arrhenius Parameters and the Compensation Effect in Crystallization and Diffusion in Amorphous Si-H(F) in the Presence or Absence of Metal Contacts. *J. Appl. Phys.* **1995,** *78*, 6504-6513.
24. Magomedov, M. N. Compensation effects for the diffusion process. *High Temp.* **2002,** *40*, 142-144.
25. Sharp, K. Entropy-enthalpy compensation: Fact or artifact? *Protein Sci.* **2001,** *10*, 661-667.
26. Barrer, R. M. Permeability in relation to viscosity and structure of rubber. *J. Chem. Soc. Faraday Trans.* **1942,** *38*, 322-330.
27. Vanamerongen, G. J. The Permeability of Different Rubbers to Gases and Its Relation to Diffusivity and Solubility. *J. Appl. Phys.* **1946,** *17*, 972-985.
28. Watanabe, K.; Ashida, K.; Sonobe, M. The Compensation Effect on Diffusion Constants of Hydrogen in Metals. *J. Nucl. Mater.* **1990,** *173*, 294-306.
29. Adam, G.; Gibbs, J. H. On Temperature Dependence of Cooperative Relaxation Properties in Glass-Forming Liquids. *J. Chem. Phys.* **1965,** *43*, 139-146.
30. Nguyen, M.; Rick, S. W. The influence of polarizability and charge transfer on specific ion effects in the dynamics of aqueous salt solutions. *J. Chem. Phys.* **2018,** *148*, 222803.
31. Swan, I.; Reid, M.; Howe, P. W. A.; Connell, M. A.; Nilsson, M.; Moore, M. A.; Morris, G. A. Sample convection in liquid-state NMR: Why it is always with us, and what we can do about it. *J. Magn. Reson.* **2015,** *252*, 120-129.
32. Easteal, A. J.; Price, W. E.; Woolf, L. A. Diaphragm Cell for High-Temperature Diffusion Measurements - Tracer Diffusion-Coefficients for Water to 363-K. *J. Chem. Soc. Faraday Trans.* **1989,** *85*, 1091-1097.
33. Price, W. S.; Ide, H.; Arata, Y. Self-diffusion of supercooled water to 238 K using PGSE NMR diffusion measurements. *J. Phys. Chem. A* **1999,** *103*, 448-450.
34. Conde, M. M.; Rovere, M.; Gallo, P. High precision determination of the melting points of water TIP4P/2005 and water TIP4P/Ice models by the direct coexistence technique. *J. Chem. Phys.* **2017,** *147*, 244506.

Chapter 6 Dynamics of Water in Nanoconfining Structures with Charged Surfaces

6.1 Introduction

Understanding confined water dynamics in ionomer membranes requires study of the effects of both the confinement medium and the water-ion interactions. As mentioned in chapter 1, researchers have studied confined water dynamics in ionic/charged surfaces with both experimental and computational model systems, including reverse micelles,[1] clay minerals,[2] and charged graphene/ nanotubes.[3-4] Experimental studies on reverse micelles indicate that the confinement effect dominates the water dynamics,[1-2, 5-6] and MD simulations further reveal the effect of charged surfaces.[7-15] In this chapter, we incorporate ions/charged groups onto the confinement surface to understand water dynamics under ionic confinement with MD simulations. Ideally, the simulation models need to mirror the real systems/materials. For our subject of study, the ionomer membranes and similar ion-containing materials, a few obstacles stand. First, as mentioned in chapter 1, the explicit nanostructure of ionomer membranes remains elusive. Imaging techniques such as cryogenic TEM[16] barely reveal the interconnect hydrophilic channels in ionomer membranes. Second, ionomer membranes are usually heterogeneous on the nanometer lengthscale, making it difficult to reproduce the full atomistic and nanoscale picture. Building excessively large simulation systems[17-18] or employing coarse-grained force fields[19] does not always provide comparable results to experiments even with large computational overheads.[20] In a quest to diversify the portfolio of useful simulation models for water dynamics in nanostructure materials, we build upon the rigid-rod model in chapter 4 and incorporate charged groups and ions onto its surface.

The simulation models in this chapter can be separated into two categories: high or low ion

density. We observe slow and anomalous diffusion with high ion density, making it challenging to obtain reliable results. With low ion density, we are able to get reproducible results and explore the effect of ions under confinement. In the previous chapters, we have shown that the activation energy of diffusion, E_a, and the residence times of water around water, τ_l and τ_s, reveal molecular information of water dynamics both in bulk and confinement media. Here we again use these two probes to investigate water dynamics in a charged confinement. Remarkably, we observe that surface charges can break the ordered water structure induced by the hydrophobic confinement. The breakage of structured water leads to decreased E_a, decreased residence time of water, and enhanced diffusion coefficient. Moreover, the structure-breaking effects of charges compete with the water-surface interactions. At relatively low ion density, the structure-breaking effect is dominant, and we observe enhanced water diffusion. At relatively high ion density, the water-ion interactions prevail, and we observe retarded water diffusion.

6.2 Simulation Methods

6.2.1 Simulation Models

All the models in this chapter are based on the rigid-rod model from chapter 4. The graphic description for each model is included in the individual sections below. **Figure 6.1** shows a sidechain-anchored model in which 600 Nafion sidechains are randomly anchored to the surface of 16 rigid carbon rods. 600 lithium ions are added to the model as counterions. The rigid rods are packed in a hexagonal pattern and are frozen in space. In this sidechain-anchored rigid-rod model, we looked at relatively low λ (H_2O/sidechain number ratio) values, or relatively high ion density. By varying rod-rod distances from 1.4 nm to 1.5 nm and solvating the system with water molecules, λ values ranging between 3.3 and 5.9 are achieved.

To paint to a more comprehensive picture of water-surface interactions, we also created models in which the ion density is relatively low. We deployed a charged rigid-rod model with the same geometry as the rigid-rod model in chapter 4, but incorporating into the rigid rods alternating positively and negatively charged carbon atoms. One positive/negative ion pair is put onto the carbon rods every four carbon ring layers. The rod-rod distance is kept at 1.2 nm while the charge of positive/negative atom pair is adjusted from $\pm 0.05e$ to $\pm 3e$ to achieve different water-surface interaction strength. For simplicity, we use the absolute charge to describe the charged rigid-rod model (e.g., when the charged carbon atom pair carries a charge of $\pm 1e$, the absolute charge is 1 atomic unit). The number of water molecules in the confined region is ~7400, while the number of positive/negative atom pairs is 320. This combination would give a water/charged atom pair ratio of ~23, which presents a much smaller ion density than the sidechain-anchored rigid-rod model.

We have also built a more realistic model of ionomer membranes by putting negative charges on a certain number of carbon atoms in the ionic rigid-rod model and an equal amount of lithium ions as counterions in the solution. The rod-rod distance in the ionic rigid-rod model is kept at 1.2 nm. The number of the ion pairs is varied from 4 to 384. TIP4P/2005 water model[21] is used to hydrate both the charged and ionic rigid-rod models. Compared to the charged rigid-rod model, the absolute charge of atoms stays unchanged here. Instead, the number of lithium ions and charged carbon atoms are varied to achieve varying water-surface interactions. In the ionic rigid-rod model, the positions of the charged atoms also vary. Depending on the number of lithium ions, there are 6800 to 7400 water molecules in this model, leading to a λ (H_2O/Li^+ molar ratio) value between 18 and 185.

6.2.2 Simulation Details

In all the simulation models, diffusion coefficients are calculated from 300 K to 340 K at 10 K intervals to generate activation energies. All the confining structures are frozen in space. General simulation input parameters and the force field parameters for the carbon atoms, the sidechains, and the counterions are the same as in the previous simulations (Appendix A). The models are equilibrated with 1 – 2 ns NPT simulations followed by NVT production runs.

6.3 Water Dynamics and Structure under Charged/Ionic Confinement

6.3.1 Water Dynamics in the Sidechain-Anchored Rigid-Rod Model

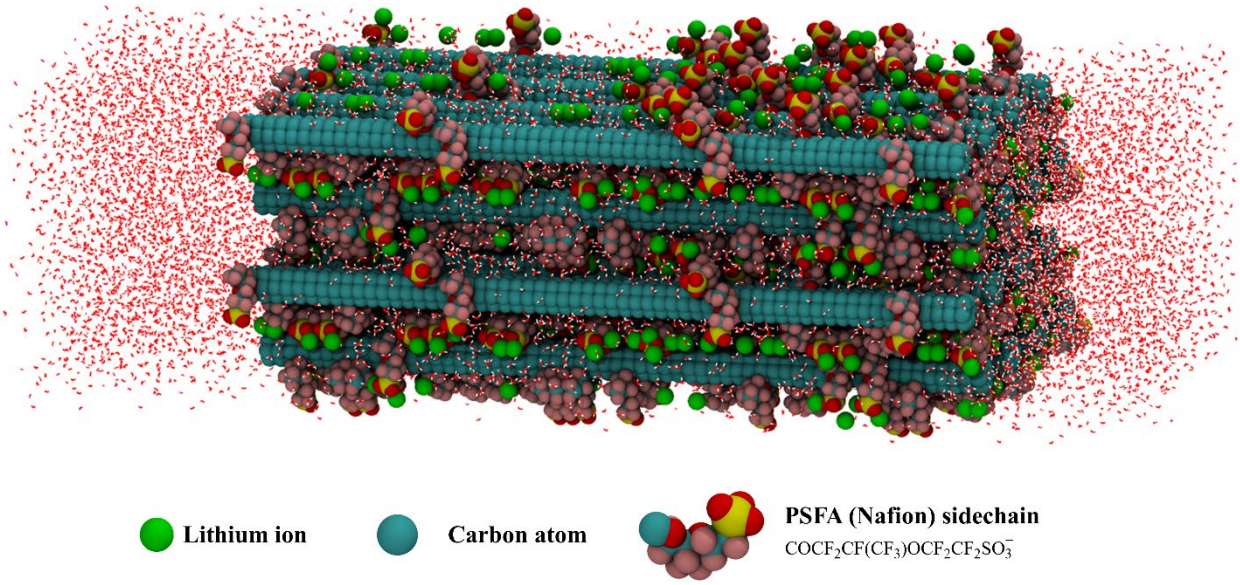

Figure 6.1 The rigid-rod model with anchored sidechains. The red and white lines represent water molecules. To achieve relatively high ion density in this model, the rod-rod distance is set to extremes that few water molecules fit between the carbon rods. Consequently, the bulky sidechains fill the inter-rod space and form pockets in which water molecules reside.

Figure 6.1 shows the rigid-rod model with anchored sidechains. Similar to the rigid-rod

model. We observe anisotropic diffusion in this sidechain-anchored rigid-rod model. Note that the Nafion sidechains are pretty bulky compared to the rod-rod distances we are using. The combination of rigid rods and bulky sidechains creates pockets in which the water molecules reside. These pockets cause substantial restrictions on the diffusion of water molecules, and we subsequently observe anomalous water diffusion in this model.

Figure 6.2a shows the mean squared displacement (MSD) of water vs. time plot for water diffusion in the sidechain-anchored rigid-rod model at 300 K. To probe the timescale of anomalous diffusion, we ran a 100-ns simulation (which takes 7 months of cpu time and 200 hours in real time) and extracted MSD up to 50 ns. We consider MSD both perpendicular ($D_{\perp}$) to the rods and parallel ($D_{\parallel}$) to the rods. By fitting the two MSD plots, we observe that both are still curved towards the end of 50 ns frame. **Figure 6.2b** shows diffusion coefficients of water calculated from different regions of the MSD plots. As diffusion time increases, the diffusion coefficients of water, both parallel and perpendicular to the rods, continuously decrease. The continuous restriction likely originates from the bulky sidechains. The sidechains create pockets that physically trap water molecules for an extended period. As a result, it takes a long time to reach equilibrium. The plots shown in **Figure 6.2** represent the results generated from a rod-rod distance of 1.5 nm and a λ value of 5.9. With smaller confinement sizes, equilibrium is even more elusive.

While the rigid-rod model used here has attractive properties, such as the ease with with its size can be scaled, the lesson we learned from this simulation model is that atomistic simulation of diffusion behavior becomes progressively more difficult when the dynamics of molecules/ions slow down. In the remaining sections, we augment our perspective by probing simulation models where the λ values are relatively high, and the confinement surface stays primarily smooth.

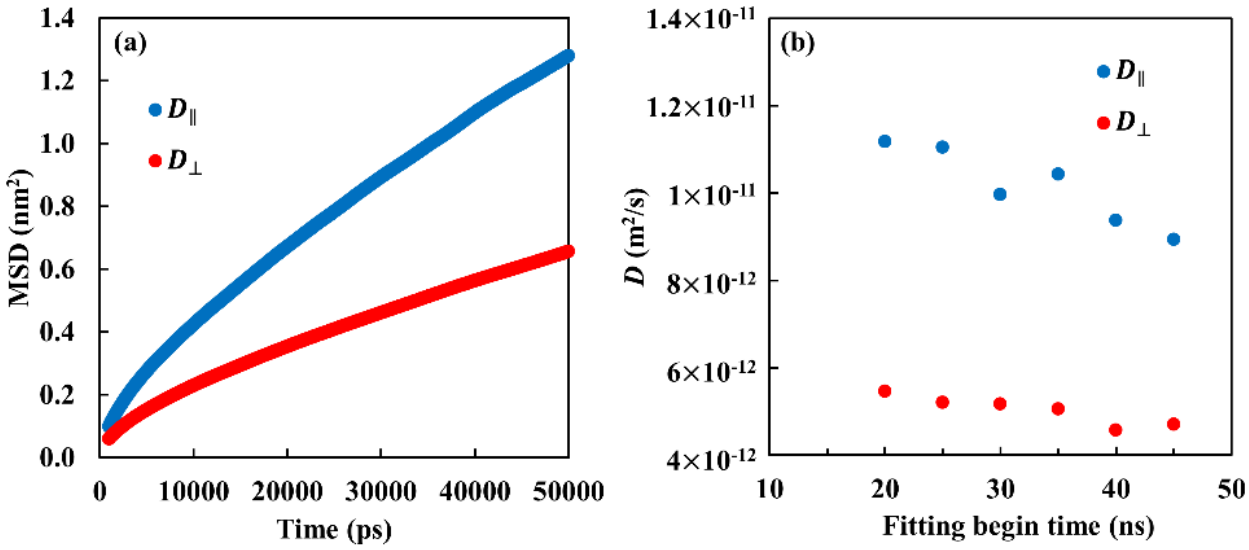

Figure 6.2 Diffusion of water molecules both parallel and perpendicular to the rods in the sidechain-anchored rigid-rod model. Panel (a) represents mean squared displacement (MSD) vs. time plot. Note that the MSD parallel to the rods barely exceeds 1 nm^2 at the end of 50 ns, which means that the water molecules on average travel ~1 nm along the axial direction. Panel (b) presents diffusion coefficients of water at 300 K from different diffusion time windows. The width of the diffusion time window is 5 ns. The x-axis represents the starting time of the time window. For example, data point at 20 ns is calculated from the MSD plots between 20 ns and 25 ns in panel (a).

6.3.2 Water Dynamics in the Charged Rigid-Rod Model

In this section, we turn to a simulation model with relatively low ion density and smooth surface. **Figure 6.3** shows the charged rigid-rod model. By periodically putting positive and negative charges onto the carbon atoms, we create charged confinement without disturbing the geometry of the rigid rods.

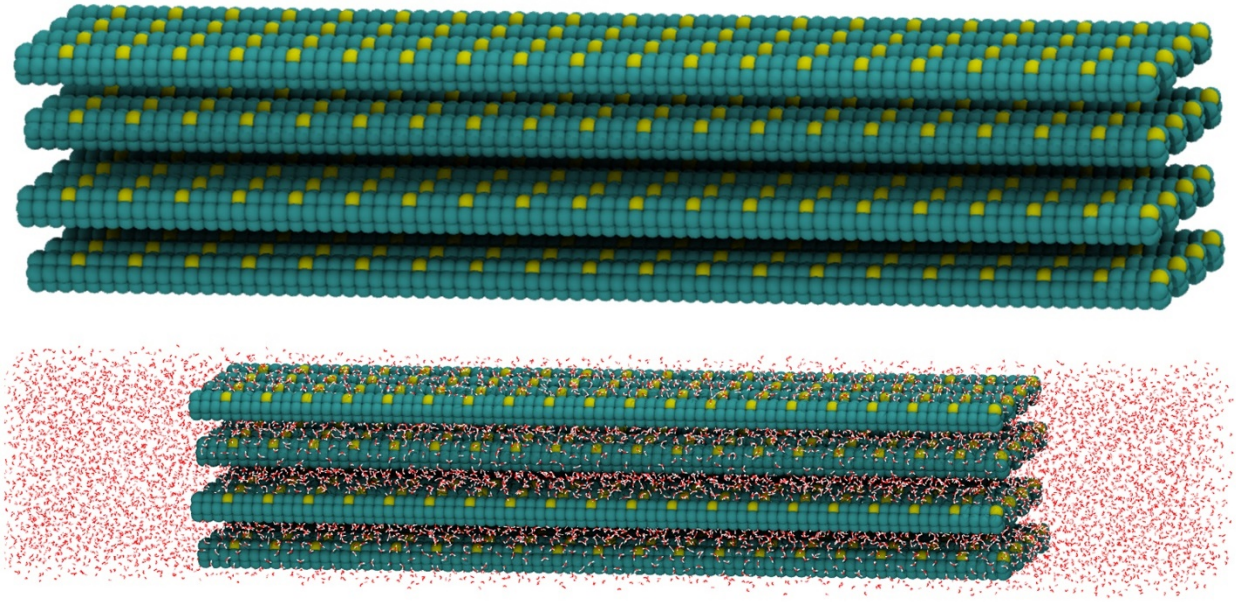

Figure 6.3 The charged rigid-rod model. The geometry of this model is the same as the rigid-rod model in chapter 4. The cyan atoms are neutral carbon atoms, while the yellow atoms represent positively charged carbon atoms. The negatively charged carbon atoms are located opposite to positively charged carbon atoms in the same ring. In this model, we keep the positions of the charged carbon atoms unchanged. We vary the absolute charges to modify the strength of water-surface interactions.

Figure 6.4 presents the diffusion coefficient (D) and activation energy (E_a) of water molecules in the charged rigid-rod model as a function of absolute charge on the charged atoms (when the charged carbon atom pair bears charges of ± 1, the absolute charge is 1). Similar to the neutral rigid-rod model in chapter 4, we again observe anisotropic diffusion in the charged rigid-rod model. While the geometry of this model does not change with the changing absolute charges, the diffusion anisotropy ($D_{\parallel}/D_{\perp}$) decreases as the absolute charge increases. Remarkably, as we increase the absolute charge from 0.05 to 0.25, the diffusion coefficients (in any direction) of water increase by over 10%. This phenomenon differs from MD simulations of bulk solutions. In

classical MD simulations of bulk aqueous solutions, the presence of ions always decreases the diffusion coefficient of water (compared to bulk water) regardless of the concentration or the type of ions.[22] In experiments, however, it is well recognized that certain salts, such as CsI and KI,[22] lead to enhanced water diffusion within a certain range of concentrations. To reconcile the difference between experimental and computational observations, researchers have developed the charge transfer model[23] and polarizable force fields[24] to account for ion-specific behaviors. However, the force field we are using here is a non-polarizable classical force field, making it especially interesting to see enhancement of water diffusion with surface charges.

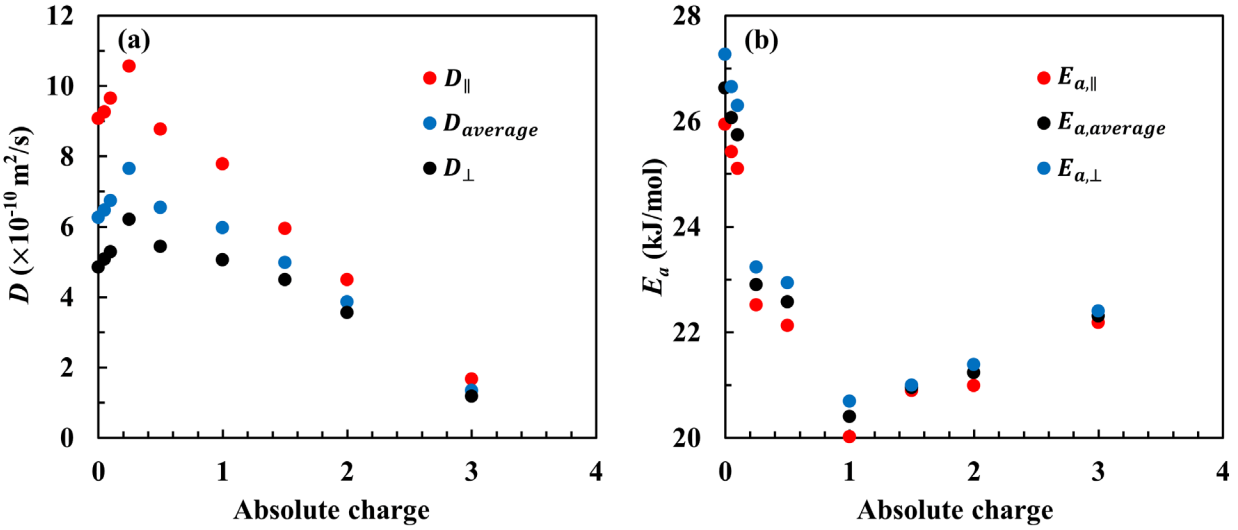

Figure 6.4 The diffusion coefficient (D) at 300 K and activation energy (E_a) of confined water in the charged rigid-rod model as a function of absolute charge on the charged carbon atoms of the rod surface. An absolute charge of zero corresponds to the neutral rigid-rod model. Panel (a) presents diffusion coefficients parallel ($D_{\parallel}$) and perpendicular ($D_{\perp}$) to the rods. Panel (b) shows activation energy of diffusion along different directions. The errors in D and E_a are estimated to be $\pm$2% and $\pm$1.5 kJ/mol.

Researchers have tried to explain the enhanced/retarded water diffusion with the concepts

of structure-making and structure-breaking salts.[22] As seen in chapter 5, ions can break the hydrogen-bonding network between water molecules while associating strongly with neighboring water molecules. When the water-ion associations are strong enough to nucleate a hydrogen-bonding network around the ion, the salt is a structure-making salt and will slow down water diffusion. When the ions disrupt the hydrogen-bonding network in water without templating a new network from ion-water associations, the salt is a structure-breaking salt and will enhance water diffusion. With classical MD simulations of bulk solutions, the overestimated Coulombic interactions,[25] induced by the lack of charge delocalization, always dominate the overall dynamics. In the charged rigid-rod model of Fig 6.3, the charged carbon atoms appear to disrupt the hydrogen-bonding network and do not provide a competing network stemming from water-surface interactions. We propose a few reasons for the changing magnitudes of the structure-breaking and structure-making effects under confinement. First, as seen in chapters 3 and 4, the hydrophobic confinement structures water, prompting longer associations between water molecules. Thus, the charges in the rigid-rod model have a more resilient confined water structure to break. Second, the number of water molecules surrounding charged atoms in this rigid-rod model is smaller than the number of water molecules solvating ions in bulk solutions. When the charged atom is in contact with fewer water molecules, the water-surface ion interactions could be weaker than in bulk aqueous ionic solutions. Third, the disruption of the hydrogen-bonding network in confinement may be similar to in bulk. As pointed out in section 5.4.1, the ions are able to pose long-range disruption on the hydrogen-bonding network. The combination of the previous effects leads to the observed enhancement of water diffusion.

The E_a of water also supports the idea that the charges on the rigid rods are structure-breaking when the absolute charge is low. When the absolute charge increases from 0.05 to 1, E_a

of water continuously decreases (**Figure 6.4b**), signaling weakened interactions between water molecules. The E_a of confined water is approaching that of bulk water (~16 kJ/mol) at an absolute charge of 1. As the absolute charge continues to increase above 1, the associations between charged atoms and water molecules finally overcome the disruption of the hydrogen-bonding network. Also, note the E_a of water increases slowly when the absolute charge is higher than 1.

The diffusion coefficients and activation energy along different directions follow similar behavior. D and E_a in any directions tend to increase/decrease simultaneously. However, we notice that the maximum of D and the minimum of E_a does not happen at the same charge, which is another evidence that D and E_a are not always correlated. As shown in section 3.3.3, the average D is based on the number average of different components, while the average E_a is impacted more heavily by the fast-diffusing species. In the charged rigid-rod model, we can identify two populations of water molecules: water molecules located around the charged carbon atoms (slow-diffusing) and those located around neutral carbon atoms (fast-diffusing). The overall E_a weighs more on the fast-diffusing water while the overall D is the number average of all components, leading to the observed lag between the D and E_a turning points. Nevertheless, the dramatic decrement of activation energy at low surface charge signals how significant the structure-breaking effect of surface charges can be.

To delve deeper into the associations between water and surface charges, we calculate the residence times (refer to section 4.2.2) of water around water and water around rods in the charged rigid-rod model. In the study of neutral rods in chapter 4, we revealed prolonged associations between water molecules when decreasing confinement size. **Figures 6.5a,b** show the residence time of water around water as a function of the absolute charge on the charged carbon atoms. Both τ_l and τ_s initially decrease with increasing charges on the rods. This trend of residence time

supports that the associations between water molecules become weaker with increasing surface charge. Both τ_l and $\tau_s$reach a minimum at a charge of between 0.25 and 1. When the absolute charge is higher than 1, we notice that a double exponential function (Equation 4.2) no longer fits the residence time correlation function. The failure of the double exponential decay model likely results from the presence of charged atoms. The behavior of water molecules around the charged atoms is different from those around the neutral atoms. When water molecules in the two environments are not exchanging fast enough, more than two relaxation modes will appear in the residence time correlation function, which challenges our biexponential fit.

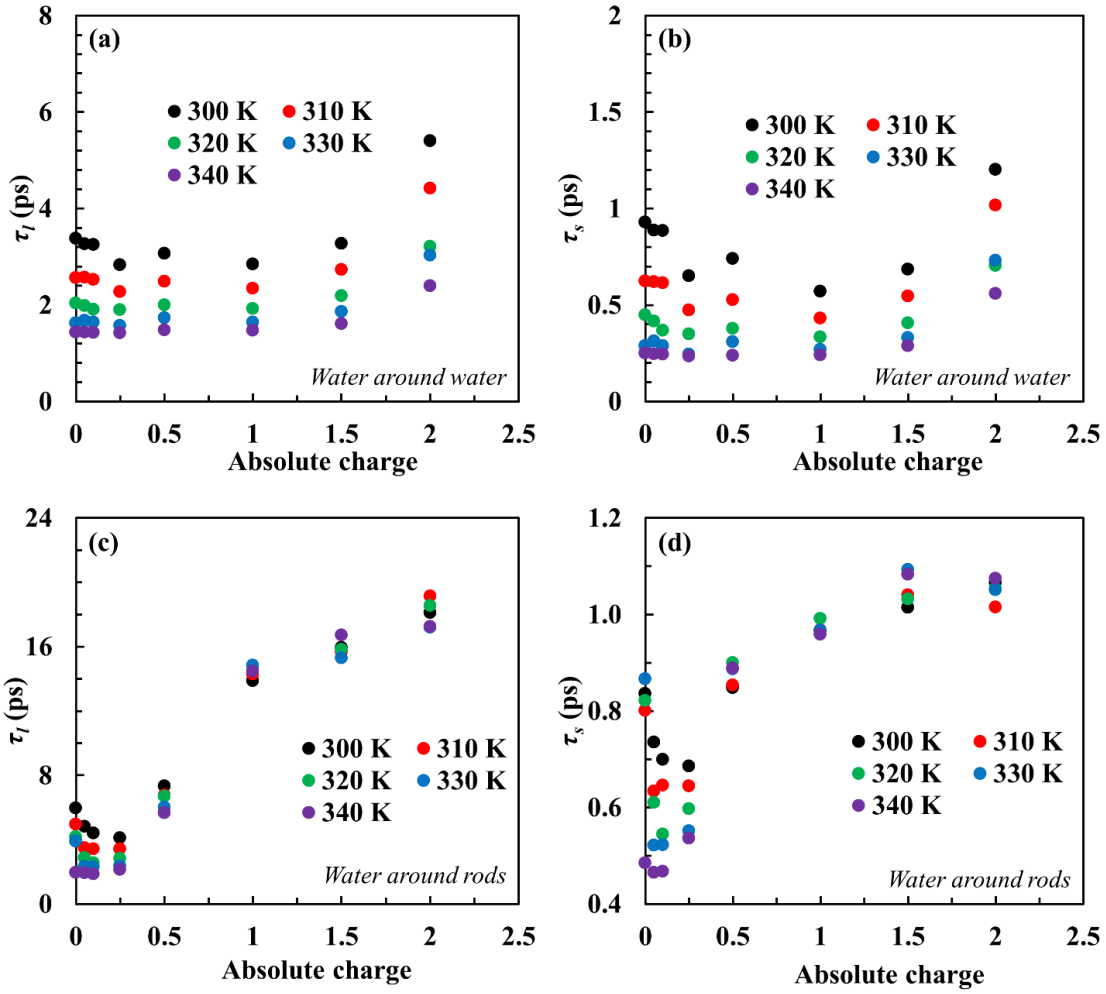

Figure 6.5 Residence times (τ_l and τ_s) of water around water (panels (a) and (b)) and water around

rods (panels (c) and (d)) as a function of absolute charge in the charged rigid-rod model. These residence times are calculated from water molecules locate within the rigid-rod region. The errors in τ_l and τ_s of water around water are estimated to be ± 0.05 ps. The residence time of water around water continuously decreases with increasing temperature, matching with our previous observations. The residence times of water around rods see large fluctuations with changing temperature due to less sampling in the calculations.

Figures 6.5c,d show the residence time of water around rods. Surprisingly, the presence of charge on the rods also decreases the duration of water-rod associations at low charges. As the absolute charge increases beyond 0.25, both τ_l and τ_s of water around rods start to increase rapidly. The increment indicates that the effect of water-ion associations becomes dominant. The residence time correlation functions here also do not fit well with a double exponential decay model when the absolute charge is higher than 0.5. Throughout the calculation of residence time in the charged rigid-rod model, we have observed the disruption of charged atoms on the associations between water molecules. When the absolute charge is low, the disruption weakens water-water and water-rod associations and enhances water diffusion. When the absolute charge gets higher, the charge-water interactions are dominant and cause retarded water dynamics. The geometric confinement effect is still present with relatively low ionic strength while competing with the effect of water-surface interactions.

To quantify the disruption of the hydrogen-bonding (HB) network, we calculated the HB properties (see details in section 2.2.4) of confined water in the charged rigid-rod model (shown in **Figure 6.6**). When the absolute charge is smaller than 0.5, there is almost no change in the coordination number (N_{CO}) of water molecules within a cut-off distance of 0.35 nm. With an

absolute charge higher than 0.5, the coordination number reveals an increased number of water molecules in the confined region. The average number of hydrogen bonds per water molecule (N_{HB}) continuously decreases with increasing absolute charge, consistent with our previous observation in bulk LiOTf solutions (see section 5.4.1). The ratio between N_{HB} and N_{CO} decreases with increasing ionic strength, supporting that the charged atoms disrupt the HB network of confined water. By comparing these results with bulk water, we noticed that the confined water in a charged confinement medium is more likely to form hydrogen bonds than bulk water when the absolute charge is lower than 2 (with a higher ratio between N_{HB} and N_{CO}), supporting that the confinement-induced structured water persists when the charge density is relatively low.

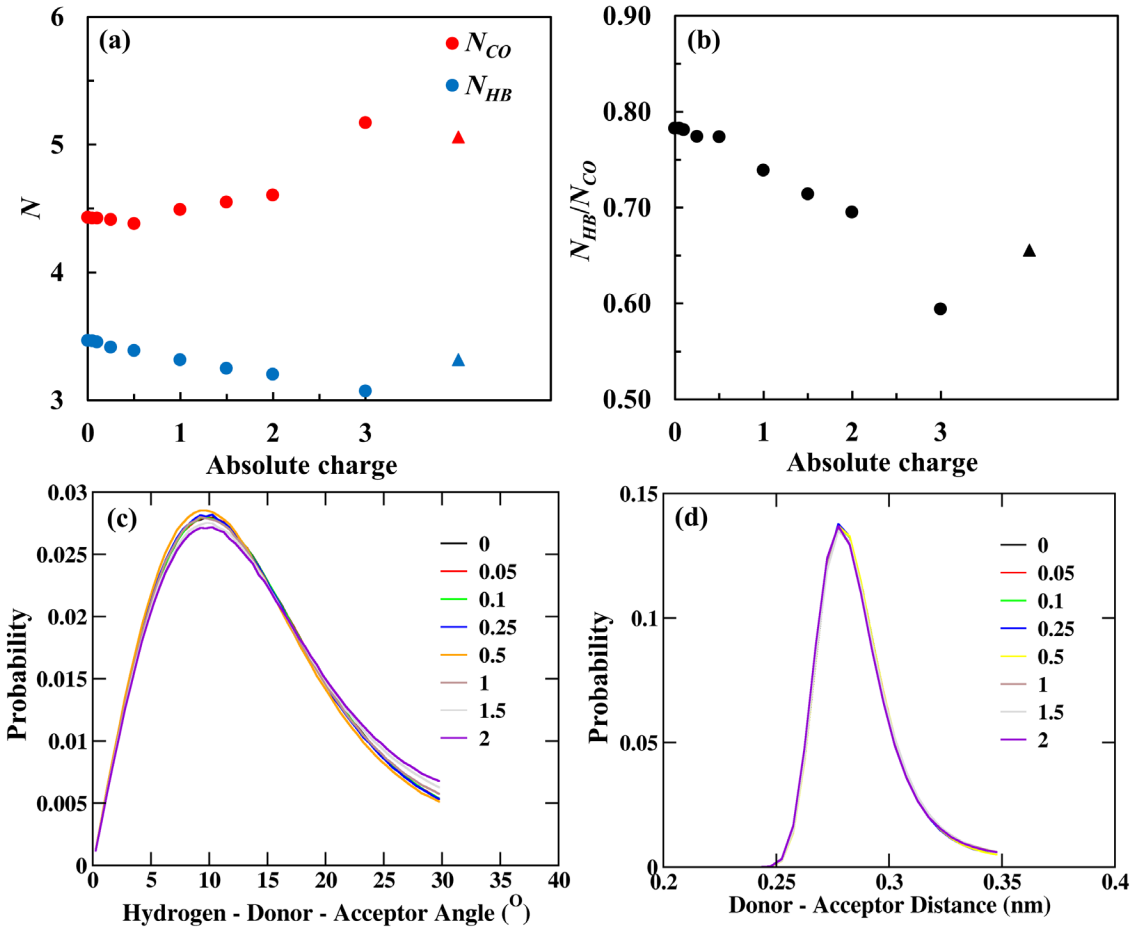

Figure 6.6 Hydrogen bonding properties of confined water in the charged rigid-rod model at 300

K. Panel (a) shows the average hydrogen-bond number per molecule (N_{HB}) and the coordination number (N_{CO}) within a cut-off distance of 0.35 nm. Panel (b) plots the ratio between N_{HB} and N_{CO}. The ratio represents the possibility for a water molecule to form hydrogen bonds with its neighbors. The triangles in panels (a) and (b) represent data from bulk water at 300 K. Panels (c) and (d) show the hydrogen-bonding angle and distance distribution with changing absolute charge.

Figures 6.6c,d show the hydrogen-bonding angle distribution and distance distribution. The donor-acceptor distance distribution is nearly constant with changing absolute charge. The angle distribution is also almost insensitive to the absolute charge. This independence is likely a result of charge density. As mentioned previously, the rigid rods are not heavily charged. The majority of water molecules are not in the vicinity of the charged carbon atoms. As a result, the hydrogen-bonding angle and distance distributions of water confined in charged rods are not significantly different from those confined in neutral rods.

6.3.3 Water Dynamics in the Ionic Rigid-Rod Model

In the charged rigid-rod model of the prior section, we aimed to carry as few independent variables as possible. We put all the charges on the carbon rods without an atomistic description of any ions or charged groups in solution. The rod-rod distance, the geometry of the model, and the position of the charged atoms stayed constant throughout the simulations. Here, we look at a slightly more realistic simulation model containing only negatively charged carbon atoms (**Figure 6.7**). We balance the negative charges with positively charged counterions. To better match experiments, we use lithium ions as counterions.

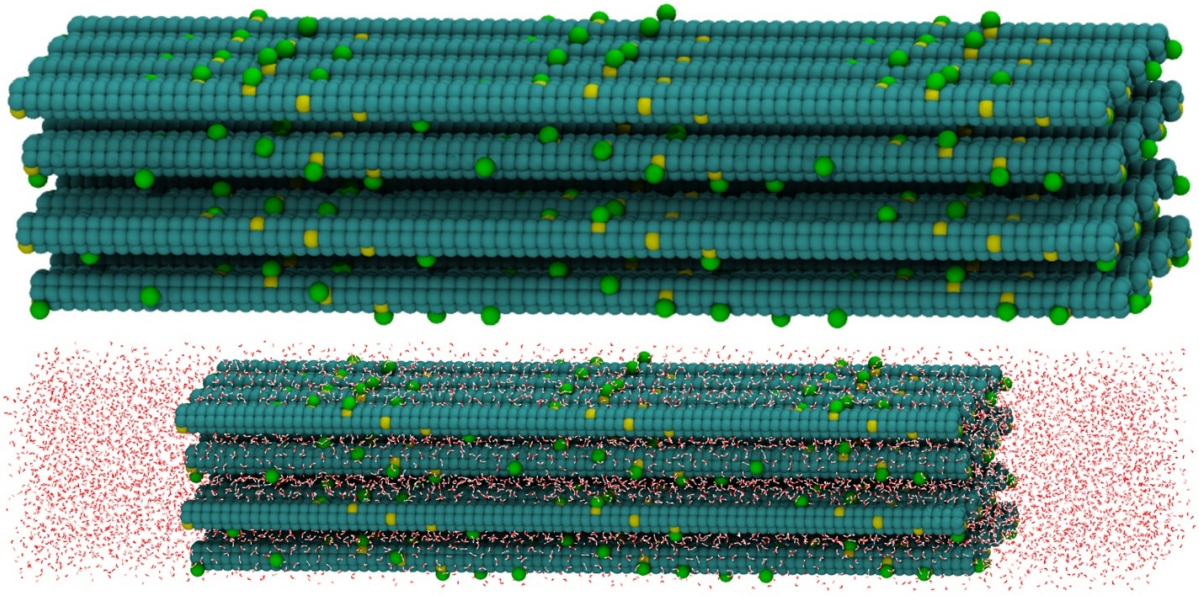

Figure 6.7 Ionic rigid-rod model. The rigid rods are composed of neutral atoms (the cyan particles) and periodically charged atoms (yellow). The green particles are lithium ions (320 shown). Two water reservoirs are put to both ends of the rods for equilibration purposes.

Figure 6.8 summarizes the diffusion coefficients (D) and residence times (τ_l and τ_s) of water in the ionic rigid-rod model. Comparing to the charged rigid-rod model, we observe a different diffusion behavior here. In the charged rigid-rod model, the diffusion coefficients parallel and perpendicular to the rod axis ($D_{\parallel}$ and $D_{\perp}$) increase/decrease simultaneously. In the ionic rigid-rod model, the simultaneity no longer stands. On the one hand, $D_{\parallel}$ Increases initially with a small number of counterions (N_{Li^+}) but then flattens with N_{Li^+} higher than 48. On the other hand, $D_{\perp}$ keeps increasing until when N_{Li^+} is higher than 240. Between $D_{\parallel}$ and $D_{\perp}$, $D_{\perp}$ contributes more to the average diffusion coefficient $D_{average}$. Thus, we also see that $D_{average}$ maximizes at an N_{Li^+} of 240. The loss of simultaneity between $D_{\parallel}$ and $D_{\perp}$ is a result of steric hindrance from the lithium ions. In the ionic rigid-rod model, the lithium ions associate tightly with the charged carbon atoms and have slow translational motions. The almost stationary lithium ions on the surface cause

restrictions to the water diffusion parallel to the rods. The diffusion perpendicular to the rods will not feel as much influence because $D_{\perp}$ is already under the restrictions from the carbon rods, and the volume of the lithium ions is negligible compared to that of the rods. In the ionic rigid-rod model, the maximum of $D_{average}$ happens at an N_{Li^+} of 240 while the minimum of $E_{a,average}$ happens at an N_{Li^+} of 320. This difference again points to the fact that D and E_a bear different information.

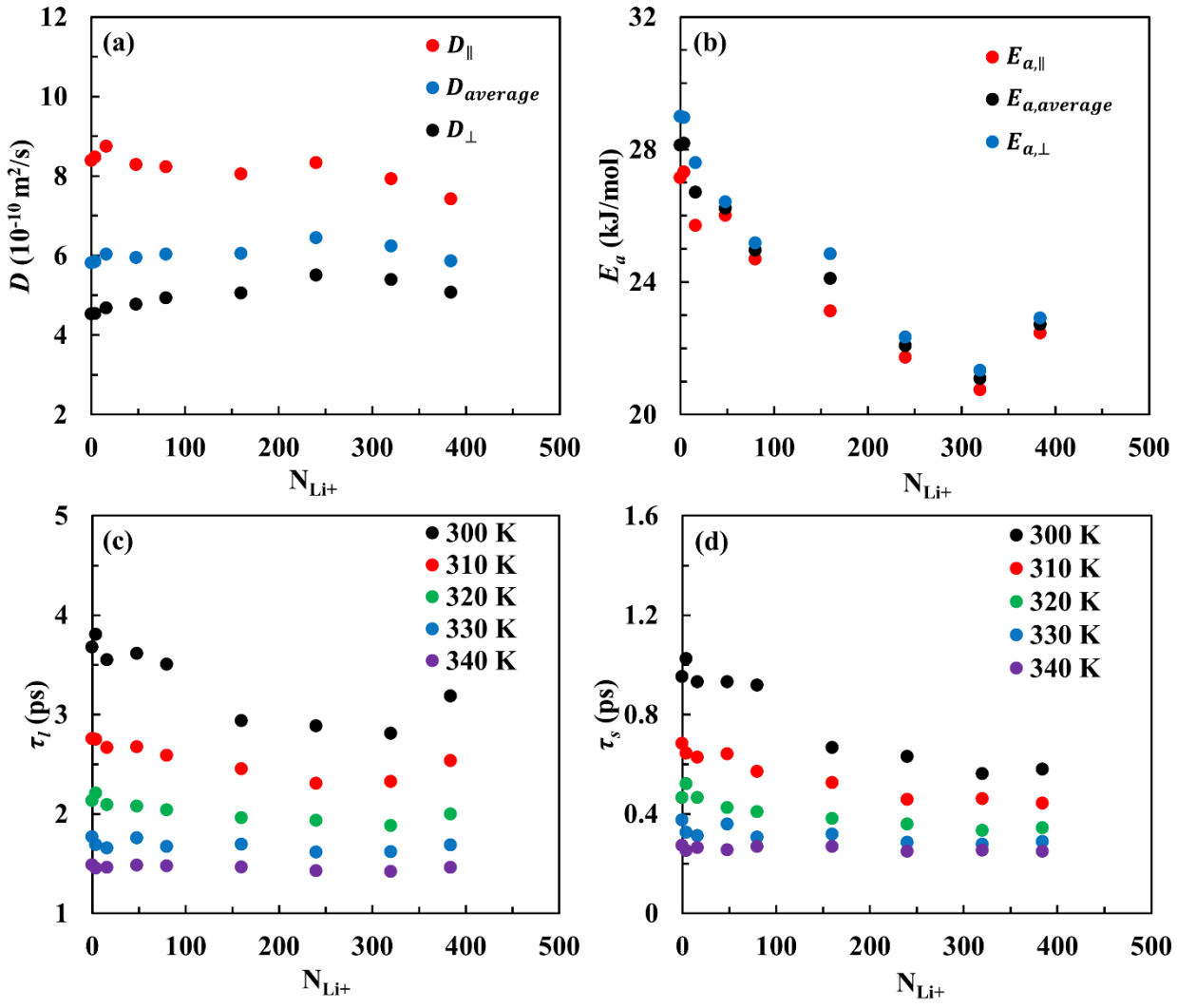

Figure 6.8 Panels (a) and (b) plot D at 300 K and E_a of confined water in the ionic rigid-rod model as a function of the number of counterions N_{Li^+}. Both D and E_a are presented in terms of directions.

Again, the parallel direction stands for the axial direction or the direction parallel to the rigid rods. The perpendicular direction stands for the direction perpendicular to the rods. The average value is the average of all three dimensions. Panels (c) and (d) show the residence times of water around water as a function of the number of counterions. The errors in τ_l and τ_s of water around water are estimated to be $\pm$0.05 ps.

To further understand the diffusion behavior in the ionic rigid-rod model, we again calculate the residence time of water around water (shown in **Figures 6.8c,d**). Both τ_l and τ_s decrease with an increasing number of lithium ions at low ionic strentgh. The decreasing residence time signals a weakened association between confined water molecules. Both τ_l and τ_s show a minimum at an N_{Li^+} of 320, which agrees with the trends of D and E_a except for $D_{\parallel}$. As previously mentioned, the unique trend of $D_{\parallel}$ originates from the steric hindrance of lithium ions (or the roughness of confinement surface). Here, the effect of the rough surface appears to decouple from the residence time of water. One reason is the short timescale of residence time. During a few picoseconds, most of the water molecules have not felt the restrictions from lithium ions along the parallel direction, and the surface roughness therefore does not play a significant role. It is worth reiterating here that the residence time has a similar timescale as the pre-diffusive regime, which relates to the activation energy of diffusion and the local diffusion coefficient. The effect of geometric restriction on the nanometer lengthscale is decoupled from the picosecond-timescale residence times.

Figure 6.9 shows the hydrogen-bonding analysis of confined water in the ionic rigid-rod model. We observe similar behavior here as in the charged rigid-rod model. With an increasing number of lithium ions (N_{Li^+}), the coordination number of water molecules within 0.35 nm (N_{CO})

is mostly flat while the average number of hydrogen bonds (N_{HB}) continuously decreases with increasing N_{Li^+}. The ratio between N_{HB} and N_{CO} continuously decreases with increasing ionic strength, again confirming a disruption to the hydrogen-bonding network with the presence of ions. While the number of hydrogen bonds changes, the distance and angle distribution (shown in **Figures 6.9c,d**) are weakly dependent on the ionic strength.

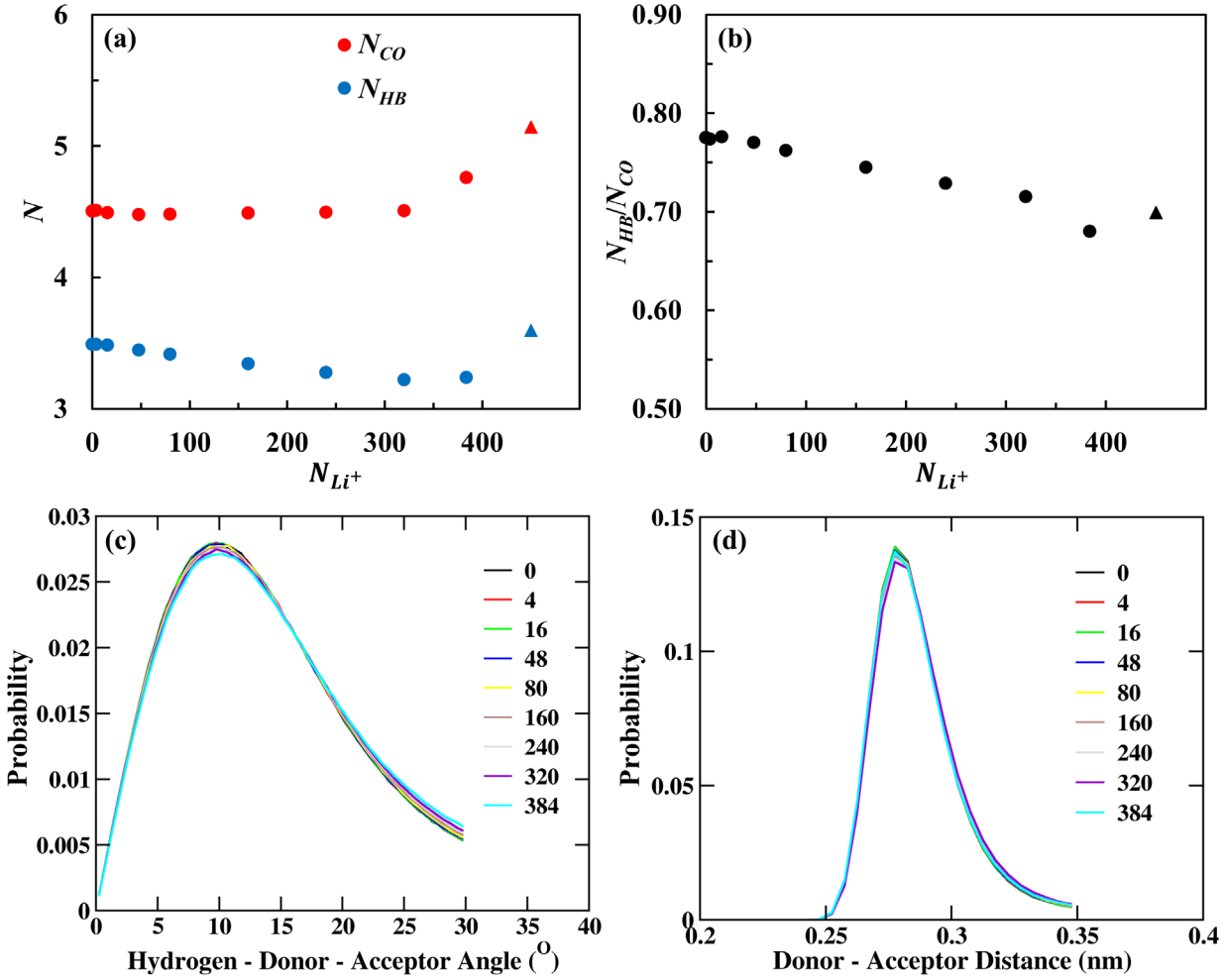

Figure 6.9 Hydrogen-bonding analysis of confined water in the ionic rigid-rod model at 300 K. Panel (a) shows the average hydrogen-bonding number per molecule (N_{HB}) and the coordination number (N_{CO}) within a cut-off distance of 0.35 nm. Panel (b) plots the ratio between N_{HB} and N_{CO}. The triangles represent data from bulk water at 300 K. Panels (c) and (d) show the hydrogen-

bonding angle and distance distribution with a changing number of lithium ions.

6.4 Conclusions

We have combined the rigid-rod model from previous chapters with surface ionic groups or charges to study water dynamics in charged confinement. In these systems, the geometric confinement and the water-surface interactions both affect the dynamics of confined water. With the sidechain-anchored rigid-rod model, we probed confined water with relatively high ion density (water/ion molar ratio λ ~5). The overwhelming number of ionic groups severely slows down water dynamics, leading to difficulties in getting reproducible results. The overestimation of electrostatic interactions in classic MD simulations localizes counterions within the vicinity of charged groups in these models. It is thus more challenging to examine the dynamics of counterions than water molecules. We argue a larger simulation model with a much longer simulation time may better examine the dynamics of confined water under a high ion-density environment.

More reliable results are obtained with the charged/ionic rigid-rod models, whose ion densities are relatively lower. When going from low ion density (λ ~200) to medium ion density (λ ~10), we observe a competition between geometric confinement and water-surface interactions. The confinement induces more structured water, supported by the analysis of activation energies, residence times, and hydrogen-bonding. The water-ion interactions, however, break the water structure induced by confinement. For the first time, we observe enhanced water dynamics in the presence of ions in classical MD simulations. We argue the surface charges/ions are able to interfere with the associations between water molecules and lead to enhanced water diffusion, lowered diffusive activation energy, and shorter residence time of water around water. This structure-breaking effect echoes our experimental observation in chapter 3, where we report the

activation energy of water in an ionomer membrane to be lower than that of bulk.

6.5 References

1. Park, S.; Moilanen, D. E.; Fayer, M. D. Water dynamics - The effects of ions and nanoconfinement. *J. Phys. Chem. B* **2008,** *112*, 5279-5290.
2. Le Caer, S.; Lima, M.; Gosset, D.; Simeone, D.; Bergaya, F.; Pommeret, S.; Renault, J. P.; Righini, R. Dynamics of Water Confined in Clay Minerals. *J. Phys. Chem. C* **2012,** *116*, 12916-12925.
3. Kumar, P.; Han, S. H. Dynamics of two-dimensional monolayer water confined in hydrophobic and charged environments. *J. Chem. Phys.* **2012,** *137*, 114510.
4. Won, C. Y.; Aluru, N. R. Structure and dynamics of water confined in a boron nitride nanotube. *J. Phys. Chem. C* **2008,** *112*, 1812-1818.
5. Fenn, E. E.; Wong, D. B.; Fayer, M. D. Water dynamics at neutral and ionic interfaces. *PNAS* **2009,** *106*, 15243-15248.
6. Baksi, A.; Ghorai, P. K.; Biswas, R. Dynamic Susceptibility and Structural Heterogeneity of Large Reverse Micellar Water: An Examination of the Core-Shell Model via Probing the Layer-wise Features. *J. Phys. Chem. B* **2020,** *124*, 2848-2863.
7. Calixte, E. I.; Samoylova, O. N.; Shuford, K. L. Confinement and surface effects of aqueous solutions within charged carbon nanotubes. *Phys. Chem. Chem. Phys.* **2016,** *18*, 12204-12212.
8. Zhou, X. Y.; Wang, C. L.; Wu, F. M.; Feng, M.; Li, J. Y.; Lu, H. J.; Zhou, R. H. The ice-like water monolayer near the wall makes inner water shells diffuse faster inside a charged nanotube. *J. Chem. Phys.* **2013,** *138*, 204710.
9. Hao, L.; Su, J. Y.; Guo, H. X. Water Permeation Through a Charged Channel. *J. Phys. Chem. B* **2013,** *117*, 7685-7694.
10. Chopra, M.; Choudhury, N. Comparison of Structure and Dynamics of Polar and Nonpolar Fluids through Carbon Nanotubes. *J. Phys. Chem. C* **2013,** *117*, 18398-18405.
11. Goldsmith, J.; Martens, C. C. Molecular Dynamics Simulation of Salt Rejection in Model Surface-Modified Nanopores. *J. Phys. Chem. Lett.* **2010,** *1*, 528-535.
12. Tran, T. H.; Phan, G. T. T.; Luc, H. T.; Nguyen, P. T.; Hoang, H. Molecular dynamics simulations on aqueous solution confined in charged nanochannels: asymmetric effect of surface charge. *Mol. Simul.* **2020,** *46*, 796-804.
13. Mukhina, T.; Hemmerle, A.; Rondelli, V.; Gerelli, Y.; Fragneto, G.; Daillant, J.; Charitat, T. Attractive Interaction between Fully Charged Lipid Bilayers in a Strongly Confined Geometry. *J. Phys. Chem. Lett.* **2019,** *10*, 7195-7199.
14. Shen, C.; Guo, W. L. Manipulation of Long-Range Water Ordering in Less Confined Nanotubes. *J. Phys. Chem. C* **2019,** *123*, 10101-10106.
15. Cazade, P. A.; Hartkamp, R.; Coasne, B. Structure and Dynamics of an Electrolyte Confined in Charged Nanopores. *J. Phys. Chem. C* **2014,** *118*, 5061-5072.
16. Allen, F. I.; Comolli, L. R.; Kusoglu, A.; Modestino, M. A.; Minor, A. M.; Weber, A. Z. Morphology of Hydrated As-Cast Nafion Revealed through Cryo Electron Tomography. *ACS Macro Lett.* **2015,** *4*, 1-5.
17. Elliott, J. A.; Wu, D. S.; Paddison, S. J.; Moore, R. B. A unified morphological description of Nafion membranes from SAXS and mesoscale simulations. *Soft Matter* **2011,** *7*, 6820-6827.
18. Savage, J.; Voth, G. A. Proton Solvation and Transport in Realistic Proton Exchange Membrane Morphologies. *J. Phys. Chem. C* **2016,** *120*, 3176-3186.
19. Vishnyakov, A.; Mao, R.; Lee, M. T.; Neimark, A. V. Coarse-grained model of nanoscale segregation, water diffusion, and proton transport in Nafion membranes. *J. Chem. Phys.* **2018,** *148*, 024108.

20. Elliott, J. A.; Paddison, S. J. Modelling of morphology and proton transport in PFSA membranes. *Phys. Chem. Chem. Phys.* **2007,** *9*, 2602-2618.
21. Abascal, J. L. F.; Vega, C. A general purpose model for the condensed phases of water: TIP4P/2005. *J. Chem. Phys.* **2005,** *123*, 234505.
22. Kim, J. S.; Wu, Z.; Morrow, A. R.; Yethiraj, A.; Yethiraj, A. Self-Diffusion and Viscosity in Electrolyte Solutions. *J. Phys. Chem. B* **2012,** *116*, 12007-12013.
23. Yao, Y.; Kanai, Y.; Berkowitz, M. L. Role of Charge Transfer in Water Diffusivity in Aqueous Ionic Solutions. *J. Phys. Chem. Lett.* **2014,** *5*, 2711-2716.
24. Nguyen, M.; Rick, S. W. The influence of polarizability and charge transfer on specific ion effects in the dynamics of aqueous salt solutions. *J. Chem. Phys.* **2018,** *148*, 222803.
25. Schroder, C. Comparing reduced partial charge models with polarizable simulations of ionic liquids. *Phys. Chem. Chem. Phys.* **2012,** *14*, 3089-3102.

Chapter 7 Additional NMR Studies: Water Dynamics in Tungsten Oxide Hydrates and Polymeric Separations Membranes, and Quantitative NMR of Wood ^{13}C Isotope Content

Section 7.1 is adapted from the following publication:

Mitchell, J. B.; Geise, N. R.; Paterson, A. R.; Osti, N. C.; Sun, Y. Y. L.; Fleischmann, S.; Zhang, R.; Madsen, L. A.; Toney, M. F.; Jiang, D. E.; Kolesnikov, A. I.; Mamontov, E.; Augustyn, V., "Confined Interlayer Water Promotes Structural Stability for High-Rate Electrochemical Proton Intercalation in Tungsten Oxide Hydrates" *ACS Energy Letters* **2019**, *4*, 2805.

7.1 Investigation of Water Dynamics in Tungsten Oxide Hydrates with Solid-State NMR (SSNMR)

7.1.1 Introduction

The electrochemical intercalation of protons into $WO_3 \cdot nH_2O$ or anhydrous WO_3 follows the general reaction

$$WO_3 \cdot nH_2O + xH^+ + xe^- \leftrightarrow H_xWO_3 \cdot nH_2O \quad (0 \leq x \leq 1, n = 0,1,2)$$

where x is the extent of proton storage, with a maximum of 1. **Figure 7.1** illustrates the crystal structure of the hydrated and anhydrous tungsten oxide. Tungsten oxide hydrates and similar redox-active materials possess both high energy density and high power density, prompting researches into their structure-property relations.[1] The charging rate of tungsten oxide hydrates is directly related to the transport of protons. Previous studies have suggested that the Grotthuss mechanism or proton hopping between water molecules is responsible for this fast proton transport.[2-3] In order to better understand the mechanism of proton transport and the role of confined water in this material, we performed SSNMR studies in this work. We present the details of the experiments and interpretations of the SSNMR spectra below.

7.1.2 Experimental Details

Detailed synthesis and physical characterization of the tungsten oxide hydrates can be found in a previous publication.[4] Proton-SSNMR spectroscopy was conducted with 400 mg (each) of $WO_3 \cdot 2H_2O$, $WO_3 \cdot H_2O$, and WO_3 powders at room temperature on a 600 MHz Bruker AVANCE™ III NMR spectrometer equipped with a Triple Resonance Broadband Inverse (TBI) 5 mm probe. A single radiofrequency pulse with a length of 1.3 μs (21° pulse) at 50 W power, a spectral width of 800 ppm, an acquisition time of 3 s, and a relaxation delay of 4 s were used with 32 scans to obtain all spectra. Additional experiments (neutron scattering, electrochemistry…) are described in detail in the publication that contains this NMR study.[1]

7.1.3 Results and Discussion

Through SSNMR measurements (**Figure 7.1**), we notice that the spectra of tungsten oxide and tungsten oxide hydrates all show a narrow peak around 5 ppm. These narrow peaks, whose intensities account for around 15 – 20 % of the total signal in the monohydrate and dihydrate, originate from the residual liquid water on the surface of the powder sample. Moreover, we observe broad doublets only in the spectra of tungsten oxide hydrates. These broad doublets correspond to dipole-dipole couplings between the two protons of a water molecule in the solid state. Dipole-dipole couplings or dipolar couplings are the direct magnetic interactions between two nuclei. The equation below describes the dipole-dipole coupling[5]

$$d_{jk} = \frac{1}{2} b_{jk}(3\cos^2\theta_{jk} - 1) \tag{7.1}$$

where the subscripts j and k represent the two nuclei involved in the dipolar couplings, d_{jk} is the (secular) dipole-dipole coupling value, θ_{jk} represents the angle between the external magnetic field and the vector connecting the two coupling nuclei (e.g., two protons in a single water molecule), b_{jk} is the dipole-dipole coupling constant. The dipolar coupling constant relates to the

distance between the two nuclei by the following equation

$$b_{jk} = -\frac{\mu_0}{4\pi}\frac{\gamma_j \gamma_k \hbar}{r_{jk}^3} \tag{7.2}$$

where μ_0 is the magnetic permeability of vacuum, γ_j and γ_k are the gyromagnetic ratios of the two nuclei, $\hbar$ is the reduced Planck's constant, and r_{jk} is the distance between the two nuclei. Assuming the equilibrium distance between the two protons of a water molecule is 0.15 nm,[6] the dipolar coupling constant for these two protons is 35.6 kHz.

The broad doublet observed in SSNMR spectra of the tungsten oxide hydrates is the classic Pake powder pattern,[7] which is a typical pattern of a powder sample of hydrated crystals. Theoretically, a Pake powder pattern (**Figure 7.1b**) will show two inner peaks and two shoulders. Experimentally, the shoulders may not be observable due to their relatively low intensity.[8] In these spectra of tungsten oxide hydrates, we observe two inner peaks and one shoulder, and the other shoulder appears to be subsumed under the inner peaks. For a homonuclear spin pair, the maximum separation between the two inner peaks is 3/2 b_{jk} or 53.4 kHz assuming an intramolecular proton distance of 0.15 nm and no rotational motions of the water molecules.[7] In a liquid such as bulk water, the dipolar coupling is not observable because of motional averaging (tumbling) much faster than the dipolar coupling constant. The rotational motions of water molecules render equal possibility for θ_{jk} to be in any angle between 0 and π, and the dipolar coupling becomes

$$d_{jk} = \frac{1}{2} b_{jk} \int_0^{\pi} (3\cos^2\theta_{jk} - 1) sin\theta_{jk} d\theta_{jk} = 0 \tag{7.3}$$

To observe dipolar couplings, the frequency of the motional average needs to be smaller than the dipolar couplings. We observe that separations between the inner peaks are ≈ 40 kHz for the monohydrate and ≈ 49 kHz for the dihydrate, which means the frequencies of rotational and translational motion of water molecules is substantially less than 50 kHz in the tungsten oxide

hydrates. The observations of dipolar couplings in the tungsten oxide hydrates confirm that water molecules are in a solid-like state.[9] Thus, the fast transport of protons is unlikely due to a vehicle mechanism in which protons are carried by translational motions of water molecules, and thus the protons must follow Grotthuss hopping transport. Further studies by small-angle neutron scattering also support the Grotthuss mechanism for proton transport in this material.[1]

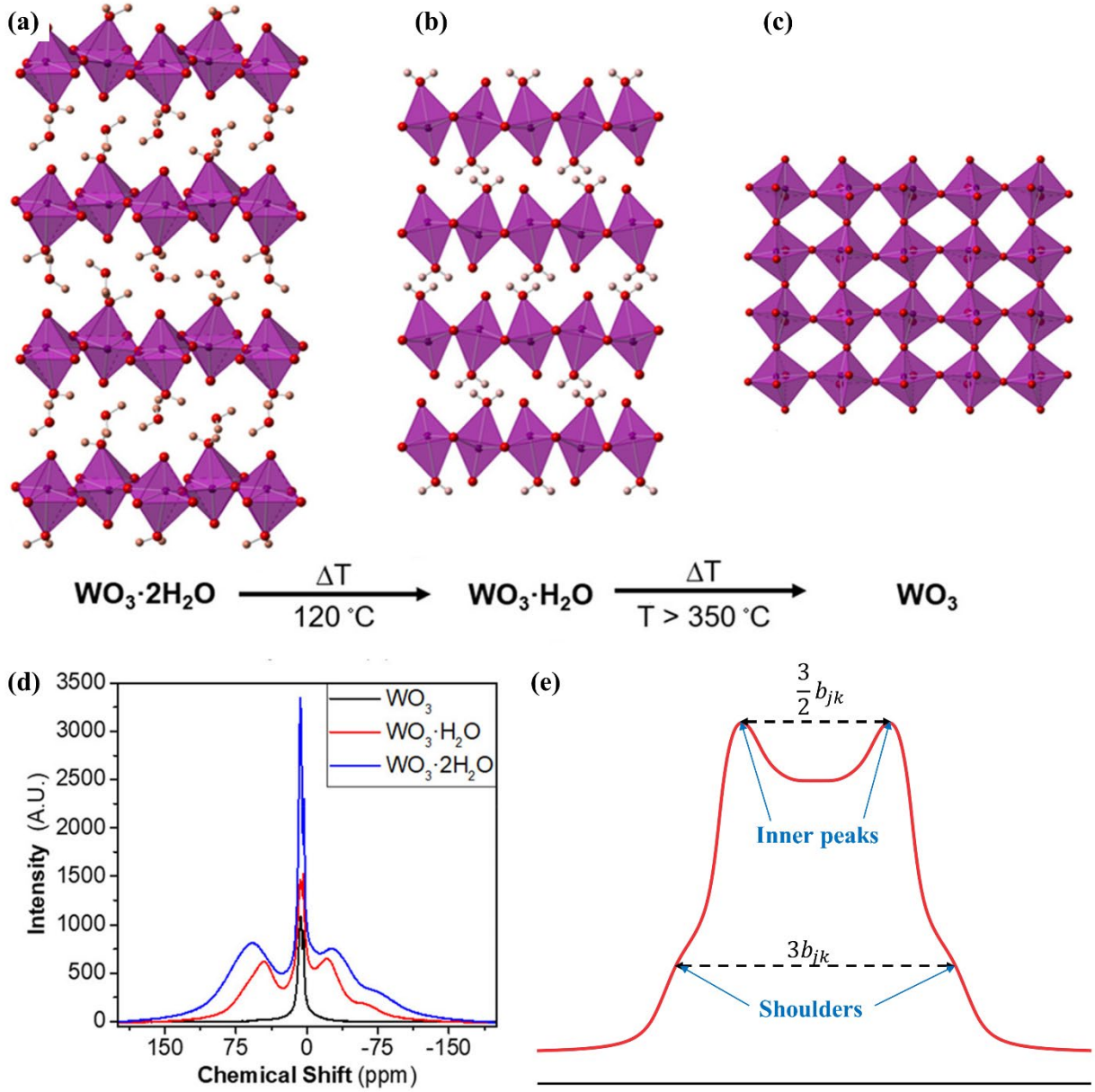

Figure 7.1 Panels (a), (b), and (c) show the crystal structures of $WO_3 \cdot 2H_2O$, $WO_3 \cdot H_2O$, sand WO_3.

Dehydration of the dihydrate at 120 °C gives the monohydrate, which further dehydrates to the anhydrous WO_3 at 350 °C. Panel (d) represents the superimposed wide-line SSNMR spectrum of tungsten oxide hydrates. Panel (e) shows a simulated Pake powder pattern where R_D is the dipolar coupling constant. Adapted with permission from Ref. 1, copyright (2019) American Chemical Society.

7.1.4 Summary

With wide-line SSNMR, we characterize the dipolar couplings between protons in tungsten oxide hydrates. We observe a Pake doublet pattern with central peaks split by approximately 3/2 b_{jk} (3/2 the value of the water dipolar coupling constant). The observation of this Pake doublet demonstrates that the water molecules are solid-like in these materials. Thus, the transport of protons likely happens through the Grotthuss mechanism rather than the vehicle mechanism.

7.2 Dynamics of Water and Phosphoric Acid in Diaminated Polysulfone Membranes

7.2.1 Introduction

In practical applications of ionomer membranes, the chemical and mechanical stability impact the lifetime of the membrane and its incorporation into real devices, while the transport of target ions mainly determines the device performance. For example, in hydrogen fuel cells, fast transport of protons leads to high power density and low internal resistance. To improve the transport properties of ionomer membranes, two major paths are available. One path involves optimizing the internal structure, either chemical or physical, of the polymer membrane to improve the transport performance. The other path involves changing the external environment, such as temperature and humidity, that is related to membrane transport.

PFSAs and most other ionomer membranes operate with substantial (a few wt% of the membrane, or greater) hydration. Without hydration, the counterions associate tightly with the ionic head group, making the ionic conductivity too low to be practical. Since hydration is usually essential, ionomer membranes cannot operate above the boiling point of water. In practice, the temperature of a hydrogen fuel cell needs to be around 70 °C.[10] However, the transport of protons is faster at higher temperature. Increased operation temperature should always have a positive impact on the transport performance of the ionomer membrane, but existing membranes will lose water at higher temperatures. The starting point in this work is to utilize an alternate proton carrier with a higher boiling point than water to enable high-temperature fuel cells. We collaborate with NanoSonic Inc. to characterize diaminated polysulfone membranes that are first synthesized and then doped with phosphoric acid. We chose phosphoric acid for two reasons. First, the boiling point of phosphoric acid is around 160 °C, making it possible to operate the fuel cell up to approximately 150 °C. Second, phosphoric acid can serve as both a proton donor and a proton acceptor, making it a suitable electrolyte for proton-exchange membrane fuel cells. in this project, NanoSonic Inc. provides the synthesized membranes to us. We present the characterization of the NanoSonic membranes and our understanding of these membranes below.

7.2.2 Experimental Details

The diaminated polysulfone membranes are synthesized and provided by NanoSonic, Inc. The chemical structure of this membrane is shown in **Figure 7.2**. We characterized two batches of sample ionomer membranes, H_3PO_4-doped and undoped membranes. In the undoped membranes, the percentage of quaternized sidechains is controllably varied to map out the impact of ion exchange capacity (IEC) on membrane performance. Varying IEC is achieved by converting a certain portion of the neutral sidechains to quaternary ammonium sidechains by titrating with a

strong acid such as HI. NanoSonic prepared membranes with varying IECs, in which x%, 1.6x%, and 2.4x% of the sidechains were quaternized. Two different quaternization methods, solution quaternized (SQ) and film quaternized (FQ), were applied to the membranes to understand the impact of processing methods. In total, six different undoped membranes, which are labeled with the percent ionization and the quaternization method below, were investigated throughout this study. The SQ membranes, which show better transport properties and uniformity, were selected as the candidates for phosphoric-acid doping. Membranes with 1.2x%, 1.6x%, and 2.2x% quaternary ammonium functionalization were doped with phosphoric acid. The 2.2x% quaternized membranes were prepared with different doping times, ranging from 35 min to 120 min, to study the impact of doping time (which affects acid uptake).

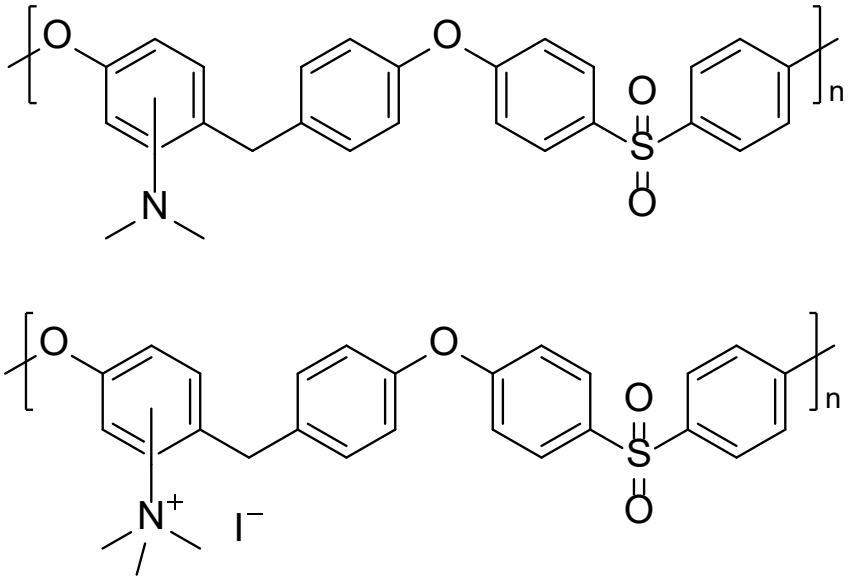

Figure 7.2 The representative structures of the diaminated polysulfone membranes. Top panel shows the chemical structure of the diaminated polysulfone. The bottom panel shows the quaternized form of the diaminated polysulfone with iodide as the counterion. In the diaminated polysulfone membranes, the IEC of the membrane is controlled between 1.0 - 2.5 meq/g.

Water dynamics in the undoped membranes were studied at full hydration after immersion in water over 48 h. The membranes were loaded into a sealed Delrin cell with the same procedure as described in chapter 3. Diffusion NMR experiments were carried out on a 400 MHz Bruker Avance III (9.4 T) spectrometer equipped with a Diff60 diffusion probe. Variable-temperature experiments were conducted between 30 °C and 40 °C to extract the activation energies of diffusion. Diffusion time was varied between 20 ms and 400 ms to study restricted diffusion in these membranes. The phosphoric-acid doped membranes were characterized on a 600 MHz Bruker AVANCE™ III NMR spectrometer equipped with a high-temperature DOTY diffusion probe. Diffusion coefficients for both proton and phosphorus were reported. Variable-temperature experiments were conducted between 0 °C and 150 °C to investigate the high-temperature performance of the doped membrane.

7.2.3 Water Dynamics in Non-Phosphoric-Doped Membranes

To understand the micro- and nano-scale dynamics of ion transport in the undoped membranes, we perform both variable-temperature and variable-diffusion time experiments. **Table 7.1** summarizes the diffusion coefficient of water as a function of diffusion time in all the undoped membranes. We label the membranes in terms of the percentage of quaternized sidechains and the quaternization method. In the undoped membranes, the water diffusion coefficient, D, decreases continuously with increasing diffusion time. We observe several general trends in these data. First, the solution-quaternized (SQ) membranes tend to have higher diffusion coefficients than the film-quaternized (FQ) membranes. Second, the tortuosity (see definition in section 1.2.2) of the SQ membranes tends to be lower than the FQ membranes, indicating a better-connected hydrophilic network in the SQ membranes. Here, we calculate the tortuosity based on the ratio between diffusion coefficient at shortest diffusion time $D(20\,\mathrm{ms})$ and diffusion coefficient at

longest diffusion time $D(400\ \text{ms})$

$$\text{tortuosity} = \frac{D(20\ \text{ms})}{D(400\ \text{ms})} \tag{7.4}$$

The above tortuosity reports on the connectivity of hydrophilic domains on 1-5 μm scale. As mentioned in chapter 1, the major structural features on this lengthscale are the boundaries between locally ordered grains. Overall, the observed tortuosity is lower in membranes with a higher percentage of quaternized sidechains, which is reasonable considering that the size of the nanoscale hydrophilic domains (pathways for water diffusion) should be larger with more ionic sidechains, thus leading to larger locally ordered grains (collections of hydrophilic pathways).

Table 7.1 Diffusion coefficients of water ($\times 10^{-11}$ m^2/s) at 25 °C in undoped membranes as a function of diffusion time.

Diffusion time (ms)	**x% SQ**	**x% FQ**	**1.6x% SQ**	**1.6x% FQ**	**2.4x% SQ**	**2.4x% FQ**
20	1.69	0.62	3.12	2.25	3.75	2.39
30	1.03	0.47	2.96	2.21	3.61	2.26
40	1.09	0.38	2.94	2.22	3.54	2.06
60	0.90	0.34	3.19	2.2	3.43	1.97
100	0.76	0.28	3.02	2.07	3.31	1.86
200	0.58	0.26	2.78	1.67	3.01	1.67
400	0.52	0.23	1.96	0.88	2.57	1.40
Tortuosity	3.2	2.7	1.6	2.5	1.5	1.7

Table 7.2 below shows a comparison of activation energies (E_a) of undoped membranes. In **Figure 7.3**, we compare the E_a of these undoped membranes to that of Nafion, the benchmark membrane for proton-exchange membrane fuel cells. The E_a of Nafion is collected at varying hydration level[11] while all the NanoSonic membranes are fully hydrated. Overall, the E_a of the undoped membranes increases with an increasing percentage of quaternized sidechains. We must

emphasize that the maximum hydration of these membranes does not considerably increase with an increasing percentage of quaternized sidechains, which may be due to the rigid backbones of these membranes. Thus, the water/ionic group ratio is actually the smallest in the 2.4x% SQ/FQ membranes. Moreover, water in the fully hydrated Nafion membrane has an E_a of 20 kJ/mol. In our previous study, we find that E_a serves as a probe for the nanoscale environment in the polymer membranes.[11-12] The activation energy of diffusion reflects interactions and restrictions on the molecular scale. Based on **Table 7.2**, the E_a in 1.6x% and 2.4x% quaternized membranes are similar, while E_a in the x% SQ membrane is lower than the rest. The low E_a agrees with the x% membrane's lower ionic content, and therefore decreased water-ion interactions.

Table 7.2 Activation energy of water in the undoped membranes

Membrane	Activation energy (kJ/mol)
x% SQ	21
1.6x% SQ	25
1.6x% FQ	27
2.4x% SQ	26
2.4x% FQ	25

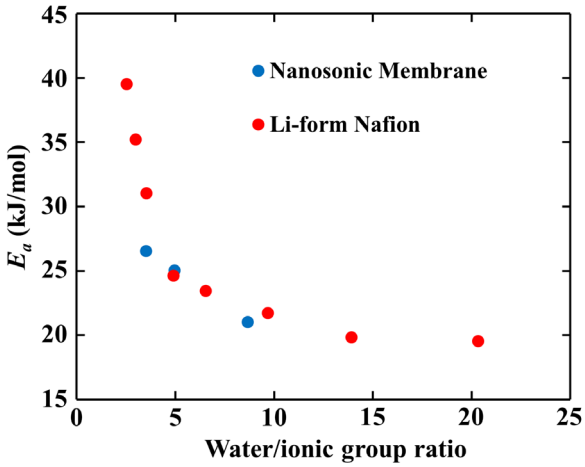

Figure 7.3 E_a in hydrated but non-phosphoric-acid-doped membranes, as compared to that in Nafion. The water/ionic group (quaternary ammonium) ratio represents the molar ratio between water molecules and quaternized sidechains in these membranes. We estimate the error of E_a to be ± 2 kJ/mol. These doped membranes have favorable water transport in that they have similar E_a to the benchmark hydrated membrane Nafion.

7.2.4 Dynamics of Proton and Phosphate in Phosphoric-Acid Doped Membranes

As mentioned above, all the phosphoric-acid-doped membranes are based on solution-quaternized membranes. In this section, we label the membranes only by their percentage of quaternized sidechains. **Figure 7.4** and **Table 7.3** compare the diffusion coefficients and E_a of the phosphoric-acid-doped 1.6x% and 1.2x% quaternized membranes. The membranes are first heated to 120 °C to remove residual water on the surface. We notice that the diffusion coefficient of protons at 120 °C is $\sim 2\times10^{-10}$ m^2/s, which is 3 times lower than water in fully hydrated Nafion at room temperature. However, we must emphasize that the diffusion coefficient here is an average of all proton-containing species such as H_3O^+, $H_4PO_4^+$, $H_2PO_4^-$, and the same rule applies to the diffusion coefficient of phosphorus. We observe small but still substantial diffusion coefficients for proton and phosphorous at a temperature as low as 0 °C, which is impressive considering that the melting point of phosphoric acid is 42 °C. Furthermore, the 1.2x% quaternized membrane exhibits diffusion coefficients a factor of two lower than those in the 1.6x% quaternized membrane. One possible contribution to the difference, as pointed out in the previous section, is that the tortuosity tends to be lower with a higher percentage of quaternized sidechains.

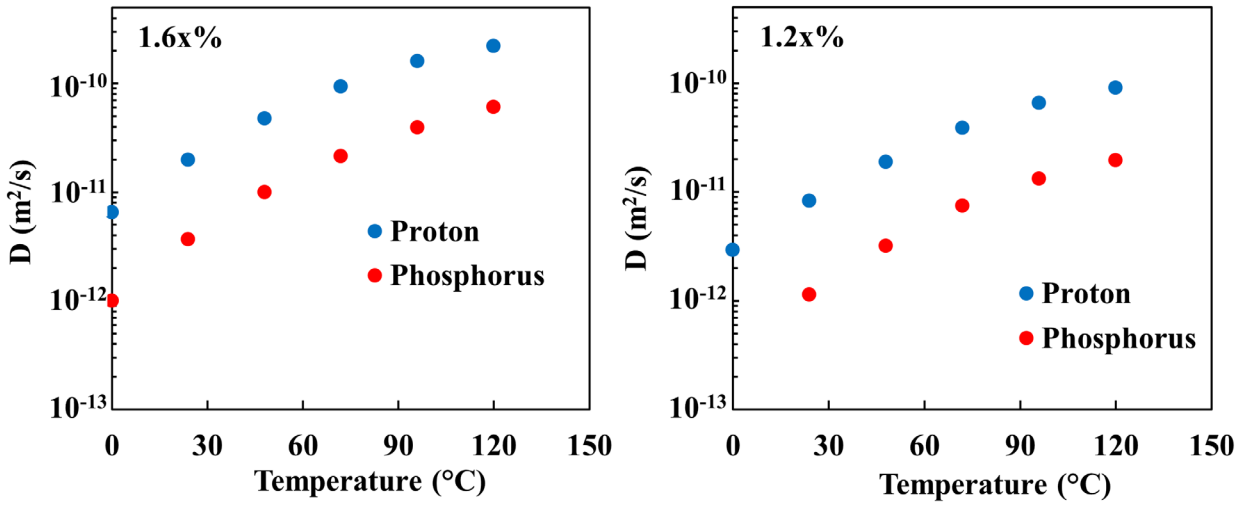

Figure 7.4 Diffusion coefficients of ^{1}H and ^{31}P in phosphoric-acid-doped membranes with 1.6x% and 1.2x% quaternary ammonium side groups. Note that we could not determine the diffusion coefficient of phosphorus in the 1.2x% quaternized membrane at 0 °C due to the slow dynamics (and short T_2 relaxation) combined with limitations of the minimum gradient pulse durations.

Table 7.3 E_a of proton and phosphorous in quaternized (1.6x% and 1.2x%) membranes that are phosphoric-acid-doped.

Membrane	$\boldsymbol{E_a}$ of proton (kJ/mol)	$\boldsymbol{E_a}$ of phosphorous (kJ/mol)
1.6x%	26	30
1.2x%	26	29

We extract the activation energy from diffusion data taken over the 0 - 120 °C temperature range. The activation energy for protons is slightly smaller than that of phosphorous while being more different from water (around 17 kJ/mol at a similar temperature range), suggesting that transport of protons is closely coupled to the phosphate and the presence of bulk water is limited. Overall, there is little difference in E_a between the 1.6x% and 1.2x% quaternized membranes. Thus,

the nanoscale environment[11-12] (e.g., interactions between mobile species and ionic head groups, and nanoconfining restrictions on the mobile species) is also similar for these membranes. The difference in diffusion coefficients among the above three membranes is more likely to relate to the tortuosity at a larger lengthscale (10 nm - 1 μm).

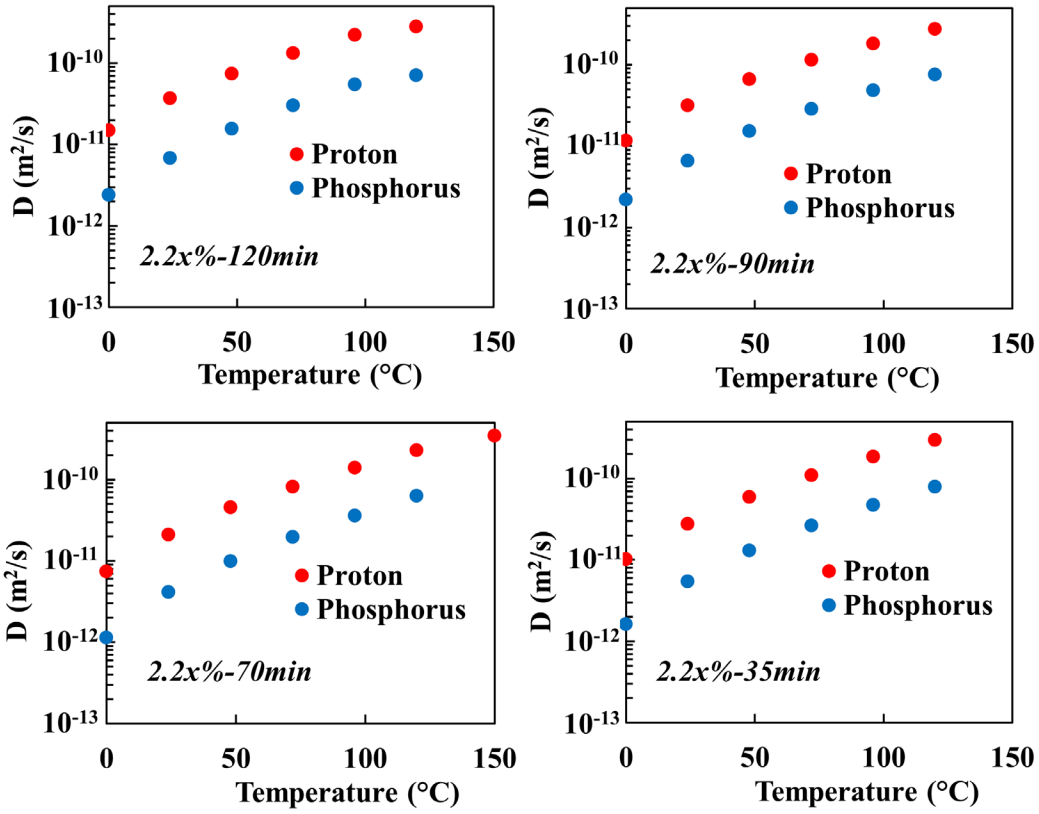

Figure 7.5 Diffusion coefficients of proton and phosphorus as a function of temperature in phosphoric-acid-doped 2.2x% quaternized membranes (doping time in minutes is labeled after the quaternization percentage).

Table 7.4 E_a of proton and phosphorous in phosphoric-acid-doped 2.2x% quaternized membranes

Membrane	E_a of proton (kJ/mol)	E_a of phosphorous (kJ/mol)
2.2x%-120min	24	27
2.2x%-90min	24	27

2.2x%-70min	25	30
2.2x%-35min	25	29

The 2.2x% quaternized membranes do exhibit different transport properties as a function of doping time (**Figure 7.5** and **Table 7.4**). Overall, the doped 2.2x% quaternized membranes all show higher diffusion coefficients than the doped 1.6x% and 30 % quaternized membranes, while exhibiting slightly lower activation energies. A longer doping time leads to lower E_a. We propose that a longer doping time leads to higher loading of phosphoric acid in the membrane, which makes the phosphoric acid more bulk-like locally. Generally, we observe higher diffusion coefficients with increasing doping time. The enhancement of diffusion mainly happens below 100 °C while the diffusion coefficients are all similar at 120 °C among these membranes. We also note that the 2.2x%-70M membrane is lightly crosslinked. We observe that it has the lowest diffusion coefficients (around 1.2x% lower than the 2.2x%-35M membrane) among all the 2.2x% membranes. Meanwhile, the E_a of the crosslinked membrane is higher than the other 2.2x% membranes. We measured proton diffusion at 150 °C for the crosslinked membrane, and the data point does fall into the trend, suggesting a stable membrane matrix and transport of mobile species at a temperature close to the boiling temperature of phosphoric acid.

The measurements of spin-spin relaxation time (T_2) in the doped membranes reveal interesting trends. **Figure 7.6** shows the T_2 of proton and phosphorus in the doped 1.2x% and 1.6x% quaternized membranes. We observe that the T_2 of proton continuously increases with increasing temperature while the T_2 of phosphorus reaches a maximum between 50 °C and 70 °C. We also notice that these trends are reproducible when either increasing temperatures or decreasing temperatures. The spin-spin relaxation time is related to the rotational motion of the molecules. A faster rotating molecule always has a higher T_2.[13] However, the T_2 trend of phosphorus in these

membranes seems to indicate that the phosphorus-containing species are rotating slower when temperature increases above 70 °C. We propose that the different trends of T_2 between phosphorus and proton are due to the condensation reaction of phosphoric acid. Even at temperatures slightly higher than room temperature,[14] the condensation of phosphoric acid may proceed as

$$2H_3PO_4 \rightleftharpoons H_2O + H_4P_2O_7$$

And larger phosphorus complexes form at elevated temperatures.[15] These reactions are reversible and shift to the products with increasing temperature. We reckon that these larger phosphorus complex would rotate slower and gives rise to a shorter T_2. With increasing temperatures, the population of the larger complex becomes dominant among the phosphorus-containing species, bringing down the T_2 even more. Meanwhile, we hypothesize that either the T_2 of proton depends more on the residual water (generated by the condensation reaction) in the doped membranes, or the proton increasingly follows Grotthuss hopping above the region where the ^{1}H and ^{31}P T_2 curves diverge. We also observe that the increasing trend of proton T_2 slows down above 90 °C. Thus, the formation of a larger phosphorus complex still might have a nontrivial impact on the average T_2 of the proton.

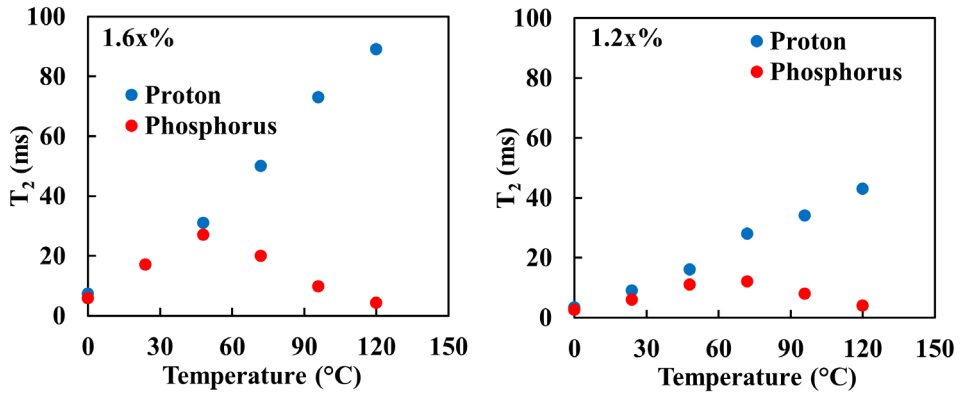

Figure 7.6 Spin-spin relaxation time (T_2) of ^{1}H and ^{31}P in the doped 1.2x% and 1.6x% quaternized membranes as a function of temperature. The T_2 in the 1.6x% quaternized membranes is about twice that in the 1.2x% quaternized membrane, consistent with the faster dynamics of mobile

species in the 1.6x% membrane.

7.2.5 Summary

In summary, we have measured the diffusion coefficients and activation energies for the phosphoric-acid-doped and undoped membranes. Activation energies indicate that these membranes are similar (in terms of the local energetic environment for protons) to the benchmark membrane Nafion on the nanometer lengthscale. The diffusion coefficients support more connected channels with an increasing percentage of quaternized sidechains. For phosphoric-acid doped membranes, increasing doping time and the percentage of quaternary ammonium both have positive effects on proton transport.

7.3 Water Dynamics in Hydrated Polyolefin-based Membranes

7.3.1 Introduction

As mentioned in chapter 1, there are two major categories of ion exchange membranes: cation exchange membranes (CEMs) and anion exchange membranes (AEMs). In fuel cell applications, CEMs are the first candidate due to their high ionic conductivity and chemical/mechanical stability. However, a few drawbacks stand in the way of a broad application of CEMs in fuel cells. In CEM-based hydrogen fuel cells, platinum-based catalyst facilitates the conversion of hydrogen gas into protons. The platinum catalyst is expensive and suffers poisoning from carbon monoxide and sulfur.[16-17] In addition, perfluorinated CEMs such as Nafion pose an environmental hazard during the synthetic process and potentially during end-of-life breakdown. Due to these drawbacks, the exploration of AEM-based fuel cells carries great scientific and practical merit.[18-20] Comparing to CEMs, AEM-based fuel cells work with cheaper catalysts and

are less vulnerable to catalyst poisoning. In this section, we look into a polyolefin-based AEM provided by Prof. Michael Hickner's[19] group at Pennsylvania State University, and evaluate its transport performance in comparison to CEMs.

7.3.2 Experimental Details

The synthesis (chemical structure shown in **Figure 7.7a**) and the fabrication of this poly(olefin)-based AEM follow a previous literature procedure.[19] The membrane is supplied by Megan Matta from Prof. Micheal Hickner's group. The IEC of the membrane is 1.64 mmol/g, defined as the moles of counterions ($n_{counterion}$) per unit mass of the dry membrane ($m_{dry\ membrane}$)

$$\mathrm{IEC} = \frac{n_{counterion}}{m_{dry\ membrane}} \tag{7.5}$$

The water/ionic group ratio (λ) of the membrane is related to IEC by

$$\lambda = \frac{m_{hydrated\ membrane} - m_{dry\ membrane}}{m_{dry\ membrane}} \times \frac{1000}{18 \times \mathrm{IEC}} \tag{7.6}$$

These polyolefin-based membranes are cut into small pieces and rolled into a cylindrical shape. The sample membranes are immersed in HPLC water for over two days before subjecting to measurements. Diffusion experiments are conducted on a 400 MHz Bruker Avance III (9.4 T) spectrometer equipped with a Diff60 diffusion probe. The diffusion coefficients and activation energy of water molecules are measured as a function of hydration level λ. Restricted diffusion is studied at a few selected hydration levels (169 wt%, 43 wt%, 9 wt% of water).

7.3.3 Result and Discussions

Figures 7.7 presents the diffusion coefficients and activation energy (E_a) of water in this poly(olefin)-based membrane at 25 °C. Again, we compare the performance of this AEM to the

benchmark CEM Nafion. The diffusion coefficient of water in the AEM appears to be slightly lower (< 10%) than that of Nafion at the same hydration. The maximum hydration of the polyolefin-based AEM is much higher than for CEMs like Nafion. While the swelling may lead to mechanical degradation of certain AEMs, we observe that this AEM stays firm at maximum hydration. The extracted activation energy of this AEM is also quite similar to that of Nafion. We observe bulk-like E_a with λ higher than 5 or 6. We observe the confinement effect at relatively low hydration.[10] Overall, the transport performance of this membrane is similar to that of Nafion, and further improvements may give rise to an AEM that is cheaper and performs better than CEMs.

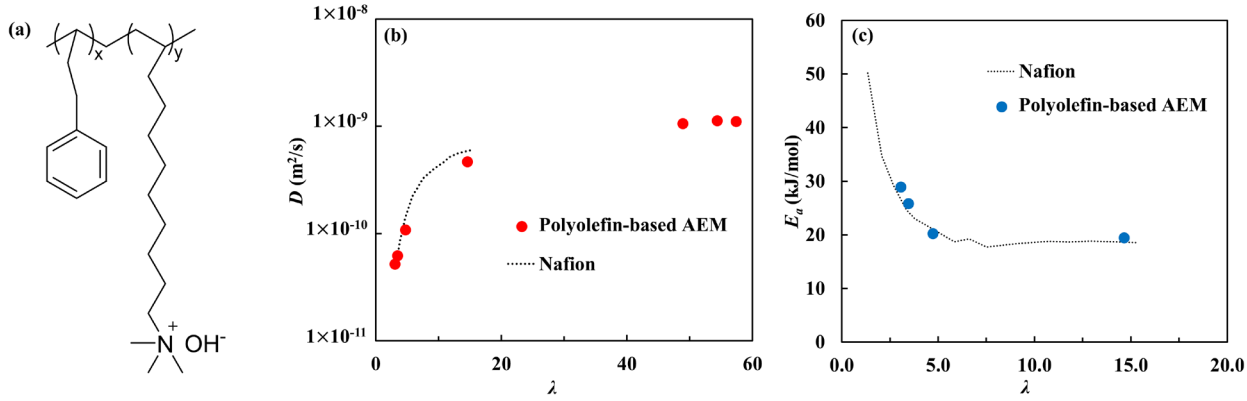

Figure 7.7 Panel (a) shows the chemical structure of the polyolefin-based ionomer. Adapted with permission from Ref. 19, copyright (2019) John Wiley and Sons. Panels (b) and (c) show the diffusion coefficient (D) and activation energy of diffusion (E_a) of water in the polyolefin-based AEM as a function of the water/counterion ratio (λ). The dashed line stands for data generated from acid-form Nafion.

Figure 7.8 shows the diffusion coefficients of water in this polyolefin-based AEM as a function of diffusion time. We select three hydration levels that correspond to almost saturated (169%), medium (43%), and low hydrations (9%). We observe modest restricted diffusion at all

selected hydration levels. Higher hydration gives rise to stronger signals, which enables measurements at a longer diffusion time. There is only around 20% - 30% drop of diffusion coefficient as the diffusion time goes from 15 ms to the longest diffusion time at each hydration. The tortuosity of this membrane, based on equation 7.4, would ranges from 1.3 to 1.5 for the three hydration levels observed here. The tortuosity barely changes when varying the hydration level quite drastically. Based on the diffusion coefficients, the diffusion length probed here ranges between 2 μm and 40 μm. These results indicate that the hydrophilic domains are well connected in these AEMs.

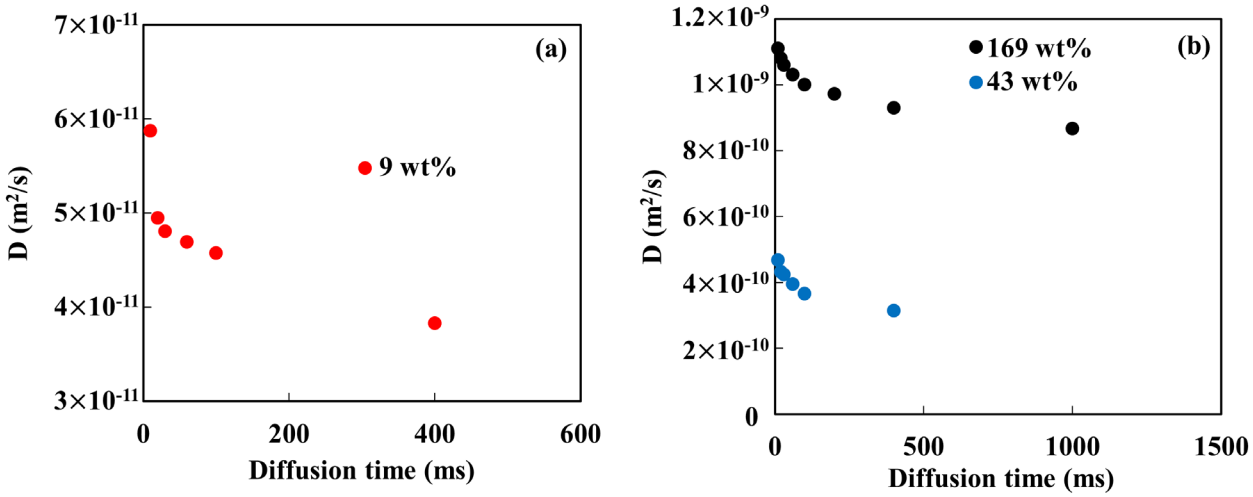

Figure 7.8 Restricted diffusion in the polyolefin-based AEM. The diffusion time ranges between 10 ms and 1 s (only at the highest hydration). The hydration level is calculated as the weight percent of water with respect to the dry membrane. A continuous decrease of the diffusion coefficient is observed at all hydration levels.

7.3.4 Summary

We investigate the transport properties of a polyolefin-based AEM. We reveal that the transport of water through this membrane is almost as fast as the benchmark CEM Nafion. The diffusive

activation energy is close to that of bulk water at high hydration levels, and we also observe the confinement effect in this membrane at low hydration. Restricted diffusion reveals well-connected hydrophilic domains on the micrometer lengthscale, and the connectivity is well maintained with varying hydration.

7.4 Quantitative ^{13}C NMR of Wood ^{13}C Isotope Content

7.4.1 Introduction

The net reaction of plant photosynthesis is selective regarding the isotope of carbon.[21-24] Most plants tend to absorb ^{12}C-containing carbon dioxide, leading to a slightly lower abundance of ^{13}C in the plants than in nature. Measuring ^{13}C abundance in plants provides rich information about the impact of geography and climate on the plants. The conventional way to measure the abundance of ^{13}C is isotope ratio mass spectroscopy (IRMS).[25] In the absence of an IRMS instrument, quantitative ^{13}C-NMR provides an alternative way to quantify the abundance of ^{13}C. Several experimental features are required for a highly quantitative NMR experiment (error < 0.1%).[26] First, the NMR experiment should use a 90° pulse for the signal excitation (refer to section 2.2.2). Second, the repetition time (the duration of one scan in an NMR experiment) needs to be at least five times the spin-lattice relaxation time T_1 (refer to). Third, the signal-to-noise ratio (SNR) should be above 600 to obtain a quantitative spectrum.[27]

Additionally, ^{13}C-NMR experiments often involve proton decoupling to avoid signal overlap and intensity reduction due to peak splitting. The standard proton decoupling sequence leads to the so-called nuclear Overhauser effect (NOE).[28] NOE originates from the dipolar cross relaxation between neighboring ^{13}C and ^{1}H nucleus and will enhance the intensity of ^{13}C signals. Signal enhancement from NOE is stronger when more protons connect to a given carbon. In other

words, the signal enhancement from NOE follows this order: primary carbon > secondary carbon > tertiary carbon > quaternary carbon. Thus, NOE enhancement is not generally quantitative and makes the resulting ^{13}C signals non-quantitative. To achieve quantitative ^{13}C-NMR, a crucial requirement is that the proton decoupling is conducted (^{1}H irradiation only during signal collection) without inducing the NOE differential signal enhancement.

The major challenge in quantitative ^{13}C-NMR, which is also why NMR is uncommon for quantitative ^{13}C analysis, is the time efficiency. The T_1 of ^{13}C is on the order of seconds to tens of seconds, which means the repetition time for a quantitative ^{13}C-NMR experiment may need to be on the timescale of minutes. Additionally, the abundance of ^{13}C is low (~ 1.1%), which means it would take a significant number of scans (usually several thousand) to get to the satisfactory signal-to-noise ratio (SNR). The combination of a long repetition time and a large number of scans makes quantitative ^{13}C-NMR experiment too long (one or two days) to be considered efficient.

To increase the time efficiency of a quantitative ^{13}C-NMR experiment, the only plausible method is to decrease the T_1 of ^{13}C. In a liquid sample, T_1 relaxation mainly relies on the dipolar couplings between NMR active nuclei. Due to the low abundance of ^{13}C, it is unlikely that a ^{13}C nucleus resides next to another ^{13}C nucleus. Thus, the T_1 relaxation of a ^{13}C nucleus primarily depends on the number of protons in close proximity (with a few angstroms). Primary ^{13}C usually has a lower T_1 than other types of ^{13}C nucleus. However, the number of protons that bond with the same carbon atom is limited (mostly less than 4). To effectively reduce the T_1 of ^{13}C to sub-second values, a relaxation agent is needed. A relaxation agent is typically a salt or metal complex made from a transition metal ion that contains unpaired electrons. The electron spin magnetism of the unpaired electrons couples with nuclear spins. The nucleus-electron coupling, which is much stronger than the dipolar couplings between nuclei, combined with the fluctuating fields due to the

electron moments effectively lower the T_1 of the observed ^{13}C nucleus. In this work, we explore experimental parameters such as the type and amount of relaxation agent to achieve a satisfactory quantitative ^{13}C-NMR spectrum within a relatively short experimental time.

7.4.2 Experimental Details

The sample is the formaldehyde-sodium bisulfite adduct ($HOCH_2SO_3Na$), which results from the reaction between formaldehyde (obtained from wood and wood product decomposition) and sodium bisulfite.

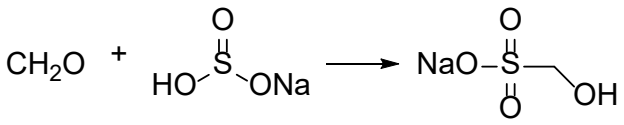

99% ^{13}C-labeled acetic acid ($^{13}CH_3{}^{13}COOH$) is used as an internal standard for quantification. The sample and the labeled standard are provided by Niloofar Y. Shivyari from Prof. Charles Frazier's group at Virginia Tech. Varying amounts of two relaxation agents (gadolinium(III) chloride ($GdCl_3$) and diethylenetriaminepentaacetic acid gadolinium (III) dihydrogen salt hydrate ($C_{14}H_{20}GdN_3O_{10}{\cdot}xH_2O$)), 50 mg of the adduct sample, and 5 mg of the internal standard are dissolved in HPLC H_2O for NMR measurements. ^{13}C-NMR is performed on a 500 MHz Bruker NMR spectrometer equipped with a cryoprobe. All the experiments are conducted at room temperature with a repetition time of $5\times T_1$. Proton-decoupling is conducted with the inverse-gated-decoupled ^{13}C NMR pulse sequence at a decoupling power of 2 W. The optimized combination (for short T_1 and yet sufficient spectral resolution) is found to contain 2 mg of the $C_{14}H_{20}GdN_3O_{10} \cdot xH_2O$ relaxation agent with a repetition time of 1.9 s and a number of scans of 4800.

7.4.3 Result and Discussions

Figure 7.9 shows the ^{13}C-NMR spectrum of the adduct $HOCH_2SO_3Na$ and the internal

standard $^{13}CH_3{}^{13}COOH$ without the presence of a relaxation agent. This adduct derives from the reaction of formaldehyde (from wood decomposition) with a solution of sodium bisulfite The adduct gives a singlet at 74.1 ppm, while the internal standard shows two doublets at 23.2 ppm and 181.5 ppm. The peak splitting comes from the ^{13}C – ^{13}C coupling (since this molecular is 99% ^{13}C labeled). The spectrum here is not quantitative as a short repetition time is used for fast acquisition of the spectrum. The T_1 relaxation time of the ^{13}C in the sample is > 10 s, which means it would take over 50 s to conduct one quantitative scan. Thus, reducing the T_1 is crucial for conducting an efficient quantitative ^{13}C-NMR experiment on this sample.

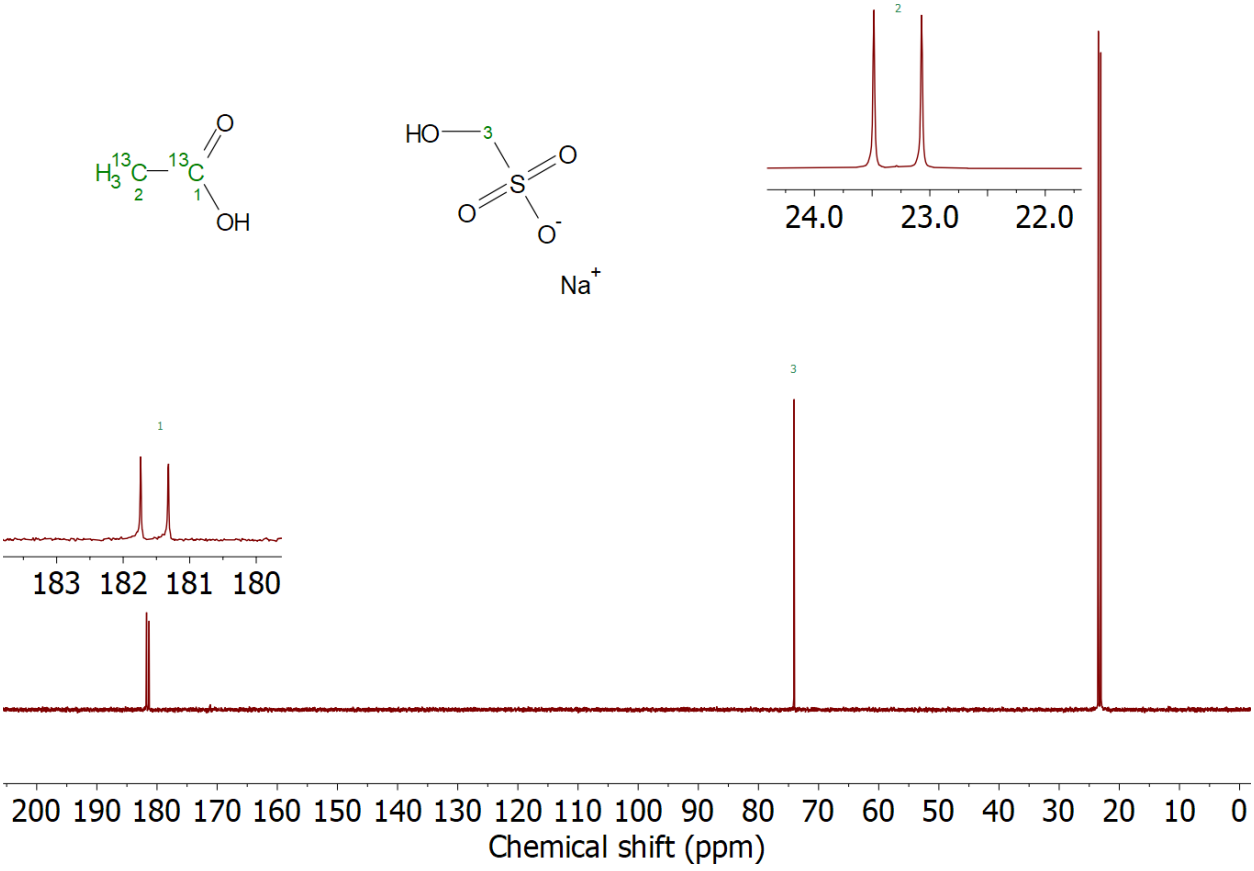

Figure 7.9 Carbon-13 spectrum of the sample and the internal standard without a relaxation agent.

Figure 7.10 shows the ^{13}C-NMR spectrum of the system with the relaxation agent $GdCl_3$.

We notice that the short relaxation time disproportionally impacts the ^{13}C signal intensities of the desired adduct and the standard. While the relaxation time of all ^{13}C nuclei are reduced, the reduction of the internal standard peak intensities is much more significant than those of the sample. After adding 1.6 mg of the relaxation agent $GdCl_3$, the T_1 of the desired adduct nucleus is still on the timescale of seconds while the T_1 of the internal standard is ~100 ms. This suggests that the relaxation agent is interacting disproportionality more strongly with the internal standard than with the sample. Moreover, the spin-spin relaxation time, T_2, of the internal standard becomes so short that the peaks broaden substantially. The massive decrease in the relaxation times of acetate ^{13}C suggests that the magnetic interactions between gadolinium and acetate group are much stronger than those between gadolinium and the adduct.

The strong magnetic interactions between gadolinium ions and acetate groups prompt fast spin-lattice relaxation of ^{13}C in the acetate. The strength of the nucleus-electron coupling depends on the distance between the unpaired electron and the nucleus. It is likely that the acetates groups are closer to the gadolinium ions due to ion-ion interactions. The change of T_1 also impacts T_2, because T_2 cannot be faster than T_1. Furthermore, the acetate groups shield the gadolinium ion from interacting with the adduct sample, making the relaxation time of the sample less dependent on the addition of $GdCl_3$. The chemical shift difference between the two spectra in **Figure 7.9** also originates from the electron-nucleus interactions. The magnetic field generated by the unpaired electrons of gadolinium ion alters the average local magnetic field strength of the acetate, thus changing the values of chemical shift.

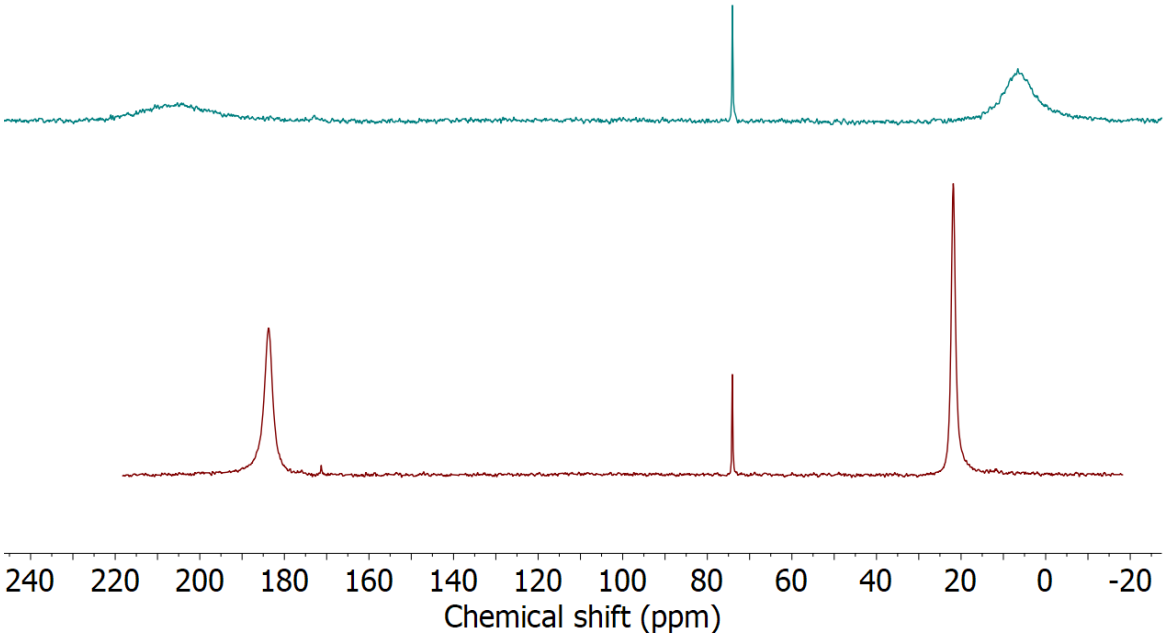

Figure 7.10 Carbon-13 spectrum of the adduct and the internal standard with 0.3 mg of $GdCl_3$ (bottom panel) and 1.6 mg of $GdCl_3$ (top panel).

Based on the trials using $GdCl_3$, a relaxation agent that interacts strongly with the acetic acid disproportionally impacts the relaxation rate of the sample and the internal standard, which is not ideal for collecting quantitative ^{13}C-NMR in a short time. As a result, we turn to a different relaxation agent, $C_{14}H_{20}GdN_3O_{10} \cdot xH_2O$, which is already a metal complex. We anticipate that the ligand in this relaxation agent binds strongly with the gadolinium ion and prevents the association of acetates with metal ions. **Figure 7.11** shows the ^{13}C-NMR spectrum with 2 mg of this relaxation agent. As expected, we observe a similar decrement in T_1 for both the adduct and the labeled acetic acid. The adduct peak carries the longest T_1, 0.36 s, among all the peaks.

Throughout literature, the isotopic signature ($\delta^{13}C$) is a typical way to quantify the abundance of ^{13}C in plants[29]

$$\delta\,^{13}\mathrm{C} = \left(\frac{(^{13}\mathrm{C}/^{12}\mathrm{C})_{adduct}}{(^{13}\mathrm{C}/^{12}\mathrm{C})_{standard}}\right) \times 1000‰ \qquad (7.8)$$

where $(^{13}\mathrm{C}/^{12}\mathrm{C})_{adduct}$ is the molar ratio between ^{13}C and ^{12}C in the adduct, and $(^{13}\mathrm{C}/^{12}\mathrm{C})_{standard}$ is the molar ratio between ^{13}C and ^{12}C in nature. By integrating the peak areas in the quantitative NMR spectrum, we determine a ^{13}C signature $\delta\,^{13}\mathrm{C}_{QNMR} = -47.40‰$. In comparison, the isotopic signature determined by isotope-ratio mass spec (IRMS) is $\delta\,^{13}\mathrm{C}_{IRMS} = -47.89‰$. The difference between the two techniques is 1%. Clearly, this ^{13}C NMR experiment can yield precise quantitation of isotopic ratio in wood-derived adduct samples that contain carbon.

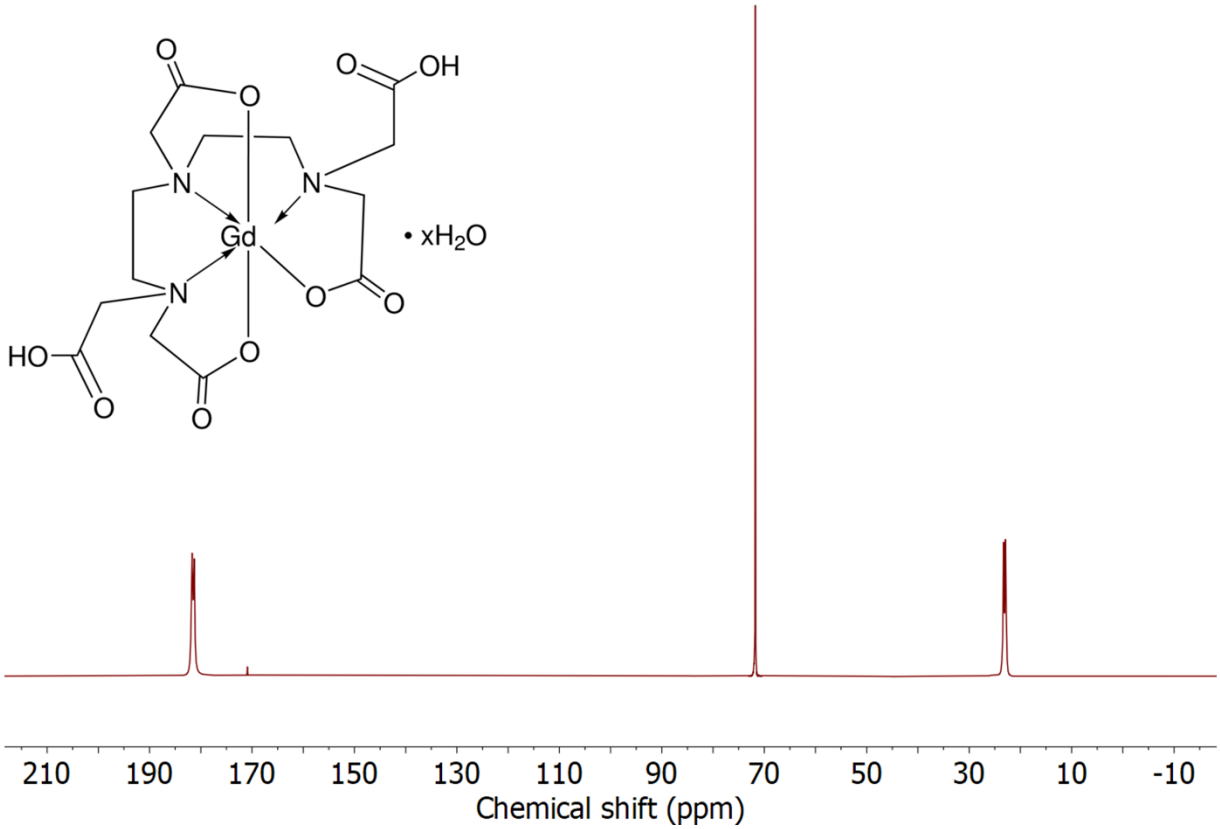

Figure 7.11 Carbon-13 spectrum of the sample and the internal standard with 2.0 mg of $C_{14}H_{20}GdN_3O_{10}{\cdot}xH_2O$. The embedded chemical structure is the relaxation agent.

7.4.4 Summary

To achieve a quantitative ^{13}C-NMR spectrum in a relatively short time, the appropriate type and amount of relaxation agent are crucial. We choose the appropriate relaxation agent that has a similar impact on the T_1 of both the sample and the internal standard. We manage to obtain a quantitative ^{13}C-NMR spectrum with an SNR of 600 within 3 hours. The difference between the result of NMR and IRMS is 1%.

7.5 References

1. Mitchell, J. B.; Geise, N. R.; Paterson, A. R.; Osti, N. C.; Sun, Y. Y. L.; Fleischmann, S.; Zhang, R.; Madsen, L. A.; Toney, M. F.; Jiang, D. E.; Kolesnikov, A. I.; Mamontov, E.; Augustyn, V. Confined Interlayer Water Promotes Structural Stability for High-Rate Electrochemical Proton Intercalation in Tungsten Oxide Hydrates. *ACS Energy Lett.* **2019,** *4*, 2805-2812.
2. Wu, X. Y.; Hong, J. J.; Shin, W.; Ma, L.; Liu, T. C.; Bi, X. X.; Yuan, Y. F.; Qi, Y. T.; Surta, T. W.; Huang, W. X.; Neuefeind, J.; Wu, T. P.; Greaney, P. A.; Lu, J.; Ji, X. L. Diffusion-free Grotthuss topochemistry for high-rate and long-life proton batteries. *Nat. Energy* **2019,** *4*, 123-130.
3. Whittingham, M. S. Hydrogen motion in oxides: from insulators to bronzes. *Solid State Ionics* **2004,** *168*, 255-263.
4. Mitchell, J. B.; Lo, W. C.; Genc, A.; LeBeau, J.; Augustyn, V. Transition from Battery to Pseudocapacitor Behavior via Structural Water in Tungsten Oxide. *Chem Mater* **2017,** *29*, 3928-3937.
5. H. Levitt, M. Spin dynamics: basics of nuclear magnetic resonance. **2001**.
6. Pedersen, B. The Equilibrium Hydrogen-Hydrogen Distances in the Water Molecules in Potassium and Rubidium Oxalate Monohydrates *Acta Cryst.* **1966,** *20*, 412-417.
7. Pake, G. E. Nuclear Resonance Absorption in Hydrated Crystals - Fine Structure of the Proton Line. *J. Chem. Phys.* **1948,** *16*, 327-336.
8. Dolinsek, J.; Apih, T.; Lahajnar, G.; Blinc, R.; Papavassiliou, G.; Pintar, M. M. Two-dimensional nuclear magnetic resonance study of a hydrated porous medium: An application to white cement. *J. Appl. Phys.* **1998,** *83*, 3535-3540.
9. Gutowsky, H. S.; Pake, G. E. Structural Investigations by Means of Nuclear Magnetism. 2. Hindered Rotation in Solids. *J. Chem. Phys.* **1950,** *18*, 162-170.
10. Guvelioglu, G. H.; Stenger, H. G. Flow rate and humidification effects on a PEM fuel cell performance and operation. *J. Power Sources* **2007,** *163*, 882-891.
11. Zhang, R.; Chen, Y.; Troya, D.; Madsen, L. A. Relating Geometric Nanoconfinement and Local Molecular Environment to Diffusion in Ionic Polymer Membranes. *Macromolecules* **2020,** *53*, 3296-3305.
12. Lingwood, M. D.; Zhang, Z.; Kidd, B. E.; McCreary, K. B.; Hou, J.; Madsen, L. A. Unraveling the local energetics of transport in a polymer ion conductor. *Chem. Commun.* **2013,** *49*, 4283-4285.
13. Bloembergen, N.; Purcell, E. M.; Pound, R. V. Relaxation Effects in Nuclear Magnetic Resonance Absorption. *Phys. Rev.* **1948,** *73*, 679-712.
14. Munson, R. A. Self-Dissociative Equilibria in Molten Phosphoric Acid. *J. Phys. Chem.* **1964,** *68*, 3374-3377.

15. Melchior, J. P.; Majer, G.; Kreuer, K. D. Why do proton conducting polybenzimidazole phosphoric acid membranes perform well in high-temperature PEM fuel cells? *Phys. Chem. Chem. Phys.* **2017,** *19*, 601-612.
16. Sung, Y. E.; Chrzanowski, W.; Zolfaghari, A.; Jerkiewicz, G.; Wieckowski, A. Structure of chemisorbed sulfur on a Pt(111) electrode. *J. Am. Chem. Soc.* **1997,** *119*, 194-200.
17. Jung, N.; Cho, Y. H.; Ahn, M.; Lim, J. W.; Kang, Y. S.; Chung, D. Y.; Kim, J.; Cho, Y. H.; Sung, Y. E. Methanol-tolerant cathode electrode structure composed of heterogeneous composites to overcome methanol crossover effects for direct methanol fuel cell. *Int J Hydrogen Energ* **2011,** *36*, 15731-15738.
18. Thieu, L. M.; Zhu, L.; Korovich, A. G.; Hickner, M. A.; Madsen, L. A. Multiscale Tortuous Diffusion in Anion and Cation Exchange Membranes. *Macromolecules* **2019,** *52*, 24-35.
19. Zhu, L.; Peng, X.; Shang, S. L.; Kwasny, M. T.; Zimudzi, T. J.; Yu, X. D.; Saikia, N.; Pan, J.; Liu, Z. K.; Tew, G. N.; Mustain, W. E.; Yandrasits, M.; Hickner, M. A. High Performance Anion Exchange Membrane Fuel Cells Enabled by Fluoropoly(olefin) Membranes. *Adv Funct Mater* **2019,** *29*, 1902059.
20. Zhu, L.; Yu, X. D.; Peng, X.; Zimudzi, T. J.; Saikia, N.; Kwasny, M. T.; Song, S. F.; Kushner, D. I.; Fu, Z. S.; Tew, G. N.; Mustain, W. E.; Yandrasits, M. A.; Hickner, M. A. Poly(olefin)-Based Anion Exchange Membranes Prepared Using Ziegler-Natta Polymerization. *Macromolecules* **2019,** *52*, 4030-4041.
21. Stewart, G. R.; Turnbull, M. H.; Schmidt, S.; Erskine, P. D. C-13 Natural-Abundance in Plant-Communities Along a Rainfall Gradient - a Biological Integrator of Water Availability. *Aust. J. Plant Physiol.* **1995,** *22*, 51-55.
22. Tibby, J.; Barr, C.; McInerney, F. A.; Henderson, A. C. G.; Leng, M. J.; Greenway, M.; Marshall, J. C.; McGregor, G. B.; Tyler, J. J.; McNeil, V. Carbon isotope discrimination in leaves of the broad-leaved paperbark tree, Melaleuca quinquenervia, as a tool for quantifying past tropical and subtropical rainfall. *Glob. Change Biol.* **2016,** *22*, 3474-3586.
23. Rao, Z. G.; Xu, Y. B.; Xia, D. S.; Xie, L. H.; Chen, F. H. Variation and paleoclimatic significance of organic carbon isotopes of Ili loess in arid Central Asia. *Org. Geochem.* **2013,** *63*, 56-63.
24. Liu, Y. J.; Zhang, L. R.; Niu, H. S.; Sun, Y.; Xu, X. L. Habitat-specific differences in plasticity of foliar delta C-13 in temperate steppe grasses. *Ecol. Evol.* **2014,** *4*, 648-655.
25. Rodionov, A.; Lehndorff, E.; Stremtan, C. C.; Brand, W. A.; Konigshoven, H. P.; Amelung, W. Spatial Microanalysis of Natural C-13/C-12 Abundance in Environmental Samples Using Laser Ablation-Isotope Ratio Mass Spectrometry. *Anal. Chem.* **2019,** *91*, 6225-6232.
26. Bharti, S. K.; Roy, R. Quantitative H-1 NMR spectroscopy. *Trac-Trend Anal. Chem.* **2012,** *35*, 5-26.
27. Bayle, K.; Grand, M.; Chaintreau, A.; Robins, R. J.; Fieber, W.; Sommer, H.; Akoka, S.; Remaudt, G. S. Internal Referencing for C-13 Position-Specific Isotope Analysis Measured by NMR Spectrometry. *Anal. Chem.* **2015,** *87*, 7550-7554.
28. Overhauser, A. W. Polarization of Nuclei in Metals. *Phys. Rev.* **1953,** *92*, 411-415.
29. Balesdent, J.; Mariotti, A.; Guillet, B. Natural C-13 Abundance as a Tracer for Studies of Soil Organic-Matter Dynamics. *Soil Biol. Biochem.* **1987,** *19*, 25-30.

Chapter 8 Summary and Future Work

8.1 Summary

This dissertation focuses on understanding the dynamics of confined liquids in ionomer membranes, focusing on two major aspects: geometric confinement and liquid-surface interactions. We investigated the diffusion behaviors of small molecules/ions under confinement with NMR diffusometry and MD simulations. Through these studies, we presented a variety of new insights into confined liquid dynamics.

In chapter 3, we investigated a lithium-form PFSA membrane experimentally and combined this work with MD simulations on variably confined water to gain key structure-dynamics insights. To understand the nanoscale structure-diffusion relations in ionomer membranes, we utilize activation energy (E_a) of diffusion as a probe for molecular-level energetics. We eliminate the effect of liquid-surface interactions by comparing E_a in membranes to E_a in solutions with similar intermolecular interactions. When comparing the PFSA membrane to bulk solutions, we notice an unusually high E_a for membrane diffusion at low hydration. By conducting MD simulations of water in carbon nanotubes, we attribute the elevation of E_a to the formation of ordered water at small confinement size (< 1.5 nm tube diameter). Such ordering happens when most water molecules become surface water. Considering that the size of a water molecule is around 2 Å and the intermolecular distance between water molecules is around 3 Å, the confinement size needs to be around 1 nm to bring most of the confined water to the confinement surface. In addition, we observe the membrane E_a to be slightly lower than bulk at high hydration. We attribute this to another nanostructure feature of the ionomer membrane−nanoscale phase separation. Nanoscale phase separation creates a substantial fraction of water that is locally bulk-like. This bulk-like water possesses E_a similar to bulk water and lower than that of water in free

solution. Such effects only happen at a relatively large confinement size, at which the population of bulk-like water becomes dominant. Through these studies, we reveal two structure-diffusion relations in ionomer membranes. At low hydration, the confined water (surface water) dominates, and we see the ordering of confined water, which gives rise to high E_a. At high hydration, bulk-like water is dominant, and we see bulk-like behavior from confined water in the ionomer membrane.

Chapter 4 expands our knowledge of the confinement effect by looking at various confining geometries, including carbon nanotubes, parallel graphene sheets, and parallel rigid carbon rods. While all these confining surfaces are hydrophobic, we observe retarded water dynamics in all of them with decreasing confinement size. Even though the increasing population of surface water molecules with smaller confinement size suggests a surface effect, we discover that the retarded water dynamics in hydrophobic confinement originates from increased associations among confined water molecules.

Starting from an observed similar effect of confinement and temperature on water dynamics, we quantify the parallel between confinement and temperature by calculating the residence time correlation function. We extract two residence times, a long and a short residence time, from the residence time correlation function. The residence times of water around water are on the timescale of picoseconds and these give insight into the association period between neighboring water molecules. We observe the residence times to increase with decreasing temperature or confinement size. We then propose that the prolonged associations between water molecules prompt retarded water dynamics under hydrophobic confinement. Additionally, we notice that the two residence times carry different meanings through further study. The long residence time directly relates to the diffusion coefficient, while the short residence time correlates

more strongly with the activation energy. These studies further reveal the physical origin of retarded water dynamics under hydrophobic confinement and rich information from the residence times.

In chapter 5, we investigate the effect of ions on liquid dynamics by studying bulk solutions of lithium triflate (LiOTf). By comparing Arrhenius plots of salt solutions at varying concentration, we notice a temperature-concentration superposition (TCS). The behavior of temperature-concentration superposition is a parallel concept to the classic time-temperature superposition observed for polymeric systems. By horizontally shifting the curves, the wide temperature range Arrhenius plot at any concentration can superimpose on the Arrhenius plot at another concentration. We can also create master curves by shifting Arrhenius plots at various concentrations to a reference concentration. We can extract the offset of reciprocal temperature from the shifting of curves. This offset of reciprocal temperature fits well with a WLF-type equation derived based on TCS. This temperature-concentration superposition behavior exists in both experimental and simulation results for LiOTf solutions. Additionally, we discover that TCS behavior is valid from the solubility limit of LiOTf to almost infinitely dilute solution. Based on the structural analysis of the LiOTf solutions, lowered temperature prompts a more ordered local water structure. However, the effect of temperature on local structuring around ions is more complicated. The presence of ions disrupts the hydrogen-bonding network (structure-breaking) between water molecules while prompting a structured and stable first solvation shell (structure-making).

In chapter 6, we investigate the confinement effect in the presence of ions/charges. Remarkably, we observe that nanoconfinement prompts longer associations between water molecules, while surface charges can disrupt the associations between water molecules. As observed in chapter 4, neutral-surface confinement leads to slower diffusion coefficients and

higher activation energies. When putting a small number of ions/charges onto the neutral confinement surface, the residence time of water decreases, accompanied by faster diffusion coefficients and lower activation energies. Inspired by the knowledge from chapter 5, we reveal the complicated effects of surface charges on confined water dynamics. First, the ion-dipole interactions between water molecules and surface charges cause extended associations (structure-making). Second, the surface charges pose long-range disruptions (structure-breaking) to the hydrogen-bonding network between water molecules. When the water-surface interactions are weak, the disruption of the hydrogen-bonding network is dominant, and we observe enhanced water dynamics. The enhancement region happens with only a relatively low fractional surface coverage of ions/charges. When the surface-bound ion density is high, the water-surface interactions overcome the structure-breaking effects, and we observe retarded water dynamics. Through these studies, we demonstrate that it is possible to observe enhanced water diffusion with the presence of ions or surface charges using classical force fields. We reveal the complicated effects of surface charges on the dynamics of confined water. Such knowledge is crucial for understanding transport in a host of ionic nanoporous materials.

In chapter 7, we review several projects that are related to the characterization of materials with NMR techniques. We collect solid-state NMR spectra of tungsten oxide hydrates to investigate the mechanism of proton transport in this material. Through the analysis of dipolar couplings, we confirm that the motions of water molecules are solid-like in this material. Thus, the observed fast proton conduction does not originate from the translational motions of water molecules. We investigate the performance of a phosphoric-acid-doped ionomer membrane (NanoSonic Inc.). In this work, we mainly focus on the diffusion coefficients of proton and phosphorus in the ionomer membrane. We study how the ion exchange capacity (IEC), casting

method, and doping time affect the transport properties of the membrane. We investigate the morphological and molecular environments by measuring restricted diffusion and activation energy. We performed high-temperature diffusion experiments up to 150 °C to investigate the thermal stability of the membrane and the mobile ions. In general, we discover that membranes with higher IEC and longer doping time have better transport performance, and we confirm the stability of membrane transport up to 150 °C. We then characterize the performance of a polyolefin-based anion exchange membrane (AEM). While AEMs are in general less stable and less conductive than cation exchange membranes (CEMs), we show that the transport performance of this polyolefin-based AEM nearly matches the benchmark Nafion. We have also optimized quantitative measurements of the abundance of ^{13}C in plant decomposition products with ^{13}C NMR. To effectively collect a quantitative ^{13}C NMR spectrum, we introduce a relaxation agent into our sample to reduce the spin-lattice relaxation time of ^{13}C. Through careful manipulation of the chemical structure and amount of the relaxation agent, we are able to achieve a quantitative ^{13}C NMR spectrum (difference with the conventional technique IRMS of less than 1%) within three hours.

8.2 Future Work

Several important questions remained to be answered. In most chapters, we have looked at the dynamics of confined water. The understandings on the dynamics of confined ions, especially protons, are important to energy storage devices such as fuel cells. In chapter 4, we calculated residence time correlation functions for both bulk and confined water. While the residence time correlation function fits best to a double exponential decay function, no first-principles theoretical explanation exists for this model. We propose that the short residence time signifies the time of

the ballistic regime while the long residence time signifies the pre-diffusive regime. However, this assumption needs much more evidence to be conclusive. We also observe the failure of the double exponential decay model when ion density in the systems is high. The failure calls for a more explicit model to properly extract the residence time of water/ions in a concentrated environment. We have also proposed that the long residence time of water is directly related to the diffusion coefficient through an inverse relationship. The exact relations between the residence times and the diffusion coefficient/activation energy remain unclear and need more dedicated work. We have investigated different 1D and 2D geometric nanoconfinement models, including carbon nanotubes, parallel graphene sheets, and rigid carbon rods. There are possibilities and needs for building up alternative confining geometries, such as the interconnected nanoporous structures. The aforementioned models have smooth surfaces and are highly symmetric. It is worth looking into models with rough surfaces and/or with more disordered geometries to approach real systems like polymer membranes.

In chapter 5, we originate and discuss a temperature-concentration superposition (TCS) effect in aqueous solutions. This superposition behavior remains an observation, and the origin of TCS is still unclear. In time-temperature superposition, the Adam-Gibbs theory[1] gives a theoretical derivation for the WLF equation. The Adam-Gibbs theory assumes a cooperative relaxation of polymer chains and that the viscosity of the material is proportional to the relaxation time. Similar reasoning can hardly be applied to the diffusion of small liquid molecules or ions in bulk solutions. However, the fact that the offset of reciprocal temperature fits well with a WLF-type equation suggests more physical insights can come from this TCS behavior. TCS behavior is almost perfect in simulation results, while we see slight deviations from the master curve in NMR experiments. Further measurements with wider temperature ranges in experiments, which may require different

instruments, should better help justify deviations from the master curve. We also observe large deviations from TCS in bulk water at low temperatures. This deviation happens with supercooling of water but not with supercooling of solutions. This unique deviation from bulk water may be related to the change of association modes between water molecules. However, the exact reason for the significant deviation, which may be instrumental for understanding TCS, is not yet known.

In chapter 6, we attempt to understand confined liquid dynamics under ionic confinement by putting ions/charges onto the confining surfaces. We discover that MD reaches a limit when simulating systems with high ionic density (water/ion molar ratio ≤ 5) due to the slow dynamics and lack of sufficient time averaging. At this moment, the major limiting factor in simulating slow dynamics is the calculation speed of current supercomputers. In the future, the development of faster computers and better simulation models or algorithms may help us better understand the confinement effect in a highly concentrated environment. However, we observe a provocative structure-breaking effect of ions and enhanced water diffusion under charged confinement, which is absent in classical MD simulations of bulk solutions. This observation may serve as a starting point for development of better force fields, and encourage further understanding of the observed enhanced water dynamics.

8.3 References

1. Adam, G.; Gibbs, J. H. On Temperature Dependence of Cooperative Relaxation Properties in Glass-Forming Liquids. *J. Chem. Phys.* **1965,** *43*, 139-146.

Appendix A: Force-Field Parameters

A1. Force-Field Parameters for Lithium Triflate

Table A.1 Lennard-Jones parameters and charges

Atom	σ (nm)	ε (kJ mol^{-1})	q
C	0.350	0.276144	0.36
F	0.295	0.221752	-0.12
S	0.355	1.406	0.20
O	0.296	0.71128	-0.40
Li	0.212645	0.764793	1.00

Table A.2 Bonding parameters (we use harmonic bond potential (equation 2.3.3) for all the bonds in the triflate group)

Atom pair	Bond length (nm)	Force constant (kJ mol^{-1} nm^{-2})
C – F	0.1332	307105.6
C – S	0.1810	185769.6
S – O	0.1440	585760

Table A.3 Bond angle parameters (we use a harmonic angle potential (equation 2.3.4) to describe all the bond angles in the triflate group)

	Angle (deg)	Force constant (kJ mol^{-1} rad^{-2})
F – C – F	109.1	644.336
O – S – O	119	870.272
F – C – S	109.8	418.4
C – S – O	95.77	619.323

Table A.4 Dihedral parameters

	φ_0	Force constant (kJ mol^{-1})	Multiplicity
F – C – S – O	0	17.00	3

We use a periodic dihedral function to describe the above dihedral

$$V_{dihe} = k\,(1 + \cos(n\varphi - \varphi_0))$$

where V_{dihe} is the potential energy, k is the force constant, n is the multiplicity, φ is the angle between the F – C – S and C – S – O planes.

A2. Force-Field Parameters for the Nafion Sidechain

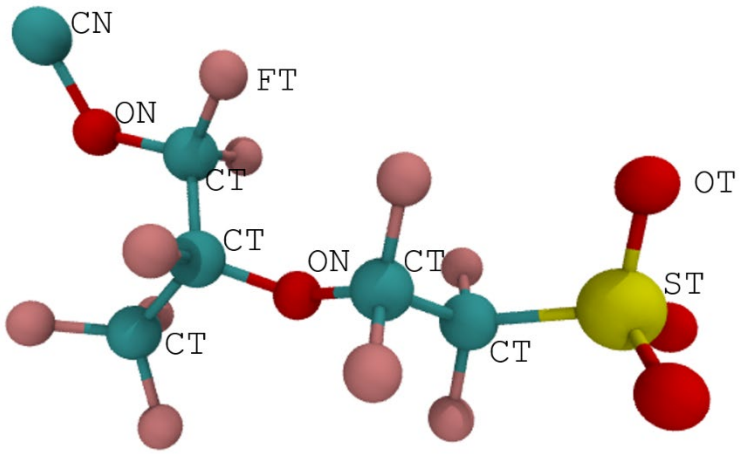

Figure A.1 Atom name description of the Nafion sidechain model. Note there are different types of oxygen atoms and carbon atoms.

Table A.5 Lennard Jones parameters and charges of atoms in the pendant sidechain (The functions we use to describe the bonds and bond angles in the Nafion sidechain model are the same as those used in the triflate group)

Atomic names	σ (nm)	ε (kJ mol^{-1})	q
CN	0.355	0.29288	0.00
ON	0.300	0.71128	-0.12
CT	0.350	0.276144	0.36
FT	0.295	0.221752	-0.12
ST	0.355	1.046	1.01
OT	0.296	0.71128	-0.67

Table A.6 Bond parameters

Bonds	Bond length (nm)	Force constant (kJ mol^{-1} nm^{-2})
CN – ON	0.1410	267144.0
CT – ON	0.1410	267144.0
CT – FT	0.1332	307105.6
CT – CT	0.1529	224362.4
CT – ST	0.1810	185769.6
ST – OT	0.1440	585760.0

Table A.7 Bond angles parameters

Bond angles	Angle (deg)	Force constant (kJ mol^{-1} rad^{-2})
CN – ON – CT	116.9	694.544

ON – CT – FT	109.8	425.000
ON – CT – CT	109.5	418.400
CT – CT – CT	112.5	488.273
CT – CT – FT	109.8	418.400
FT – CT – FT	109.1	644.336
CT – ON – CT	116.9	694.544
CT – CT – ST	114.7	418.400
CT – ST – OT	108.9	619.232
FT – CT – ST	109.5	418.400
OT – ST – OT	119.0	870.272

Table A.8 Dihedral parameters (Here, we employ Ryckaert-Bellemans function (equation 2.3.5) to describe the dihedral angles in the Nafion sidechain)

Dihedrals	C_0 (kJ/mol)	C_1 (kJ/mol)	C_2 (kJ/mol)	C_3 (kJ/mol)	C_4 (kJ/mol)	C_5 (kJ/mol)
CN – ON – CT – FT	0.239	0.717	0	-0.956	0	0
CN – ON – CT – CT	0.239	0.717	0	-0.956	0	0
ON – CT – CT – FT	0.239	0.717	0	-0.956	0	0
ON – CT – CT – ON	0.239	0.717	0	-0.956	0	0
CT – CT – CT – FT	0.985	-2.956	0	3.941	0	0
FT – CT – CT – FT	0.966	2.898	0	-3.865	0	0
CT – ON – CT – FT	0.239	0.717	0	-0.956	0	0
ON – CT – CT – ST	0.239	0.717	0	-0.956	0	0
CT – CT – ST – OT	0.239	0.717	0	-0.956	0	0
FT – CT – CT – ST	0.239	0.717	0	-0.956	0	0
FT – CT – ST – OT	0.239	0.717	0	-0.956	0	0

Appendix B: Written Programs

In addition to pre-built programs such as GROMACS and nanotube generator (which we use to generate initial coordinates for the carbon atoms in the carbon nanotubes), we also wrote computer programs to achieve desired functions, such as building up a new simulation model and conducting analyses that are not readily available. Most of these programs are written in Fortran programming language. We present two representative programs and their purpose in our simulations. The blue contents are comments/explanations to the codes.

B1. Building the rigid-rod model

The rigid-rod model appears multiple times throughout this dissertation, here we include the program that we use to build the parallel rigid-rod geometry.
In the rigid-rod model, each rod consists of stacked six-member carbon rings. The major geometry parameters include the distance between carbon atoms in the same ring, the distance between stacked carbon rings, the number of stacked rings in each rod, and the distance between parallel rods.

```
implicit none
double precision lcc,ltl            !Define carbon-to-carbon , layer-to-layer distance
double precision rhex               !Define rod-rod distance
integer nlayer,natom                !Define numbers of stacked rings and atoms
parameter (lcc=1.73,ltl=2.1,rhex=9.2)  !Assign numerical values to geometric parameters
parameter (nlayer=80)
double precision hexco(3,nlayer*6)      !Define an array to store the coordinate of the
                                        !carbon atoms in a template rod
double precision pi                     !Define π for later operations
integer i
double precision xi,yi
xi=SQRT(3.)*rhex/4.                 !All the rods are parallel in the z-direction, we can shift the
yi=rhex/4                           !coordinates of one rod in x- and y-directions to generate
                                    !the coordinates of other rods.
                                    !The xi and yi here, generated from the rod-rod distance,
                                    !serve as units for shifting.
```

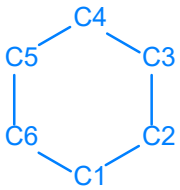


```
!                                   !These are the arrangement of the carbon atoms in the
!                                   !initial rod we are going to create in the next section.

      pi=4.*atan(1.)                !Assign the value of π to pi.
      natom=nlayer*6*4              !The total number of atoms equals the number of rings in
                                    !each rod times the number of carbon atoms in each ring
                                    !times the number of rods.
      write (6,*) natom
      write (6,*) 'RIGID ROD MODEL'

      do i=1,nlayer*6               !The loop here stores the coordinate of a carbon rod with
            if(mod(i,6)==1)then     !defined layers of rings centered at the origin.
            hexco(1,i)=lcc*sin(pi/3.)   !The mod(i,6) line determines the position of the atom in
            hexco(2,i)=-lcc*cos(pi/3.)  !the ring. When mod(i,6) equals 1, we are looking at the
            hexco(3,i)=ltl*(i/6)        !C1 atom in the description above
            else if(mod(i,6)==2)then    !hexco(1,i) stands for the x coordinate of atom i.
            hexco(1,i)=lcc*sin(pi/3.)   !hexco(2,i) stands for the y coordinate of atom i.
            hexco(2,i)=lcc*cos(pi/3.)   !hexco(3,i) stands for the z coordinate of atom i.
            hexco(3,i)=ltl*(i/6)
            else if(mod(i,6)==3)then
            hexco(1,i)=0
            hexco(2,i)=lcc
            hexco(3,i)=ltl*(i/6)
            else if(mod(i,6)==4)then
            hexco(1,i)=-lcc*sin(pi/3.)
            hexco(2,i)=lcc*cos(pi/3.)
            hexco(3,i)=ltl*(i/6)
            else if(mod(i,6)==5)then
            hexco(1,i)=-lcc*sin(pi/3.)
            hexco(2,i)=-lcc*cos(pi/3.)
            hexco(3,i)=ltl*(i/6)
            else if(mod(i,6)==0)then
            hexco(1,i)=0
            hexco(2,i)=-lcc
            hexco(3,i)=ltl*(i/6-1)
            endif
      enddo

100   FORMAT (a4,3f10.5)            !Defines the format for output.
                                    !“a4” means a character that takes up 4 spaces.
                                    !”3f10.5” means three floating-point number that takes a
                                    !total of 10 spaces while having five decimals.
```

```
!The four loops below create the final output .xyz file for a rigid-rod model with four rods.
!We applied shifts to the coordinates of the stored rod to generate four parallel rods in a
!hexagonal pattern
      do i=1,nlayer*6
      write (6,100) '  C',hexco(1,i)+3*xi,hexco(2,i)+yi,hexco(3,i)
      enddo
      do i=1,nlayer*6
      write (6,100) '  C',hexco(1,i)+3*xi,hexco(2,i)+5*yi,hexco(3,i)
      enddo
      do i=1,nlayer*6
      write (6,100) '  C',hexco(1,i)+xi,hexco(2,i)+3*yi,hexco(3,i)
      enddo
      do i=1,nlayer*6
      write (6,100) '  C',hexco(1,i)+xi,hexco(2,i)+7*yi,hexco(3,i)
      enddo

      end
```

B2. Calculation of the residence time

Here we describe the program to calculate residence time correlation function (S(t)) of confined water in the rigid-rod model. Detailed description of the residence time correlation function can be found in Ref. 19 of chapter 4.
This program first read a coordinate file from the simulation output. The coordinate file contains thousands of snapshots of the oxygen-atom coordinates. The program finds the oxygen atoms that are within the confined region and looks for the neighbors of all those oxygen atoms within a certain cut-off distance. Next, the program looks for how long the neighboring oxygen atoms stay together and generates the correlation function.

```
      implicit none
      integer i,j,k,l,m,n,io,m0,x,t,x1,x2          !Loop counters to be used in loops
      integer Nw, Nt                               !Define and assign values to the number of water
      parameter (Nw =10553, Nt = 6000)             !molecules and the number of snapshots
      double precision C0(3,Nw),T0(Nt)                        !Define the arrays to store the
      double precision oz(Nw),oy(Nw),ox(Nw)                   !coordinates of oxygen atoms
      double precision dist(Nw,Nw)                 !Define the array to store inter-oxygen distances
      double precision dmim
      integer nen                                  !Define the maximum number of neighbors
      parameter (nen=10)
      double precision Zl,Zr                !Define the left and right limits of the confined region
      double precision cuto,dt                     !Define the cut-off distance and the time interval
      parameter (cuto=0.33,dt=0.01)                !between snapshots
      double precision lx,ly,cr                          !Define and assign values to the box size
      parameter (lx=4.11025,ly=4.74610,cr=0.34)    !and a minimum distance
      integer nb(Nt,Nw,nen+1)                      !Define an array to record the index of neighbors
                                                   !for each molecule and the state of the molecule
```

```
  integer s(Nt/2),ss(Nt/2),flag           !Define the denominator and numerator of the
                                          !correlation function and a flag value
  character(8) :: date
  character(10) :: t1,t2                  !For time efficiency estimation
  character(5) :: zone
  integer,dimension(8) :: values
  call date_and_time(date,t1,zone,values)         !Record program start time

  Zl = 3.0                                !Assign values to the left and right limits of the
  Zr = 21.59                              !confined region. These values depend on the size
                                          !of water reservoirs.

  do i=1,Nt/2                             !!!!!!!!!!!!!!!!!!!!!!!!!!!!!!!!!!!!!!!!!!!!!!!!!!!!!!!!!!!!!!!!!!!!!!!!!!!!!!!!
    s(i)=0                                !
    ss(i)=0                               !
  enddo                                   !
                                          !
  do i=1,nen+1                            !
    nb(:,:,i)=0                           !        Assign initial values to the arrays
  enddo                                   !
                                          !
  do i=1,Nw                               !
  do j=1,Nw                               !
  dist(i,j)=0.0                           !
  enddo                                   !
  enddo                                   !!!!!!!!!!!!!!!!!!!!!!!!!!!!!!!!!!!!!!!!!!!!!!!!!!!!!!!!!!!!!!!!!!!!!!!!!!!!!!!!!

  DO i = 1,Nt
  READ(5,*,IOSTAT=io) T0(i),C0(:,:)       !Read the coordinate file
    do j = 1,Nw                           !Store the coordinates of the oxygen atoms
      oz(j)=C0(3,j)
      ox(j)=C0(1,j)
      oy(j)=C0(2,j)
    enddo
    do k=1,Nw
      if (oz(k)>Zl+0.6.and.oz(k)<Zr-0.6)then      !If the atom is within the confined region,
      nb(i,k,nen+1)=1                             !then store the state as "1"
      do l=1,Nw
      if (l/=k.and.oz(l)>Zl.and.oz(l)<Zr.and.             !From the line until the next
&   ABS(oz(k)-oz(l))<0.6)then                             !comment, the program fins the
      dist(k,l)=sqrt((oz(k)-oz(l))**2+(ox(k)-ox(l))**2+   !minimum distance between atom
&     (oy(k)-oy(l))**2)                                   !k and atom l, with periodic boundary
      if (ox(k)<cr)then                                   !conditions considered.
      ox(k)=ox(k)+lx
      if (ox(l)>lx-cr)then
      dist(k,l)=sqrt((oz(k)-oz(l))**2+(ox(k)-ox(l))**2+
&     (oy(k)-oy(l))**2)
      endif
      ox(k)=ox(k)-lx
      else if(ox(k)>lx-cr)then
```

```
      ox(k)=ox(k)-lx
      if (ox(l)<cr)then
      dist(k,l)=sqrt((oz(k)-oz(l))**2+(ox(k)-ox(l))**2+
&    (oy(k)-oy(l))**2)
      endif
      ox(k)=ox(k)+lx
      endif
      if (oy(k)<cr)then
      oy(k)=oy(k)+ly
      if (oy(l)>ly-cr)then
      dist(k,l)=sqrt((oz(k)-oz(l))**2+(ox(k)-ox(l))**2+
&    (oy(k)-oy(l))**2)
      endif
      oy(k)=oy(k)-ly
      else if(oy(k)>ly-cr)then
      oy(k)=oy(k)-ly
      if (oy(l)<cr)then
      dist(k,l)=sqrt((oz(k)-oz(l))**2+(ox(k)-ox(l))**2+
&    (oy(k)-oy(l))**2)
      endif
      oy(k)=oy(k)+ly
      endif
      if (ox(k)<cr.and.oy(k)<cr)then
      ox(k)=ox(k)+lx
      oy(k)=oy(k)+ly
      if (ox(l)>lx-cr.and.oy(l)>ly-cr)then
      dist(k,l)=sqrt((oz(k)-oz(l))**2+(ox(k)-ox(l))**2+
&    (oy(k)-oy(l))**2)
      endif
      ox(k)=ox(k)-lx
      oy(k)=oy(k)-ly
      else if(ox(k)<cr.and.oy(k)>ly-cr)then
      ox(k)=ox(k)+lx
      oy(k)=oy(k)-ly
      if (ox(l)>lx-cr.and.oy(l)<cr)then
      dist(k,l)=sqrt((oz(k)-oz(l))**2+(ox(k)-ox(l))**2+
&    (oy(k)-oy(l))**2)
      endif
      ox(k)=ox(k)-lx
      oy(k)=oy(k)+ly
      else if(ox(k)>lx-cr.and.oy(k)>ly-cr)then
      ox(k)=ox(k)-lx
      oy(k)=oy(k)-ly
      if (ox(l)<cr.and.oy(l)<cr)then
      dist(k,l)=sqrt((oz(k)-oz(l))**2+(ox(k)-ox(l))**2+
&    (oy(k)-oy(l))**2)
      endif
      ox(k)=ox(k)+lx
      oy(k)=oy(k)+ly
      else if(ox(k)>lx-cr.and.oy(k)<cr)then
      ox(k)=ox(k)-lx
```

```
      oy(k)=oy(k)+ly
      if (ox(l)<cr.and.oy(l)>ly-cr)then
      dist(k,l)=sqrt((oz(k)-oz(l))**2+(ox(k)-ox(l))**2+
&    (oy(k)-oy(l))**2)
      endif
      ox(k)=ox(k)+lx
      oy(k)=oy(k)-ly
      endif
     endif
     enddo
     endif
     enddo

      do k=1,Nw              !This loop finds all the atom l that is with the cut-off distance of
        x=0                  !atom k. The index of atom l is store into the array.
        do l=1,Nw
          if(dist(k,l)<cuto.and.l/=k.and.dist(k,l)>0.1)then
          x=x+1
          nb(i,k,x)=l
          dmim=dist(k,l)
          endif
        enddo
        dmim=10.0
      enddo

    ENDDO

    do i=1,Nt/2              !This part calculates the residence time correlation function
    do k=1,Nw
    if(nb(i,k,nen+1)==1)then !Start calculation when the atom is within the confined region
      do m=1,Nt/2                  !Start counting from different starting points
      n=i+m
      if(nb(n,k,nen+1)==1)then     !When a molecule continuously stays within the confined
      ss(m)=ss(m)+1                !region, increase the denominator by 1.
      else                         !Otherwise, stop the loop
      exit
      endif
      enddo

      do m=1,Nt/2                  !The loop here looks for the first neighbor of atom k in
      n=i+m                        !snapshot n and see if its neighbor stays continuously
      IF(nb(n,k,nen+1)==1)then     !within the cut-off distance of same molecule.
      flag=0
      do x=1,nen
      if(nb(i,k,1)/=0.and.nb(n,k,x)/=0.and.nb(n,k,x)==nb(i,k,1))then
      flag=1                       !If yes, set the flag to 1
      else if(nb(i,k,1)==0)then
      flag=0
      exit
      else if(nb(n,k,x)==0)then
      exit
```

```
endif
enddo                          !When the flag equals to 1, the neighbor continuously
if (flag==1)then               !stays with the same molecule for a period of m steps.
  s(m)=s(m)+1                  !Then increase the numerator by 1.
else if (flag==0)then
  exit
endif
else if(nb(n,k,nen+1)==0)then
exit
endif
enddo

do m=1,Nt/2                    !The loop here looks for the second neighbor. Similar
n=i+m                          !loop is repeated until the tenth neighbor. It is quite rare
IF(nb(n,k,nen+1)==1)then       !that a water molecule would have ten neighbors within the
flag=0                         !cut-off distance of 0.33 nm, which happens less than once
do x=1,nen                     !per million instances.
if(nb(i,k,2)/=0.and.nb(n,k,x)/=0.and.nb(n,k,x)==nb(i,k,2))then
flag=1
else if(nb(i,k,2)==0)then
flag=0
exit
else if(nb(n,k,x)==0)then
exit
endif
enddo
if (flag==1)then
  s(m)=s(m)+1
else if (flag==0)then
  exit
endif
else if(nb(n,k,nen+1)==0)then
exit
endif
enddo

do m=1,Nt/2
n=i+m
IF(nb(n,k,nen+1)==1)then
flag=0
do x=1,nen
if(nb(i,k,3)/=0.and.nb(n,k,x)/=0.and.nb(n,k,x)==nb(i,k,3))then
flag=1
else if(nb(i,k,3)==0)then
flag=0
exit
else if(nb(n,k,x)==0)then
exit
endif
enddo
if (flag==1)then
```

```
  s(m)=s(m)+1
else if (flag==0)then
  exit
endif
else if(nb(n,k,nen+1)==0)then
exit
endif
enddo

do m=1,Nt/2
n=i+m
IF(nb(n,k,nen+1)==1)then
flag=0
do x=1,nen
if(nb(i,k,4)/=0.and.nb(n,k,x)/=0.and.nb(n,k,x)==nb(i,k,4))then
flag=1
else if(nb(i,k,4)==0)then
flag=0
exit
else if(nb(n,k,x)==0)then
exit
endif
enddo
if (flag==1)then
  s(m)=s(m)+1
else if (flag==0)then
  exit
endif
else if(nb(n,k,nen+1)==0)then
exit
endif
enddo

do m=1,Nt/2
n=i+m
IF(nb(n,k,nen+1)==1)then
flag=0
do x=1,nen
if(nb(i,k,5)/=0.and.nb(n,k,x)/=0.and.nb(n,k,x)==nb(i,k,5))then
flag=1
else if(nb(i,k,5)==0)then
flag=0
exit
else if(nb(n,k,x)==0)then
exit
endif
enddo
if (flag==1)then
  s(m)=s(m)+1
else if (flag==0)then
  exit
```

```
endif
else if(nb(n,k,nen+1)==0)then
exit
endif
enddo

do m=1,Nt/2
n=i+m
IF(nb(n,k,nen+1)==1)then
flag=0
do x=1,nen
if(nb(i,k,6)/=0.and.nb(n,k,x)/=0.and.nb(n,k,x)==nb(i,k,6))then
flag=1
else if(nb(i,k,6)==0)then
flag=0
exit
else if(nb(n,k,x)==0)then
exit
endif
enddo
if (flag==1)then
  s(m)=s(m)+1
else if (flag==0)then
  exit
endif
else if(nb(n,k,nen+1)==0)then
exit
endif
enddo

do m=1,Nt/2
n=i+m
IF(nb(n,k,nen+1)==1)then
flag=0
do x=1,nen
if(nb(i,k,7)/=0.and.nb(n,k,x)/=0.and.nb(n,k,x)==nb(i,k,7))then
flag=1
else if(nb(i,k,7)==0)then
flag=0
exit
else if(nb(n,k,x)==0)then
exit
endif
enddo
if (flag==1)then
  s(m)=s(m)+1
else if (flag==0)then
  exit
endif
else if(nb(n,k,nen+1)==0)then
exit
```

```
endif
enddo

do m=1,Nt/2
n=i+m
IF(nb(n,k,nen+1)==1)then
flag=0
do x=1,nen
if(nb(i,k,8)/=0.and.nb(n,k,x)/=0.and.nb(n,k,x)==nb(i,k,8))then
flag=1
else if(nb(i,k,8)==0)then
flag=0
exit
else if(nb(n,k,x)==0)then
exit
endif
enddo
if (flag==1)then
  s(m)=s(m)+1
else if (flag==0)then
  exit
endif
else if(nb(n,k,nen+1)==0)then
exit
endif
enddo

do m=1,Nt/2
n=i+m
IF(nb(n,k,nen+1)==1)then
flag=0
do x=1,nen
if(nb(i,k,9)/=0.and.nb(n,k,x)/=0.and.nb(n,k,x)==nb(i,k,9))then
flag=1
else if(nb(i,k,9)==0)then
flag=0
exit
else if(nb(n,k,x)==0)then
exit
endif
enddo
if (flag==1)then
  s(m)=s(m)+1
else if (flag==0)then
  exit
endif
else if(nb(n,k,nen+1)==0)then
exit
endif
enddo
```

```
  do m=1,Nt/2
  n=i+m
  IF(nb(n,k,nen+1)==1)then
  flag=0
  do x=1,nen
  if(nb(i,k,10)/=0.and.nb(n,k,x)/=0.and.nb(n,k,x)==nb(i,k,10))then
  flag=1
  else if(nb(i,k,10)==0)then
  flag=0
  exit
  else if(nb(n,k,x)==0)then
  exit
  endif
  enddo
  if (flag==1)then
    s(m)=s(m)+1
  else if (flag==0)then
    exit
  endif
  else if(nb(n,k,nen+1)==0)then
  exit
  endif
  enddo
endif
enddo
enddo

do m=1,Nt/2       !This loop outputs the residence time correlation function
   print *,m*dt,real(s(m))/real(ss(m))
enddo

call date_and_time(date,t2,zone,values)          !Record the program end time
print *,t1              !Output program start and end time for estimation of time efficiency
print *,t2

end
```